A SYSTEMATIC APPROACH TO OPTIMIZED DESIGN OF PERMANENT MAGNET MOTORS WITH REDUCED TORQUE PULSATIONS

by

Damir Zarko

A dissertation submitted in partial fulfillment of
the requirements for the degree of

Doctor of Philosophy

(Electrical Engineering)

at the

UNIVERSITY OF WISCONSIN–MADISON

2004

A SYSTEMATIC APPROACH TO OPTIMIZED DESIGN OF PERMANENT MAGNET MOTORS WITH REDUCED TORQUE PULSATIONS

Damir Zarko

Under the supervision of Professor Thomas A. Lipo
At the University of Wisconsin-Madison

This thesis deals with optimal design of surface and interior permanent magnet motors with an emphasis on reduced torque pulsations while maximizing the motor performance in all regimes of operation and minimizing the size of the motor. The optimization for both types of motors has been formulated as a constrained multiobjective minimization problem where a population of non-dominant solutions is determined from which a single solution is selected as the best compromise. This optimization scheme is based on Differential Evolution optimization algorithm.

A novel approach to analytical field calculation in the air gap of a surface PM motor has been developed. The concept of complex relative air gap permeance has been derived based on conformal mapping of the slot geometry and used to accurately calculate the radial and tangential components of the flux density in the slotted air gap. This model of air gap permeance has been utilized to calculate the motor parameters, including losses and efficiency, needed for the design optimization.

For an interior PM motor the finite element method has been used to calculate its parameters during the optimization process. The principle of permeance freezing has been applied to extract lumped parameters from the FE model at any steady state operating point. A combined analytical and numerical technique has also been developed to reduce the time required for cogging torque calculations which utilizes the complex relative air gap permeance to estimate the cogging torque waveform based on only two magnetostatic FE simulations.

The effectiveness of the proposed design methodology has been shown on examples of a 5 kW SPM motor and a 1.65 kW IPM motor with two layers of cavities in the rotor for which a prototype has been built and tested. In addition, a comparative analysis has been carried out for the optimized 5 kW, 50 kW and 200 kW IPM motors with two and three layers of cavities in the rotor to show

design trade-offs between goals to minimize the motor volume while maximizing the power output in the field weakening regime with the back emf constraint as the main limiting factor in the design.

Thomas A. Lipo

ABSTRACT

This thesis deals with optimal design of surface and interior permanent magnet motors with an emphasis on reduced torque pulsations while maximizing the motor performance in all regimes of operation and minimizing the size of the motor. The optimization for both types of motors has been formulated as a constrained multiobjective minimization problem where a population of non-dominant solutions is determined from which a single solution is selected as the best compromise. This optimization scheme is based on Differential Evolution optimization algorithm.

A novel approach to analytical field calculation in the air gap of a surface PM motor has been developed. The concept of complex relative air gap permeance has been derived based on conformal mapping of the slot geometry and used to accurately calculate the radial and tangential components of the flux density in the slotted air gap. This model of air gap permeance has been utilized to calculate the motor parameters, including losses and efficiency, needed for the design optimization.

For an interior PM motor the finite element method has been used to calculate its parameters during the optimization process. The principle of permeance freezing has been applied to extract lumped parameters from the FE model at any steady state operating point. A combined analytical and numerical technique has also been developed to reduce the time required for cogging torque calculations which utilizes the complex relative air gap permeance to estimate the cogging torque waveform based on only two magnetostatic FE simulations.

The effectiveness of the proposed design methodology has been shown on examples of a 5 kW SPM motor and a 1.65 kW IPM motor with two layers of cavities in the rotor for which a prototype has been built and tested. In addition, a comparative analysis has been carried out for the optimized 5 kW, 50 kW and 200 kW IPM motors with two and three layers of cavities in the rotor to show

design trade-offs between goals to minimize the motor volume while maximizing the power output in the field weakening regime with the back emf constraint as the main limiting factor in the design.

ACKNOWLEDGMENTS

I would like to thank my advisor, Professor Thomas A. Lipo, for all his generous support, expert guidance and constant willingness to run stimulating discussions about every aspect of my work.

I am also grateful to other WEMPEC professors, namely Thomas M. Jahns, Robert D. Lorenz and Giri Venkataramanan for everything I learned from them throughout the lectures and discussions we had. I also thank Professor Annette Muetze for accepting my last minute invitation to serve in the defense committee and for enthusiasm and interest she showed about my work.

I am very thankful to my office mates Ayman El-Refaie and Jonathan Bird for valuable discussions about the mysteries of electrical machines and to Eric Benedict for helping me to master LaTeX.

I also wish to express my gratitude to Mr. Stevo Marčetić from KONČAR-MES, Zagreb, Croatia, Mr. Branimir Čurkov, Professor Gorazd Štumberger from University of Maribor, Slovenia and all other people in Croatia who invested their valuable time and effort to construct the prototype IPM motor.

A special thanks also goes to Ray Marion for all the help he provided me during the time I spent in Madison.

A very special thanks goes to my colleague Jackson Wai for generously sharing his hardware setup and for valuable help he provided me while conducting experiments on the prototype motor. I also thank Dr. Pierluigi Tenca for his help with the experiments.

I also express my gratitude to Professor Grahame Holmes from Monash University in Melbourne, Australia for his help in organizing the video conference with Australia and enabling me to execute my final defense.

I thank Kellian, Deri and Bo for proofreading the thesis.

I also thank my previous advisor Professor Drago Ban and all my colleagues from University of Zagreb, Croatia for their support, encouragement and patience during my absence from the university to which I am returning.

I also thank my dear friends Jelena and Snežana for all the joy that their love and friendship brought to my life.

Finally, I express my deepest love and gratitude to my parents, my sister and my grandmother for all their love and support during the time I spent here in Madison, Wisconsin.

DISCARD THIS PAGE

TABLE OF CONTENTS

DISCARD THIS PAGE

LIST OF TABLES

Table Page

DISCARD THIS PAGE

LIST OF FIGURES

Figure Page

Figure Page

Figure Page

Figure Page

Figure Page

Figure Page

Figure Page

Figure Page

Chapter 1

Introduction and Literature Review

The permanent magnet motors have become essential parts of modern motor drives. Some of the advantages they possess over their counterparts with electromagnetic excitation include higher torque density, higher efficiency (because there are no losses associated with the field excitation system) and simpler construction and maintenance.

The presence of magnets as a constant source of flux which cannot be turned off provides the PM motor with some intrinsic properties which can be challenging for the motor designer. One of these properties is the inevitable presence of torque pulsations which are highly undesirable in some applications like servo drives or electric steering. The main sources of torque pulsations are the cogging torque and the ripple torque. The cogging torque occurs due to the tendency of the rotor to line up with the stator in a particular direction where the permeance of the magnetic circuit seen by the magnets is maximized. The ripple torque is caused by the mismatch between the back emf and the current waveforms and also by the presence of slots.

The two main approaches to pulsating torque minimization are based on either an adequate motor design with intrinsically low pulsating torque for the assumed current waveform or on control techniques which actively compensate the pulsating torque. Most of the techniques used for reduction of the pulsating torque in PM motors based on motor design and control have already been reviewed in detail by Jahns and Soong in 1996 [1]. Therefore the review of the pulsating torque minimization has been covered in this introduction in a more general form with the addition of the period from 1996 until the present.

One of the design techniques for cogging torque reduction which has not been mentioned in [1] is teeth pairing reported by Hwang et al. [2, 3]. It involves the shifting of the slot openings in the opposite direction to each other for every two consecutive slots by an appropriate angle which can result in the elimination of the fundamental component of the cogging torque.

Two more useful reviews which are focused on the cogging torque reduction techniques based on motor design are given by Zhu and Howe [4] and Bianchi and Bolognani [5].

Some of the commonly used techniques for cogging torque reduction analyzed in these papers with their benefits and drawbacks have been summarized in Table 1.1. All of the techniques summarized in this table are applicable to surface PM motors, but not all of them can be used for interior PM motors. The techniques which involve modification of the stator, like skewing of the slots, fractional slot winding or teeth pairing, are applicable to interior PM motors as well, but techniques which involve the rotor are reduced to skewing and magnet shaping. The skewing of magnets may be technologically difficult to achieve and quite expensive. Since magnets in interior PM motors come in different shapes, it is difficult to set a unique rule about the magnet angular span and position which yields minimum cogging torque. Finite element simulations, usually combined with optimization, are required to find the optimal magnet shape [6–9]. Recently Zhu et al. [10] showed that the rule which defines the optimal pole arc length for cogging torque reduction derived for surface PM motors can be used for interior PM motors as well. The rotor of their motor had a single flux barrier, which is only one of many possible magnet shapes. Nevertheless, the correctness of this approach has also been confirmed in this thesis for the case of an IPM motor with two layers of flux barriers in the rotor. It has been shown that the angular span of the flux barriers for which a minimum cogging torque is achieved follows the same rule as presented in [10].

This thesis does not propose a new technique for cogging torque reduction, but it uses some of the techniques in Table 1.1 for the purpose of designing the surface and interior PM motors with reduced pulsating torque.

The main control based techniques for pulsating torque minimization include the following:

Table 1.1 Commonly used techniques for cogging torque reduction

Method	Benefits	Drawbacks
Skewing of stator slots or rotor magnets (1)	+ ideally eliminates cogging torque + reduces higher order back emf harmonics	– makes automatic slot filling very difficult – expensive to manufacture – reduces average torque – increases leakage inductance and stray losses – increases torque ripple in square-wave motors
Stepped skewing of magnet blocks (2)	+ cancels all cogging torque harmonics except for the multiples of the number of blocks + reduces higher order back emf harmonics except for the multiples of the number of blocks	– the same as for continuous skewing
Fractional slot winding (3)	+ reduces cogging torque by increasing its fundamental frequency	– higher harmonic leakage inductance – reduced fundamental component of flux linkage
Magnet pole arc width (4)	+ cancels fundamental component of the cogging torque	– sensitive to manufacturing tolerances
Magnet pole arc positioning (5)	+ cogging torque reduction similar to that of stepped skewing of rotor magnets	– creates problems for windings with parallel paths due to non-equal distribution of flux linkage under different poles – sensitive to manufacturing tolerances
Dummy slots and dummy teeth (6)	+ reduce cogging torque by increasing its fundamental frequency	– do not have a significant effect unless the dominant harmonic component of the cogging torque is much higher than the other harmonics
Teeth pairing (7)	+ cancels fundamental component of the cogging torque	– not feasible with narrow slots if the required shift of the slot opening is too high

(1) [4, 5, 11–13, 13–18]

(2) [5, 12]

(3) [1, 4]

(4) [4, 5, 12, 13, 19]

(5) [5, 19–21]

(6) [5, 12, 13, 16]

(7) [2, 3]

- The adjustment of the current waveform to cancel the pulsating torque components which would be generated when using sinusoidal or square wave current excitation [22–26],
- The techniques based on observers which treat the pulsating torque as a disturbance and add its estimated value to the torque command as a disturbance input decoupling term [27–34]
- The control of the current build-up in the on-going phase of the trapezoidal PM machines to prevent the torque spikes during commutation either with or without the use of additional current sensors [35–39],
- The use of the velocity state feedback to attenuate the torque pulsation which acts as a disturbance [29].

One of the problems of the open-loop techniques based on adjustment of the current waveform is their sensitivity to imperfect knowledge and variations of the motor parameters. Some alternative approaches using closed-loop control algorithms with online estimation techniques have been proposed [40, 41].

Although control based techniques for reduction of pulsating torque in PM motors can be quite effective, the main focus of this thesis is the optimized design of surface and interior PM motors which, besides satisfying the fundamental requirement for torque production, also need to have small pulsating torque for the assumed current waveform. The emphasis is given primarily to the motors for sinusoidal PM drives.

The goal of a motor designer is to find a good balance between satisfying all the requirements imposed by the specific task the motor should perform and utilizing the available materials in the best possible manner to reduce the cost. In every motor design the knowledge of the field distribution in the air gap is essential for prediction of the developed torque, the induced voltage and for determining the flux densities in specific parts of the motor (teeth, yoke etc.). Although accurate field calculations in electrical machines can be carried out using finite element method, numerical methods are in general more time consuming and do not provide closed form solutions. Alternatively analytical field solutions can be commonly expressed in the form of Fourier series which makes them more flexible as a design tool for predicting the motor performance. This is crucial when optimization is involved, because it requires numerous repetitive calculations before reaching the optimal solution which can be very time consuming. Unfortunately, the analytical field solutions are in most cases limited to surface PM motor designs. The concept of interior PM motor is often based on saturation of the flux paths in certain parts of the rotor, especially if magnets are fully buried and enclosed by the rotor core. In such a case only numerical techniques or lumped parameter models can be used to predict the motor performance and calculate its parameters.

An exact field solution in the air gap of a surface PM motor with radial or parallel magnetization has been given by Zhu et al. in [42, 43]. The method is based on a 2-D analytical solution of the Laplacian and Quasi-Poissonian equations with assumptions that the iron is infinitely permeable and the air gap is slotless. The effect of slotting was subsequently modelled in [44] by using relative air gap permeance obtained from the results of conformal transformation of the slot geometry. This general approach to modelling the effect of slotting, also used in several other papers [45–48] is based on multiplying the field distribution in the slotless air gap with the relative permeance function expressed as an infinite Fourier series. The solutions in [45–48] were able to provide fairly good estimates of the field in the slotted air gap only for radial component of the flux density. The tangential component was not included in the results even in the cases when conformal transformation was used. The method presented in this thesis provides a more complete analytical field solution than found in literature and allows one to calculate accurately both radial and tangential components of the air gap flux density in the slotted air gap (Chapter 2). It uses more extensively the complex nature of the conformal transformation and defines the relative air gap permeance as a complex number. This solution follows directly from the Schwarz-Christoffel transformation which is a complex function by nature [49]. It has been shown in this thesis that the results of proposed method show very good agreement with those obtained by the FE method for surface PM motors with radial and parallel magnetization. This verifies the correctness of the new approach.

The knowledge of both radial and tangential components of the air gap flux density allows one to derive closed form solutions for the cogging torque and the electromagnetic torque based on integration of the Maxwell's stress tensor along the circular line inside the air gap (Sections 2.6 and 3.3).

Another contribution of this thesis is the analytical expression for the cogging torque based on integration of the lateral forces on the slot sides (Section 2.7). The first attempt to calculate cogging torque using this approach was made by Zhu and Howe in [50]. Their approach assumes that the flux lines which enter the slot opening follow the circular arc before entering the slot sides. This may not be a good approximation for all sizes of the slot opening and in the cases of small tooth tips relative to the size of the slot opening which the authors themselves have noticed. The identical approach was used later by Proca et al. [46]. The approach used in this thesis is mathematically more rigorous and is based on calculation of the field distribution on the slot sides calculated from conformal mapping of the slot opening. However, it is affected by numerical problems that occur in the vicinity of the tooth tips which are singular points with infinite flux density. This is an artifact of conformal mapping which assumes infinite permeability of the iron core.

The proposed technique for field calculations in surface PM motors based on analytical solution of the field in the slotless air gap, combined with conformal mapping to take into account the effect of slotting, can be successfully used to determine all the motor parameters required for the design. This includes the time domain waveforms of the electromagnetic and cogging torque (Sections 2.6 and 3.3), the back emf waveform (Chapter 4) and the waveforms of the flux density in the stator teeth and yoke which are important for calculation of the core losses (Chapter 7). The results of the field calculations are then used in the optimized design of the motor (Chapter 8).

The optimization of a PM motor has been formulated as a constrained multiobjective minimization problem (Section 8.2). The main design objectives are to maximize efficiency and minimize the active volume of the motor. These two objectives generally lead to good motor performance, optimal utilization of the material and hence low cost of the machine. In addition, the maximum allowed torque ripple, current sheet density and flux densities in the core region and the minimum required power factor have been imposed as constraints.

The interior PM motor structure which has been the target of the optimization is a slightly modified version of the integrated starter-alternator with two layers of cavities designed by Lovelace [51]

(Section 8.3). Since the interior PM motor design in this thesis does not have a particular targeted application, as does the one in [51], but is rather used to show the effectivness of the proposed optimization scheme, the initial optimization goals have been set to minimize the cogging torque and to come as close as possible to satisfying the design criterion for optimal field weakening first shown by Schiferl and Lipo [52]. This criterion insures theoretically constant power operation up to infinite speed. For most practical IPM motor designs it is not possible to satisfy this criterion because the back emf is usually constrained to prevent uncontrolled generation in the entire speed range of operation. Lovelace also developed an optimized design of the motor based on the lumped parameter model and Monte Carlo optimization method. However, the lumped parameter model does not allow calculation of the cogging torque which is the emphasis of this thesis. Therefore, the finite element method had to be used here to carry out field calculations and determine motor parameters which are needed during optimization. Since FE simulations are time consuming and cogging torque calculation requires at least a dozen calculations for different rotor positions within one half-period of the cogging torque, a combined numerical and analytical approach has been developed which reduces the number of necessary FE calculations (Section 8.3.2). This approach uses complex relative air gap permeance to calculate the flux density distribution in the air gap as if no slots were present. Then the analytical solution based on integration of the Maxwell's stress tensor in the air gap is used to calculate the cogging torque. This approach requires only two magnetostatic FE simulations per one period of the cogging torque to estimate its waveform for all intermediate rotor positions. This saves a significant amount of time during optimization, where cogging torque needs to be calculated for hundreds of designs, before reaching the optimal solution. The main disadvantage of using the FE method compared to the lumped parameter model is the longer time needed to perform calculations which extends significantly the total computational time needed for reaching the optimal solution.

In general, there are two main approaches to multiobjective optimization. The first approach combines multiple objective functions into a single function defined as a weighted sum of individual objective functions [21]. The problem with this approach is how to determine the weight coefficients which are used to assign the level of importance to each individual objective. Although the result of the optimization can be some low value of the single objective function, some of the goals may end up not being sufficiently minimized or maximized, depending on the nature of the optimization. An alternative approach used in this thesis is to evaluate all the objective functions simultaneously and use nondominated selection to find a population of solutions which belong to the Pareto optimal set. A vector of decision variables $\vec{X}_0$ is Pareto optimal if there exists no feasible vector of decision variables $\vec{X}$ from the feasible region of the problem (i.e. where the constraints are satisfied) which would decrease some objectives without causing a simultaneous increase in at least one other criterion [53]. The set of solutions which satisfies this condition is called the *Pareto optimal set* and the vectors $\vec{X}_0$ corresponding to the solutions in the Pareto optimal set are called *nondominated*. The decision maker then chooses a single solution from the Pareto set as the compromise which suits his objectives the best.

The selected optimization method is *Differential Evolution* (Chapter 8). This algorithm was invented by Storn and Price in 1995 [54]. Since then it has proven to be very robust and fast converging population based global function minimizer for single objective [55, 56] and multiobjective [57–59] optimization problems. It has been successfully used in this thesis for multiobjective optimizations of the 5 kW surface PM motor and 1.65 kW interior PM motor with two layers of cavities in the rotor. A prototype of the optimal IPM motor design has been built and tested (Section 8.4). The motor performance determined by measurement was somewhat degraded compared to the performance predicted by the FE method due to lower value od the q axis inductance ($\sim$10-20%) and higher value of the d axis inductance ($\sim$10%), which both contributed to a significant loss of the reluctance torque. This difference between measured and calculated L_q and L_d has been attributed primarily to the increase of the effective air gap due to altered properties of the core material in the vicinity of the air gap caused by punching and laser cutting. However, this explanation cannot be completely supported by solid evidence without building one or more additional prototype motors which could then be compared.

An additional analysis has been carried out for the IPM motor which compares motors of different power ratings with two or three layers of cavities in the rotor (Section 8.5). The finite element based multiobjective optimization scheme has been utilized to design 5 kW, 50 kW and 200 kW motors. The design objectives observed simultaneously have been to minimize the active volume of the motor and to achieve the best possible match between the characteristic and the rated current (optimal field weakening criterion). The main design constraint has been the value of the back emf at maximum speed which has not been allowed to exceed the rated terminal voltage. In addition the motor must produce minimum required torque in the constant torque regime (zero to corner speed). Some useful observations have been made which show the design trade-offs between goals of minimizing the motor volume and maximizing the power output in the field weakening regime.

Chapter 2

Calculation of Cogging Torque in Surface PM Motors

The analytical approach to cogging torque calculation most commonly found in literature is either based on calculation of the rate of change of total magnetic energy in the air gap with respect to the rotor angular position [3, 18, 47] or on summation of the lateral magnetic forces along the sides of the stator teeth [50]. In analytical calculations it is commonly assumed that iron is infinitely permeable and that the rate of change of energy in iron is negligible. Therefore, only the change of magnetic energy in the air gap will contribute to cogging torque production.

For precise cogging torque calculation the former method requires detailed knowledge of the flux density distribution in the entire air gap. The knowledge of both radial and tangential components of the flux density is necessary because, although the tangential component is small, its contribution to the rate of change of energy with respect to the rotor position is significant. If the field in the air gap is known precisely, an alternative to calculating the rate of change of magnetic energy in the air gap volume is to calculate the cogging torque by integrating Maxwell's stress tensor along the circular surface inside the air gap. In the motor design it is commonly assumed that the field distribution is equal in every cross-sectional plane in the axial direction. Thus the integration of Maxwell's stress is reduced to a solution of the line integral, whereas the air gap energy requires the solution of a surface integral which is computationally more expensive. Two different approaches to cogging torque calculation, both based on integration of the Maxwell's stress tensor in the air gap, have been developed. In the first approach the closed form solution for the cogging torque has been found by integrating the tangential component of the stress tensor along the circular arc inside the air gap. In the second approach the cogging torque is calculated by numerical integration of the normal component of the stress tensor along the slot sides.

A novel approach to analytical air gap field calculation is developed in this thesis which is used to calculate the Maxwell's stress tensor. The analytical field solution is found by combining the field solution in the slotless air gap developed by Zhu et al. [42, 43] and the complex relative air gap permeance calculated from conformal transformation of the slot geometry. The notion of complex permeance and its usefulness for calculation of the radial and tangential components of the air gap field in the slotted motor will be explained in detail in Section 2.2.

In order to simplify the calculations certain assumptions are made which can be summarized in the following manner:

a) the permeability of iron is infinite,

b) the field distribution does not change in the axial direction, i.e. the end effects are neglected,

c) the slot openings have rectangular shape and are infinitely deep,

d) the magnetic field distribution is determined from the product of the flux density produced by the magnets in a slotless stator and the complex relative air gap permeance,

e) the relative air gap permeance is determined using conformal transformation of the slot geometry.

2.1 Magnetic Field Distribution in the Slotless Surface PM Motor

The initial phase of cogging torque calculation is the evaluation of the flux density in the air gap of a slotless PM motor. The analytical technique developed by Howe and Zhu [42, 43] has been used to calculate this field distribution. The main focus at this point will be PM motors with surface-mounted magnets and radial or parallel magnetization. The effect of slotting will be added subsequently by using conformal transformation of the slot geometry.

In the air gap of a PM machine the area occupied by the magnets and the area occupied by air have to be distinguished, as shown in Fig. 2.1, because the magnetic field in these two areas is governed by different equations.
The relation between the magnetic flux density $\vec{B}$ and the field intensity $\vec{H}$ in the air is

$$\vec{B}_I = \mu_0 \vec{H}_I \tag{2.1}$$

and in the permanent magnet is

$$\vec{B}_{II} = \mu_0 \mu_r \vec{H}_{II} + \mu_0 \vec{M} \tag{2.2}$$

where $\vec{M}$ is the magnetization vector and μ_r is the relative permeability of the magnet. For magnets with linear demagnetization characteristic the magnetization expressed in terms of remanent flux density is

$$\vec{M} = \frac{\vec{B}_r}{\mu_0} \tag{2.3}$$

For magnetostatic fields in a current-free region the two fundamental postulates that specify the divergence and the curl of $\vec{B}$ in free space are

$$\nabla \vec{B} = 0 \tag{2.4}$$

$$\nabla \times \vec{B} = 0 \tag{2.5}$$

Since the magnetic flux density has a zero curl, it can be expressed as a gradient of a scalar field. Let

$$\vec{B} = -\mu_0 \mu_r \nabla \varphi \tag{2.6}$$

If (2.6) is substituted into (2.4), the governing equation for magnetostatic field in the air in terms of the scalar magnetic potential is

$$\nabla(\nabla \varphi_I) = \triangle \varphi_I = 0 \tag{2.7}$$

A slightly different approach is required to evaluate the scalar magnetic potential inside the magnet. For field calculations a magnetized body can be replaced by an equivalent fictitious magnetization volume charge such that [60]

$$\rho_m = -\nabla(\mu_0 \vec{M}) \tag{2.8}$$

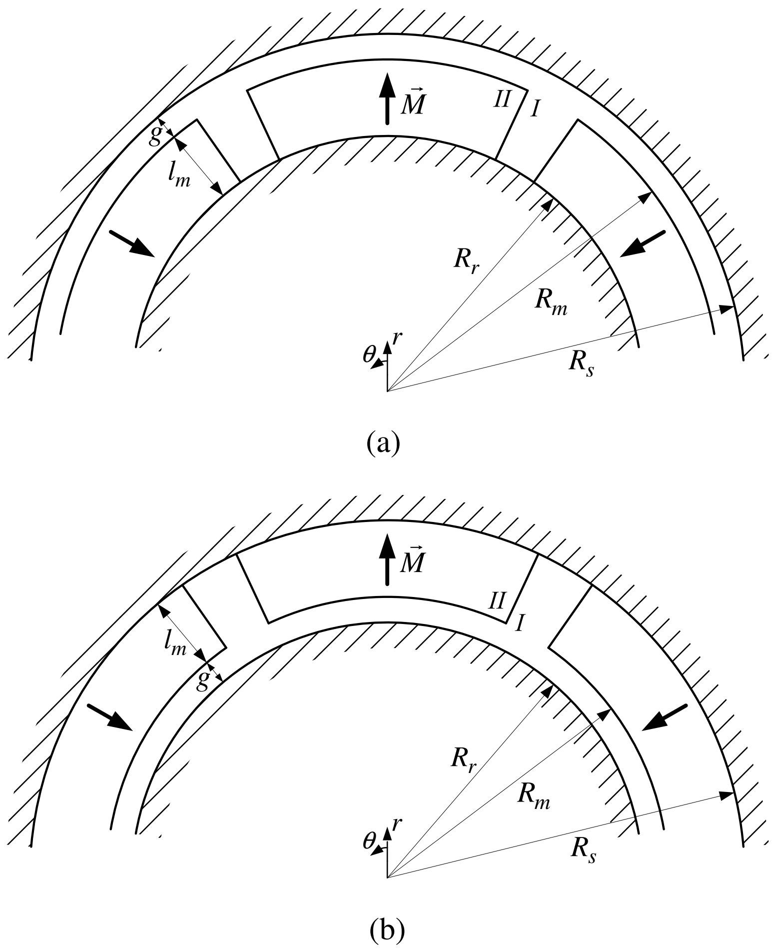

Fig. 2.1 Motor topologies: (a) internal rotor, (b) external rotor

The Maxwell's equation which relates the field $\vec{B}$ to its source, the magnetization charge, is given by

$$\nabla \vec{B} = \rho_m \tag{2.9}$$

Substituting (2.6) and (2.8) into (2.9) yields

$$\nabla(-\mu_0\mu_r\nabla\varphi_{II}) = -\nabla(\mu_0\vec{M}) \Rightarrow \triangle\varphi_{II} = \frac{1}{\mu_r}\nabla\vec{M} \tag{2.10}$$

In polar coordinates the magnetization vector $\vec{M}$ is given by

$$\vec{M} = M_r\vec{a}_r + M_\theta\vec{a}_\theta \tag{2.11}$$

Fig. 2.2 shows directions of the vector $\vec{M}$ for radial or parallel magnetization. In the case of radial magnetization the vector $\vec{M}$ is always perpendicular to the curved surface of the magnet and is parallel to its lateral edges. Hence the tangential component of the magnetization vector is always equal to zero. In the case of parallel magnetization the direction of magnetization is always parallel to the centerline of the magnet arc. Hence both radial and tangential components of the vector $\vec{M}$ exist. The waveforms of the radial and tangential components of $\vec{M}$ for both cases of magnetization are shown in Fig. 2.3.

For both radial and parallel magnetization the components M_r and M_θ can be expressed as Fourier series, i.e.

$$\begin{aligned} M_r &= \sum_{n=1,3,5...}^{\infty} M_{rn}\cos(np\theta) \\ M_\theta &= \sum_{n=1,3,5...}^{\infty} M_{\theta n}\sin(np\theta) \end{aligned} \tag{2.12}$$

where p is the number of pole pairs and θ is the angular displacement relative to the center of the magnet as shown in Fig. 2.2. For radial magnetization

$$\begin{aligned} M_{rn} &= \frac{B_r}{\mu_0}\frac{4}{n\pi}\sin\frac{n\pi\alpha_p}{2} \\ M_{\theta n} &= 0 \end{aligned} \tag{2.13}$$

where α_p is the magnet pole arc to pole pitch ratio.

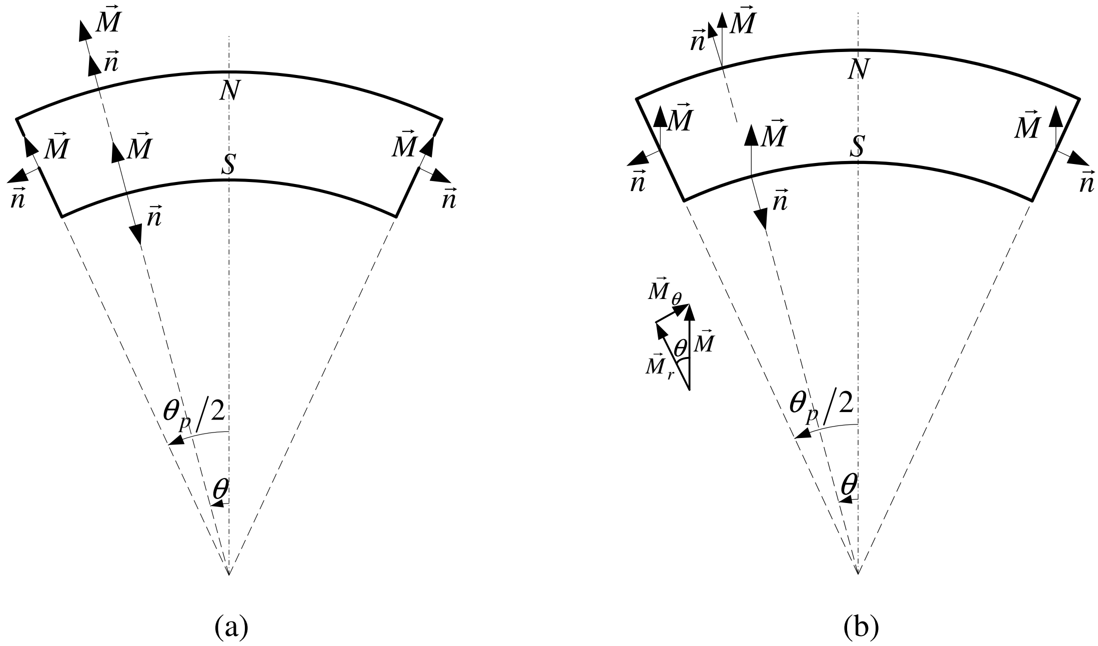

Fig. 2.2 Directions of magnetization: (a) radial, (b) parallel

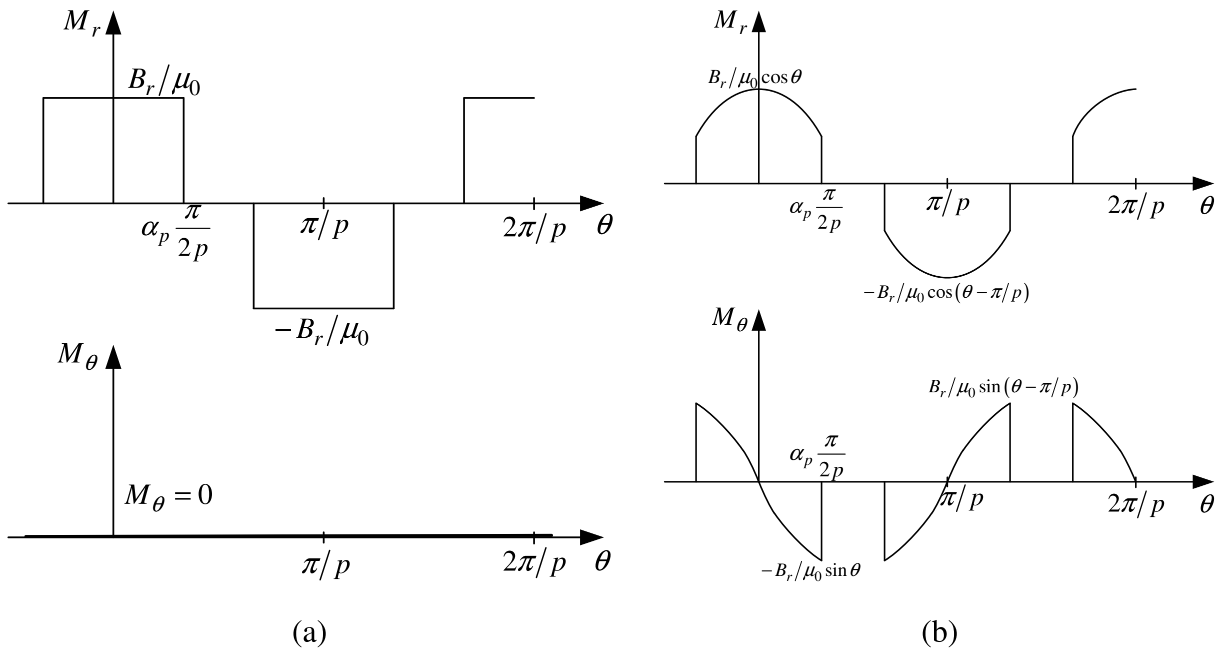

Fig. 2.3 Waveforms of magnetization components M_r and M_θ:
(a) radial magnetization, (b) parallel magnetization

For parallel magnetization

$$\begin{aligned} M_{rn} &= \tfrac{B_r}{\mu_0}\alpha_p(A_{1n}+A_{2n}) \\ M_{\theta n} &= \tfrac{B_r}{\mu_0}\alpha_p(A_{1n}-A_{2n}) \end{aligned} \tag{2.14}$$

where

$$\begin{aligned} A_{1n} &= \frac{\sin\left[(np+1)\alpha_p\frac{\pi}{2p}\right]}{(np+1)\alpha_p\frac{\pi}{2p}} \\ A_{2n} &= 1 \ \text{ for } \ np=1 \\ A_{2n} &= \frac{\sin\left[(np-1)\alpha_p\frac{\pi}{2p}\right]}{(np-1)\alpha_p\frac{\pi}{2p}} \ \text{ for } \ np\neq 1 \end{aligned}$$

The scalar magnetic potential distribution in the air is governed by Laplace's equation (2.7), which expressed in cylindrical coordinates is

$$\frac{\partial^2\varphi_I}{\partial r^2}+\frac{1}{r}\frac{\partial\varphi_I}{\partial r}+\frac{1}{r^2}\frac{\partial^2\varphi_I}{\partial\theta^2}=0 \tag{2.15}$$

The scalar potential in the permanent magnet is governed by quasi-Poissonian equation (2.10). The divergence of the magnetization vector, with its radial and tangential components given by (2.12), is

$$\nabla\vec{M}=\frac{1}{r}M_r+\frac{\partial M_r}{\partial r}+\frac{1}{r}\frac{\partial M_\theta}{\partial\theta}=\sum_{n=1,3,5\ldots}^{\infty}\frac{1}{r}M_n cos(np\theta) \tag{2.16}$$

where

$$M_n = M_{rn}+npM_{\theta n} \tag{2.17}$$

Combining (2.10) and (2.16) yields

$$\frac{\partial^2\varphi_{II}}{\partial r^2}+\frac{1}{r}\frac{\partial\varphi_{II}}{\partial r}+\frac{1}{r^2}\frac{\partial^2\varphi_{II}}{\partial\theta^2}=\frac{1}{\mu_r}\sum_{n=1,3,5\ldots}^{\infty}\frac{1}{r}M_n cos(np\theta) \tag{2.18}$$

Since

$$\vec{H}=-\nabla\varphi=-\frac{\partial\varphi}{\partial r}\vec{a}_r-\frac{1}{r}\frac{\partial\varphi}{\partial\theta}\vec{a}_\theta \tag{2.19}$$

the relation between the radial and tangential components of the field intensity $\vec{H}$ and the scalar magnetic potential is

$$H_r=-\frac{\partial\varphi}{\partial r}$$

$$H_\theta = -\frac{1}{r}\frac{\partial \varphi}{\partial \theta} \tag{2.20}$$

2.1.1 General Solutions in Polar Coordinates

For both internal and external rotor motors the problem of finding the scalar magnetic potential distribution in the air is a Laplacian problem in two dimensions. This can be solved by the separation of variables [61]. It entails seeking a solution which breaks up into a product of functions, each one involving only one of the variables. Hence the unknown scalar magnetic potential $\varphi(r,\theta)$ can be written in the form

$$\varphi_I(r,\theta) = R(r)F(\theta) \tag{2.21}$$

Substituting (2.21) into (2.15) and dividing through by RF/r^2 results in

$$\frac{r^2}{R}\frac{d^2R}{dr^2} + \frac{r}{R}\frac{dR}{dr} = -\frac{1}{F}\frac{d^2F}{d\theta^2} = \lambda^2 \tag{2.22}$$

where λ is the separation constant. Thus the separated equations are

$$F'' + \lambda^2 F = 0 \tag{2.23}$$

$$r^2R'' + rR' - \lambda^2 R = 0 \tag{2.24}$$

It is evident that (2.23) has the general solution of the form

$$F(\theta) = C_1\cos(\lambda\theta) + C_2\sin(\lambda\theta) \tag{2.25}$$

Since distribution of magnetization shown in Fig. 2.2 is a periodic even function, the function $F(\theta)$ should also be periodic and even. Thus $C_2 = 0$, $\lambda = np$ and (2.25) now becomes

$$F(\theta) = C_1\cos(\lambda\theta) \tag{2.26}$$

Equation (2.24), known as Cauchy-Euler equation, can be solved by making a substitution $r = e^u$ and reducing to an equation with constant coefficients. This leads to

$$R(r) = C_3r^{np} + C_4r^{-np},\ n = 1, 2, 3, ... \tag{2.27}$$

Substitution of (2.26) and (2.27) into (2.21) yields

$$\varphi_{nI}(r,\theta) = \left(A_{nI}r^{np} + B_{nI}r^{-np}\right)\cos(np\theta) \tag{2.28}$$

where A_{nI} and B_{nI} are constants to be determined. According to the superposition principle a linear combination of the solutions φ_{nI}, each with different value of n and with arbitrary coefficients A_{nI} and B_{nI}, is also a solution of (2.15). Thus the solution $\varphi_I(r,\theta)$ can be represented as an infinite series

$$\varphi_I(r,\theta) = \sum_{n=1}^{\infty}\left(A_{nI}r^{np} + B_{nI}r^{-np}\right)\cos(np\theta) \tag{2.29}$$

In the magnets the governing equation is (2.18). The general solution for $\varphi_{II}(r,\theta)$ is equal to the sum of the general solution of the homogenous equation $\triangle\varphi_{II} = 0$ and any solution of the nonhomogenous equation (2.18). The general solution of the homogenous equation is often referred to as the complementary solution [62] and can be denoted by $\varphi_{IIc}(r,\theta)$. The solution $\varphi_{IIc}(r,\theta)$ will have the same form as (2.29), i.e.

$$\varphi_{IIc}(r,\theta) = \sum_{n=1}^{\infty}\left(A_{nII}r^{np} + B_{nII}r^{-np}\right)\cos(np\theta) \tag{2.30}$$

A solution of the nonhomogenous equation is usually called a particular solution and can be denoted by $\varphi_{IIp}(r,\theta)$. A particular solution of the form

$$\varphi_{IIp}(r,\theta) = \sum_{n=1,3,5\ldots}^{\infty} C_1 r\cos(np\theta) \tag{2.31}$$

can be assumed. Substituting (2.31) into (2.18) the constant C_1 is obtained as

$$C_1 = \frac{1}{1-(np)^2}\frac{M_n}{\mu_r} \tag{2.32}$$

Therefore

$$\varphi_{IIp}(r,\theta) = \sum_{n=1,3,5\ldots}^{\infty}\frac{M_n}{\mu_r\left[1-(np)^2\right]}r\cos(np\theta) \tag{2.33}$$

However, this solution is not valid for the particular case of $np = 1$. Hence for $np = 1$, by letting $r = e^t$, (2.18) becomes

$$\frac{\partial^2\varphi_{IIp}}{\partial t^2} + \frac{\partial^2\varphi_{IIp}}{\partial\theta^2} = \frac{M_1}{\mu_r}e^t\cos\theta \tag{2.34}$$

Now assuming

$$\varphi_{IIp} = C_2 t e^t \cos\theta \tag{2.35}$$

and substituting into (2.34), the constant C_2 is obtained as

$$C_2 = \frac{1}{2}\frac{M_1}{\mu_r} \tag{2.36}$$

Therefore for $np = 1$

$$\varphi_{IIp}(r,\theta) = \frac{1}{2}\frac{M_1}{\mu_r} t e^t \cos\theta = \frac{1}{2}\frac{M_1}{\mu_r} r \ln r \cos\theta \tag{2.37}$$

The general solution of (2.18) for $np \neq 1$ is

$$\begin{aligned} \varphi_{II}(r,\theta) &= \varphi_{IIc}(r,\theta) + \varphi_{IIp}(r,\theta) \\ &= \sum_{n=1}^{\infty} \left(A_{nII} r^{np} + B_{nII} r^{-np} \right) \cos(np\theta) \\ &\quad + \sum_{n=1,3,5\ldots}^{\infty} \frac{M_n}{\mu_r\left[1-(np)^2\right]} r \cos(np\theta) \end{aligned} \tag{2.38}$$

and for $np = 1$

$$\varphi_{II}(r,\theta) = \left(A_{1II} r + B_{1II} r^{-1} \right) \cos\theta + \frac{M_1}{2\mu_r} r \ln r \cos\theta \tag{2.39}$$

The boundary conditions for the internal and external rotor motors of Fig. 2.1 are defined by

$$\begin{aligned} H_{\theta I}(r,\theta)\big|_{r=R_s} &= 0 \\ H_{\theta II}(r,\theta)\big|_{r=R_r} &= 0 \\ B_{rI}(r,\theta)\big|_{r=R_m} &= B_{rII}(r,\theta)\big|_{r=R_m} \\ H_{\theta I}(r,\theta)\big|_{r=R_m} &= H_{\theta II}(r,\theta)\big|_{r=R_m} \end{aligned} \tag{2.40}$$

where g is the air gap length, l_m is the radial thickness of the magnets, $R_m = R_s - g$ and $R_r = R_s - g - l_m$ for an internal rotor motor and $R_m = R_s + g$ and $R_r = R_s + g + l_m$ for an external rotor motor. The field components in equations (2.40) can be calculated by substituting solutions for the scalar magnetic potential (2.29), (2.38) and (2.39) into (2.20). Thus the unknown coefficients A_{nI}, B_{nI}, A_{nII} and B_{nII} can be obtained.

The complete solution for the magnetic field components in the air gap and the magnet regions is given by the following equations [42]:

For internal rotor motors ($np \neq 1$)

$$B_{rI}(r,\theta) = \sum_{n=1,3,5...}^{\infty} \frac{\mu_0 M_n}{\mu_r} \frac{np}{(np)^2-1} \left[\left(\frac{r}{R_s}\right)^{np-1} \left(\frac{R_m}{R_s}\right)^{np+1} + \left(\frac{R_m}{r}\right)^{np+1} \right] \left\{ \frac{(A_{3n}-1) + 2\left(\frac{R_r}{R_m}\right)^{np+1} - (A_{3n}+1)\left(\frac{R_r}{R_m}\right)^{2np}}{\frac{\mu_r+1}{\mu_r}\left[1-\left(\frac{R_r}{R_s}\right)^{2np}\right] - \frac{\mu_r-1}{\mu_r}\left[\left(\frac{R_m}{R_s}\right)^{2np} - \left(\frac{R_r}{R_m}\right)^{2np}\right]} \right\} \cos(np\theta) \tag{2.41}$$

$$B_{\theta I}(r,\theta) = \sum_{n=1,3,5...}^{\infty} \frac{\mu_0 M_n}{\mu_r} \frac{np}{(np)^2-1} \left[-\left(\frac{r}{R_s}\right)^{np-1} \left(\frac{R_m}{R_s}\right)^{np+1} + \left(\frac{R_m}{r}\right)^{np+1} \right] \left\{ \frac{(A_{3n}-1) + 2\left(\frac{R_r}{R_m}\right)^{np+1} - (A_{3n}+1)\left(\frac{R_r}{R_m}\right)^{2np}}{\frac{\mu_r+1}{\mu_r}\left[1-\left(\frac{R_r}{R_s}\right)^{2np}\right] - \frac{\mu_r-1}{\mu_r}\left[\left(\frac{R_m}{R_s}\right)^{2np} - \left(\frac{R_r}{R_m}\right)^{2np}\right]} \right\} \sin(np\theta) \tag{2.42}$$

$$\begin{aligned} B_{rII}(r,\theta) = & \sum_{n=1,3,5...}^{\infty} \mu_0 M_n \frac{np}{(np)^2-1} \left[\left(\frac{r}{R_m}\right)^{np-1} + \left(\frac{R_r}{R_m}\right)^{np-1} \left(\frac{R_r}{r}\right)^{np+1} \right] \\ & \left\{ \frac{(A_{3n}-\frac{1}{\mu_r})\left(\frac{R_m}{R_s}\right)^{2np} + (1+\frac{1}{\mu_r})\left(\frac{R_r}{R_m}\right)^{np+1}\left(\frac{R_m}{R_s}\right)^{2np} - \left(A_{3n}+\frac{1}{\mu_r}\right) -}{\frac{\mu_r+1}{\mu_r}\left[1-\left(\frac{R_r}{R_s}\right)^{2np}\right] - \frac{\mu_r-1}{\mu_r}\left[\left(\frac{R_m}{R_s}\right)^{2np} - \left(\frac{R_r}{R_m}\right)^{2np}\right]} \right. \\ & \left. \frac{\left(1-\frac{1}{\mu_r}\right)\left(\frac{R_r}{R_m}\right)^{np+1}}{\frac{\mu_r+1}{\mu_r}\left[1-\left(\frac{R_r}{R_s}\right)^{2np}\right] - \frac{\mu_r-1}{\mu_r}\left[\left(\frac{R_m}{R_s}\right)^{2np} - \left(\frac{R_r}{R_m}\right)^{2np}\right]} \right\} \cos(np\theta) \\ & + \sum_{n=1,3,5...}^{\infty} \mu_0 M_n \frac{np}{(np)^2-1} \left[\left(\frac{R_r}{r}\right)^{np+1} + A_{3n} \right] \cos(np\theta) \end{aligned} \tag{2.43}$$

$$B_{\theta II}(r,\theta) = \sum_{n=1,3,5...}^{\infty} -\mu_0 M_n \frac{np}{(np)^2-1}\left[\left(\frac{r}{R_m}\right)^{np-1} - \left(\frac{R_r}{R_m}\right)^{np-1}\left(\frac{R_r}{r}\right)^{np+1}\right]$$
$$\left\{\frac{(A_{3n}-\frac{1}{\mu_r})\left(\frac{R_m}{R_s}\right)^{2np} + (1+\frac{1}{\mu_r})\left(\frac{R_r}{R_m}\right)^{np+1}\left(\frac{R_m}{R_s}\right)^{2np} - \left(A_{3n}+\frac{1}{\mu_r}\right) -}{\frac{\mu_r+1}{\mu_r}\left[1-\left(\frac{R_r}{R_s}\right)^{2np}\right] - \frac{\mu_r-1}{\mu_r}\left[\left(\frac{R_m}{R_s}\right)^{2np} - \left(\frac{R_r}{R_m}\right)^{2np}\right]}\right.$$
$$\left.\frac{\left(1-\frac{1}{\mu_r}\right)\left(\frac{R_r}{R_m}\right)^{np+1}}{\frac{\mu_r+1}{\mu_r}\left[1-\left(\frac{R_r}{R_s}\right)^{2np}\right] - \frac{\mu_r-1}{\mu_r}\left[\left(\frac{R_m}{R_s}\right)^{2np} - \left(\frac{R_r}{R_m}\right)^{2np}\right]}\right\}\sin(np\theta)$$
$$+\sum_{n=1,3,5...}^{\infty} \mu_0 M_n \frac{1}{(np)^2-1}\left[np\left(\frac{R_r}{r}\right)^{np+1} - A_{3n}\right]\sin(np\theta) \tag{2.44}$$

For external rotor motors ($np \neq 1$)

$$B_{rI}(r,\theta) = \sum_{n=1,3,5...}^{\infty} -\frac{\mu_0 M_n}{\mu_r}\frac{np}{(np)^2-1}\left[\left(\frac{r}{R_m}\right)^{np-1} + \left(\frac{R_s}{R_m}\right)^{np-1}\left(\frac{R_s}{r}\right)^{np+1}\right]$$
$$\left\{\frac{(A_{3n}-1)\left(\frac{R_m}{R_r}\right)^{2np} + 2\left(\frac{R_m}{R_r}\right)^{np-1} - (A_{3n}+1)}{\frac{\mu_r+1}{\mu_r}\left[1-\left(\frac{R_s}{R_r}\right)^{2np}\right] - \frac{\mu_r-1}{\mu_r}\left[\left(\frac{R_s}{R_m}\right)^{2np} - \left(\frac{R_m}{R_r}\right)^{2np}\right]}\right\}\cos(np\theta) \tag{2.45}$$

$$B_{\theta I}(r,\theta) = \sum_{n=1,3,5...}^{\infty} -\frac{\mu_0 M_n}{\mu_r}\frac{np}{(np)^2-1}\left[\left(-\frac{r}{R_m}\right)^{np-1} + \left(\frac{R_s}{R_m}\right)^{np-1}\left(\frac{R_s}{r}\right)^{np+1}\right]$$
$$\left\{\frac{(A_{3n}-1)\left(\frac{R_m}{R_r}\right)^{2np} + 2\left(\frac{R_m}{R_r}\right)^{np-1} - (A_{3n}+1)}{\frac{\mu_r+1}{\mu_r}\left[1-\left(\frac{R_s}{R_r}\right)^{2np}\right] - \frac{\mu_r-1}{\mu_r}\left[\left(\frac{R_s}{R_m}\right)^{2np} - \left(\frac{R_m}{R_r}\right)^{2np}\right]}\right\}\sin(np\theta) \tag{2.46}$$

$$B_{rII}(r,\theta) = \sum_{n=1,3,5...}^{\infty} -\mu_0 M_n \frac{np}{(np)^2-1}\left[\left(\frac{r}{R_r}\right)^{np-1}\left(\frac{R_m}{R_r}\right)^{np+1} + \left(\frac{R_m}{r}\right)^{np+1}\right]$$
$$\left\{\frac{(A_{3n}-\frac{1}{\mu_r}) + (1+\frac{1}{\mu_r})\left(\frac{R_s}{R_m}\right)^{np+1}\left(\frac{R_s}{R_r}\right)^{np-1} - \left(A_{3n}+\frac{1}{\mu_r}\right)\left(\frac{R_s}{R_m}\right)^{2np} -}{\frac{\mu_r+1}{\mu_r}\left[1-\left(\frac{R_s}{R_r}\right)^{2np}\right] - \frac{\mu_r-1}{\mu_r}\left[\left(\frac{R_s}{R_m}\right)^{2np} - \left(\frac{R_m}{R_r}\right)^{2np}\right]}\right.$$
$$\left.\frac{\left(1-\frac{1}{\mu_r}\right)\left(\frac{R_m}{R_r}\right)^{np-1}}{\frac{\mu_r+1}{\mu_r}\left[1-\left(\frac{R_s}{R_r}\right)^{2np}\right] - \frac{\mu_r-1}{\mu_r}\left[\left(\frac{R_s}{R_m}\right)^{2np} - \left(\frac{R_m}{R_r}\right)^{2np}\right]}\right\}\cos(np\theta)$$
$$+\sum_{n=1,3,5...}^{\infty} \mu_0 M_n \frac{np}{(np)^2-1}\left[-\left(\frac{r}{R_r}\right)^{np-1} + A_{3n}\right]\cos(np\theta) \tag{2.47}$$

$$B_{\theta II}(r,\theta) = \sum_{n=1,3,5...}^{\infty} \mu_0 M_n \frac{np}{(np)^2-1}\left[\left(\frac{r}{R_r}\right)^{np-1}\left(\frac{R_m}{R_r}\right)^{np+1} - \left(\frac{R_m}{r}\right)^{np+1}\right]$$
$$\left\{\frac{(A_{3n}-\frac{1}{\mu_r}) + (1+\frac{1}{\mu_r})\left(\frac{R_s}{R_m}\right)^{np+1}\left(\frac{R_s}{R_r}\right)^{np-1} - \left(A_{3n}+\frac{1}{\mu_r}\right)\left(\frac{R_s}{R_m}\right)^{2np} -}{\frac{\mu_r+1}{\mu_r}\left[1-\left(\frac{R_s}{R_r}\right)^{2np}\right] - \frac{\mu_r-1}{\mu_r}\left[\left(\frac{R_s}{R_m}\right)^{2np} - \left(\frac{R_m}{R_r}\right)^{2np}\right]}\right.$$
$$\left.\frac{\left(1-\frac{1}{\mu_r}\right)\left(\frac{R_m}{R_r}\right)^{np-1}}{\frac{\mu_r+1}{\mu_r}\left[1-\left(\frac{R_s}{R_r}\right)^{2np}\right] - \frac{\mu_r-1}{\mu_r}\left[\left(\frac{R_s}{R_m}\right)^{2np} - \left(\frac{R_m}{R_r}\right)^{2np}\right]}\right\}\sin(np\theta)$$
$$+ \sum_{n=1,3,5...}^{\infty} \mu_0 M_n \frac{1}{(np)^2-1}\left[np\left(\frac{r}{R_r}\right)^{np-1} - A_{3n}\right]\sin(np\theta) \quad (2.48)$$

For internal and external rotor motors ($np = 1$)

$$B_{rI}(r,\theta) = \frac{\mu_0 M_1}{2\mu_r}\left[1+\left(\frac{R_s}{r}\right)^2\right]$$
$$\left\{\frac{A_{3n}\left(\frac{R_m}{R_s}\right)^2 - A_{3n}\left(\frac{R_r}{R_s}\right)^2 + \left(\frac{R_r}{R_s}\right)^2 \ln\left(\frac{R_m}{R_r}\right)^2}{\frac{\mu_r+1}{\mu_r}\left[1-\left(\frac{R_r}{R_s}\right)^2\right] - \frac{\mu_r-1}{\mu_r}\left[\left(\frac{R_m}{R_s}\right)^2 - \left(\frac{R_r}{R_m}\right)^2\right]}\right\}\cos(\theta) \quad (2.49)$$

$$B_{\theta I}(r,\theta) = \frac{\mu_0 M_1}{2\mu_r}\left[-1+\left(\frac{R_s}{r}\right)^2\right]$$
$$\left\{\frac{A_{3n}\left(\frac{R_m}{R_s}\right)^2 - A_{3n}\left(\frac{R_r}{R_s}\right)^2 + \left(\frac{R_r}{R_s}\right)^2 \ln\left(\frac{R_m}{R_r}\right)^2}{\frac{\mu_r+1}{\mu_r}\left[1-\left(\frac{R_r}{R_s}\right)^2\right] - \frac{\mu_r-1}{\mu_r}\left[\left(\frac{R_m}{R_s}\right)^2 - \left(\frac{R_r}{R_m}\right)^2\right]}\right\}\sin(\theta) \quad (2.50)$$

$$B_{rII}(r,\theta) = \frac{\mu_0 M_1}{2}\left\{\frac{A_{3n}\left(\frac{R_m}{R_s}\right)^2 - A_{3n} + \ln\left(\frac{R_m}{R_r}\right)\left[\frac{\mu_r+1}{\mu_r}\left(\frac{R_r}{R_s}\right)^2 - \frac{\mu_r-1}{\mu_r}\left(\frac{R_r}{R_m}\right)^2\right]}{\frac{\mu_r+1}{\mu_r}\left[1-\left(\frac{R_r}{R_s}\right)^2\right] - \frac{\mu_r-1}{\mu_r}\left[\left(\frac{R_m}{R_s}\right)^2 - \left(\frac{R_r}{R_m}\right)^2\right]}\right\}$$
$$\left[1+\left(\frac{R_r}{r}\right)^2\right]\sin(\theta) + \frac{\mu_0 M_1}{2}\left[A_{3n} - \ln\left(\frac{r}{R_m}\right) + \left(\frac{R_r}{r}\right)^2 \ln\left(\frac{R_m}{R_r}\right)\right]\sin(\theta) \quad (2.51)$$

$$B_{\theta II}(r,\theta) = -\frac{\mu_0 M_1}{2}\left\{\frac{A_{3n}\left(\frac{R_m}{R_s}\right)^2 - A_{3n} + \ln\left(\frac{R_m}{R_r}\right)\left[\frac{\mu_r+1}{\mu_r}\left(\frac{R_r}{R_s}\right)^2 - \frac{\mu_r-1}{\mu_r}\left(\frac{R_r}{R_m}\right)^2\right]}{\frac{\mu_r+1}{\mu_r}\left[1-\left(\frac{R_r}{R_s}\right)^2\right] - \frac{\mu_r-1}{\mu_r}\left[\left(\frac{R_m}{R_s}\right)^2 - \left(\frac{R_r}{R_m}\right)^2\right]}\right\}$$
$$\left[1-\left(\frac{R_r}{r}\right)^2\right]\sin(\theta) - \frac{\mu_0 M_1}{2}\left[-1 + A_{3n} - \ln\left(\frac{r}{R_m}\right) - \left(\frac{R_r}{r}\right)^2 \ln\left(\frac{R_m}{R_r}\right)\right]\sin(\theta) \quad (2.52)$$

where for $np \neq 1$

$$A_{3n} = \begin{cases} \left(np - \frac{1}{np}\right)\frac{M_{rn}}{M_n} + \frac{1}{np} & \text{for parallel magnetization} \\ np & \text{for radial magnetization} \end{cases}$$

end for $np = 1$

$$A_{3n} = \begin{cases} 2\frac{M_{r1}}{M_1} - 1 & \text{for parallel magnetization} \\ 1 & \text{for radial magnetization} \end{cases}$$

For the purpose of cogging torque calculation the radial and tangential components of the air gap flux density are of particular interest. Theoretically the integration of the Maxwell's stress tensor can be carried out along the circular path which completely encloses the rotor at any radius between the magnet surface and the stator surface. Hence for internal rotor motors the radius can be

$$R_m < r < R_s$$

and for external rotor motors

$$R_r < r < R_m$$

The field solution in the middle of the air gap, i.e. at $r = R_m + g/2$ for internal and at $r = R_m - g/2$ for external rotor motors is often the most convenient for cogging torque and electromagnetic torque calculations. In finite element simulations the position of the integration path in the air gap when using Maxwell's stress tensor is an important issue which affects the accuracy of the force calculations.

The field distribution in the middle of the air gap at $r = R_m + g/2$ for a six pole internal rotor surface PM motor, with parameters given in Table 2.1, has been calculated using (2.41) and (2.42). The results for one pole pair and for both radial and parallel magnetization are shown in Figs. 2.4 and 2.5. The first 400 terms of the Fourier series were used to calculate the flux density.

Table 2.1 Parameters of the 36 slot, six pole surface PM motor

Parameter	*Symbol*	*Value*	*Unit*
Rated power	P_r	3.7	kW
Rated voltage	V_r	450	V
Rated speed	n_r	2000	rpm
Pole number	$2p$	6	–
Slot number	Q_s	36	–
Magnet arc/Pole pitch ratio	α_p	0.865	–
Air gap length	g	0.5	mm
Magnet radial thickness	l_m	2	mm
Radius of the rotor surface	R_r	55	mm
Radius of the magnet surface	R_m	57	mm
Stator inner radius	R_s	57.5	mm
Magnet remanence	B_r	0.82	T
Relative recoil permeability	μ_r	1.07	–

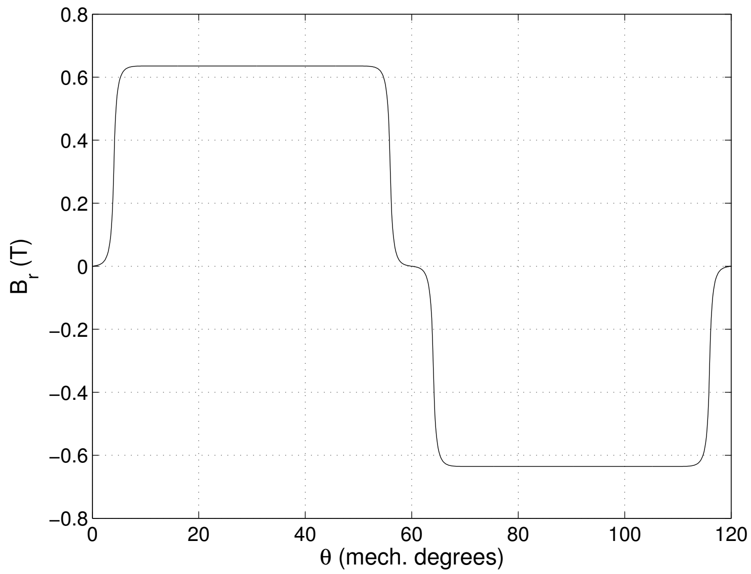

(a)

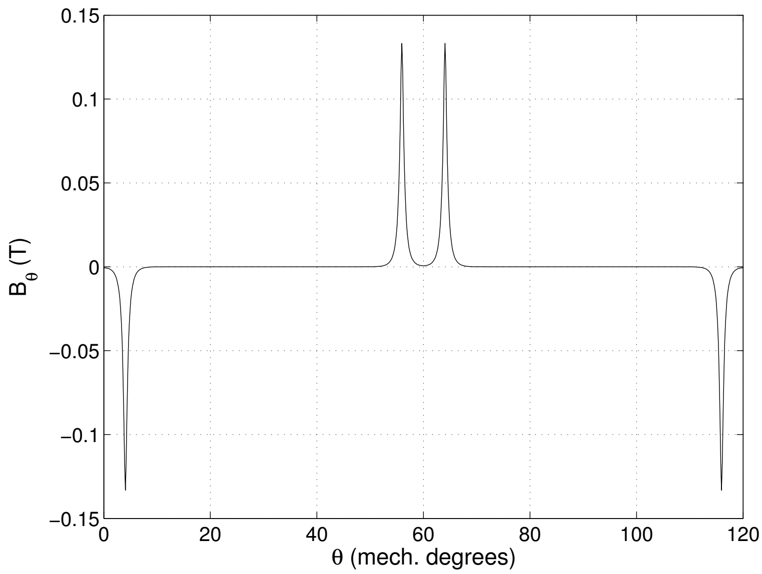

(b)

Fig. 2.4 Waveform of the flux density in the middle of the air gap of a slotless surface PM motor with radial magnetization: (a) radial component, (b) tangential component

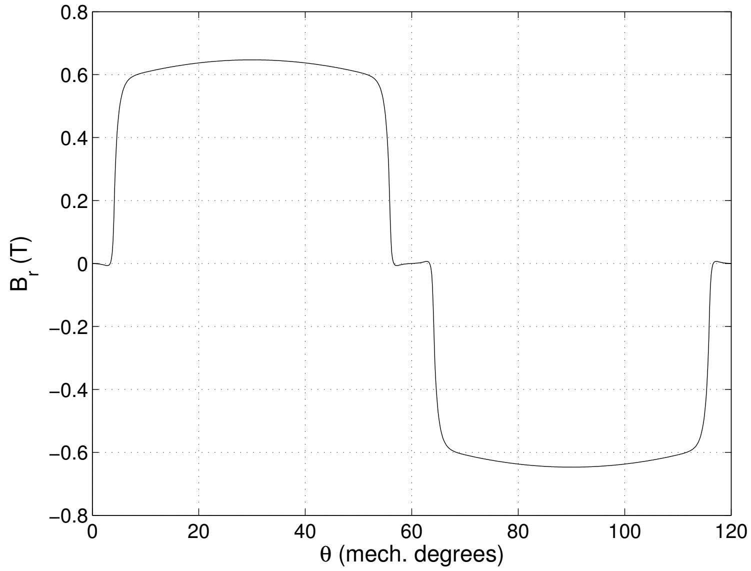

(a)

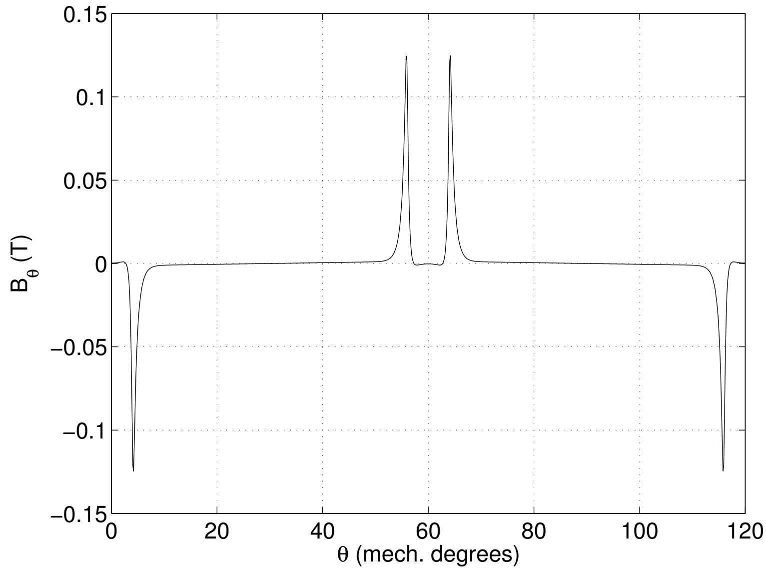

(b)

Fig. 2.5 Waveform of the flux density in the middle of the air gap of a slotless surface PM motor with parallel magnetization: (a) radial component, (b) tangential component

2.2 Approximation of the Air Gap Permeance

The presence of slots in the motor affects the flux distribution in the air gap and in the magnets. Slots also decrease the total flux per pole which is usually accounted for using the Carter coefficient. Moreover the interaction of the magnetic field with the tooth sides generates forces which create a cogging torque.

So far the field distribution for the slotless PM motor is known. The actual open-circuit flux density is then determined from the product of the flux density produced by the magnets in a slotless rotor and the relative air gap permeance $\lambda(r, \theta)$, i.e.

$$B(r, \theta, \alpha) = B_{slotless}(r, \theta, \alpha)\lambda(r, \theta) \tag{2.53}$$

where α is the angle of rotation of the magnets relative to the referent position. The referent position for which $\alpha = 0$ is when the centerline of the magnet is aligned with the angular position $\theta = 0$ of the (r, θ) coordinate system positioned as shown in Fig. 2.1.

To determine the relative permeance, the actual flux paths in the region of the slot opening need to be known. The flux paths are a function of the slot geometry. Conformal transformation is an analytical technique which allows one to calculate the field distribution for the geometric shape of the slot opening. The method is based on the theory of functions of a complex variable.

2.2.1 Conformal Transformation of the Slot Opening

Conformal transformation or conformal mapping is the representation of a bounded area in the plane of another complex variable. When it is required to find a field distribution between the equipotential boundaries of somewhat awkward shape, as the slot opening structure is, then it becomes very suitable to find a transformation from one complex plane to another in which the shapes of the boundaries become something for which the field distribution is both regular and known.

The basic principle of the method will be explained on the example of an infinitely deep slot opening shown in Fig. 2.6. The idea is to transform the geometric shape in Fig. 2.6 into a slotless air gap in which the field solution can be found using the method described in Section 2.1. That solution is then mapped back into the complex plane where the actual slot shape exists. For the purpose of the transformation it is assumed that the depth of the slot is infinite. The depth of penetration of the field into the slot opening is usually small so the assumption of infinite slot depth will have a negligible effect on the results and at the same time will greatly simplify the transformation.

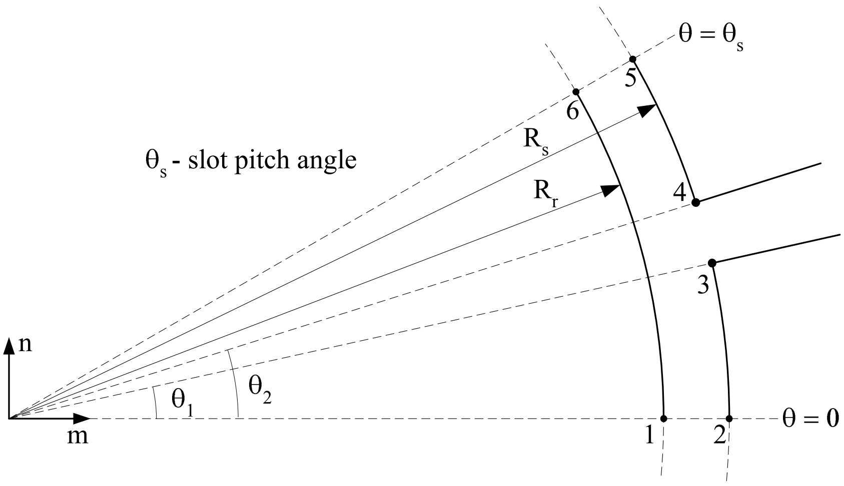

Fig. 2.6 Single infinitely deep slot opening in the S plane

Four conformal transformations are required to transform the actual slotted air gap into a slotless air gap where the field solution is known. This is shown in Fig. 2.7. S plane contains the original slot geometry, K plane contains the slotless air gap, while Z, W and T planes are used for intermediate transformations.

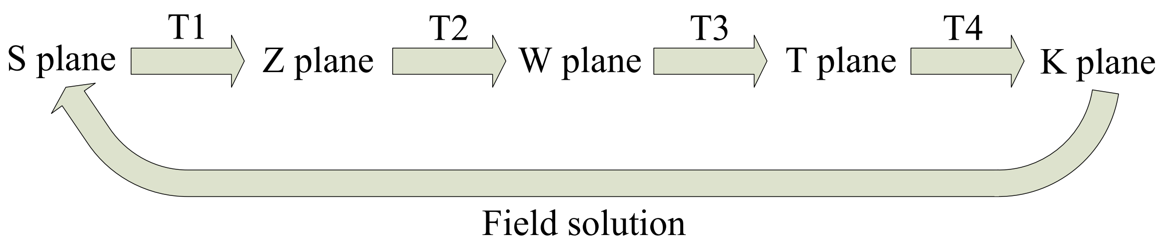

Fig. 2.7 Basic steps required for finding the field solution in the slotted air gap based on conformal mapping of the slot opening

a) Transformation from S plane into Z plane

The slot geometry in the S plane in its original circular arrangement needs to be transformed into a linear model in the Z plane. This can be achieved by using logarithmic conformal transformation which transforms cylindrical coordinates into Cartesian coordinates [63, 64]. The conventional approach of "cutting" the motor circumference axially and "opening" it would be acceptable only in the case of a small air gap relative to the size of the slot opening and a small curvature of the stator and rotor surface. The surface PM motors have a large air gap and a relatively small radius. Consequently the radii of the rotor and stator surfaces can be quite different in which case the conventional approach is no longer valid. The logarithmic conformal transformation between the S plane and the Z plane is given by

$$z = \ln(s) \tag{2.54}$$

where

$$\begin{aligned} s &= m + jn = re^{j\theta} \\ z &= x + jy \end{aligned}$$

The link between coordinates in the S and Z planes is

$$\begin{aligned} x &= \ln(r) \\ z &= \theta \end{aligned} \tag{2.55}$$

The resulting linear slot model in the Z plane is shown in Fig. 2.8.

b) Transformation from Z plane into W plane

The next step in finding the field distribution in the slotted air gap is to transform the area bounded by the geometric structure defined in the Z plane into the upper half of the W plane. The transformation which opens out the interior of a polygon in the Z plane to the upper half of the W plane is known as Schwarz-Christoffel transformation [49]. The sides of the polygon in the Z plane after the transformation become the real axis of the W plane. The slot configuration in the Z plane with values of w at the corner points is shown in Fig. 2.9.

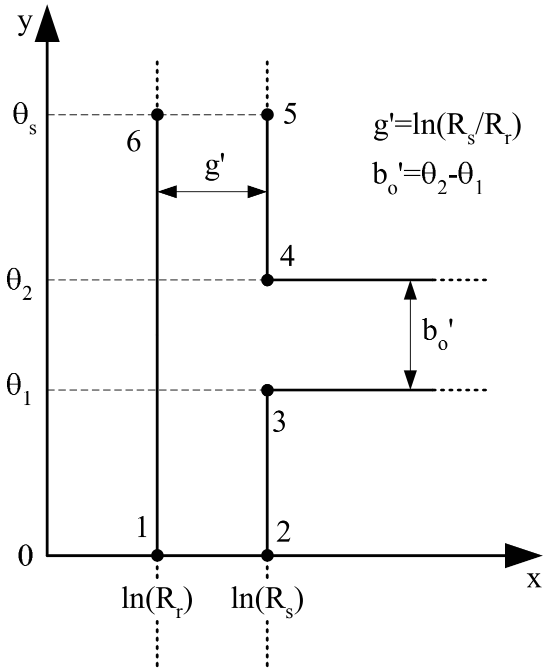

Fig. 2.8 Slot opening in the Z plane

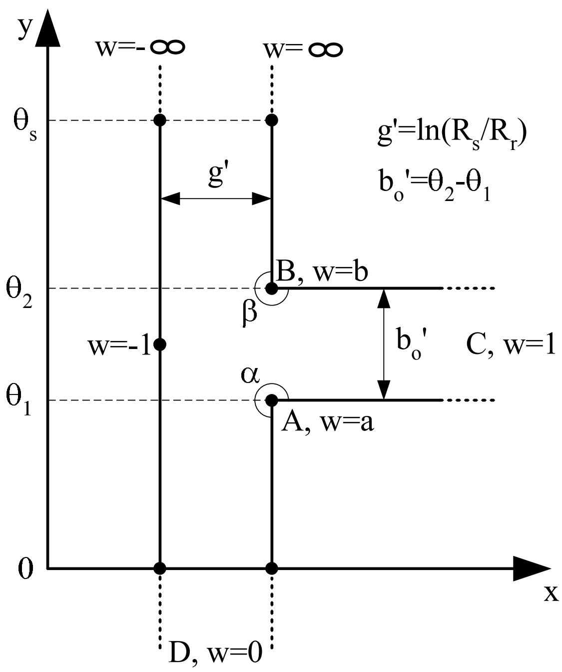

Fig. 2.9 Slot opening in the Z plane with marked values of w at the corner points

There are several ways of opening this configuration into the upper half of the W plane. Since it will be advantageous to have the resulting flux lines in the W plane semicircles, it is best to make the origin of the W plane where the imaginary part of z is at minus infinity. Then at the left surface where $z = +j\infty$ one makes $w = -\infty$ and at the right surface $w = +\infty$. These are the values of w shown in Fig. 2.9. There are three more corners, shown as A, B and C where values of w have to be fixed. It is assumed that the slot walls merge into the corner point C at the point where the real part of z is infinity.

Only two of those three corners can have arbitrary values assigned to them so that one value of w is left unspecified to be found later in terms of the ratio b_o'/g'. Let the unspecified value be denoted by a. Now the value of w at each of the corners A, B and C must be positive because those points lie between the points $w = 0$ and $w = \infty$. The following choice of values can be made: at A let $w = a$, at C let $w = 1$ and at B let $w = b$. The values a and b will not be independent because there is only one definite ratio in the Z plane. The W plane is shown in Fig. 2.10.

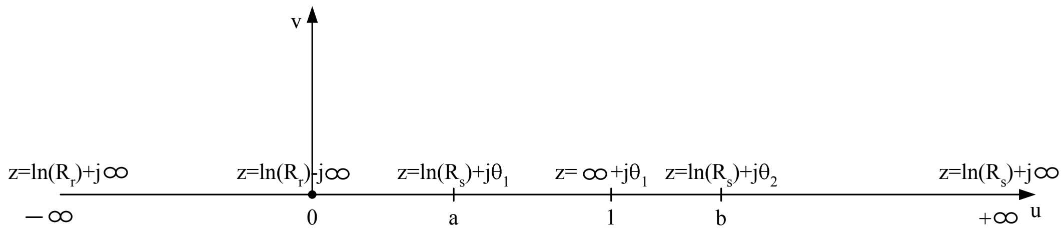

Fig. 2.10 Slot opening in the W plane

Since the opening of the polygon will be made in the corner where Im$(z) = \infty$, i.e. $w = \infty$, that corner will take no part in the transformation. The angles at the corners A and B will be $\alpha = \beta = 3\pi/2$. The angles at the corners C and D are zero. Since there are four corners to be opened, the Schwarz-Christoffel transformation will have the form

$$\frac{\mathrm{d}z}{\mathrm{d}w} = A(w-a)^{\frac{\alpha}{\pi}-1}(w-b)^{\frac{\beta}{\pi}-1}(w-c)^{\frac{\gamma}{\pi}-1}(w-d)^{\frac{\delta}{\pi}-1} \tag{2.56}$$

After substituting the values of w and the angles at the corner points into (2.56), the transformation from the Z plane to the upper half of the w plane becomes

$$\frac{\mathrm{dz}}{\mathrm{d}w} = A\frac{(w-a)^{\frac{1}{2}}(w-b)^{\frac{1}{2}}}{(w-1)w} \tag{2.57}$$

The constants A, a and b can now be determined before integration of (2.57). The value of A can be found by using the method of integration along a large semicircle in the w plane. In the Z plane the distance between the surfaces as the imaginary part of z approaches infinity is the constant value g' so that, taking direction into account, the value of the integration across the air gap is $-g'$ at all points after $w = b$. In the W plane the path of integration is along a large semicircle of an arbitrary large radius R. In polar coordinates the points on the semicircle will be

$$w = Re^{j\theta}$$

The differential of w is then

$$\mathrm{d}w = jRe^{j\theta}\mathrm{d}\theta$$

Substitution into (2.57) gives

$$\int \mathrm{d}z = \int_0^\pi \frac{A\left(Re^{j\theta} - a\right)^{\frac{1}{2}}\left(Re^{j\theta} - b\right)^{\frac{1}{2}}}{Re^{j\theta}\left(Re^{j\theta} - 1\right)} jRe^{j\theta}\mathrm{d}\theta \tag{2.58}$$

As $R \to \infty$ it greatly exceeds a, b and unity. Hence for values of R approaching infinity

$$\int \mathrm{d}z = \int_0^\pi \frac{A\left(Re^{j\theta}Re^{j\theta}\right)^{\frac{1}{2}}}{Re^{j\theta}Re^{j\theta}} jRe^{j\theta}\mathrm{d}\theta = \int_0^\pi jA\mathrm{d}\theta = j\pi A \tag{2.59}$$

In the Z plane $\int \mathrm{d}z = -g'$ and therefore

$$A = j\frac{g'}{\pi} \tag{2.60}$$

A similar integration can be done in the area where the imaginary part of z approaches negative infinity, i.e. where $w = 0$. The value of the integral in the Z plane across the air gap is again $-g'$. In the W plane the path of integration is a small semicircle centered at the origin of radius r which can be made arbitrarily small. Then as before

$$w = re^{j\theta}$$

$$\mathrm{d}w = jre^{j\theta}\mathrm{d}\theta$$

$$\int \mathrm{d}z = \int_0^{\pi} \frac{A\left(re^{j\theta} - a\right)^{\frac{1}{2}}\left(re^{j\theta} - b\right)^{\frac{1}{2}}}{re^{j\theta}\left(re^{j\theta} - 1\right)} jre^{j\theta}\mathrm{d}\theta \tag{2.61}$$

As r approaches zero it becomes much smaller than either a, b or unity, and hence for values of r approaching zero

$$\int \mathrm{d}z = \int_0^{\pi} -\frac{A\,(ab)^{\frac{1}{2}}}{re^{j\theta}(-1)} jre^{j\theta}\mathrm{d}\theta = \int_0^{\pi} jA(ab)^{\frac{1}{2}}\mathrm{d}\theta = j \cdot j\frac{g'}{\pi}(ab)^{\frac{1}{2}}\pi = -g'(ab)^{\frac{1}{2}} \tag{2.62}$$

Since $\int \mathrm{d}z = -g'$, hence

$$(ab)^{\frac{1}{2}} = 1 \quad \Rightarrow \quad b = \frac{1}{a} \tag{2.63}$$

Substituting (2.60) into (2.57) gives

$$\mathrm{d}z = j\frac{g'}{\pi}\frac{(w-a)^{\frac{1}{2}}(w-b)^{\frac{1}{2}}}{(w-1)w}\mathrm{d}w \tag{2.64}$$

Hence

$$z = j\frac{g'}{\pi}\int \frac{(w-a)^{\frac{1}{2}}(w-b)^{\frac{1}{2}}}{(w-1)w}\mathrm{d}w \tag{2.65}$$

The integrand is not in the form for which the solution can be found in the tables of integrals. If substitution

$$p^2 = \frac{w-b}{w-a} \tag{2.66}$$

is made so that

$$w = \frac{ap^2 - b}{p^2 - 1} \tag{2.67}$$

then (2.65) becomes

$$z = j\frac{2g'}{\pi}\int \frac{(b-a)^2 p^2}{a(1-a)(p^2-1)(p^2-b^2)(p^2+b)}\mathrm{d}p \tag{2.68}$$

Substituting $\frac{1}{b}$ for a gives

$$z = j\frac{2g'}{\pi}\int \frac{(b+1)^2(b-1)p^2}{(1-p^2)(b^2-p^2)(p^2+b)}\mathrm{d}p \tag{2.69}$$

After splitting the integrand into partial fractions (2.69) takes the form

$$z = j\frac{2g'}{\pi}\int \left(\frac{1}{1-p^2} - \frac{b}{b^2-p^2} - \frac{b-1}{b+p^2}\right)\mathrm{d}p \tag{2.70}$$

Using tables of integrals [65] the solution of the integral is

$$z = j\frac{g'}{\pi}\left[\ln\left|\frac{1+p}{1-p}\right| - \ln\left|\frac{b+p}{b-p}\right| - \frac{2(b-1)}{\sqrt{b}}\tan^{-1}\frac{p}{\sqrt{b}}\right] + C_1 \tag{2.71}$$

The constant of integration in (2.71) can be calculated by making the value of z at one of the corner points calculated according to (2.71) equal to the value of z according to Fig. 2.9. It can be noted that when p is zero

$$z = j\frac{g'}{\pi}\left[\ln 1 - \ln 1 - \frac{2(b-1)}{\sqrt{b}}\tan^{-1} 0\right] + C_1 = C_1$$

From (2.66) when p is zero $w = b$. Hence from Fig. 2.9

$$C_1 = \ln(R_s) + j\theta_2 \tag{2.72}$$

The unknown value of b depends on the ratio $\frac{b_o}{g'}$. Since

$$p^2 = \frac{w-b}{w-a}$$

as $w \rightarrow a, p \rightarrow \infty$. Therefore near the point $w = a$ the value of p is very large and in the limit where $w = a$

$$\begin{aligned}
z &= \lim_{p\rightarrow\infty}\left\{j\frac{g'}{\pi}\left[\ln\left|\frac{1+p}{1-p}\right| - \ln\left|\frac{b+p}{b-p}\right| - \frac{2(b-1)}{\sqrt{b}}\tan^{-1}\frac{p}{\sqrt{b}}\right] + \ln(R_s) + j\theta_2\right\} \\
&= j\frac{g'}{\pi}\left[\ln(-1) - \ln(-1) - \frac{2(b-1)}{\sqrt{b}}\tan^{-1}\infty\right] + \ln(R_s) + j\theta_2 \\
&= -j\frac{g'}{\pi}\frac{2(b-1)}{\sqrt{b}}\frac{\pi}{2} + \ln(R_s) + j\theta_2 = -jg'\frac{b-1}{\sqrt{b}} + \ln(R_s) + j\theta_2
\end{aligned}$$

According to Fig. 2.9 $w = a$ at point A where $z = \ln(R_s) + j\theta_1$. Hence

$$-jg'\frac{b-1}{\sqrt{b}} + \ln(R_s) + j\theta_2 = \ln(R_s) + j\theta_1$$

$$-g'\frac{b-1}{\sqrt{b}} = -(\theta_2 - \theta_1) = -b'_o \tag{2.73}$$

from which

$$b = \left[\frac{b'_o}{2g'} + \sqrt{\left(\frac{b'_o}{2g'}\right)^2 + 1}\right]^2 \tag{2.74}$$

c) Transformation from T plane into W plane

In order to find the field distribution in the slot area, another transformation from the T plane shown in Fig. 2.11 to the W plane from Fig. 2.10 is required. The slot opening in the T plane represents two parallel plates extending an infinite distance in all directions. Note that the characteristic points numbered **1** to **2** no longer have the same angular coordinates $\theta = 0$ as in Fig. 2.8. The same is valid for the points **5** and **6** which no longer have the angular coordinates $\theta = \theta_s$. This difference will be explored in more detail in Section 2.3.

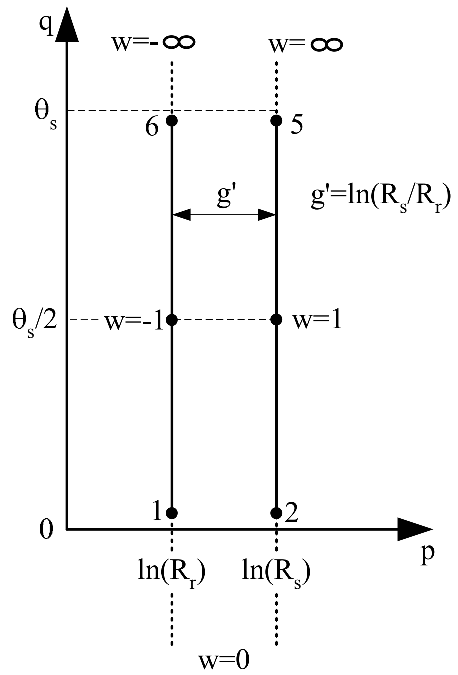

Fig. 2.11 Slot opening in the T plane

From the Schwarz-Christoffel equation the mapping between the T plane and the W plane is given by

$$\frac{\mathrm{d}t}{\mathrm{d}w} = A_1(w - a_1)^{\frac{\alpha_1}{\pi}-1} \tag{2.75}$$

If the polygon is opened at the corner where $w = a_1 = 0$ and $\alpha_1 = 0$, then (2.75) becomes

$$\mathrm{d}t = \frac{A_1}{w}\mathrm{d}w \tag{2.76}$$

Hence by integration

$$t = A_1 \ln w + B_1 \tag{2.77}$$

The constants A_1 and B_1 can be determined from the points marked in Fig. 2.11 where $w = -1$ and $w = 1$. From (2.77) it follows that

$$\ln(R_r) + j\frac{\theta_s}{2} = A_1 \ln(-1) + B_1 = j\pi A_1 + B_1 \tag{2.78}$$

$$\ln(R_s) + j\frac{\theta_s}{2} = A_1 \ln(1) + B_1 = B_1 \tag{2.79}$$

From (2.78) and (2.79) one has

$$A_1 = \frac{1}{j\pi} \ln \frac{R_r}{R_s} = j\frac{g'}{\pi} \tag{2.80}$$

$$B_1 = \ln(R_s) + j\frac{\theta_s}{2} \tag{2.81}$$

It is apparent that the value of A_1 depends on the distance between the plates in the T plane which is g' by choice. The transformation (2.77) now becomes

$$t = j\frac{g'}{\pi} \ln w + \ln(R_s) + j\frac{\theta_s}{2} \tag{2.82}$$

d) Transformation from T plane into K plane

The last transformation maps the two parallel plates in Fig. 2.11 into a circular shape which models the air gap of a slotless PM motor. To achieve this the exponential conformal transformation is used in the form

$$k = e^t \tag{2.83}$$

The shape which results from (2.83) is shown in Fig. 2.12. The next task is to map the known field solution in the K plane, calculated using the method from Section 2.1, into the S plane where the slot exists.

e) Field solution in the S plane

From the theory of complex numbers it is known that any function of a complex variable $s = m + jn$ in the S plane automatically satisfies Laplace's equation [49]. These functions are called conjugate functions. Let $k = u(m, n) + jv(m, n)$ be any function of $s = m + jn$. Then both u

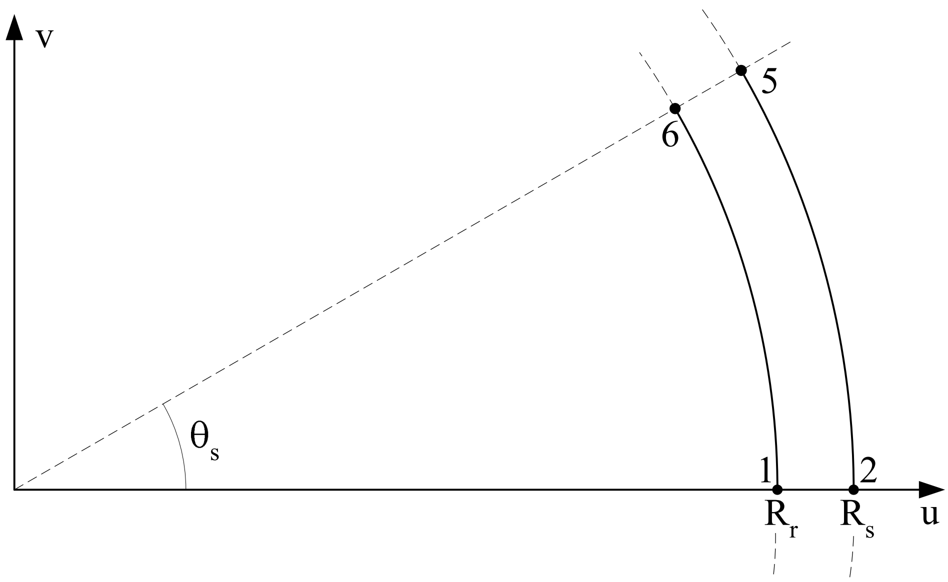

Fig. 2.12 Slot opening in the K plane

and v will satisfy Laplace's equation

$$\begin{aligned}\frac{\partial^2 u}{\partial m^2}+\frac{\partial^2 u}{\partial n^2}&=0\\ \frac{\partial^2 v}{\partial m^2}+\frac{\partial^2 v}{\partial n^2}&=0\end{aligned} \tag{2.84}$$

Moreover, these functions will also satisfy Cauchy-Riemann conditions

$$\begin{aligned}\frac{\partial u}{\partial m}&=\frac{\partial v}{\partial n}\\ \frac{\partial v}{\partial m}&=-\frac{\partial u}{\partial n}\end{aligned} \tag{2.85}$$

If $\varphi(m,n)$ is a scalar potential function in the S plane and $\psi(u,v)$ is a transformed scalar potential function in the T plane, then the following condition can be set [60]

$$\varphi(m,n)=\psi\left[u(m,n),v(m,n)\right] \tag{2.86}$$

The field intensity in the S plane is equal to the negative gradient of the scalar magnetic potential, i.e.

$$H_s=H_m+jH_n=-\frac{\partial\varphi}{\partial m}-j\frac{\partial\varphi}{\partial n} \tag{2.87}$$

and in the K plane

$$H_k = H_u + jH_v = -\frac{\partial\psi}{\partial u} - j\frac{\partial\psi}{\partial v} \tag{2.88}$$

From the condition (2.86) one has

$$\begin{aligned}\frac{\partial\varphi}{\partial m} &= \frac{\partial\psi}{\partial u}\frac{\partial u}{\partial m} + \frac{\partial\psi}{\partial v}\frac{\partial v}{\partial m}\\ \frac{\partial\varphi}{\partial n} &= \frac{\partial\psi}{\partial u}\frac{\partial u}{\partial n} + \frac{\partial\psi}{\partial v}\frac{\partial v}{\partial n}\end{aligned} \tag{2.89}$$

Combining (2.87), (2.88) and (2.89) yields

$$H_s = H_u\frac{\partial u}{\partial m} + H_v\frac{\partial v}{\partial m} + j\left(H_u\frac{\partial u}{\partial n} + H_v\frac{\partial v}{\partial n}\right) \tag{2.90}$$

After applying Cauchy-Riemann conditions, (2.90) becomes

$$H_s = (H_u + jH_v)\left(\frac{\partial u}{\partial m} - j\frac{\partial v}{\partial m}\right) = H_k\left(\frac{\partial u}{\partial m} - j\frac{\partial v}{\partial m}\right) \tag{2.91}$$

Since $k = u(m,n) + jv(m,n) = k(s)$, then

$$\frac{\partial k}{\partial m} = \frac{\partial u}{\partial m} + j\frac{\partial v}{\partial m} = \frac{\partial k}{\partial s}\frac{\partial s}{\partial m} = \frac{\partial k}{\partial s} \tag{2.92}$$

Hence the complex conjugate of $\frac{\partial k}{\partial s}$ will be

$$\left(\frac{\partial k}{\partial s}\right)^* = \left(\frac{\partial u}{\partial m} + j\frac{\partial v}{\partial m}\right)^* = \frac{\partial u}{\partial m} - j\frac{\partial v}{\partial m} \tag{2.93}$$

If (2.93) is substituted into (2.91), the equation which maps the field solution from the K plane to the S plane is obtained, i.e.

$$H_s = H_k\left(\frac{\partial k}{\partial s}\right)^* \tag{2.94}$$

The same type of equation is valid for the flux density as well because the field is calculated in the air gap.

$$B_s = B_k\left(\frac{\partial k}{\partial s}\right)^* \tag{2.95}$$

The partial derivative $\frac{\partial k}{\partial s}$ can be expressed as

$$\frac{\partial k}{\partial s} = \frac{\partial k}{\partial t}\frac{\partial t}{\partial s} = \frac{\partial k}{\partial t}\frac{\partial t}{\partial w}\frac{\partial w}{\partial s} = \frac{\partial k}{\partial t}\frac{\partial t}{\partial w}\frac{\partial w}{\partial z}\frac{\partial z}{\partial s} \tag{2.96}$$

The partial derivatives in (2.96) are defined by conformal transformations between the corresponding complex planes.

$$
\begin{aligned}
\frac{\partial k}{\partial t} &= e^t = e^{\ln k} = k \\
\frac{\partial t}{\partial w} &= j\frac{g'}{\pi}\frac{1}{w} \\
\frac{\partial w}{\partial z} &= -j\frac{\pi}{g'}\frac{(w-1)w}{(w-a)^{\frac{1}{2}}(w-b)^{\frac{1}{2}}} \\
\frac{\partial z}{\partial s} &= \frac{1}{s}
\end{aligned}
\tag{2.97}
$$

Substituting (2.96) and (2.97) into (2.95) yields

$$
\begin{aligned}
B_s &= B_k\left[kj\frac{g'}{\pi}\frac{1}{w}(-j)\frac{\pi}{g'}\frac{(w-1)w}{(w-a)^{\frac{1}{2}}(w-b)^{\frac{1}{2}}}\frac{1}{s}\right]^* \\
&= B_k\left[\frac{k}{s}\frac{(w-1)}{(w-a)^{\frac{1}{2}}(w-b)^{\frac{1}{2}}}\right]^*
\end{aligned}
\tag{2.98}
$$

Since B_s is the flux density in the slotted air gap, the part of (2.98) which multiplies B_k can be defined as a complex relative air gap permeance λ. Equation (2.98) then becomes

$$B_s = B_k\lambda^* \tag{2.99}$$

where

$$\lambda = \frac{k}{s}\frac{(w-1)}{(w-a)^{\frac{1}{2}}(w-b)^{\frac{1}{2}}} \tag{2.100}$$

with a and b calculated according to (2.63) and (2.74).

Since k is a function of t which in turn is a function of w and s is the known coordinate in the actual geometry which is also a function of w, the complex permeance λ is indirectly a nonlinear function of w as well. The main problem is that w is linked with z through a nonlinear equation (2.71). If it is required to evaluate the flux density at a certain geometric point in the slotted air gap in the S plane, then the value of z which corresponds to that point in the Z plane can simply be calculated as $z = \ln(s)$. However, the value of w which corresponds to that value of z cannot be calculated explicitly from (2.71) because that equation is in the form $z = f(w)$ where f is a nonlinear function of w. Therefore an iterative technique is required to solve this nonlinear equation and find the value of w for the given z. The nonlinear least-squares optimization algorithm built into MATLAB (function $lsqnonlin$) has been used to solve this problem. The residual norm which is being minimized is defined as

$$\|F\| = [Re(z - z(w))]^2 + [Im(z - z(w))]^2 \tag{2.101}$$

where z is the actual value and $z(w)$ is the value calculated using (2.71) with w from the current iteration.

Since λ is a complex number, it can be written in the form

$$\lambda = \lambda_a + j\lambda_b \tag{2.102}$$

For the motor with parameters given in Table 2.1 the complex permeance λ has been calculated using (2.100) in the middle of the air gap $(r = R_s - g/2)$ along the line covering the angular span of one slot pitch $(0 < \theta < \theta_s)$. The resulting waveforms of the real and imaginary parts of λ are shown in Fig. 2.13. These two waveforms will repeat with every slot pitch. Hence they can be expressed in the form of Fourier series to give the complex relative permeance function for all angular positions in the middle of the air gap. The Fourier series is given by

$$\begin{aligned}\lambda_a(r,\theta) &= \lambda_0(r) + \sum_{n=1}^{N_\lambda} \lambda_{an}(r,\theta)\cos(nQ_s\theta) \\ \lambda_b(r,\theta) &= \sum_{n=1}^{N_\lambda} \lambda_{bn}(r,\theta)\sin(nQ_s\theta)\end{aligned} \tag{2.103}$$

where Q_s is the number of slots and N_λ is the maximum order of the Fourier coefficients. The Fourier coefficients λ_{an} and λ_{bn} are calculated from the waveforms shown in Fig. 2.13 using discrete Fourier transform. The distribution of the relative air gap permeance for one pole pitch calculated using (2.103) is shown in Fig. 2.14.

2.3 Magnetic Field Distribution in the Slotted Surface PM Motor

The field distribution in the slotted air gap can now be calculated by multiplying the complex relative air gap permeance shown in Fig. 2.14 with the field solution in the slotless air gap shown

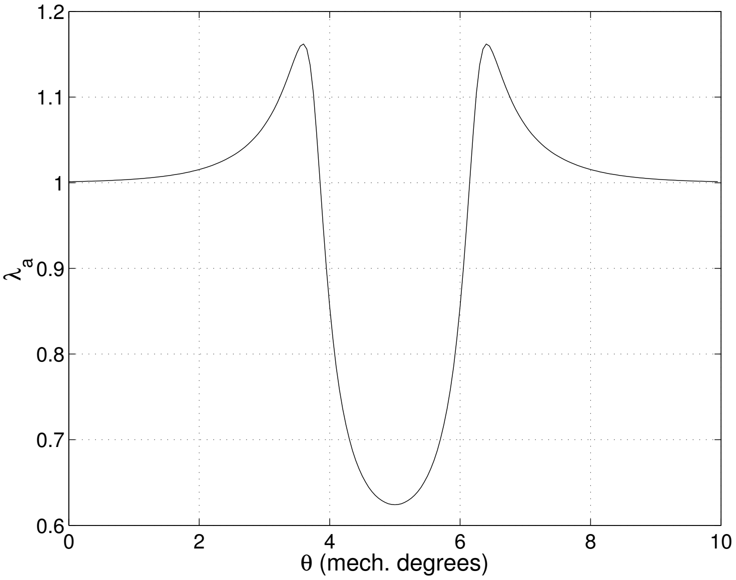

(a)

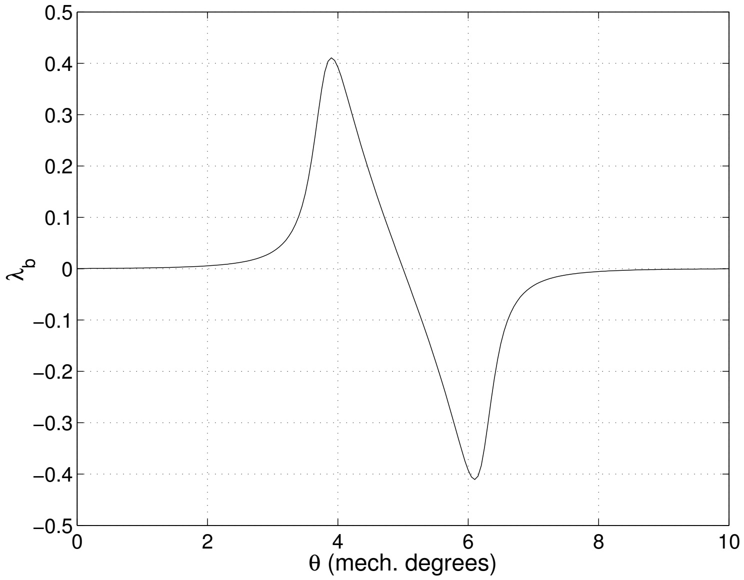

(b)

Fig. 2.13 Complex relative permeance per one slot pitch in the middle of the air gap of a six pole surface PM motor: (a) real component, (b) imaginary component

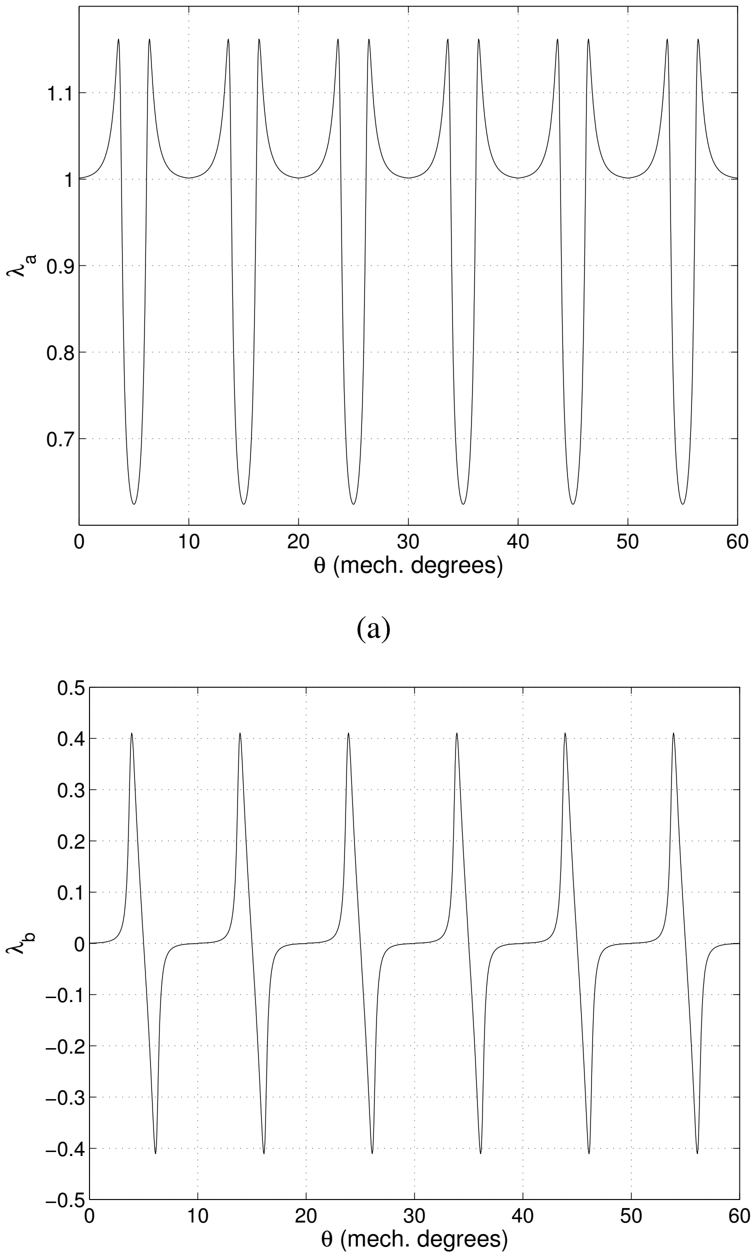

(a)

(b)

Fig. 2.14 Complex relative permeance per one pole pitch in the middle of the air gap of a six pole surface PM motor: (a) real component, (b) imaginary component in Figs. 2.4 and 2.5. If the radial and tangential components of the flux density in the slotless air gap are taken as the real and imaginary parts of the flux density distribution in the K plane, then the expressions for the radial and tangential components of the flux density in the S plane will be

$$B_{sr} = Re(B_k\lambda^*) = Re\left[(B_r + jB_\theta)(\lambda_a - j\lambda_b)\right] = B_r\lambda_a + B_\theta\lambda_b \tag{2.104}$$

$$B_{s\theta} = Im(B_k\lambda^*) = Im\left[(B_r + jB_\theta)(\lambda_a - j\lambda_b)\right] = B_\theta\lambda_a - B_r\lambda_b \tag{2.105}$$

where B_r and B_θ are the radial and tangential components of the flux density in the slotless air gap and λ_a and λ_b are the real and imaginary parts of the complex relative air gap permeance. It is important to notice that the radial component of the flux density in the slotted air gap B_{sr} is a function of both the radial and tangential components of the flux density in the slotless air gap. This is a significantly different result from the ”classical” approach which assumes λ to be a real number. With that assumption it is not possible to calculate the tangential component of the flux density in the slotted air gap.

If the flux density needs to be calculated at a location defined by the coordinates $s = m + jn$ in the S plane, then the value of the flux density in the slotless air gap which is used in (2.104) and (2.105) needs to be evaluated at a point $k = u + jv$ in the K plane into which the point s is transformed. Note that the outline of the slot opening in Fig. 2.6 will be transformed into the outline of the slotless air gap in Fig. 2.12. However, the radial and the angular coordinates of the points in the S plane will not be exactly transformed into the same coordinates of the points in the K plane. For instance, if the field distribution in the slotted air gap needs to be evaluated along the circular line with radius r where $s = re^{j\theta}$ and $R_m < r < R_s$, then the field distribution in the K plane needs to be evaluated along the contour into which the circular arc is transformed. For the previously used six pole surface PM motor the circular arc located in the middle of the air gap, with the radius $r = R_s - g/2$ and an angular span of one slot pitch, and the contour in the K plane into which this arc is transformed have been compared in Fig. 2.15. If the points in the S plane are given in the form $s = r_s e^{j\theta_s}$ and the points in the K plane are given in the form $s = r_k e^{j\theta_k}$, then Fig. 2.15a shows the ratio of the radii r_k/r_s and Fig. 2.15b shows the angular displacement $\theta_k - \theta_s$. It is apparent that the transformed line is very close to the circular arc. Hence an approximation is made in which it is assumed that the transformed line in the K plane is also a circular arc with the same radial and angular coordinates as the original arc in the S plane. This approximation can be conveniently used later in the cogging torque calculation and the calculation of the back emf waveform which has been explained in detail in Section 2.6 and Chapter 4.

In addition, conformal mapping also transforms the shape of the magnets in the K plane. Therefore, a similar approximation has been made again assuming that the magnets will retain their original shape as in the S plane to simplify the field calculations.

As an example, the field distribution in the middle of the air gap of the six pole surface PM motor with parameters given in Table 2.1 has been calculated using (2.104) and (2.105). The same assumption has been made that the transformed contour in the K plane is identical to the circular arc in the S plane with the radius $r = R_s - g/2$ and that the magnets retain their original shape. The results for the radial and parallel magnetization are shown in Figs. 2.16 and 2.17.

2.4 Comparison of Analytical and Numerical Field Solution in the Slotted Surface PM Motor

2.4.1 Unsaturated Finite Element Model

The analytical field solution in the slotted air gap of a surface PM motor calculated in Section 2.3 has been compared to the results of finite element simulations. The commercial FE software FEMLAB 2.3 has been used to simulate the no-load operation of the motor for the cases of radial and parallel magnetization. In analytical calculations it was assumed that the iron is infinitely permeable. The same approximation is used in the FE simulations as well. Since the field is always perpendicular to an infinitely permeable boundary, the rotor and stator iron have been replaced by Neumann boundary conditions on the boundary between the air and iron. To insure high accuracy of the numerical simulations third order triangular elements have been used and the size of the largest triangle in the finite element mesh in the air gap region has been limited to one quarter of the size of the air gap between the magnet surface and the stator surface. In addition, the size of the elements in the vicinity of the tooth tips is made equal to one tenth of the air gap size. The mesh

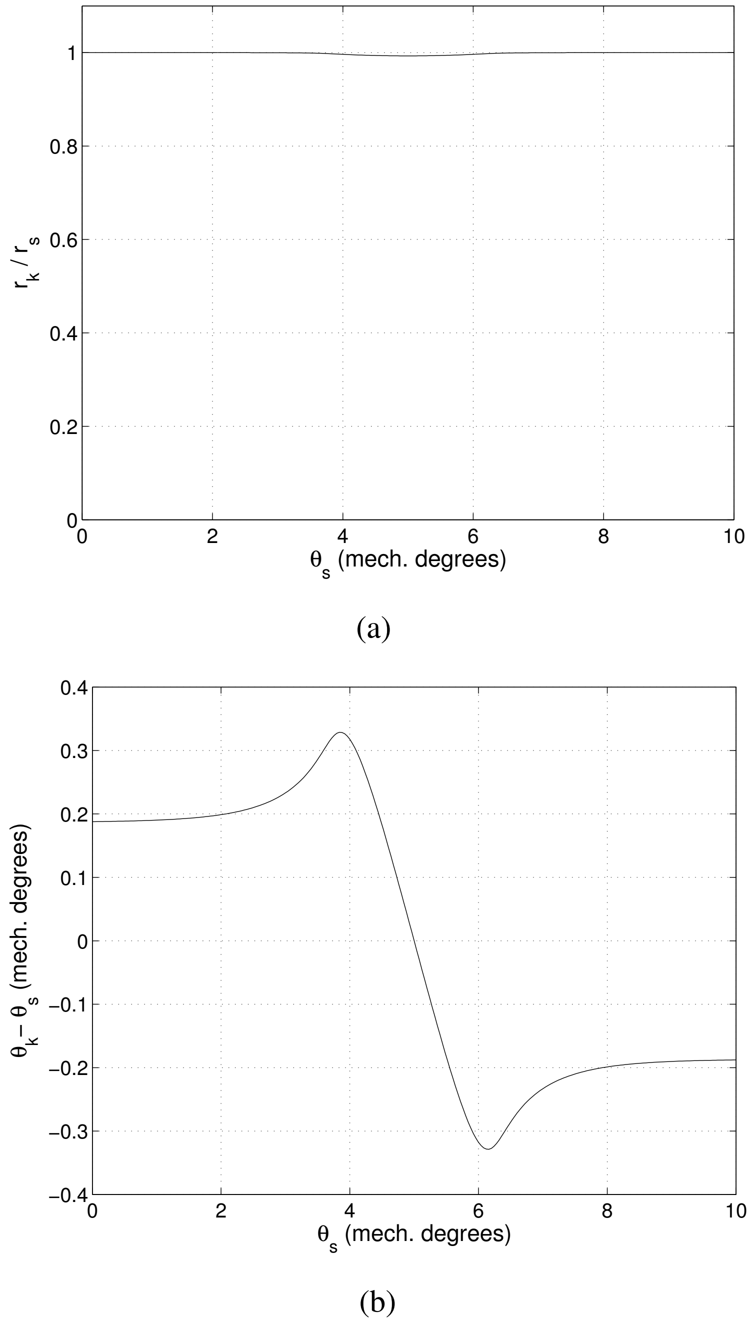

Fig. 2.15 Comparison of the circular arc in the middle of the air gap of a six pole surface PM motor extending one slot pitch in the S plane and its transformed shape in the K plane: (a) ratio r_k/r_s, (b) angular displacement $\theta_k - \theta_s$

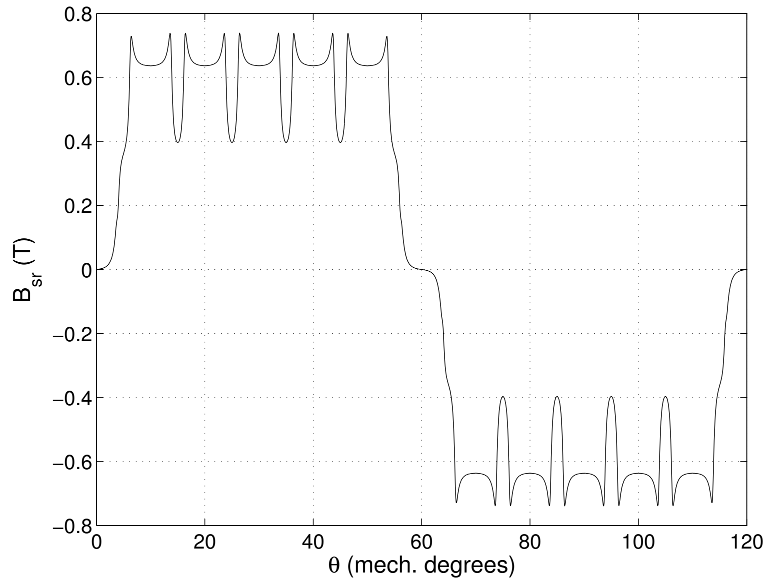

(a)

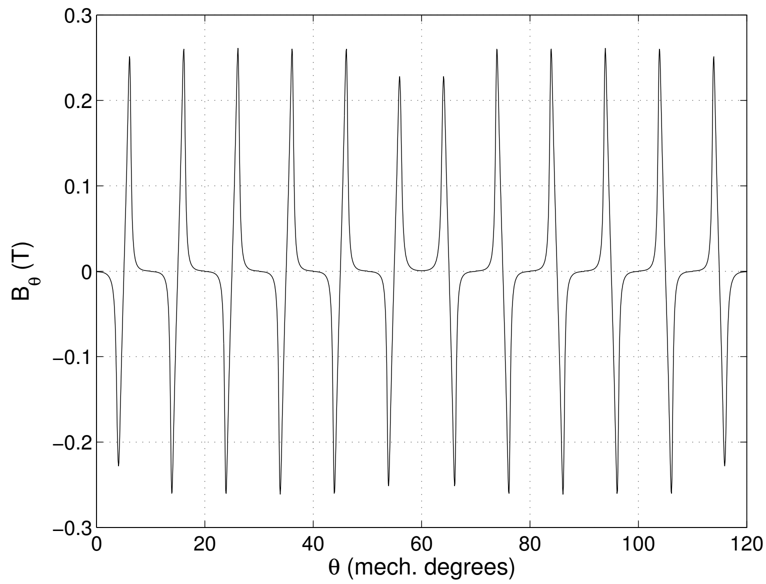

(b)

Fig. 2.16 Flux density in the middle of the air gap of a slotted surface PM motor with radial magnetization: (a) radial component, (b) tangential component

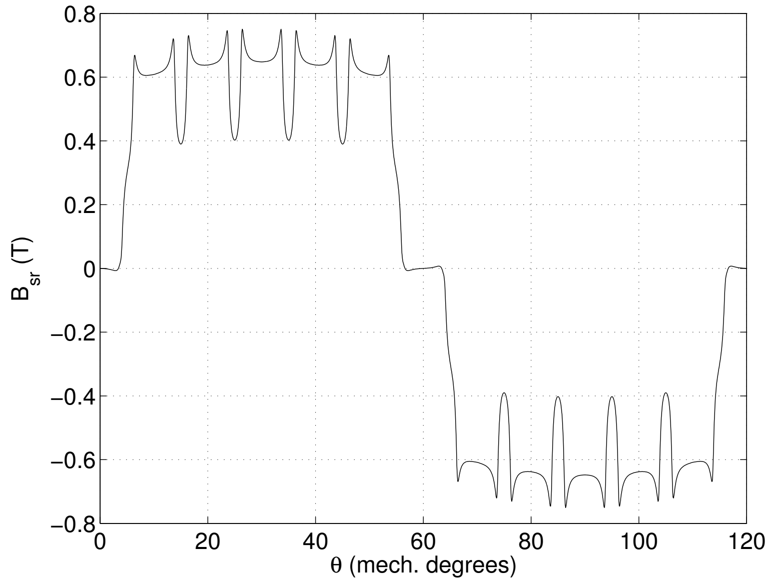

(a)

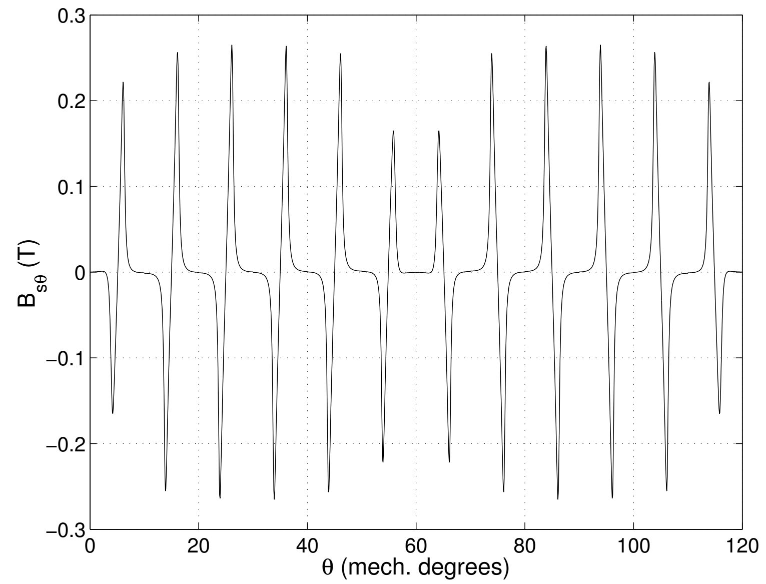

(b)

Fig. 2.17 Flux density in the middle of the air gap of a slotted surface PM motor with parallel magnetization: (a) radial component, (b) tangential component of the FE model is shown in Fig. 2.18 and the zoomed detail of the mesh near the slot opening is shown in Fig. 2.19.

The overlayed plots of the analytical and numerical field solutions for one pole pitch are shown in Figs. 2.20 and 2.21. There is excellent agreement between analytically and numerically calculated flux density distribution. This verifies the correctness of the methodology described in the previous sections. Moreover, these results show that the approximation of the actual slot shape with a simplified infinitely deep slot opening does not introduce significant errors in the flux density calculations. This may not be true for all slot shapes. Therefore, conformal mapping of more complex slot shapes is introduced in Section 2.5 which can be used to better approximate the actual slot shape. Before dealing with more complex slot shapes it is important to assess the effect of saturation on the accuracy of analytically predicted flux density waveforms.

2.4.2 Saturated Finite Element Model

In the analysis of electrical machines the problems are almost always nonlinear. In order to fully utilize the magnetic material and reduce the size of the machine, it is common to design machines which operate near the saturation point. In that case the magnetic permeability of the iron core will be a function of the local flux density. In the air gap region the highest saturation occurs at the tooth tips which locally reduces the permeability of the core material to values almost as low as the permeability of air. As a result the field distribution in the air gap may be significantly affected thus making the previously shown analytical solution based on the assumption of infinitely permeable iron invalid. In addition, the saturation of the stator teeth and the stator and rotor yoke increases the overall reluctance of the magnetic circuit which shifts the operating point at which the magnets operate to lower values of the flux density. These are the factors which affect the accuracy of the analytical prediction of the air gap field distribution and consequently the accuracy of the back emf, cogging torque and electromagnetic torque waveforms.

The finite element simulation of the no-load operation of the six pole surface PM motor previously used has been carried out with saturation taken into account. The B-H curve of the core material and its relative permeability as a function of flux density are shown in Figs. 2.22 and 2.23. The

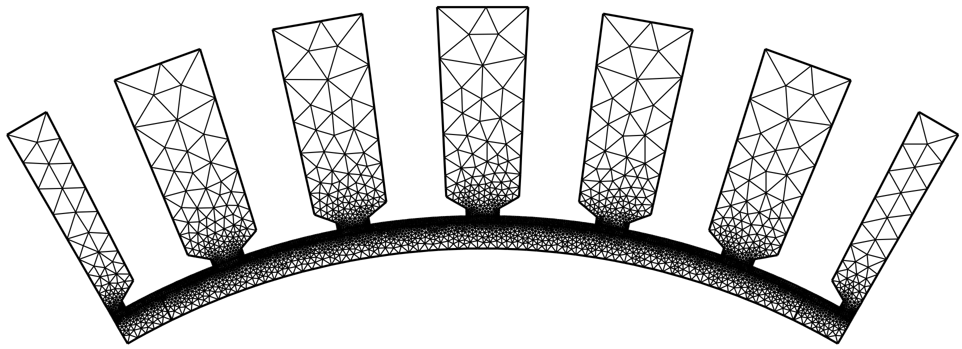

Fig. 2.18 Finite element mesh of the surface PM motor model

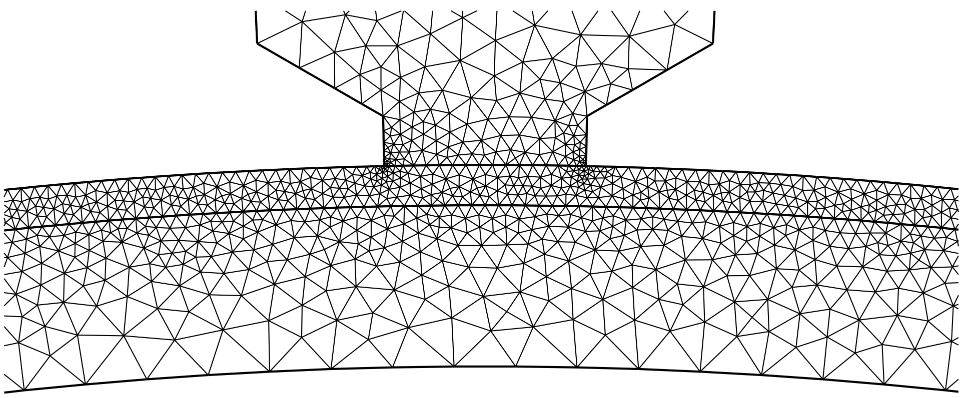

Fig. 2.19 Detail of the finite element mesh near the slot opening

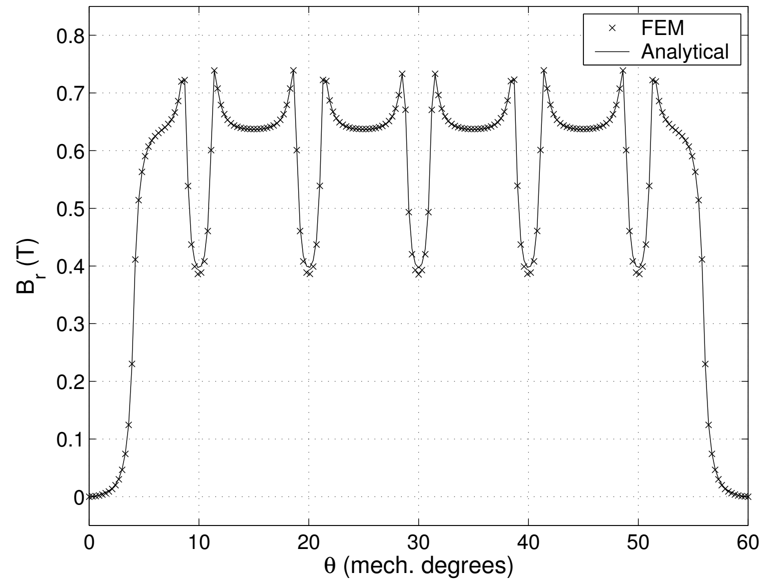

(a)

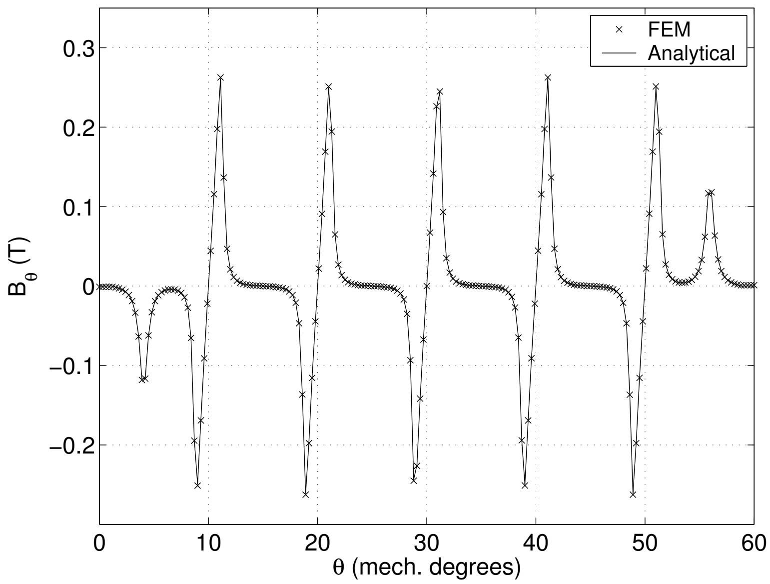

(b)

Fig. 2.20 Comparison of analytical and numerical field solution in the middle of the air gap of a slotted surface PM motor with radial magnetization: (a) radial component, (b) tangential component

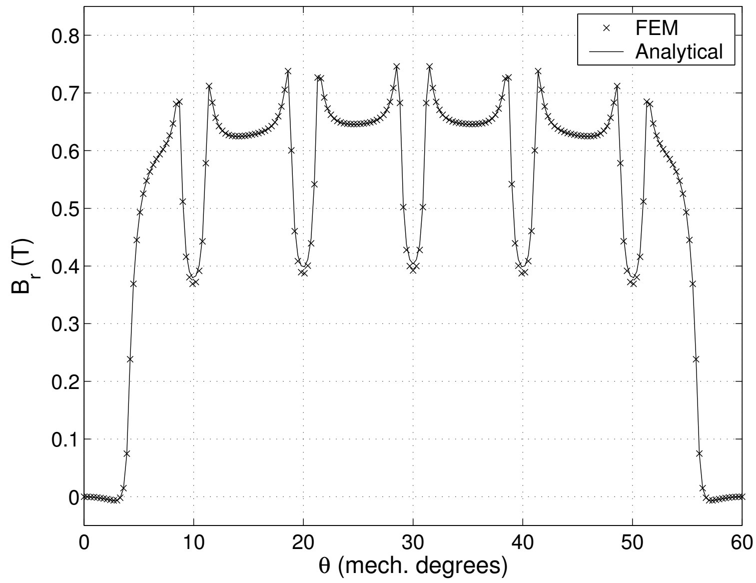

(a)

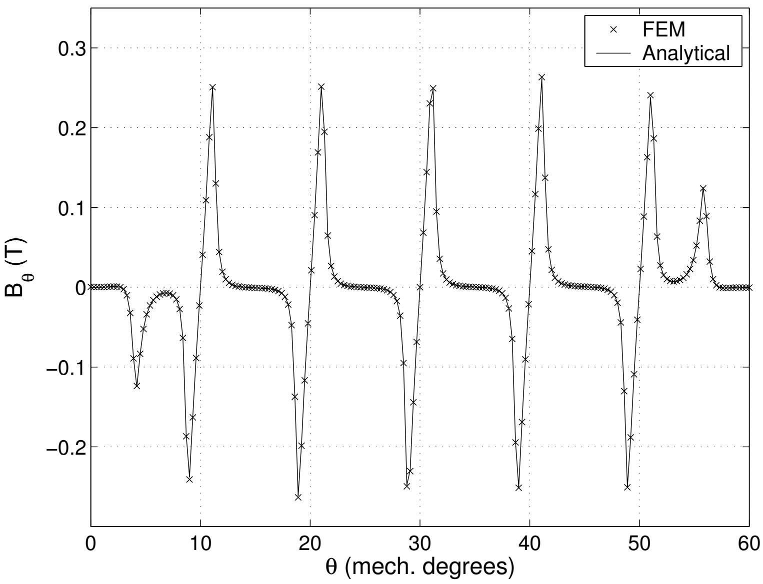

(b)

Fig. 2.21 Comparison of analytical and numerical field solution in the middle of the air gap of a slotted surface PM motor with parallel magnetization: (a) radial component, (b) tangential component saturation point or the knee of the B-H curve occurs around 1.5 T. The finite element mesh is shown in Fig. 2.24. The high mesh density in the air gap area is the same as used before in the unsaturated FE model to increase the accuracy of the flux density calculation.

The flux distributions in no-load operation for the cases of radial and parallel magnetization are shown in Figs. 2.25 and 2.26. The surface plots of the relative permeability distribution for the cases of radial and parallel magnetization shown in Figs. 2.27 and 2.28 provide information about how local saturation affects the magnetic properties of the core material. The peak values of the flux density in the stator teeth and the stator yoke are around 1.23 T and 1.38 T.

The analytical field solution and the numerical field solution with saturation included for the cases of radial and parallel magnetization are compared in Figs. 2.29 and 2.30. It is apparent from these figures that the effect of saturation does not compromise the analytical solution obtained earlier. The agreement of analytically and numerically calculated waveforms in Figs. 2.29 and 2.30 is still close to the agreement observed in Figs. 2.20 and 2.21 when infinite permeability of the iron core was assumed, although some small differences can be noticed. These differences are more noticeable in the waveforms of the radial component of the flux density. The tangential component seems to be almost unaffected by saturation. However, this may not be the case if the motor becomes more severely saturated. The analytical and finite element calculations have been repeated with the magnet remanence increased to 1.1 T in order to observe the extent to which the higher saturation of the iron core affects the air gap flux density distribution. The higher level of saturation in the stator teeth and yoke is noticeable in Figs. 2.31 and 2.32, which show distribution of relative permeability for both cases of magnetization. The differences between the analytical and numerical results in terms of air gap flux density distribution are now more significant as shown in Figs. 2.33 and 2.34. Note that the values of the radial component of the flux density obtained numerically are now significantly lower than the values predicted analytically. The main reason is the increase of the total reluctance of the magnetic circuit due to saturation which shifts the operating point of the magnets to lower values of the flux density. It is apparent that in the case of a highly saturated motor the proposed analytical approach no longer provides satisfying results.

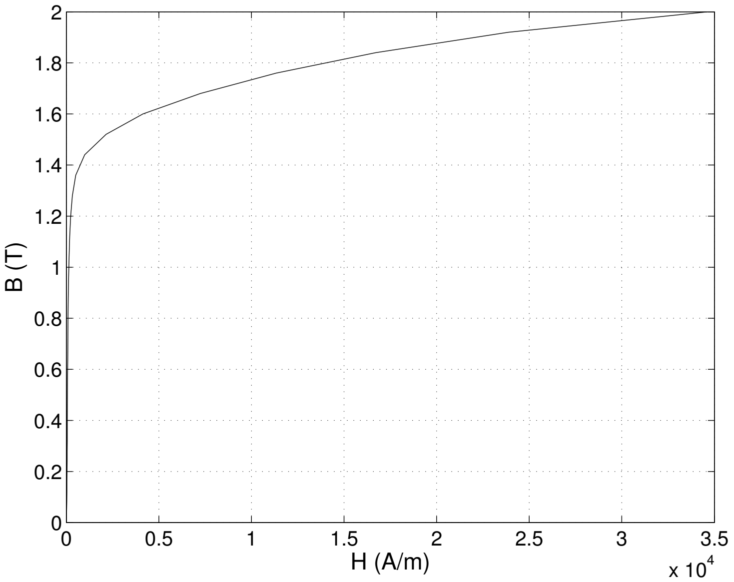

Fig. 2.22 B-H curve of the magnetic material used in the six pole surface PM motor

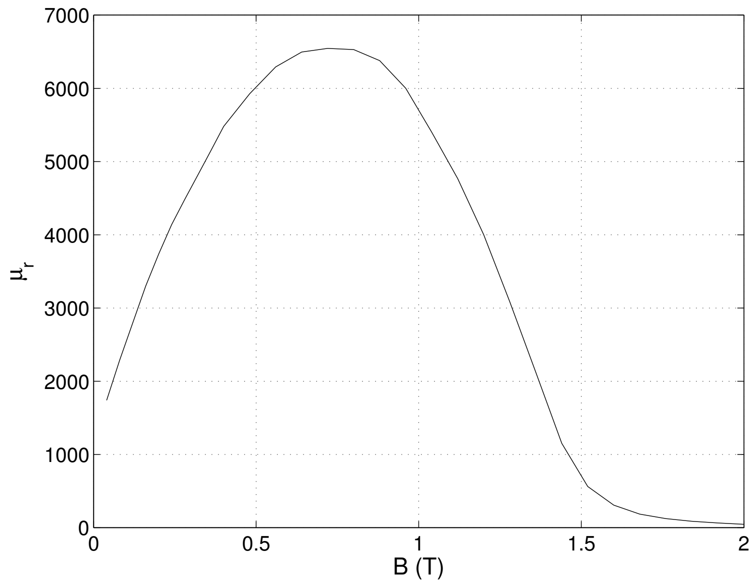

Fig. 2.23 Relative permeability of the magnetic material used in the six pole surface PM motor shown as a function of flux density

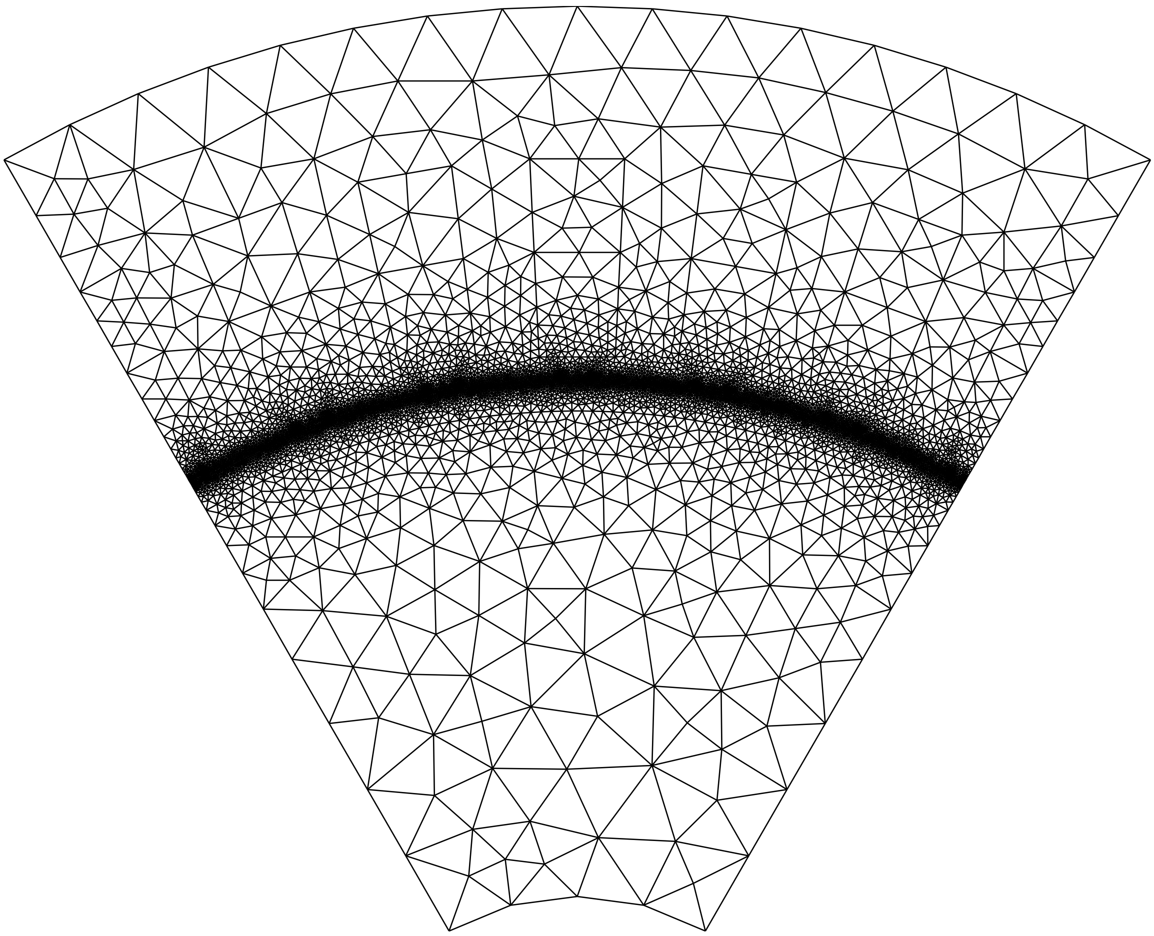

Fig. 2.24 Finite element mesh for the saturated model of the six pole surface PM motor

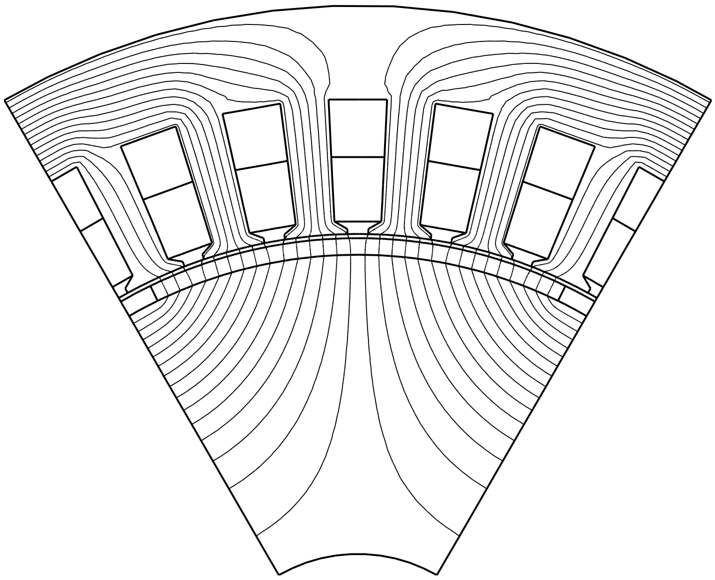

Fig. 2.25 Flux lines in no-load operation of the saturated six pole surface PM motor with radial magnetization

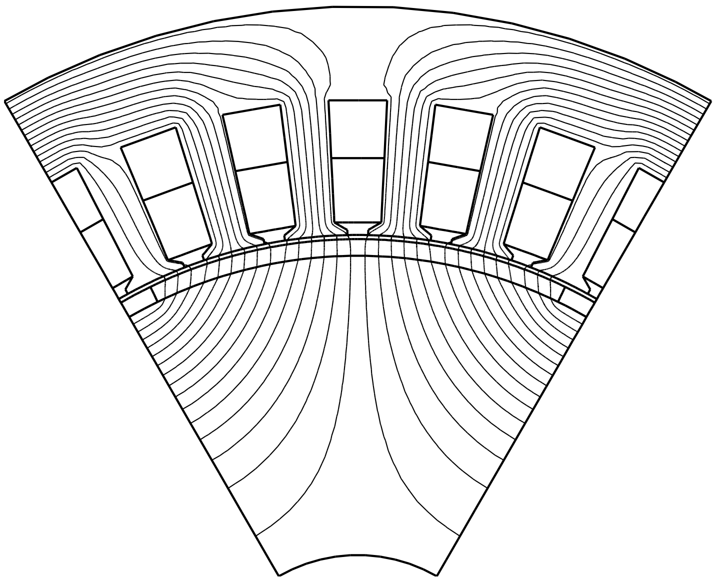

Fig. 2.26 Flux lines in no-load operation of the saturated six pole surface PM motor with parallel magnetization

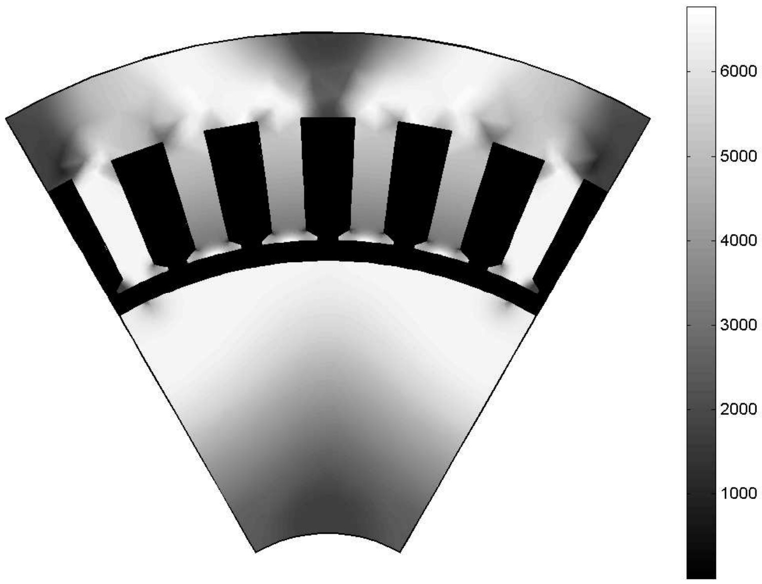

Fig. 2.27 Distribution of the relative permeability in no-load operation of the saturated six pole surface PM motor with radial magnetization

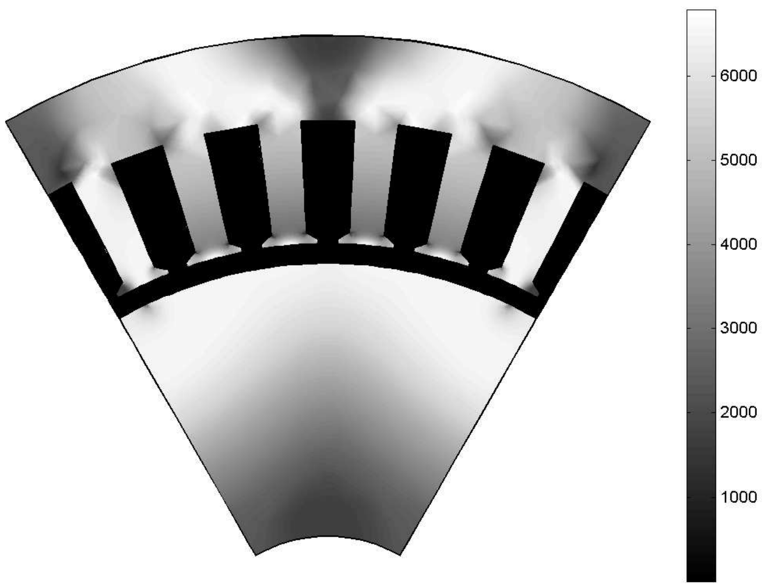

Fig. 2.28 Distribution of the relative permeability in no-load operation of the saturated six pole surface PM motor with parallel magnetization

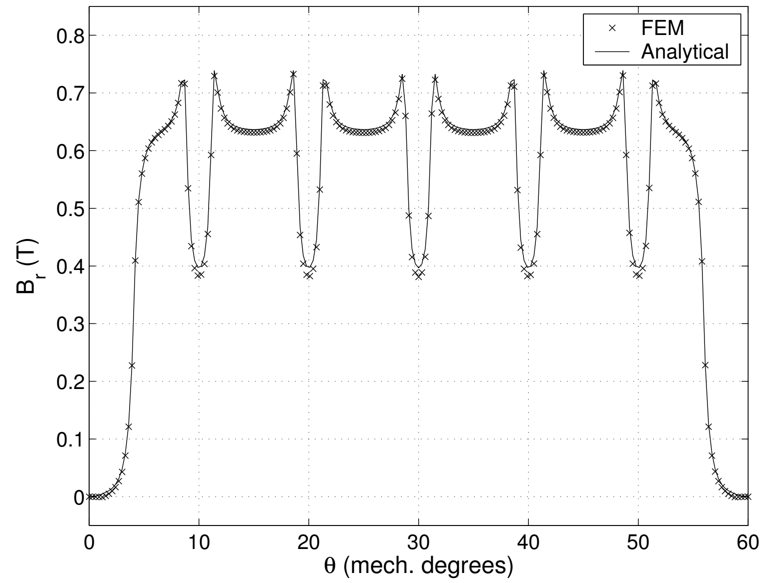

(a)

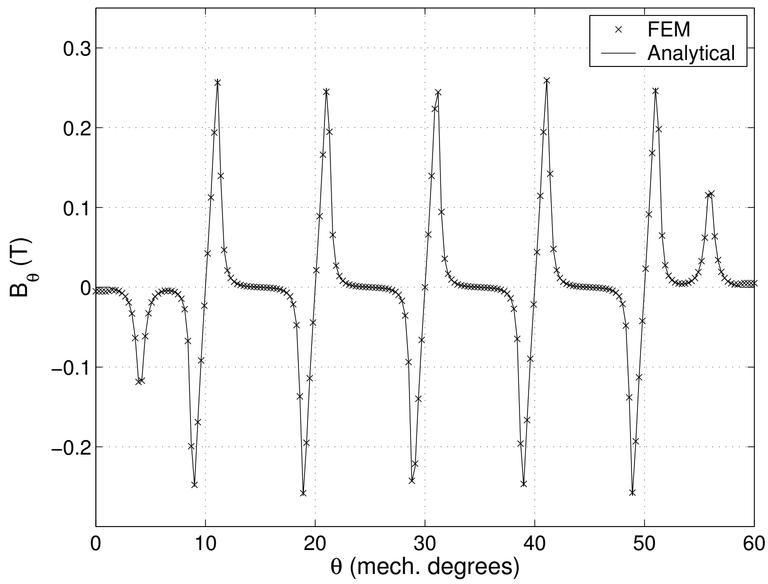

(b)

Fig. 2.29 Comparison of analytical and numerical field solution in the middle of the air gap of a saturated, slotted surface PM motor with radial magnetization: (a) radial component, (b) tangential component

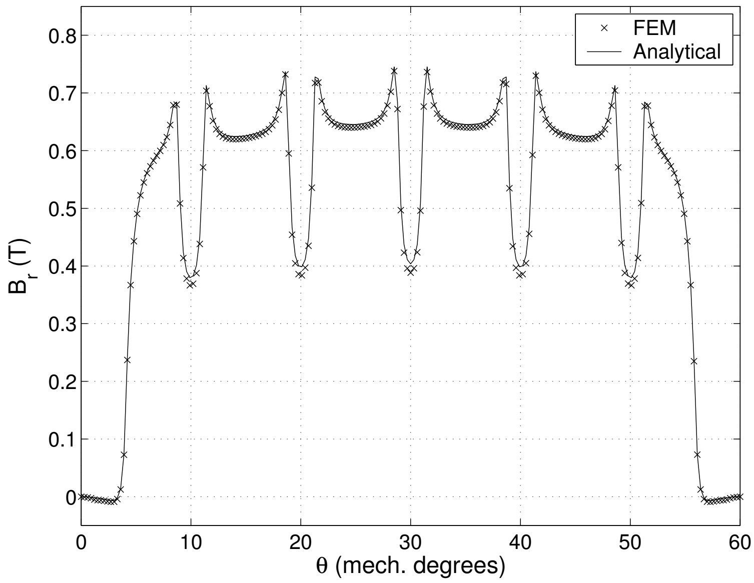

(a)

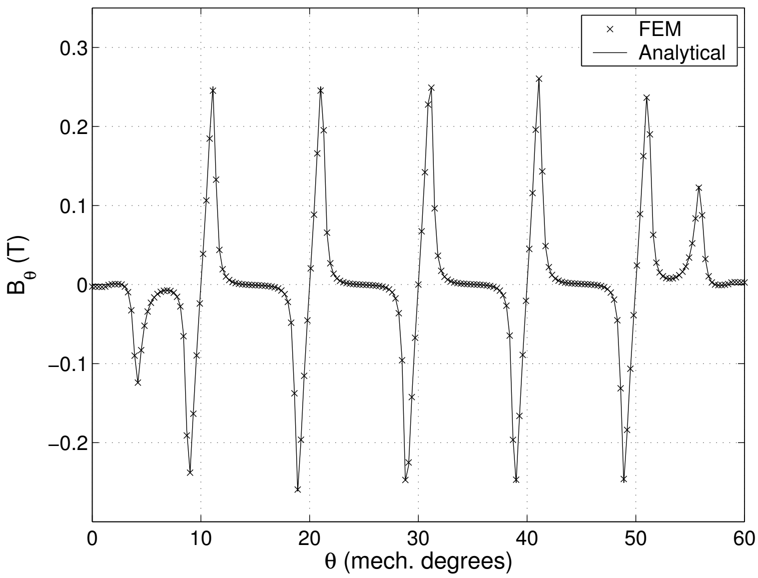

(b)

Fig. 2.30 Comparison of analytical and numerical field solution in the middle of the air gap of a saturated, slotted surface PM motor with parallel magnetization: (a) radial component, (b) tangential component

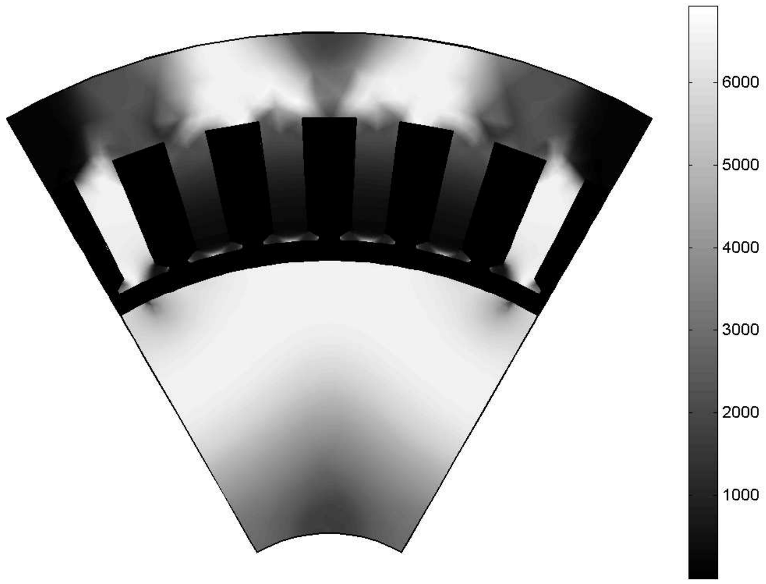

Fig. 2.31 Distribution of the relative permeability in no-load operation of the highly saturated 6 pole surface PM motor with radial magnetization and $B_r = 1.1$ T

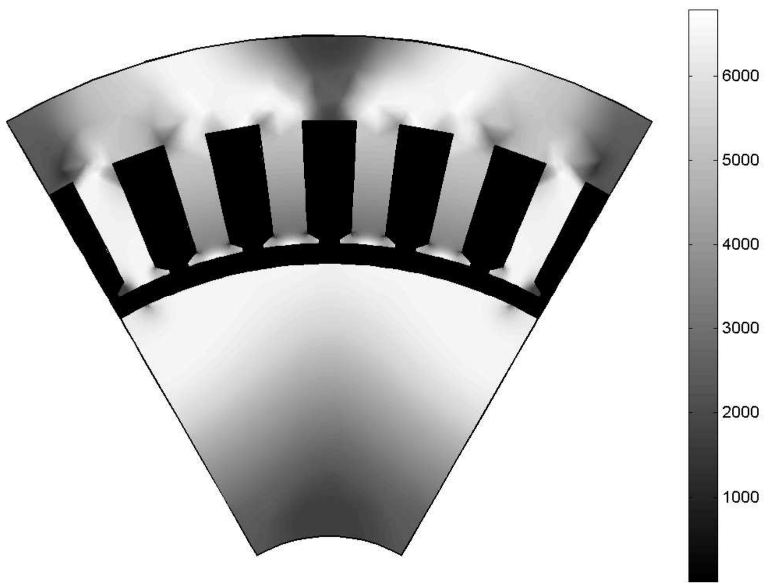

Fig. 2.32 Distribution of the relative permeability in no-load operation of the highly saturated 6 pole surface PM motor with parallel magnetization and $B_r = 1.1$ T

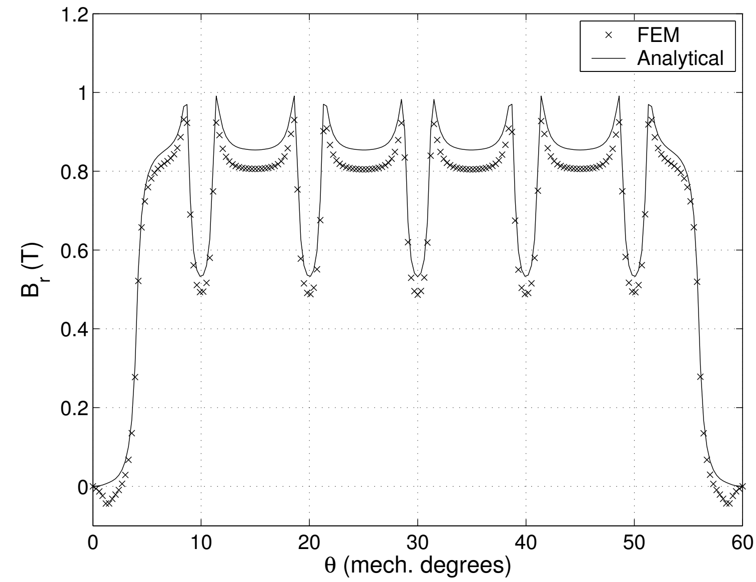

(a)

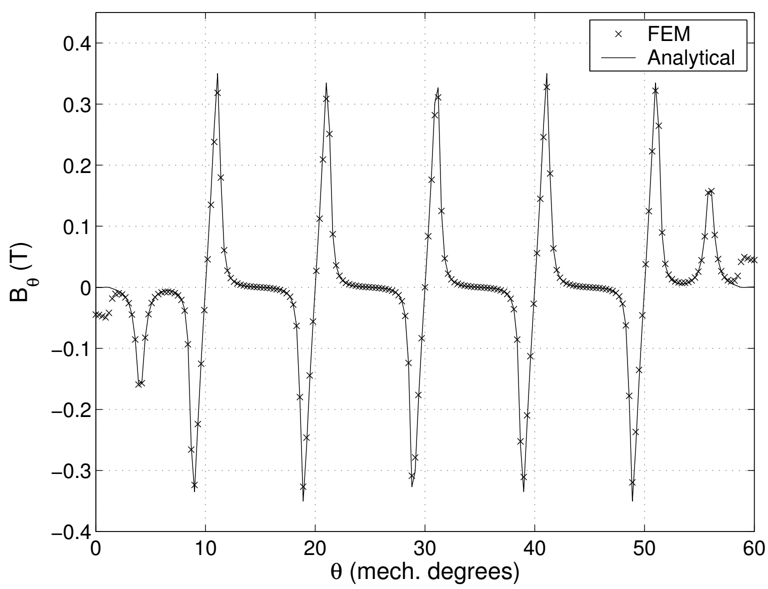

(b)

Fig. 2.33 Comparison of analytical and numerical field solution in the middle of the air gap of a highly saturated, slotted surface PM motor with radial magnetization and $B_r = 1.1$ T: (a) radial component, (b) tangential component

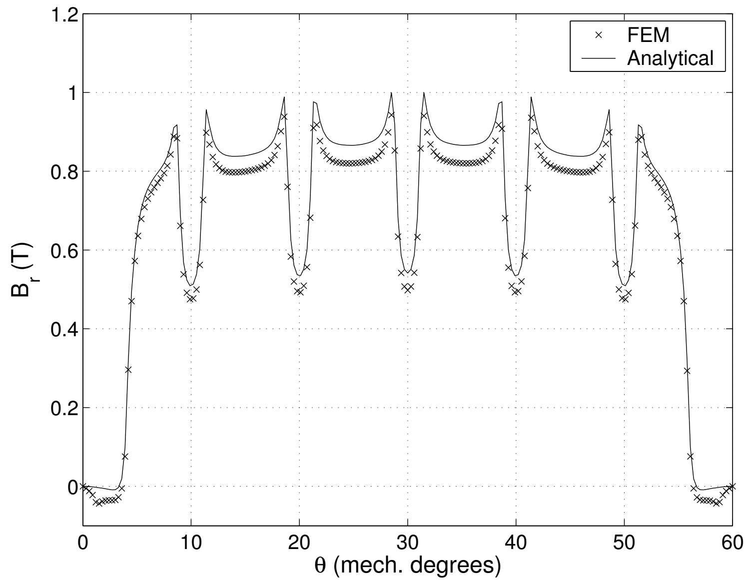

(a)

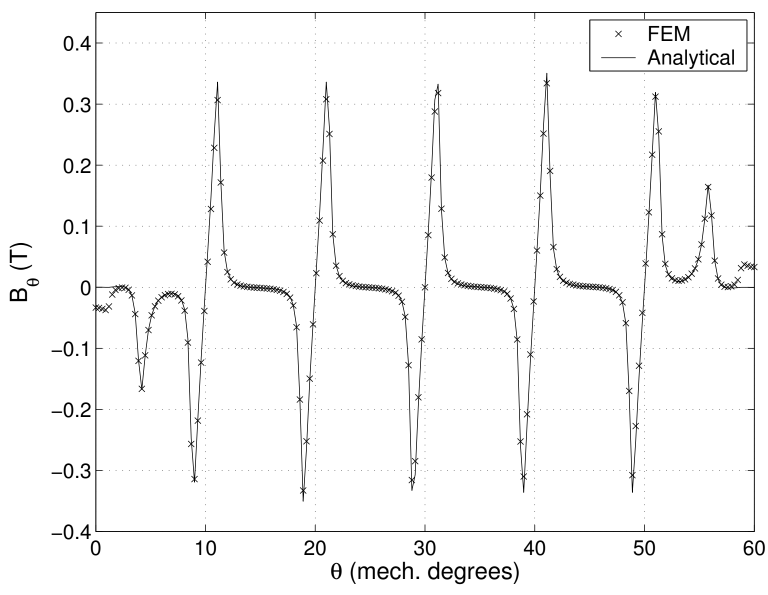

(b)

Fig. 2.34 Comparison of analytical and numerical field solution in the middle of the air gap of a highly saturated, slotted surface PM motor with parallel magnetization and $B_r = 1.1$ T: (a) radial component, (b) tangential component

2.5 Conformal Transformation of More Complex Slot Shapes

The simple slot opening with parallel sides used in Section 2.2 can be a good approximation of the actual slot shape if the width of the slot opening b_o is not large relative to its depth d_o. Very often this is not the case in the actual PM motors. The motor manufacturers prefer to have a fairly large slot opening relative to the size of the wire which is inserted into the slot in order to facilitate the winding insertion and to reduce the time and cost needed for the winding assembly. Fig. 2.35 shows two cases of the slot opening. In the case (a) the approximation with the slot shape from Section 2.2 can be used, while in the case (b) this approximation may no longer provide satisfying results.

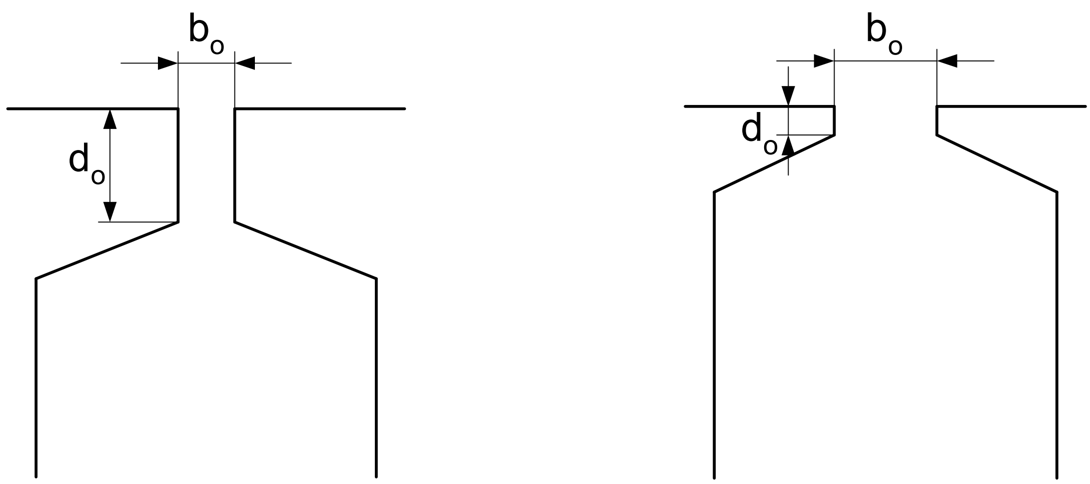

(a) (b)

Fig. 2.35 Two cases of the slot opening: (a) small width, large depth, (b) large width, small depth

The large slot opening is not desirable from the aspect of cogging torque reduction, but for the reason of manufacturing cost reduction it is often unavoidable. In such a case it may be necessary to obtain conformal transformation of the actual slot shape to calculate the air gap field more accurately. The example of a more complex slot shape which is often used in PM motors is shown in Fig. 2.36. It is assumed that the slot is infinitely deep. This assumption simplifies conformal mapping and at the same time does not affect the results because the field at the bottom of the actual slot is negligible.

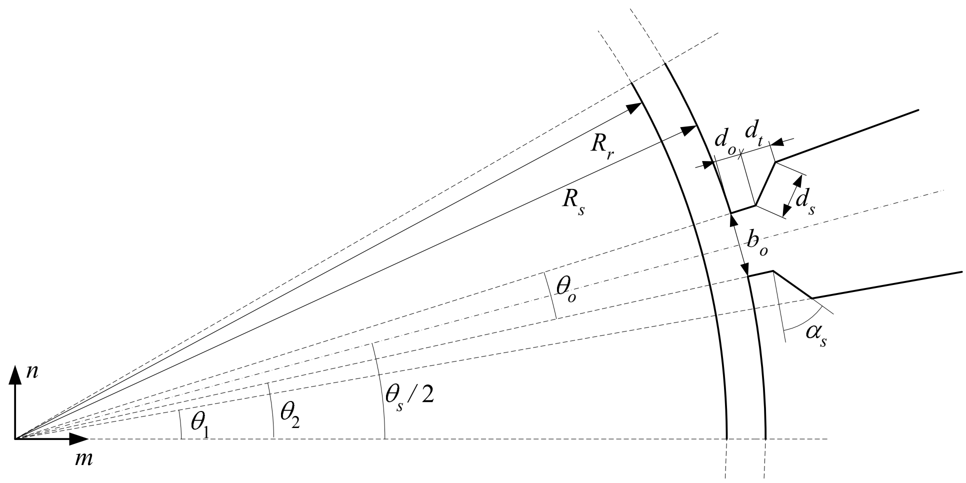

Fig. 2.36 Infinitely deep slot with more complex shape compared to the simple slot opening with parallel sides

The basic approach to conformal mapping of the slot shape in Fig. 2.36 is identical to the one used for the simple slot opening in Section 2.2. Therefore, in this section the emphasis will be put on details in which conformal transformations of the two slot shapes differ.

The original slot shape in Fig. 2.36 is transformed into its linear model in the Z plane using logarithmic conformal transformation. The slot configuration in the Z plane with the unknown values of w at the vertices of the polygon is shown in Fig. 2.37. The Schwarz-Christoffel transformation is given by

$$\begin{aligned}\frac{\mathrm{d}z}{\mathrm{d}w} &= A(w-0)^{\frac{0}{\pi}-1}(w-1)^{\frac{0}{\pi}-1}(w-a)^{\frac{\alpha}{\pi}-1}(w-f)^{\frac{\alpha}{\pi}-1}(w-b)^{\frac{\beta}{\pi}-1}(w-e)^{\frac{\beta}{\pi}-1}\\ &\quad (w-c)^{\frac{\gamma}{\pi}-1}(w-d)^{\frac{\gamma}{\pi}-1} \qquad (2.106)\end{aligned}$$

After substituting the values of the angles α, β and γ into (2.106), the transformation from the Z plane to the upper half of the W plane is given by

$$\frac{\mathrm{d}z}{\mathrm{d}w} = f(w) = A\frac{(w-a)^{\frac{1}{2}}(w-f)^{\frac{1}{2}}(w-b)^{\frac{1}{2}-\frac{\alpha_s}{\pi}}(w-e)^{\frac{1}{2}-\frac{\alpha_s}{\pi}}}{w(w-1)(w-c)^{\frac{1}{2}-\frac{\alpha_s}{\pi}}(w-d)^{\frac{1}{2}-\frac{\alpha_s}{\pi}}} \qquad (2.107)$$

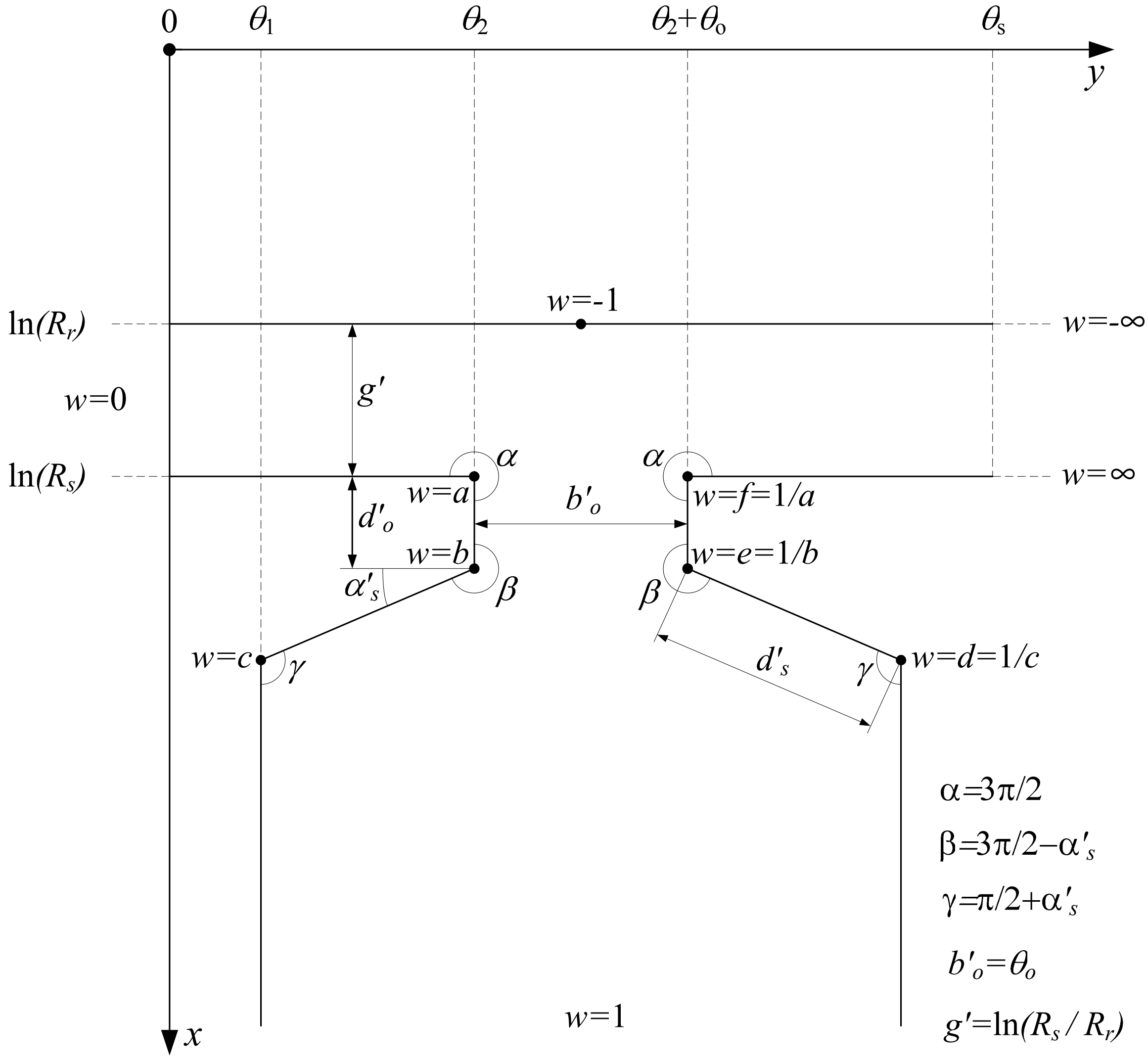

Fig. 2.37 Complex slot shape in the Z plane

The constant A can be found by using the method of integration along a large semicircle in the W plane as shown before. Thus

$$\int \mathrm{d}z = \int_0^\pi A \frac{\left(Re^{j\theta}-a\right)^{\frac{1}{2}}\left(Re^{j\theta}-f\right)^{\frac{1}{2}}\left(Re^{j\theta}-b\right)^{\frac{1}{2}-\frac{\alpha_s}{\pi}}\left(Re^{j\theta}-e\right)^{\frac{1}{2}-\frac{\alpha_s}{\pi}}}{Re^{j\theta}\left(Re^{j\theta}-1\right)\left(Re^{j\theta}-c\right)^{\frac{1}{2}-\frac{\alpha_s}{\pi}}\left(Re^{j\theta}-d\right)^{\frac{1}{2}-\frac{\alpha_s}{\pi}}} jRe^{j\theta}\mathrm{d}\theta \tag{2.108}$$

As $R \to \infty$, (2.108) becomes

$$\int \mathrm{d}z = \int_0^\pi A \frac{\left(Re^{j\theta}\right)^{\frac{1}{2}}\left(Re^{j\theta}\right)^{\frac{1}{2}}\left(Re^{j\theta}\right)^{\frac{1}{2}-\frac{\alpha_s}{\pi}}\left(Re^{j\theta}\right)^{\frac{1}{2}-\frac{\alpha_s}{\pi}}}{Re^{j\theta}\left(Re^{j\theta}\right)\left(Re^{j\theta}\right)^{\frac{1}{2}-\frac{\alpha}{\pi}}\left(Re^{j\theta}\right)^{\frac{1}{2}-\frac{\alpha_s}{\pi}}} jRe^{j\theta}\mathrm{d}\theta = \int_0^\pi jA\mathrm{d}\theta = j\pi A \tag{2.109}$$

In the Z plane $\int \mathrm{d}z = -g'$ and therefore

$$A = j\frac{g'}{\pi} \tag{2.110}$$

The values of constants a to f are more difficult to determine since there is no explicit analytical solution of the integral of equation (2.107). To find the constants it is necessary to recognize that the complex distance z_{mn} between any two points in the Z plane defined by parameters w_m and w_n is equal to the integral [66]

$$z_{mn} = \int_{w_m}^{w_n} f(w)\mathrm{d}w \tag{2.111}$$

Equation (2.111) can be used to connect each of the known dimensions of the slot with the unknown constants a to f, thus giving a set of equations

$$\begin{aligned} d_o' &= \int_a^b |f(w)|\,\mathrm{d}w \\ d_s' &= \int_b^c |f(w)|\,\mathrm{d}w \\ \frac{b_o'}{2} &= \int_0^{-1} |f(w)|\,\mathrm{d}w - \int_0^a |f(w)|\,\mathrm{d}w \end{aligned} \tag{2.112}$$

Since the limits of the integrals in (2.112) contain the unknown constants, the problem of finding these constants can be solved by using the nonlinear least-squares optimization algorithm (MATLAB function $lsqnonlin$). It is sufficient to determine only a, b and c, because, due to the symmetry, one has

$$d = \frac{1}{c}$$

$$
\begin{aligned}
e &= \frac{1}{b} \\
f &= \frac{1}{a}
\end{aligned}
\tag{2.113}
$$

The error function to be minimized is given by

$$
\begin{aligned}
F &= \left(d_o' - \int_a^b |f(w)|\,\mathrm{d}w\right)^2 + \left(d_s' - \int_b^{\left(1-10^{-12}\right)c} |f(w)|\,\mathrm{d}w\right)^2 + \\
&\quad \left[\frac{b_o'}{2} - \left(\int_{-10^{-12}}^{-1} |f(w)|\,\mathrm{d}w - \int_{10^{-12}}^{a} |f(w)|\,\mathrm{d}w\right)\right]^2
\end{aligned}
\tag{2.114}
$$

Since $f(w)$ is infinite at $w = 0$ and $w = c$, the limits of the integrals in (2.114) are slightly modified to avoid numerical problems during integration. For calculation purposes, zero is replaced by 10^{-12} and c is replaced by $\left(1 - 10^{-12}\right) c$. This approximation will cause a negligible error in the final result. The error tolerance for the value of F is set to 10^{-24}.

The models of the slot in the T and K planes are identical to the ones shown in Figs. 2.11 and 2.12.

It was shown earlier in Section 2.2 that the flux density in the S plane is given by

$$
B_s = B_k \left(\frac{\partial k}{\partial s}\right)^* = B_k \left(\frac{\partial k}{\partial t}\frac{\partial t}{\partial w}\frac{\partial w}{\partial z}\frac{\partial z}{\partial s}\right)^*
\tag{2.115}
$$

The partial derivatives can be expressed as

$$
\begin{aligned}
\frac{\partial k}{\partial t} &= e^t = e^{\ln k} = k \\
\frac{\partial t}{\partial w} &= j\frac{g'}{\pi}\frac{1}{w} \\
\frac{\partial w}{\partial z} &= -j\frac{\pi}{g'}\frac{w(w-1)(w-c)^{\frac{1}{2}-\frac{\alpha_s}{\pi}}(w-d)^{\frac{1}{2}-\frac{\alpha_s}{\pi}}}{(w-a)^{\frac{1}{2}}(w-f)^{\frac{1}{2}}(w-b)^{\frac{1}{2}-\frac{\alpha_s}{\pi}}(w-e)^{\frac{1}{2}-\frac{\alpha_s}{\pi}}} \\
\frac{\partial z}{\partial s} &= \frac{1}{s}
\end{aligned}
\tag{2.116}
$$

Substituting (2.116) and into (2.115) yields

$$
B_s = B_k \left[kj\frac{g'}{\pi}\frac{1}{w}(-j)\frac{\pi}{g'}\frac{w(w-1)(w-c)^{\frac{1}{2}-\frac{\alpha_s}{\pi}}(w-d)^{\frac{1}{2}-\frac{\alpha_s}{\pi}}}{(w-a)^{\frac{1}{2}}(w-f)^{\frac{1}{2}}(w-b)^{\frac{1}{2}-\frac{\alpha_s}{\pi}}(w-e)^{\frac{1}{2}-\frac{\alpha_s}{\pi}}}\frac{1}{s}\right]^*
\tag{2.117}
$$

The final expression for the flux density in the S plane is

$$B_s = B_k \left[\frac{k}{s} \frac{(w-1)(w-c)^{\frac{1}{2}-\frac{\alpha_s}{\pi}}(w-d)^{\frac{1}{2}-\frac{\alpha_s}{\pi}}}{(w-a)^{\frac{1}{2}}(w-f)^{\frac{1}{2}}(w-b)^{\frac{1}{2}-\frac{\alpha_s}{\pi}}(w-e)^{\frac{1}{2}-\frac{\alpha_s}{\pi}}} \right]^* \tag{2.118}$$

The complex relative air gap permeance is defined as

$$\lambda = \frac{k}{s} \frac{(w-1)(w-c)^{\frac{1}{2}-\frac{\alpha_s}{\pi}}(w-d)^{\frac{1}{2}-\frac{\alpha_s}{\pi}}}{(w-a)^{\frac{1}{2}}(w-f)^{\frac{1}{2}}(w-b)^{\frac{1}{2}-\frac{\alpha_s}{\pi}}(w-e)^{\frac{1}{2}-\frac{\alpha_s}{\pi}}} \tag{2.119}$$

The slot dimensions for the motor with parameters given in Table 2.1 are shown in Table 2.2. The waveforms of the real and imaginary parts of λ for the actual slot shape calculated according to (2.119) and for the simple slot opening calculated according to (2.100) are compared in Fig. 2.38.

Table 2.2 Slot dimensions of the six pole surface PM motor

Parameter	*Symbol*	*Value*	*Unit*
Slot opening width	b_o	2.5	mm
Slot opening depth	h_o	0.62	mm
Slot width at the bottom	b_s	7.48	mm
Slot depth	d_s	16.2	mm
Depth of the slanted part	d_t	0.9	mm
Slant angle	α_s	30^0	–

It is apparent from Fig. 2.38 that the difference between the complex permeance of these two slot shapes is very small. Therefore, in this case the simple slot opening with parallel sides is a very good approximation of the actual slot shape.

The waveforms of the flux density distribution in the middle of the slotted air gap have been calculated using the actual slot shape and compared to numerical results in Figs. 2.39 and 2.40. The analytically and numerically calculated waveforms are in a slightly better agreement in the case of an actual slot shape than in the case of a simple slot opening, especially in terms of radial components of the field. This is expected since complex relative air gap permeance is calculated more accurately when the actual slot shape is used in conformal mapping.

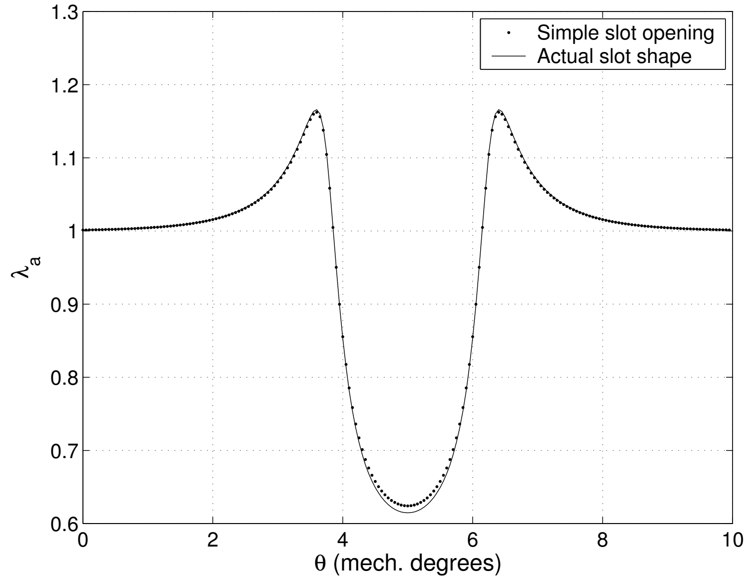

(a)

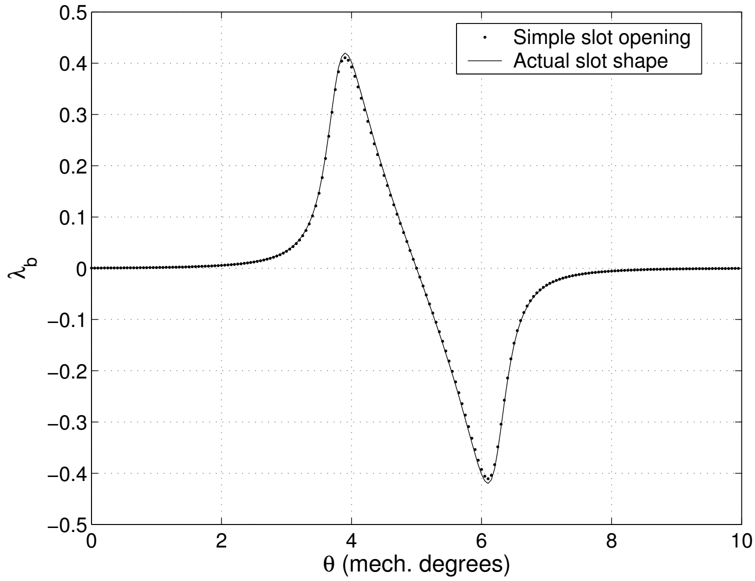

(b)

Fig. 2.38 Comparison of complex relative permeance for the actual slot shape and for the simplified slot opening: (a) real component, (b) imaginary component

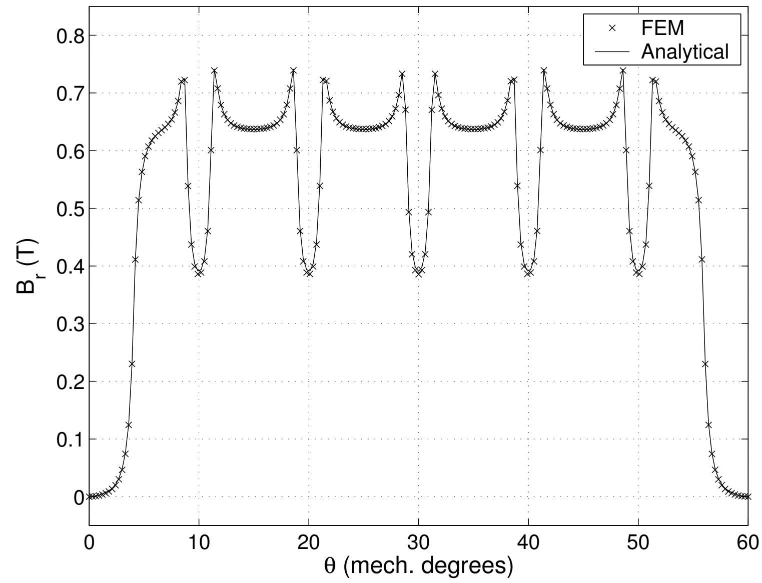

(a)

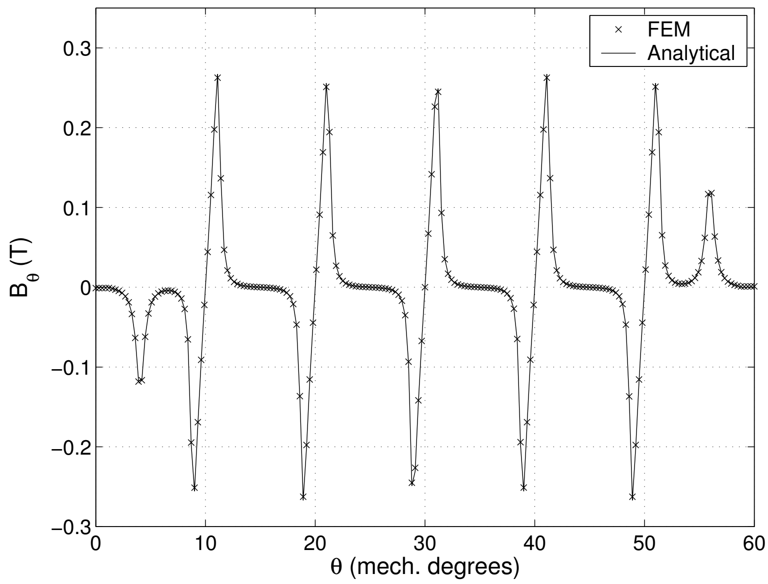

(b)

Fig. 2.39 Comparison of analytical field solution with the actual slot shape and numerical solution in the middle of the air gap of a slotted surface PM motor with radial magnetization: (a) radial component, (b) tangential component

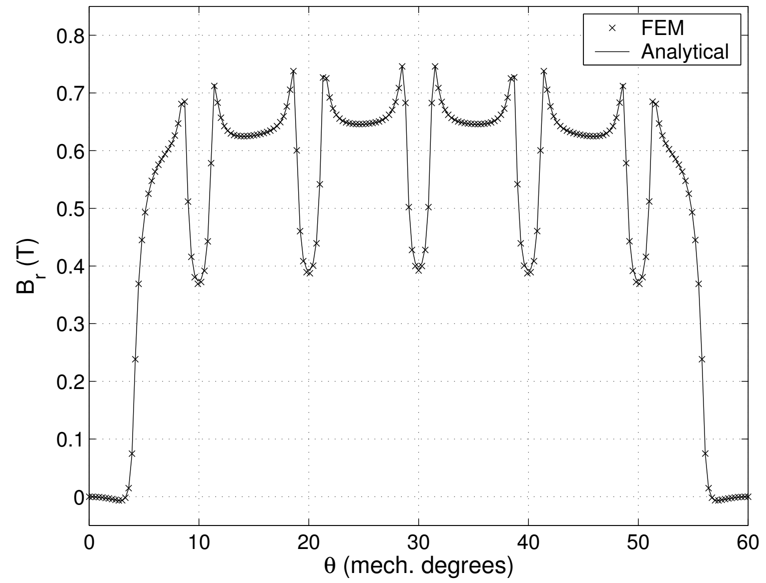

(a)

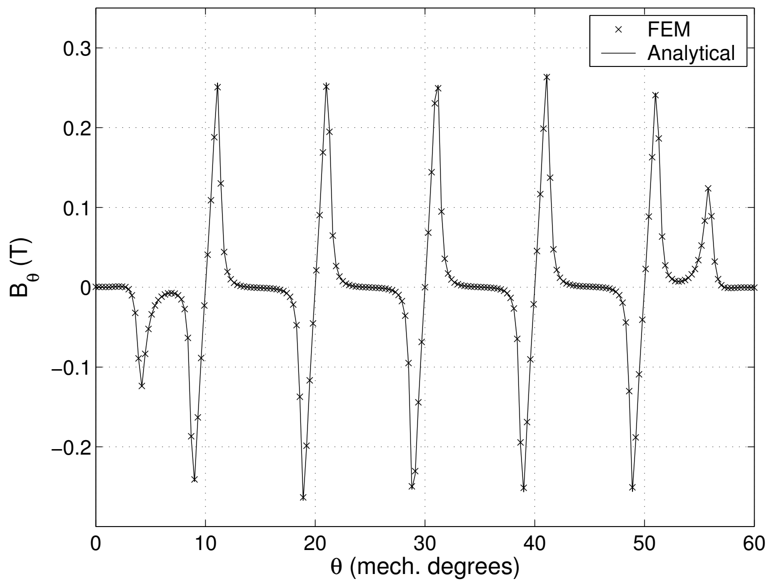

(b)

Fig. 2.40 Comparison of analytical field solution with the actual slot shape and numerical solution in the middle of the air gap of a slotted surface PM motor with parallel magnetization: (a) radial component, (b) tangential component

2.6 Cogging Torque Calculation Based on Maxwell's Stress Theory

According to Maxwell's theory it is possible to calculate the total force on a rigid body placed in the electromagnetic field by integrating the magnetic stress on the closed surface around the body. The magnetic stress vector, i.e. the force per unit surface, is given by [60]

$$\vec{t}_m = \left(\vec{n} \cdot \frac{\vec{B}}{\mu_0}\right) \vec{B} - \vec{n}\frac{1}{2}\frac{\left|\vec{B}\right|^2}{\mu_0} \tag{2.120}$$

where $\vec{n}$ is the surface normal vector and $\vec{B}$ is the flux density vector on the surface of the body. It is clear from (2.120) that the stress vector consists of two components. One component of the vector $\vec{t}_m$ is in the direction of the field $\vec{B}$ and the other is perpendicular to the surface and directed towards it as shown in Fig. 2.41.

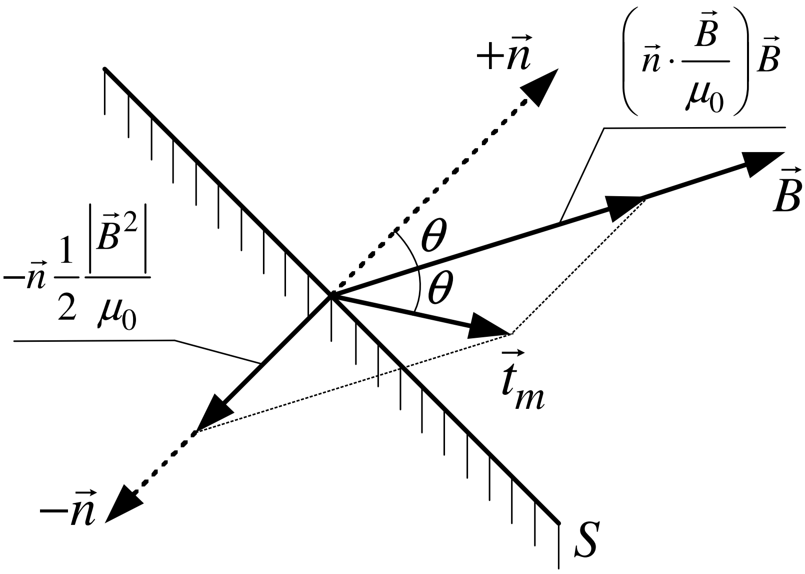

Fig. 2.41 Relationship between vectors $\vec{n}$, $\vec{B}$ and $\vec{t}_m$

It has been mentioned earlier that the surface which encloses the rotor of the surface PM motor is in the shape of a cylinder placed entirely inside the air gap. In that case the surface normal vector will be equal to the unit length vector in the radial direction, i.e.

$$\vec{n} = \vec{a}_r \tag{2.121}$$

The flux density vector $\vec{B}$ will have a radial and a tangential component which can be written in the form

$$\vec{B} = B_r\vec{a}_r + B_\theta\vec{a}_\theta \tag{2.122}$$

Substituting (2.121) and (2.122) into (2.120) yields

$$\begin{aligned}
\vec{t}_m &= \frac{1}{\mu_0}\left[\vec{a}_r \cdot (B_r\vec{a}_r + B_\theta\vec{a}_\theta)\right](B_r\vec{a}_r + B_\theta\vec{a}_\theta) - \vec{a}_r\frac{1}{2}\frac{|\vec{B}|^2}{\mu_0} \\
&= \frac{1}{\mu_0}B_r(B_r\vec{a}_r + B_\theta\vec{a}_\theta) - \vec{a}_r\frac{1}{2}\frac{|\vec{B}|^2}{\mu_0} \\
&= \frac{1}{\mu_0}\left(B_r^2 - \frac{1}{2}|\vec{B}|^2\right)\vec{a}_r + \frac{1}{\mu_0}B_rB_\theta\vec{a}_\theta
\end{aligned} \tag{2.123}$$

The tangential component of the magnetic stress vector is of particular interest for torque calculations. The total tangential force on the rotor is equal to the surface integral of the tangential component of the stress vector. Hence the motor torque is equal to the total force multiplied by the radius of the cylindrical integration surface. If it is assumed that the field is uniform in the axial direction, then the surface integral becomes a line integral multiplied by the active length of the machine. The torque equation in the integral form can then be written as

$$T = \frac{1}{\mu_0}l_aR^2\int_0^{2\pi}B_r(\theta)B_\theta(\theta)d\theta \tag{2.124}$$

where μ_0 is the permeability of vacuum, l_a is the active length of the machine, R is the radius of the integration surface, B_r is the radial and B_θ is the tangential component of the flux density at radius R.

The radius inside the air gap at which the integration surface is positioned is arbitrary, but for calculation purposes it can be problematic if the surface is placed too close to the stator inner surface. The problem occurs at the tooth tips because at those points the complex relative air gap permeability λ has an infinite value. For a simple slot opening the tooth tips are located at the points where $w = a$ and $w = b$. It is apparent from(2.100) that at these points λ is infinite. The same result follows from (2.119) for the actual slot shape when $w = a$ or $w = f$. The complex permeance of the actual slot shape will also have an infinite value when $w = c$ or $w = d$. However, these points are located inside the slot opening and for torque calculations only the points inside the air gap are of interest. To avoid numerical problems of dealing with infinite numbers or with very large values of λ at the radius very close to the stator surface, the analysis will be done in the middle of the air gap at the radius $r = R_s - g/2$ at which the complex permeance λ and the flux density distribution have been evaluated earlier.

At this point the field solution in the air gap of a surface PM motor at no-load operation is known. That field solution can now be used to calculate the cogging torque by integrating the Maxwell's stress vector according to (2.124).

It has been shown earlier that the flux density in the slotted air gap can be written in the form

$$\begin{aligned} B_s(r,\theta,\alpha) &= B_{sr}(r,\theta,\alpha) + jB_{s\theta}(r,\theta,\alpha) \\ &= [B_r(r,\theta,\alpha) + jB_\theta(r,\theta,\alpha)][\lambda_a(r,\theta) - j\lambda_b(r,\theta)] \end{aligned} \tag{2.125}$$

where B_r and B_θ are the radial and tangential components of the flux density in the slotless air gap and λ_a and λ_b are the real and imaginary components of the complex relative air gap permeance. The flux density and the complex permeance can both be written in the form of Fourier series

$$\begin{aligned} B_r(r,\theta,\alpha) &= \sum_n B_{rn}(r)\cos[np(\theta-\alpha)] \\ B_\theta(r,\theta,\alpha) &= \sum_k B_{\theta n}(r)\sin[np(\theta-\alpha)] \\ \lambda_a(r,\theta) &= \lambda_0(r) + \sum_m \lambda_{am}(r)\cos(mQ_s\theta) \\ \lambda_b(r,\theta) &= \sum_m \lambda_{bm}(r)\sin(mQ_s\theta) \end{aligned} \tag{2.126}$$

where p is the number of pole pairs, Q_s is the number of stator slots and α is the angular position of the rotor. The Fourier coefficients B_{rn} and $B_{\theta n}$ are calculated directly from (2.41) and (2.42) while λ_0, λ_{am} and λ_{bm} are calculated from (2.100) or (2.119) using discrete Fourier transform. The rotor position α is equal to

$$\alpha = \omega_{rm}t \tag{2.127}$$

where ω_{rm} is the mechanical rotor speed in rad/s.

The use of B_{rn} and $B_{\theta n}$ is based on the approximation made earlier which assumes that the field in the K plane can be evaluated along the circular arc instead of the actual contour into which the circular arc from the S plane is transformed.

According to (2.125) the radial and tangential components of the flux density in the slotted air gap can be written as

$$\begin{aligned}
B_{sr}(r,\theta,\alpha) &= B_r(r,\theta,\alpha)\lambda_a(r,\theta) + B_\theta(r,\theta,\alpha)\lambda_b(r,\theta) \\
&= \sum_n B_{rn}(r)\cos[np(\theta-\alpha)]\left[\lambda_0(r) + \sum_m \lambda_{am}(r)\cos(mQ_s\theta)\right] + \\
&\quad \sum_n B_{\theta n}(r)\sin[np(\theta-\alpha)]\sum_m \lambda_{bm}(r)\sin(mQ_s\theta) \\
&= \lambda_0(r)\sum_n B_{rn}(r)\cos[np(\theta-\alpha)] + \\
&\quad \sum_n\sum_m B_{rn}(r)\lambda_{am}(r)\cos[np(\theta-\alpha)]\cos(mQ_s\theta) + \\
&\quad \sum_n\sum_m B_{\theta n}(r)\lambda_{bm}(r)\sin[np(\theta-\alpha)]\sin(mQ_s\theta)
\end{aligned} \tag{2.128}$$

$$\begin{aligned}
B_{s\theta}(r,\theta,\alpha) &= B_\theta(r,\theta,\alpha)\lambda_a(r,\theta) - B_r(r,\theta,\alpha)\lambda_b(r,\theta) \\
&= \sum_n B_{\theta n}(r)\sin[np(\theta-\alpha)]\left[\lambda_0(r) + \sum_m \lambda_{am}(r)\cos(mQ_s\theta)\right] - \\
&\quad \sum_n B_{rn}(r)\cos[np(\theta-\alpha)]\sum_m \lambda_{bm}(r)\sin(mQ_s\theta) \\
&= \lambda_0(r)\sum_n B_{\theta n}(r)\sin[np(\theta-\alpha)] + \\
&\quad \sum_n\sum_m B_{\theta n}(r)\lambda_{am}(r)\sin[np(\theta-\alpha)]\cos(mQ_s\theta) - \\
&\quad \sum_n\sum_m B_{rn}(r)\lambda_{bm}(r)\cos[np(\theta-\alpha)]\sin(mQ_s\theta)
\end{aligned} \tag{2.129}$$

The cogging torque expression is now

$$T_c(\alpha) = \frac{1}{\mu_0} l_a R^2 \int_0^{2\pi} B_{sr}(R,\theta,\alpha) B_{s\theta}(R,\theta,\alpha) d\theta \tag{2.130}$$

The integrand of (2.130) includes the terms consisting of multiple sums. Using a different variable name for each sum in (2.128) and (2.129) and knowing that the Fourier coefficients in the expressions for the flux density and the complex permeance are calculated at the radius $r = R$, the cogging torque expression becomes

$$T_c(\alpha) = \frac{1}{\mu_0} l_a R^2 \left\{ \lambda_0^2 \sum_n \sum_k B_{rn} B_{\theta k} \int_0^{2\pi} \cos[np(\theta-\alpha)]\sin[kp(\theta-\alpha)] d\theta + \right.$$

$$\lambda_0 \sum_n \sum_k \sum_h B_{rn} B_{\theta k} \lambda_{ah} \int_0^{2\pi} \cos[np(\theta-\alpha)] \sin[kp(\theta-\alpha)] \cos(hQ_s\theta) d\theta -$$
$$\lambda_0 \sum_n \sum_k \sum_h B_{rn} B_{rk} \lambda_{bh} \int_0^{2\pi} \cos[np(\theta-\alpha)] \cos[kp(\theta-\alpha)] \sin(hQ_s\theta) d\theta +$$
$$\lambda_0 \sum_n \sum_k \sum_m B_{rn} B_{\theta k} \lambda_{am} \int_0^{2\pi} \cos[np(\theta-\alpha)] \sin[kp(\theta-\alpha)] \cos(mQ_s\theta) d\theta +$$
$$\lambda_0 \sum_n \sum_k \sum_m B_{\theta n} B_{\theta k} \lambda_{bm} \int_0^{2\pi} \sin[np(\theta-\alpha)] \sin[kp(\theta-\alpha)] \sin(mQ_s\theta) d\theta +$$
$$\sum_n \sum_k \sum_m \sum_h B_{rn} B_{\theta k} \lambda_{am} \lambda_{ah} \int_0^{2\pi} \cos[np(\theta-\alpha)] \sin[kp(\theta-\alpha)] \cos(mQ_s\theta) \cos(hQ_s\theta) d\theta +$$
$$\sum_n \sum_k \sum_m \sum_h B_{\theta n} B_{\theta k} \lambda_{bm} \lambda_{ah} \int_0^{2\pi} \sin[np(\theta-\alpha)] \sin[kp(\theta-\alpha)] \sin(mQ_s\theta) \cos(hQ_s\theta) d\theta -$$
$$\sum_n \sum_k \sum_m \sum_h B_{rn} B_{rk} \lambda_{am} \lambda_{bh} \int_0^{2\pi} \cos[np(\theta-\alpha)] \cos[kp(\theta-\alpha)] \cos(mQ_s\theta) \sin(hQ_s\theta) d\theta -$$
$$\sum_n \sum_k \sum_m \sum_h B_{\theta n} B_{rk} \lambda_{bm} \lambda_{bh} \int_0^{2\pi} \sin[np(\theta-\alpha)] \cos[kp(\theta-\alpha)] \sin(mQ_s\theta) \sin(hQ_s\theta) d\theta \Big\} \tag{2.131}$$

The integrals in (2.131) will yield a result different from zero only for certain values of n, k, m and h. One of the terms from (2.131) is used below as an example to show for which combinations of n, k, m and h the integral $\int_0^{2\pi}$ will be different from zero.

The integrands in (2.131) are expressed as the products of **sine** and **cosine** functions. Before integration they need to be transformed into the sums of **sine** and **cosine** functions using the basic identities for trigonometric functions which are

$$\begin{aligned} \sin x \cos y &= \frac{1}{2}[\sin(x+y) + \sin(x-y)] \\ \cos x \cos y &= \frac{1}{2}[\cos(x+y) + \cos(x-y)] \\ \sin x \sin y &= -\frac{1}{2}[\cos(x+y) - \cos(x-y)] \end{aligned} \tag{2.132}$$

For the second term in (2.131) one has

$$I = \lambda_0 \sum_n \sum_k \sum_h B_{rn} B_{\theta k} \lambda_{ah} \int_0^{2\pi} \cos[np(\theta-\alpha)] \sin[kp(\theta-\alpha)] \cos(hQ_s\theta) d\theta =$$
$$\lambda_0 \sum_n \sum_k \sum_h B_{rn} B_{\theta k} \lambda_{ah} \int_0^{2\pi} \frac{1}{2} \left\{ \sin[(kp+np)\theta - (kp+np)\alpha)] + \right.$$

$$\sin[(kp-np)\theta-(kp-np)\alpha)]\}\cos(hQ_s\theta)d\theta =$$
$$\lambda_0\sum_n\sum_k\sum_h B_{rn}B_{\theta k}\lambda_{ah}\int_0^{2\pi}\frac{1}{4}\{\sin[(kp+np+hQ_s)\theta-(kp+np)\alpha)]+$$
$$\sin[(kp+np-hQ_s)\theta-(kp+np)\alpha)]+\sin[(kp-np+hQ_s)\theta-(kp-np)\alpha)]+$$
$$\sin[(kp-np-hQ_s)\theta-(kp-np)\alpha)]\} \tag{2.133}$$

It is easy to show from (2.133) that when

$$kp+np-hQ_s=0$$

the value of I will be

$$I=-\sum_n\sum_k\sum_h\lambda_0\frac{\pi}{2}B_{rn}B_{\theta k}\lambda_{ah}\sin[p(n+k)\alpha] \tag{2.134}$$

Similarly, when

$$kp-np+hQ_s=0 \text{ or } kp-np-hQ_s=0$$

the value of I will be

$$I=\sum_n\sum_k\sum_h\lambda_0\frac{\pi}{2}B_{rn}B_{\theta k}\lambda_{ah}\sin[p(n-k)\alpha] \tag{2.135}$$

For all other combinations of k, n and h, I is equal to zero.

The same principle can be used for all other terms in (2.131). Hence the final expression for the cogging torque as a function of the rotor position can be given in the following form:

$kp+np-mQ_s=0$

$$\begin{aligned}T_c(\alpha) &= \frac{1}{\mu_0}l_aR^2\sum_n\sum_k\sum_m\lambda_0\frac{\pi}{2}(-2B_{rn}B_{\theta k}\lambda_{am}-B_{\theta n}B_{\theta k}\lambda_{bm}-\\ &\quad B_{rn}B_{rk}\lambda_{bm})\sin[p(n+k)\alpha]\end{aligned}$$

$kp-np+mQ_s=0$

$$\begin{aligned}T_c(\alpha) &= \frac{1}{\mu_0}l_aR^2\sum_n\sum_k\sum_m\lambda_0\frac{\pi}{2}(2B_{rn}B_{\theta k}\lambda_{am}+B_{\theta n}B_{\theta k}\lambda_{bm}-\\ &\quad B_{rn}B_{rk}\lambda_{bm})\sin[p(n-k)\alpha]\end{aligned}$$

$kp - np - mQ_s = 0$

$$T_c(\alpha) = \frac{1}{\mu_0} l_a R^2 \sum_n \sum_k \sum_m \lambda_0 \frac{\pi}{2}(2B_{rn}B_{\theta k}\lambda_{am} - B_{\theta n}B_{\theta k}\lambda_{bm} + B_{rn}B_{rk}\lambda_{bm}) \sin[p(n-k)\alpha]$$

$kp + np + mQ_s - hQ_s = 0$

$$T_c(\alpha) = \frac{1}{\mu_0} l_a R^2 \sum_n \sum_k \sum_m \sum_h \frac{\pi}{4}(-B_{rn}B_{rk}\lambda_{am}\lambda_{bh} - B_{rn}B_{\theta k}\lambda_{am}\lambda_{ah} + B_{\theta n}B_{\theta k}\lambda_{bm}\lambda_{ah} + B_{\theta n}B_{rk}\lambda_{bm}\lambda_{bh}) \sin[p(n+k)\alpha]$$

$kp + np - mQ_s + hQ_s = 0$

$$T_c(\alpha) = \frac{1}{\mu_0} l_a R^2 \sum_n \sum_k \sum_m \sum_h \frac{\pi}{4}(B_{rn}B_{rk}\lambda_{am}\lambda_{bh} - B_{rn}B_{\theta k}\lambda_{am}\lambda_{ah} - B_{\theta n}B_{\theta k}\lambda_{bm}\lambda_{ah} + B_{\theta n}B_{rk}\lambda_{bm}\lambda_{bh}) \sin[p(n+k)\alpha]$$

$kp + np - mQ_s - hQ_s = 0$

$$T_c(\alpha) = \frac{1}{\mu_0} l_a R^2 \sum_n \sum_k \sum_m \sum_h \frac{\pi}{4}(-B_{rn}B_{rk}\lambda_{am}\lambda_{bh} - B_{rn}B_{\theta k}\lambda_{am}\lambda_{ah} - B_{\theta n}B_{\theta k}\lambda_{bm}\lambda_{ah} - B_{\theta n}B_{rk}\lambda_{bm}\lambda_{bh}) \sin[p(n+k)\alpha]$$

$kp - np + mQ_s + hQ_s = 0$

$$T_c(\alpha) = \frac{1}{\mu_0} l_a R^2 \sum_n \sum_k \sum_m \sum_h \frac{\pi}{4}(-B_{rn}B_{rk}\lambda_{am}\lambda_{bh} + B_{rn}B_{\theta k}\lambda_{am}\lambda_{ah} + B_{\theta n}B_{\theta k}\lambda_{bm}\lambda_{ah} - B_{\theta n}B_{rk}\lambda_{bm}\lambda_{bh}) \sin[p(n-k)\alpha]$$

$kp - np + mQ_s - hQ_s = 0$

$$T_c(\alpha) = \frac{1}{\mu_0} l_a R^2 \sum_n \sum_k \sum_m \sum_h \frac{\pi}{4}(B_{rn}B_{rk}\lambda_{am}\lambda_{bh} + B_{rn}B_{\theta k}\lambda_{am}\lambda_{ah} + B_{\theta n}B_{\theta k}\lambda_{bm}\lambda_{ah} + B_{\theta n}B_{rk}\lambda_{bm}\lambda_{bh}) \sin[p(n-k)\alpha]$$

$kp - np - mQ_s + hQ_s = 0$

$$T_c(\alpha) = \frac{1}{\mu_0} l_a R^2 \sum_n \sum_k \sum_m \sum_h \frac{\pi}{4}(-B_{rn}B_{rk}\lambda_{am}\lambda_{bh} + B_{rn}B_{\theta k}\lambda_{am}\lambda_{ah} - B_{\theta n}B_{\theta k}\lambda_{bm}\lambda_{ah} + B_{\theta n}B_{rk}\lambda_{bm}\lambda_{bh}) \sin[p(n-k)\alpha]$$

$kp - np - mQ_s - hQ_s = 0$

$$\begin{aligned} T_c(\alpha) &= \frac{1}{\mu_0} l_a R^2 \sum_n \sum_k \sum_m \sum_h \frac{\pi}{4} (B_{rn} B_{rk} \lambda_{am} \lambda_{bh} + B_{rn} B_{\theta k} \lambda_{am} \lambda_{ah} - \\ & \quad B_{\theta n} B_{\theta k} \lambda_{bm} \lambda_{ah} - B_{\theta n} B_{rk} \lambda_{bm} \lambda_{bh}) \sin[p(n-k)\alpha] \end{aligned} \quad (2.136)$$

The cogging torque for the six pole surface PM motor has been calculated using (2.136) and compared with the finite element solution in Figs. 2.42 and 2.43. The FE model has been created using **Magsoft**, **Flux 2D** commercial software and the cogging torque has been calculated using the virtual work method. The time stepping transient method with moving air gap and constant angular velocity of 1/6 rpm has been used. The mesh size in the moving air gap is adjusted to ensure that for each consecutive rotor position the nodes on the boundary between the moving air gap and the rest of the air gap coincide to reduce numerical errors in the cogging torque calculation. This is shown in Fig. 2.44. The cogging torque has been evaluated at 60 consecutive rotor positions. Two cogging torque waveforms have been calculated numerically, one for the case of infinitely permeable iron and the other for the case when saturation is taken into account. For calculation purposes, the infinite relative permeability of iron has been replaced with 10^9.

There is a significant discrepancy between the analytically and numerically calculated cogging torque waveforms. One possible explanation is that this difference can be attributed to the approximation made earlier in which it was assumed that the transformed contour in the K plane is identical to the circular arc in the S plane from which it originated. When the analytical and numerical field solutions are compared, this approximation does not seem to have a significant effect, but it appears that its effect on the computed cogging torque waveform could be severe. This could be explained by the fact that the waveform of the product $B_r(r,\theta)B_\theta(r,\theta)$ is a sequence of narrow pulses as shown in Fig. 2.45. The cogging torque for the given rotor position is directly proportional to the integral of this waveform. The integral is equal to the difference between the positive and negative areas of the narrow pulses which consequently can be very sensitive to numerical errors. However, the advantage of the proposed method is the ability to calculate the cogging torque much faster on the digital computer than with the finite element method. This is important if cogging torque needs to be calculated repeatedly during an iterative motor design procedure. It

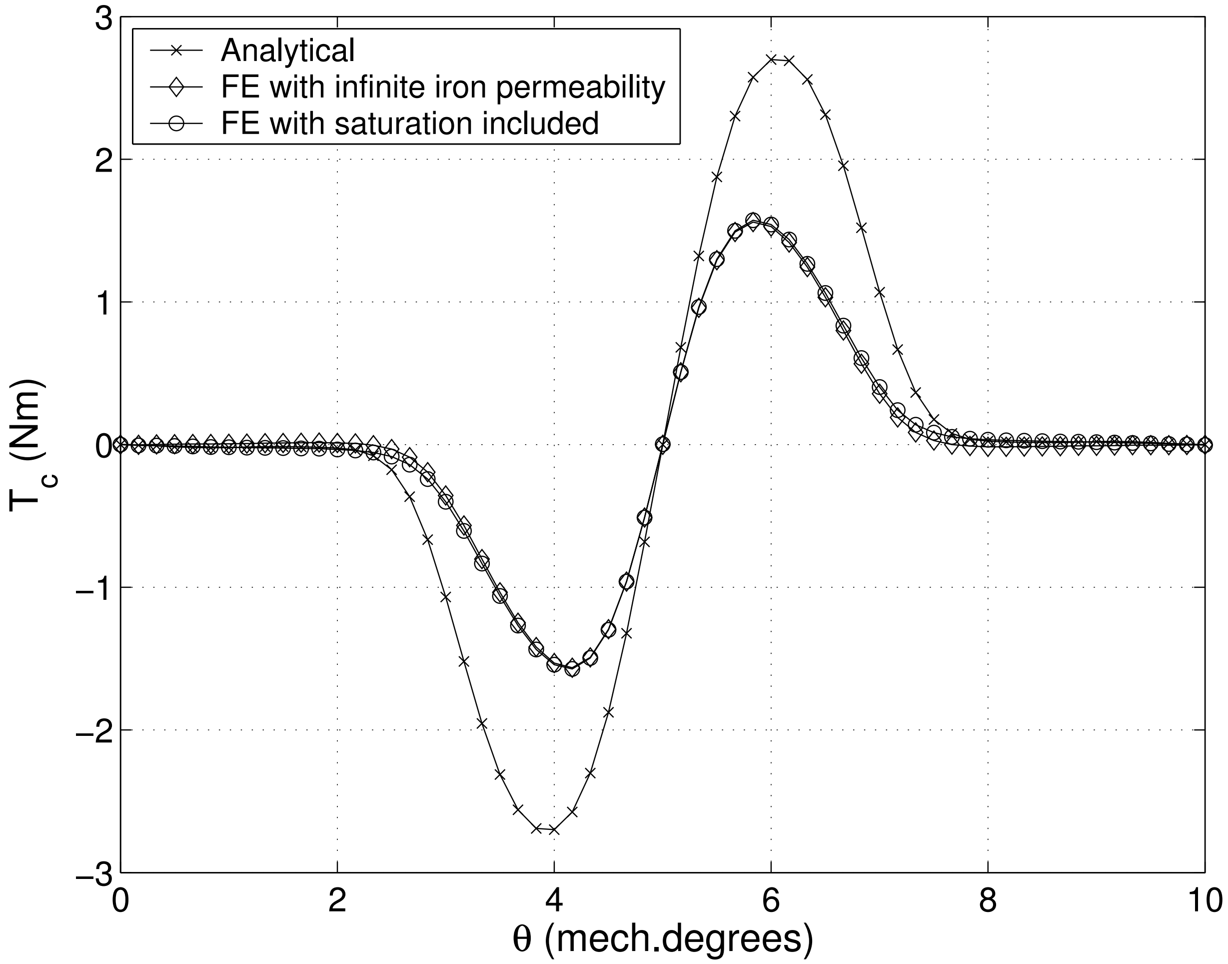

Fig. 2.42 Comparison of the cogging torque waveforms, for the six pole surface PM motor with radial magnetization, calculated analytically using Maxwell's stress theory and calculated numerically using FE method with and without saturation

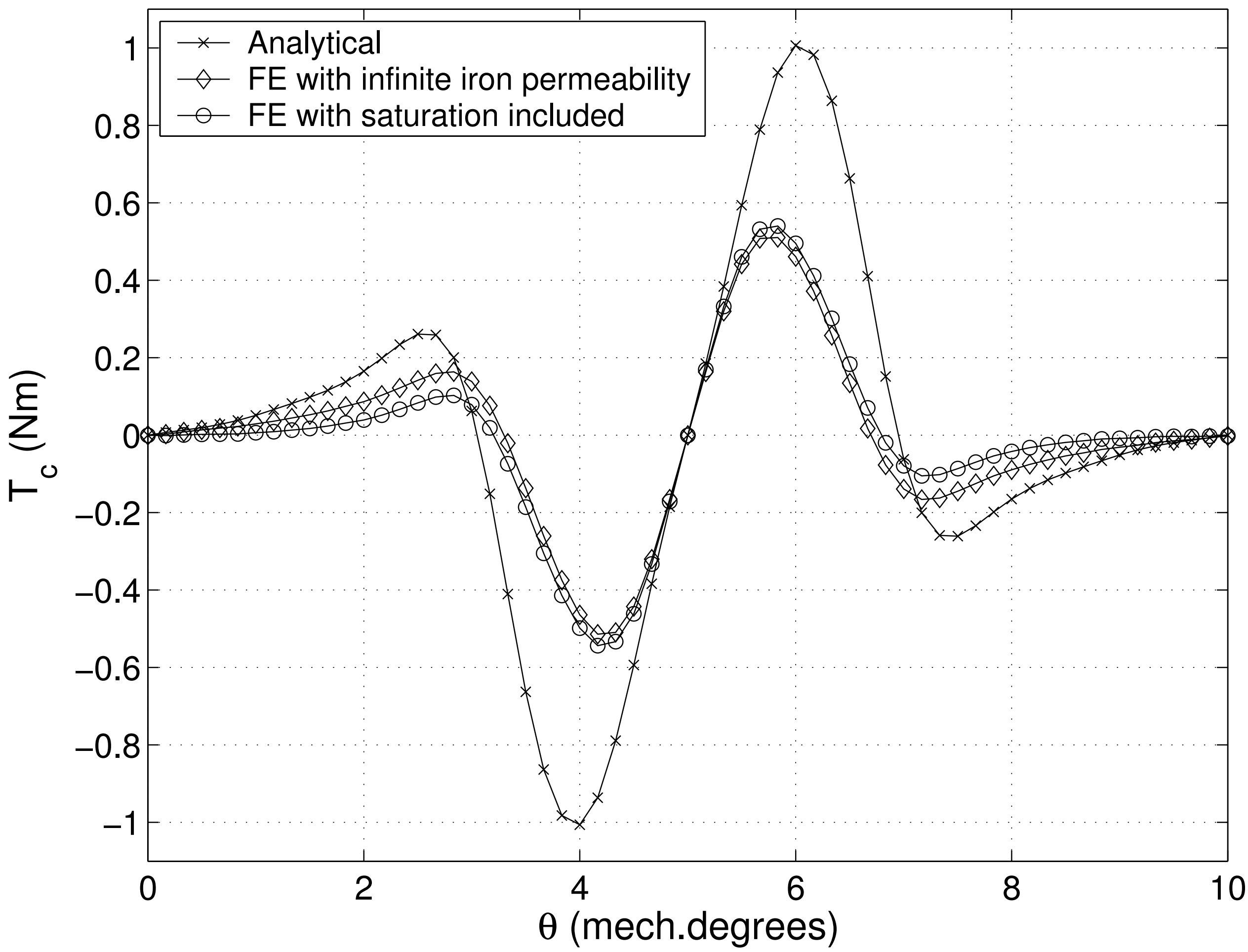

Fig. 2.43 Comparison of the cogging torque waveforms, for the six pole surface PM motor with parallel magnetization, calculated analytically using Maxwell's stress theory and calculated numerically using FE method with and without saturation

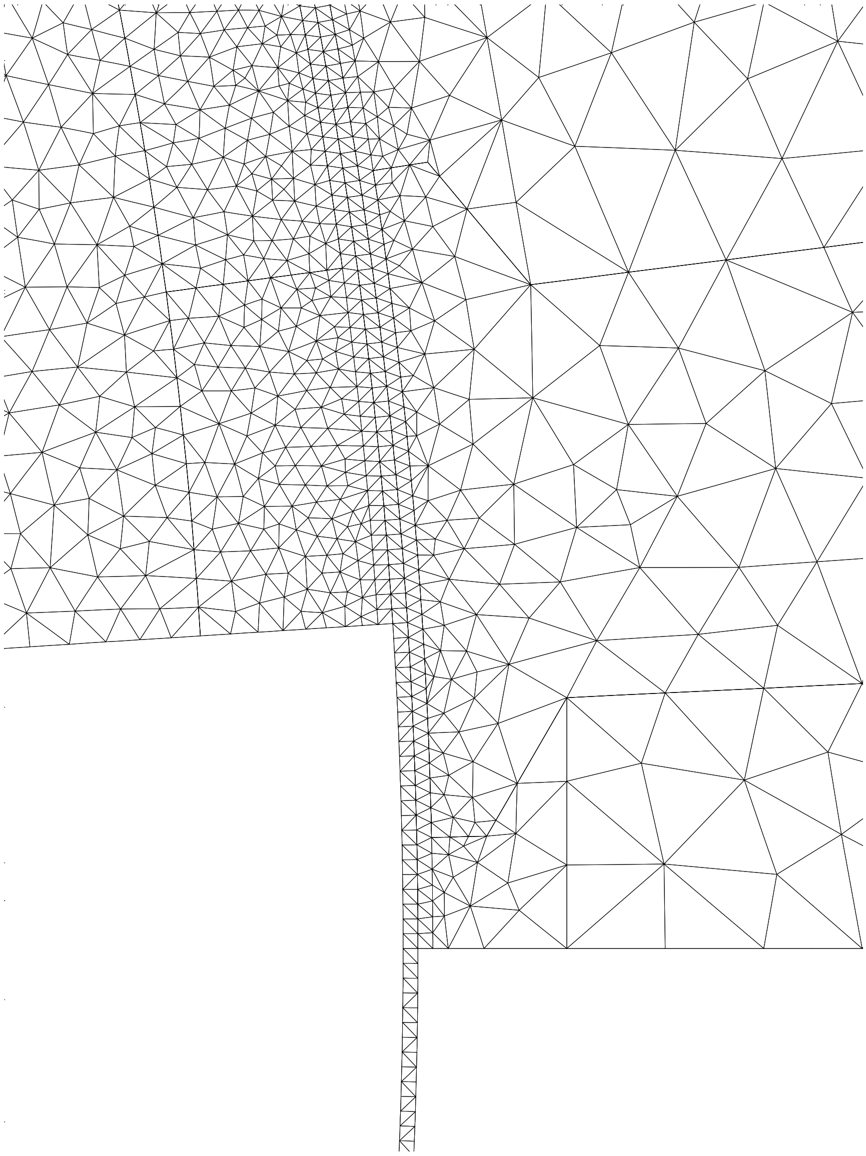

Fig. 2.44 Detail of the finite element mesh to show the position of the nodes on the boundary between the moving air gap and the rest of the air gap

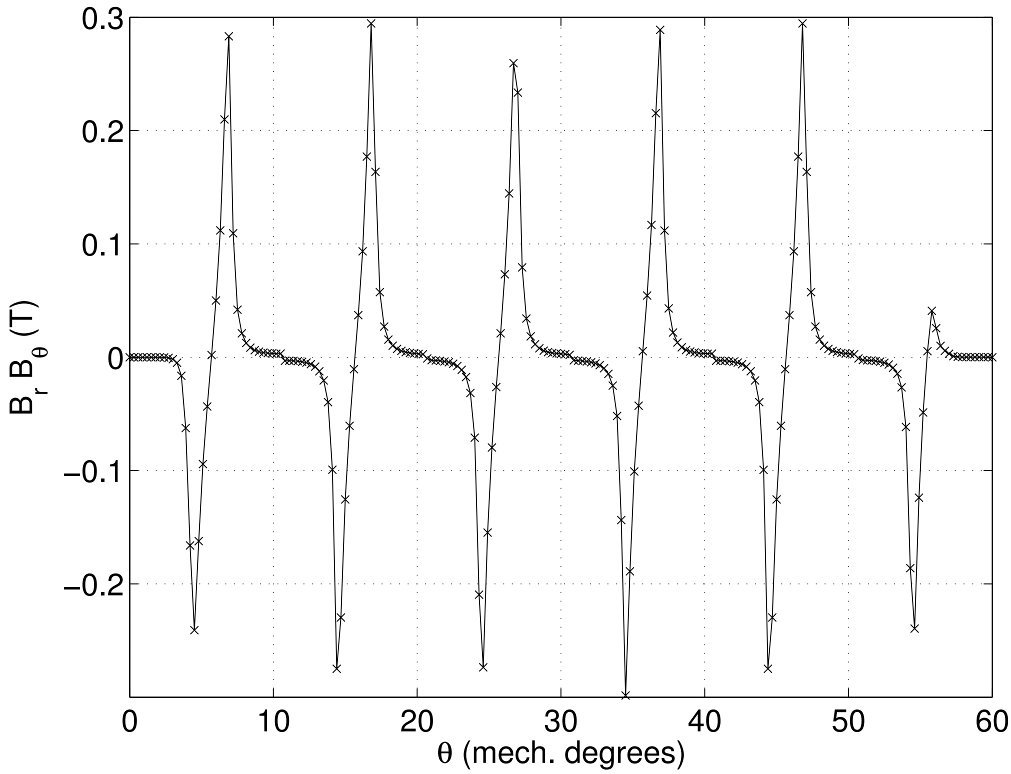

Fig. 2.45 The waveform of $B_r B_\theta$ for the rotor position at which the maximum cogging torque occurs

is also important to notice that the shape of the cogging torque waveform follows the finite element solution for both types of magnetization. This means that analytical and numerical solutions have a similar relative harmonic content. Therefore, it should be possible to correctly predict, using the described analytical approach, the effects that cogging torque reduction techniques have on the harmonic content and on the magnitude of the cogging torque waveform. These results can then be used in the optimized motor design.

An alternative analytical approach to cogging torque calculation also based on conformal mapping of the slot opening and Maxwell's stress theory is shown in the next section. This approach gives a deeper insight into reasons for the discrepancy between analytical and numerical results displayed in Figs. 2.42 and 2.43.

2.7 Cogging Torque Calculation Based on Summation of the Lateral Forces Along the Slot Sides

An alternative approach to cogging torque calculation which is also based on Maxwell's stress theory (see Section 2.6) is to integrate the magnetic stress vector along the slot sides. The expression for the lateral force per one slot can be derived from Fig. 2.41 and (2.120). According to Fig. 2.41 the angle between vectors $\vec{B}$ and $\vec{n}$ is θ. Hence the dot product $\vec{B} \cdot \vec{n} = |\vec{B}| \cos\theta$ and the normal component of $\vec{t}_m$ is

$$\begin{aligned} t_m^n &= \vec{n} \cdot \vec{t}_m = \vec{n} \cdot \left[\left(\vec{n} \cdot \frac{\vec{B}}{\mu_0} \right) \vec{B} - \vec{n} \frac{1}{2} \frac{|\vec{B}|^2}{\mu_0} \right] \\ &= \frac{1}{\mu_0} \left[\left(\vec{n} \cdot \vec{B} \right)^2 - \frac{1}{2} |\vec{B}|^2 \right] = \frac{1}{\mu_0} \left(|\vec{B}|^2 \cos^2\theta - \frac{1}{2} |\vec{B}|^2 \right) \\ &= \frac{1}{\mu_0} \left[|\vec{B}|^2 \left(\frac{1}{2} + \cos 2\theta \right) - \frac{1}{2} |\vec{B}|^2 \right] = \frac{|\vec{B}|^2}{2\mu_0} \cos 2\theta = |\vec{t}_m| \cos 2\theta \end{aligned} \tag{2.137}$$

In the case of an infinitely permeable body the flux density vector $\vec{B}$ will be perpendicular to the body surface so the angle θ will be zero. Hence the force will also be perpendicular to the body surface. In the case of a simple slot opening the flux density vector and the lateral forces acting on the slot sides will be perpendicular to the slot side surfaces as shown in Fig. 2.46. Since the slot sides extend radially, the forces perpendicular to them will be acting in the tangential direction, thus producing cogging torque.

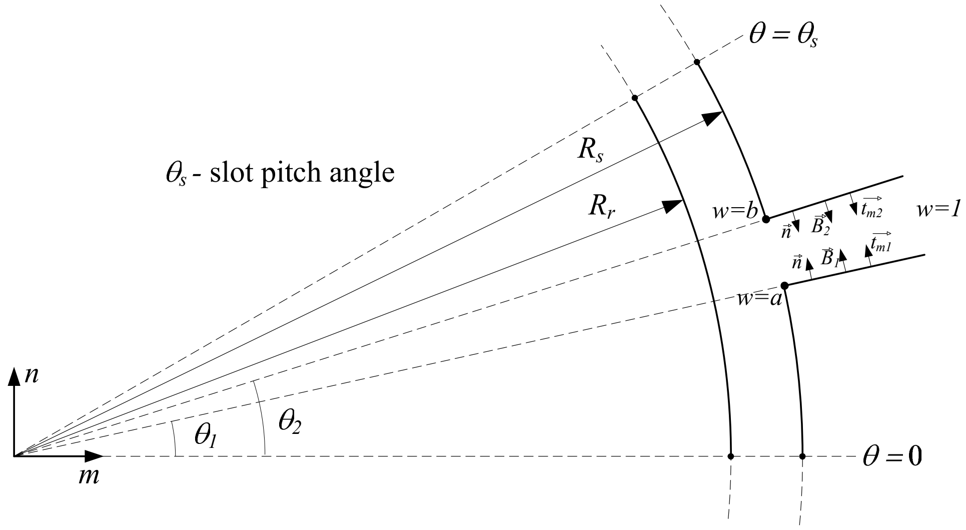

Fig. 2.46 Magnetic stress vectors acting on the slot sides

The net magnetic stress per one slot can then be calculated according to

$$|\vec{t}_{slot}| = |\vec{t}_{m1}| - |\vec{t}_{m2}| = \frac{1}{2\mu_0}\left(\left|\vec{B}_1\right|^2 - \left|\vec{B}_2\right|^2\right) \tag{2.138}$$

The total lateral force per slot is equal to the surface integral of the magnetic stress. The integration can be performed in the S plane in the radial direction along the slot side from the stator surface $(r = R_s)$ to the depth at which the flux density becomes negligible. However, the more efficient approach would be to perform the integration in the W plane by changing the variable of integration. Since conformal mapping transforms field values in the direct geometric transformation ratio in every point, the integration of the force density, i.e. the magnetic stress, over corresponding slot surfaces in the two planes gives the same result.

The total lateral force per slot is equal to the surface integral of the magnetic stress on both slot sides. According to Fig. 2.46, the forces on the opposite slot sides are acting in the opposite directions. The total force per slot expressed in the S plane is then

$$F_{slot} = \frac{l_a}{2\mu_0}\lim_{r\to\infty}\left[\int_{R_s e^{j\theta_1}}^{re^{j\theta_1}} |B_s|^2 \mathrm{d}s - \int_{R_s e^{j\theta_2}}^{re^{j\theta_2}} |B_s|^2 \mathrm{d}s\right] \tag{2.139}$$

Taking into consideration the fact that

$$|B_s| = |B_k| \left|\frac{\partial k}{\partial s}\right| \tag{2.140}$$

and

$$\mathrm{d}s = \left|\frac{\partial s}{\partial w}\right| \mathrm{d}w \tag{2.141}$$

the force per slot is equal to

$$\begin{aligned} F_{slot} &= \frac{l_a}{2\mu_0}\left[\int_a^1 |B_k|^2 \left|\frac{\partial k}{\partial s}\right|^2 \left|\frac{\partial s}{\partial w}\right| \mathrm{d}w - \int_b^1 |B_k|^2 \left|\frac{\partial k}{\partial s}\right|^2 \left|\frac{\partial s}{\partial w}\right| \mathrm{d}w\right] \\ &= \frac{l_a}{2\mu_0}\int_a^b |B_k|^2 \left|\frac{\partial k}{\partial s}\right|^2 \left|\frac{\partial s}{\partial w}\right| \mathrm{d}w \end{aligned} \tag{2.142}$$

Since $\left|\frac{\partial s}{\partial w}\right| = \left|\frac{\partial s}{\partial k}\right| \left|\frac{\partial k}{\partial w}\right|$, equation (2.142) can be written in the form

$$F_{slot} = \frac{l_a}{2\mu_0}\int_a^b |B_k|^2 \left|\frac{\partial k}{\partial s}\right| \left|\frac{\partial k}{\partial w}\right| \mathrm{d}w \tag{2.143}$$

The total torque per slot is equal to the integral of the product of force and radius at which the force acts. The radius is equal to $|s|$ and hence the torque per slot is

$$T_{slot} = \frac{l_a}{2\mu_0}\int_a^b |B_k|^2 \left|\frac{\partial k}{\partial s}\right| \left|\frac{\partial k}{\partial w}\right| |s|\mathrm{d}w \tag{2.144}$$

where the partial derivatives are given by

$$\left|\frac{\partial k}{\partial s}\right| = \left|\frac{\partial k}{\partial t}\frac{\partial t}{\partial w}\frac{\partial w}{\partial z}\frac{\partial z}{\partial s}\right| = \left|k\frac{w-1}{(w-a)^{\frac{1}{2}}(w-b)^{\frac{1}{2}}}\frac{1}{s}\right| \tag{2.145}$$

$$\left|\frac{\partial k}{\partial w}\right| = \left|\frac{\partial k}{\partial t}\frac{\partial t}{\partial w}\right| = \left|\frac{g\prime}{\pi}\frac{k}{w}\right| \tag{2.146}$$

The torque per slot is then

$$T_{slot} = \frac{l_a}{2\mu_0}\int_a^b |B_k|^2 \left|\frac{g\prime}{\pi}k^2\frac{w-1}{w(w-a)^{\frac{1}{2}}(w-b)^{\frac{1}{2}}}\right| \mathrm{d}w \tag{2.147}$$

The value of k in (2.147) is calculated from

$$k = e^t = e^{j\frac{g\prime}{\pi}\ln w + \ln R_s + j\frac{\theta_s}{2}} = R_s e^{j\left(\frac{g\prime}{\pi}\ln w + \frac{\theta_s}{2}\right)} \tag{2.148}$$

while $B_k = B_r + jB_\theta$ is calculated from (2.41) for internal rotor motors with $r = R_s$ and $\theta = \frac{g'}{\pi}\ln w + \frac{\theta_s}{2}$. The tangential component B_θ is equal to zero since the flux density is evaluated at $r = R_s$ which is the boundary between air and infinitely permeable iron core where only radial component of the flux density exists.

The total cogging torque is then equal to

$$T_c = \sum_{k=1}^{Q_s} T_{slot} \tag{2.149}$$

where Q_s is the number of stator slots. For practical implementation on the digital computer the integration of (2.147) needs to be performed from $a+\varepsilon$ to $b-\varepsilon$ where ε is a small number relative to a and b. This approximation is necessary because the denominator of the expression for the partial derivative $\left|\frac{\partial k}{\partial s}\right|$ is equal to zero at the tooth tips where $w = a$ and $w = b$. This causes numerical problems due to division by zero. Hence the tooth tips are singular points where flux density has an infinite value. This is a consequence of the assumption that the iron core is infinitely permeable. The flux density drops exponentially as one moves away from the tooth tips $(w = a, w = b)$ to the bottom of the slot $(w = 1)$ along the slot sides. Therefore, a very small displacement from the singular points will result in a large change of the flux density which causes ε to have a significant impact on the calculated maximum value of the cogging torque.

In the actual motor the iron core is not infinitely permeable, so the tooth tips will saturate, resulting in finite values of the flux density at those points. Although the analytical approach based on conformal mapping predicts an infinite value of the flux density at the tooth tips, the finite element method will not give the same result even with the assumption of infinitely permeable iron core. The main reason for that are numerical errors due to finite discretization of the computational domain. A comparison is made between the flux density distributions along the slot side calculated analytically and numerically for the slot located at the centerline of the magnet with radial magnetization. In order to make the valid comparison, the actual slot shape in the FE model has been replaced by a simple slot opening, while the relative permeability of iron has been set to 10^{12}. The model for one pole pitch is shown in Fig. 2.47. The flux density distributions are compared in Fig. 2.48 from the the tooth tip down to the depth equal to twice the size of the slot opening b_o.

There is a good agreement between the results except in the vicinity of the tooth tip at $r = R_s$. The finite element method gives the value of the flux density at that point equal to 2.05 T. The flux density calculated analytically is several hundred times larger. However, it drops rapidly for a very small displacement from the tooth tip.

The cogging torque waveforms calculated analytically and numerically for different values of ϵ are shown in Fig. 2.49a while Table 2.3 shows the values of the flux density at the tooth tips. Note that if integration of the force density starts very close to the tooth tip ($\epsilon \ll$), the resulting flux density becomes very high and the calculated cogging torque has a peak value higher than calculated by the FE method. However, if ϵ is chosen so that the flux density in the vicinity of the tooth tip is close to the value calculated by the FE method, then the peak value of the cogging torque calculated analytically is also close to the peak cogging torque calculated numerically. Similar analysis can be done for the case of parallel magnetization for which the cogging torque waveforms are compared in Fig. 2.49b.

If the number of triangles in the finite element mesh in the vicinity of the tooth tips increases while reducing their size, then the value of the flux density exactly at the tooth tip also increases. With an infinitely small triangle at the tooth tip, the FE result would come close to the result from conformal mapping. The conclusion is that singularity at the tooth tip affects the analytical cogging torque calculation and results in higher peak values than obtained by FE simulations. Although FE simulation is also in error when it is assumed that permeability is infinite (i.e. 10^{12}), the resulting peak value of the cogging torque from FE simulations is closer to reality, because core laminations have a finite permeability and tooth tips saturate very quickly, thus resulting in lower values of the flux density at those points than predicted by conformal mapping.

Table 2.3 Flux density at the tooth tip of the six pole surface PM motor with radial magnetization for different values of the displacement ϵ

	Analytical		*Finite*
	$\epsilon/a = 10^{-9}$	$\epsilon/a = 0.03$	*Element*
Flux density	$1.32 \cdot 10^4$ T	2.37 T	2.05 T

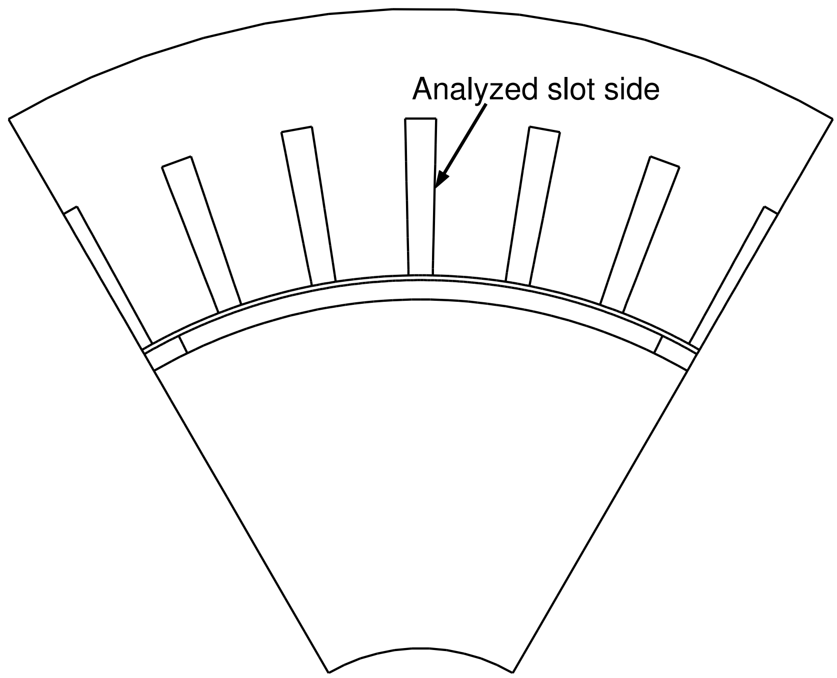

Fig. 2.47 FE model of the six pole surface PM motor used for calculation of the flux density distribution along the slot side

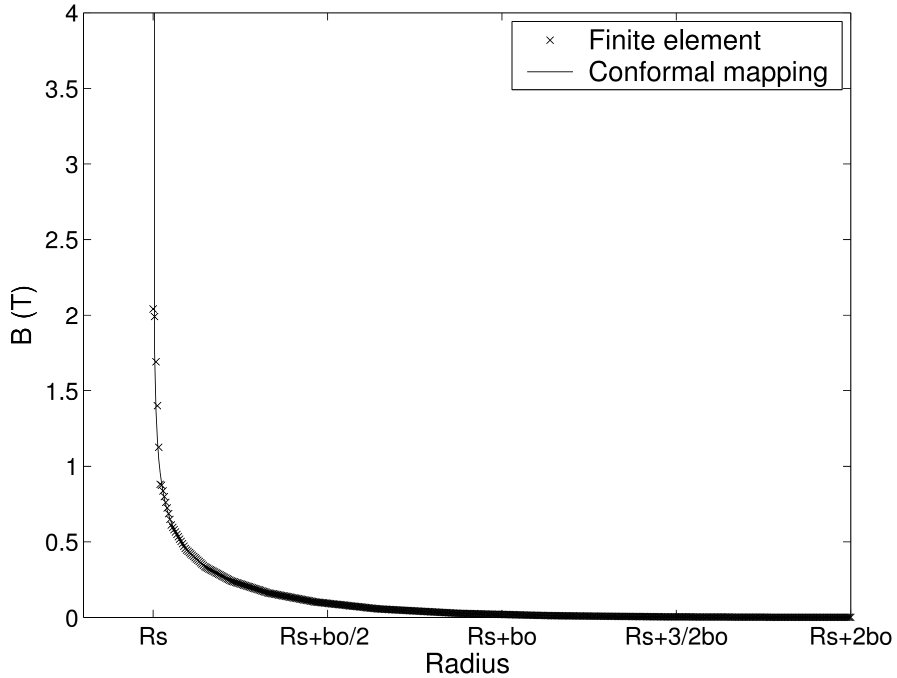

Fig. 2.48 Comparison of the flux density distribution along the slot side calculated analytically and numerically

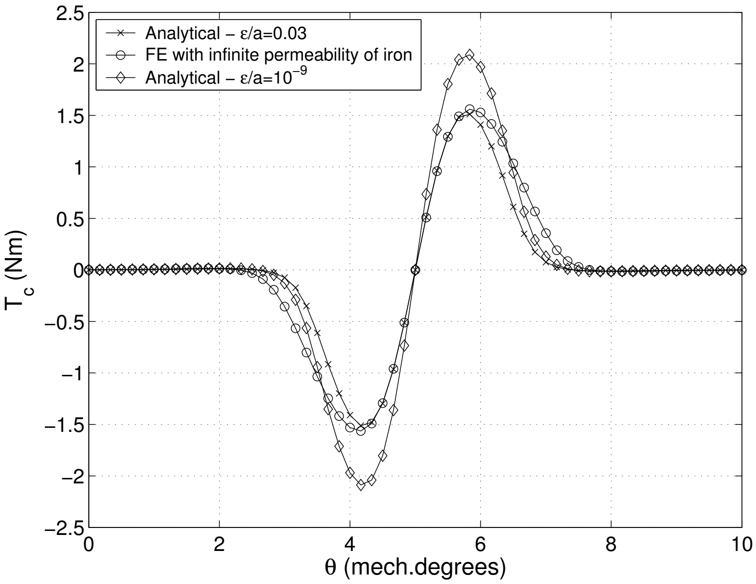

(a)

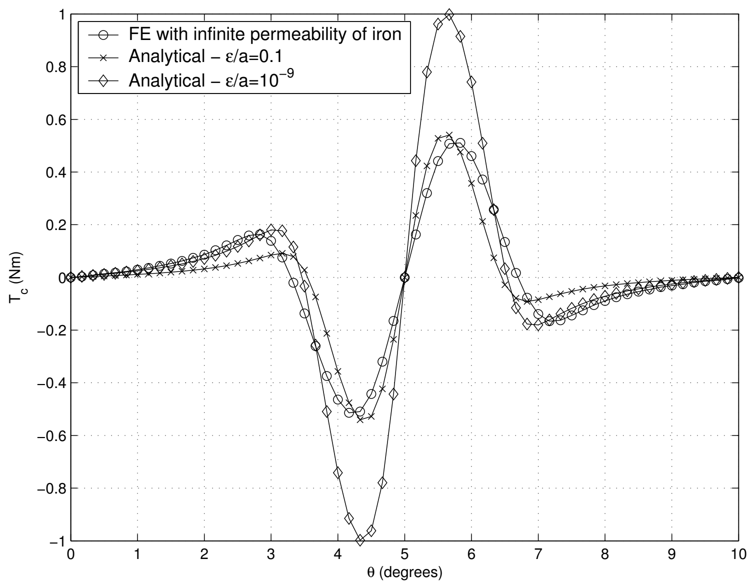

(b)

Fig. 2.49 Comparison of the cogging torque waveforms for the six pole surface PM motor calculated numerically by FE method and analytically by integrating the magnetic stress vector along the slot sides: (a) radial magnetization, (b) parallel magnetization

Chapter 3

Calculation of Electromagnetic Torque in Surface PM Motors

The electromagnetic force exerted on a non-magnetic conducting region can be calculated using the Lorenz expression

$$\vec{F} = \iiint_V \vec{J} \times \vec{B} \mathrm{d}V \tag{3.1}$$

where V is the volume of the current carrying region, $\vec{J}$ is the current density and $\vec{B}$ is the flux density in the region. The electromagnetic torque resulting from the Lorenz force is then

$$\vec{T} = \iiint_V \vec{r} \times (\vec{J} \times \vec{B}) \mathrm{d}V \tag{3.2}$$

where $\vec{r}$ is the position vector of the infinitesimal volume $\mathrm{d}V$ in the conducting region. The Lorenz force expression is very suitable and accurate in finite element simulations, but it is not very convenient for analytical calculations. The main problem is the difficulty to determine precisely the flux density distribution in the conducting region which is a function of the currents in all other conducting regions and the additional field sources like permanent magnets.

Another approach [21, 45, 67–69] is to calculate the back emf waveform from the field distribution in no-load operation and then determine the electromagnetic torque from the equation

$$T_{em} = \frac{1}{\omega_{rm}} \left(e_a i_a + e_b i_b + e_c i_c \right) \tag{3.3}$$

where e_a, e_b, e_c are the back emf waveforms and i_a, i_b and i_c are the current waveforms of the phases a, b and c, while ω_{rm} is the rotor mechanical speed.

The third approach used in this thesis is to calculate the total field in the air gap and then integrate the Maxwell's stress tensor to calculate the tangential force exerted on the rotor. If saturation is neglected, the field in the air gap can be calculated by adding the field solutions due to currents flowing in each individual conducting region, while assuming that the currents in other regions are equal to zero. If permanent magnets are present, their contribution to the overall field is calculated with the currents in all conducting regions equal to zero.

The permanent magnet field in the air gap of a surface PM motor has been calculated analytically in Chapter 2. The field solution due to currents flowing in the armature winding needs to be found next.

One approach to calculation of the armature winding field found in literature [45, 46, 70, 71] is to solve the Laplacian equation in the air gap for a distributed current sheet on the stator surface. The current sheet is distributed so that the current density is uniform along an arc whose length is equal to the size of the slot opening b_o. This field solution is then multiplied by the relative air gap permeance to take into account the presence of slots.

The alternative approach used in this thesis is based on finding the field solution of current in a slot by means of conformal transformation [72]. The field solutions for all the slots are then added to obtain the total armature winding field.

3.1 The Field of a Current in a Slot by Conformal Transformation

The fundamental approach to conformal transformation of a slot opening with the presence of current in the slot is similar to the approach used earlier in Section 2.2 . The first transformation which maps the slot opening in its circular arrangement in the S plane into a linear model in the Z plane is the same as used before, i.e.

$$z = \log(s) \tag{3.4}$$

The next transformation from the Z plane into the upper half of the W plane is somewhat different because the presence of current in a slot needs to be taken into account. The slot can be treated as infinitely deep, as shown earlier, to simplify the transformation. For a slot current IN_c, where N_c is the number of turns in a coil, the potentials of the adjacent teeth are $I\frac{N_c}{2}$ and $-I\frac{N_c}{2}$ with respect to the rotor surface at zero potential [72]. The potential on the line of symmetry down the slot center is also zero. Thus, one half of the slot can be represented in the Z plane, as shown in Fig. 3.1.

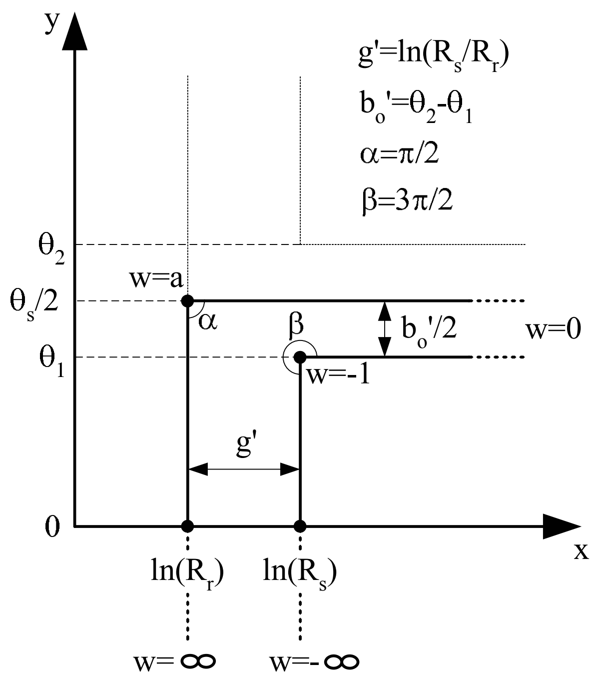

Fig. 3.1 Representation of one half of the slot opening in the Z plane

The mapping from the Z plane to the W plane by means of the Schwarz-Christoffel transformation is given by

$$\begin{aligned}\frac{\mathrm{d}z}{\mathrm{d}w} &= A(w+1)^{\frac{3\pi}{2}\frac{1}{\pi}-1}(w-0)^{\frac{0}{\pi}-1}(w-a)^{\frac{\pi}{2}\frac{1}{\pi}-1} \\ &= A\frac{(w+1)^{\frac{1}{2}}}{w(w-a)^{\frac{1}{2}}}\end{aligned} \tag{3.5}$$

Making the substitution

$$p^2 = \frac{w-a}{w+1}$$

equation (3.5) can be simply integrated to yield

$$z = 2A\left[\frac{1}{\sqrt{a}}\arctan\frac{p}{\sqrt{a}} + \frac{1}{2}\ln\left(\frac{1+p}{1-p}\right)\right] + C_1 \tag{3.6}$$

The constant A can be determined by integration along a large semicircle of an arbitrary large radius R. For values of R approaching infinity

$$\int \mathrm{d}z = \int_0^{\pi} \frac{A\left(Re^{j\theta}+1\right)^{\frac{1}{2}}}{Re^{j\theta}\left(Re^{j\theta}-a\right)} jRe^{j\theta}\mathrm{d}\theta \overset{R\to\infty}{=} \int_0^{\pi} \frac{A\left(Re^{j\theta}\right)^{\frac{1}{2}}}{\left(Re^{j\theta}\right)\left(Re^{j\theta}\right)^{\frac{1}{2}}} jRe^{j\theta}\mathrm{d}\theta = \int_0^{\pi} jA\mathrm{d}\theta = j\pi A$$

In the Z plane $\int \mathrm{d}z = g'$, so

$$A = -j\frac{g'}{\pi} \tag{3.7}$$

The constant a can be determined by integration along a small semicircle centered at $w = 0$. For radius r approaching zero

$$\int \mathrm{d}z = \int_0^{\pi} \frac{A\left(re^{j\theta}+1\right)^{\frac{1}{2}}}{re^{j\theta}\left(re^{j\theta}-a\right)} jre^{j\theta}\mathrm{d}\theta \overset{r \to 0}{=} -\int_0^{\pi} j\frac{g\prime}{\pi}\frac{1^{\frac{1}{2}}}{(-a)^{\frac{1}{2}}} j\mathrm{d}\theta = -j\frac{g\prime}{\sqrt{a}}$$

Since $\int \mathrm{d}z = -j\frac{b'_o}{2}$, the constant a is

$$a = \left(\frac{2g\prime}{b'_o}\right)^2 \tag{3.8}$$

The constant of integration C_1 can be determined if $p = 0$ is substituted into (3.6). Then

$$z = -j\frac{2g\prime}{\pi}\left[\frac{1}{\sqrt{a}}\arctan\frac{0}{\sqrt{a}} + \frac{1}{2}\ln(1)\right] + C_1 = C_1$$

When p is zero $w = a$. Hence from Fig. 3.1

$$C_1 = \ln(R_r) + j\frac{\theta_s}{2} \tag{3.9}$$

The geometric structure in which the field solution can be easily found represents two parallel plates extending an infinite distance in both directions. The location and the distance between the plates can be set arbitrarily. If the lower plate is aligned with the real axis of the T plane and the distance to the upper plate is 1, as shown in Fig. 3.2, then transformation from the T plane to the W plane is given by

$$t = \frac{1}{\pi}\ln w \tag{3.10}$$

The potential of the lower plate is $\varphi = 0$ and of the upper plate $\varphi = -\frac{N_c}{2}I$. Since potential changes only in the direction of the imaginary axis, the field solution in the T plane is given by

$$B_t = -j\mu_0\frac{\partial\varphi}{\partial q} = j\mu_0\frac{N_c}{2}I \tag{3.11}$$

That field solution is mapped back to the S plane using

$$B_s = B_t\left(\frac{\partial t}{\partial s}\right)^* = B_t\left(\frac{\partial t}{\partial w}\frac{\partial w}{\partial z}\frac{\partial z}{\partial s}\right)^* \tag{3.12}$$

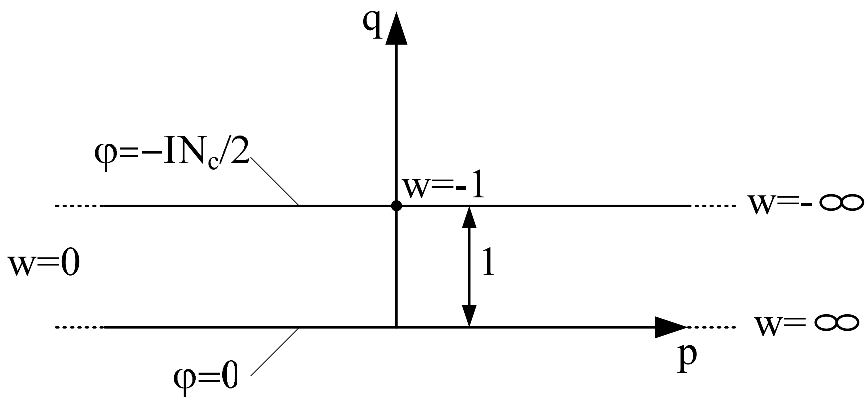

Fig. 3.2 Representation of one half of the slot opening in the T plane

With

$$\begin{aligned} \frac{\partial t}{\partial w} &= \frac{1}{\pi}\frac{1}{w} \\ \frac{\partial w}{\partial z} &= j\frac{\pi}{g'}\frac{w(w-a)^{\frac{1}{2}}}{(w+1)^{\frac{1}{2}}} \\ \frac{\partial z}{\partial s} &= \frac{1}{s} \end{aligned} \tag{3.13}$$

the flux density B_s is

$$B_s = B_t\left[\frac{1}{\pi}\frac{1}{w}j\frac{\pi}{g'}\frac{w(w-a)^{\frac{1}{2}}}{(w+1)^{\frac{1}{2}}}\frac{1}{s}\right]^* = -jB_t\frac{1}{g\prime}\left(\frac{1}{s}\sqrt{\frac{w-a}{w+1}}\right)^* \tag{3.14}$$

After substituting (3.11) into (3.14)

$$B_s = B_m + jB_n = \mu_0\frac{N_c}{2g\prime}I\left(\frac{1}{s}\sqrt{\frac{w-a}{w+1}}\right)^* \tag{3.15}$$

Since the field solution B_t in the T plain is given in Cartesian coordinates with components $B_p = 0$ and $B_q = \mu_0\frac{N_c}{2}I$, the resulting field solution B_s is also given in Cartesian coordinates with components B_m and B_n calculated according to (3.15). Since one deals with the air gap of an electrical motor, it is convenient to use the cylindrical coordinate system in the S plane with radial and tangential components of the flux density calculated according to

$$\begin{aligned} B_{ar} &= B_m\cos\theta + B_n\sin\theta \\ B_{a\theta} &= -B_m\sin\theta + B_n\cos\theta \end{aligned} \tag{3.16}$$

For the six pole surface PM motor with $N_c = 14$ and $I = 1$ A, the flux density in the middle of the air gap calculated according to (3.15) is shown in Fig. 3.3. Since coils in electrical machines occupy two slots with currents in the slots flowing in the opposite directions, the waveforms of the air gap flux density for one coil in Fig. 3.4 can be assembled from the waveforms in Fig. 3.3 if negative current $-I$ is assumed for the other coil side. To take into account the presence of all other slots, the waveforms in Fig. 3.4 need to be multiplied by the complex permeance from Fig. 2.13 for the angles θ outside the areas of the slots occupied by the coil because those slots have already been taken into account by (3.15). The result are the waveforms of the flux density for one coil in the slotted air gap shown in Fig. 3.5.

3.2 The Armature Winding Field

The waveforms of the air gap flux density due to the current in a single coil shown in Fig. 3.5 can be expressed in the form of Fourier series using discrete Fourier transformation. The expressions for B_{ar} and $B_{a\theta}$ are then

$$\begin{aligned} B_{ar} &= N_c \sum_{n=1}^{N_a} B_{arn} \cos n\theta \\ B_{a\theta} &= N_c \sum_{n=1}^{N_a} B_{a\theta n} \sin n\theta \end{aligned} \tag{3.17}$$

where N_a is the maximum number of Fourier coefficients, N_c is the number of turns per coil and B_{arn} and $B_{\theta n}$ are the Fourier coefficients of the radial and tangential components of the flux density with $N_c = 1$. One should bear in mind that the waveforms in Fig. 3.5 were obtained with 1 A of current. Therefore, for any other value of the coil current I the expressions (3.17) should be multiplied by I. The contributions of all other coils to the overall armature winding field solution are obtained by adding these waveforms with appropriate phase shifts while paying attention to the orientation of the current in the coils and to which phases the coils belong. The location and the orientation of each coil in a two-layer three phase winding can be determined systematically by using a winding table which can be formed in a unique manner for both integral slot and fractional slot windings [73]. Since an integral slot winding is just a special case of the fractional slot winding, the general approach to the winding table assembly will be explained on

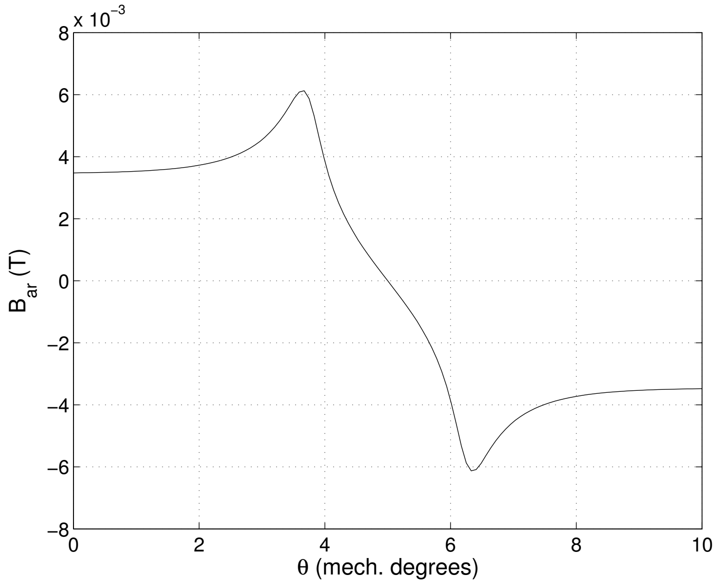

(a)

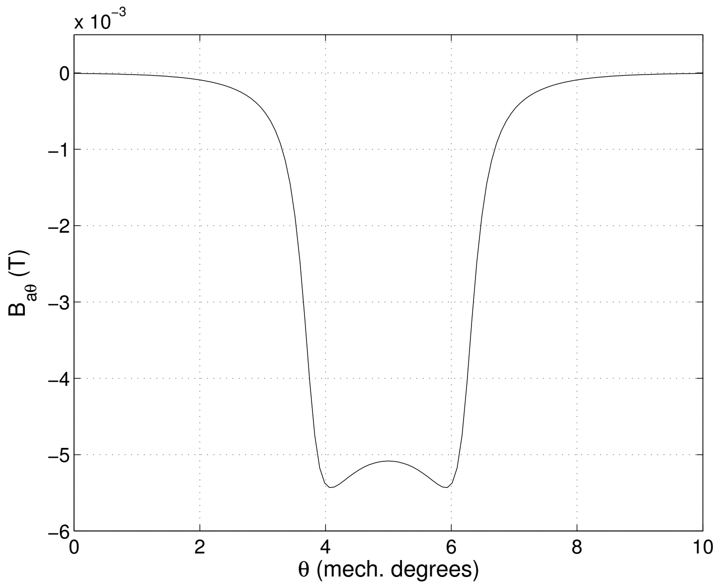

(b)

Fig. 3.3 The waveforms of the flux density in the middle of the air gap of a six pole surface PM motor for one slot pitch resulting from the conformal mapping of a single slot opening with $N_c = 14$ and 1 A of current per turn: (a) radial component, (b) tangential component

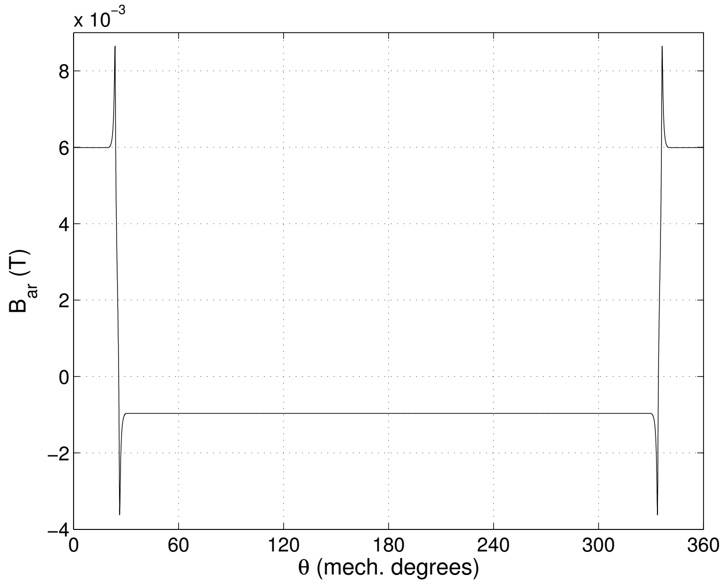

(a)

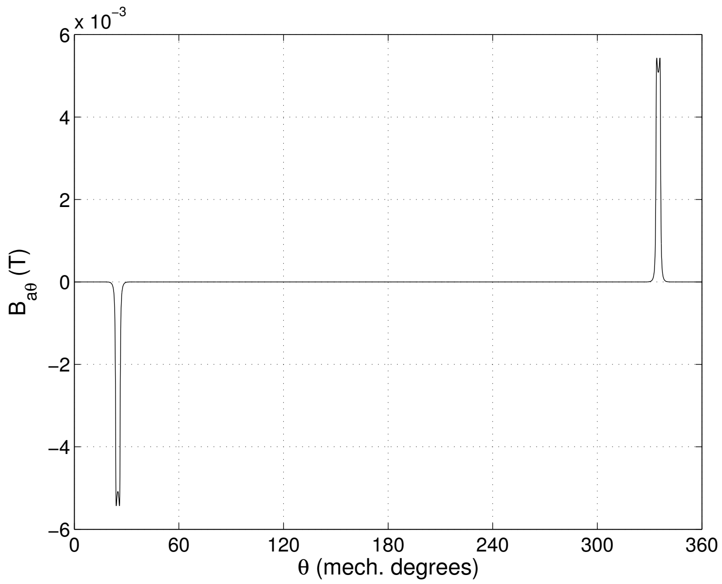

(b)

Fig. 3.4 The waveforms of the flux density in the middle of the air gap of a six pole surface PM motor for one coil with $N_c = 14$ and 1 A of current per turn: (a) radial component, (b) tangential component

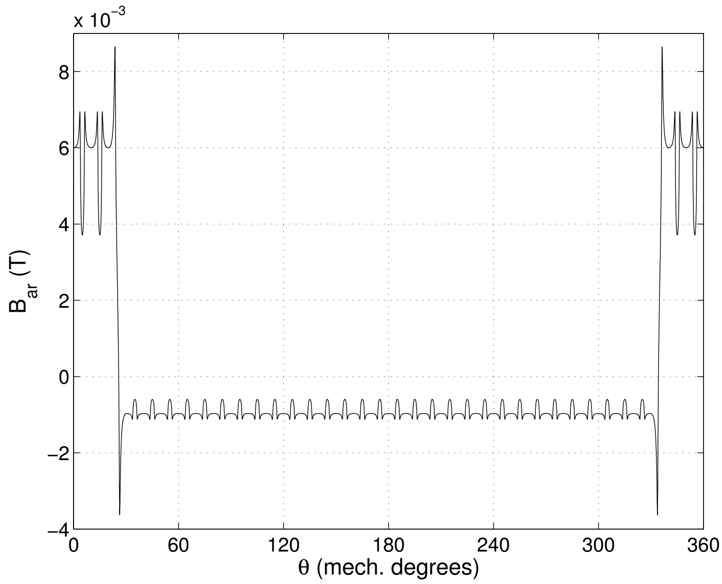

(a)

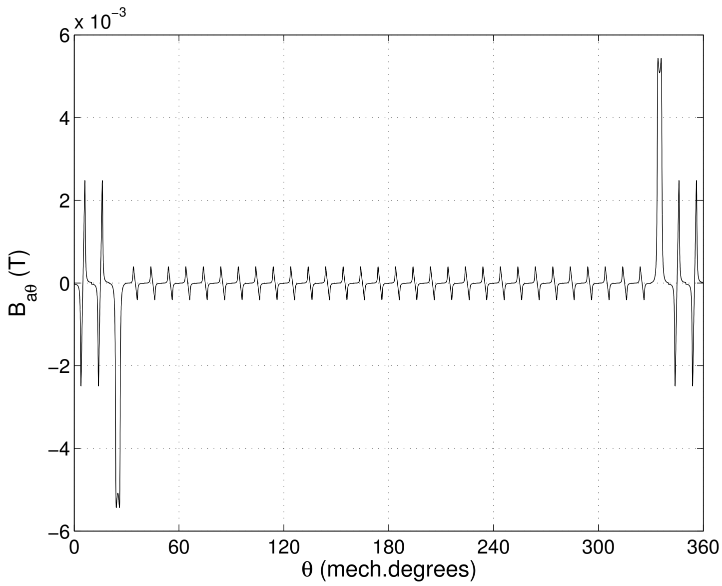

(b)

Fig. 3.5 The waveforms of the flux density in the middle of the slotted air gap of a six pole surface PM motor for one coil with $N_c = 14$ and 1 A of current per turn. The presence of the slots not occupied by the coil is taken into account by means of relative complex air gap permeance: (a) radial component, (b) tangential component an example of a fractional slot winding with $Q_s = 27$ slots and $2p = 6$ poles. In a general case of the fractional slot winding the number of slots per pole and phase is not an integer number. In our example

$$q = \frac{Q_s}{2pm} = \frac{27}{2 \cdot 3 \cdot 3} = \frac{3}{2} \tag{3.18}$$

where m is the number of phases. Let t be the greatest common denominator between Q_s and p, i.e.

$$t = \mathrm{gcd}(Q_s, p) = \mathrm{gcd}(27, 3) = 3 \tag{3.19}$$

The number of voltage phasors in the phasor diagram with different phase angles is then

$$Q_t = \frac{Q_s}{t} = \frac{27}{3} = 9 \tag{3.20}$$

with t phasors in every position as shown in Fig. 3.6. The phase angle between the voltages induced in two consecutive slots is given by

$$\alpha = p\frac{360^0}{Q_s} = 3 \cdot \frac{360^0}{27} = 40^0 \tag{3.21}$$

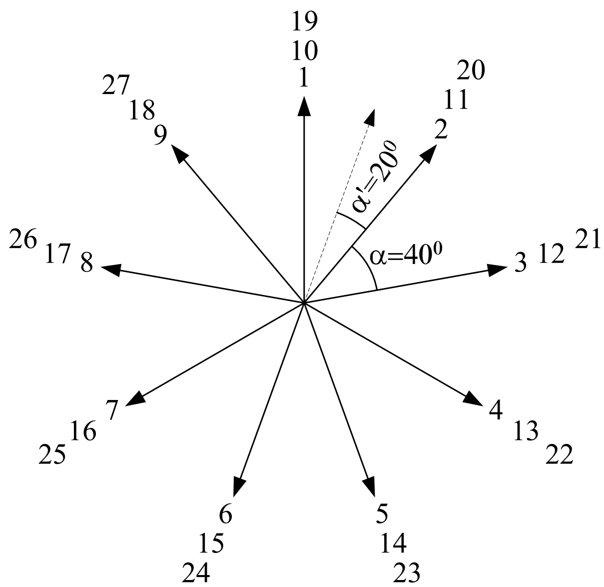

Fig. 3.6 Phasor diagram of the fractional slot winding with 27 slots and six poles

In order to have a symmetrical three phase winding the number of phasors Q_t must be divisible by the number of phases, i.e.

$$\frac{Q_t}{m} = \frac{Q_s}{mt} = \frac{27}{3 \cdot 3} = 3 = \text{integer number} \tag{3.22}$$

This constraint must be satisfied if all the slots are to be filled with coils. Although $q = 3/2 = 1.5$, the fractional slot winding in Fig. 3.6 has $q' = 3$ phasors which have to be added to get the voltage induced in one apparent pole zone. In general, the apparent number of slots per pole and phase is given by

$$\begin{aligned} q' &= \frac{Q_s}{2mt} \left(\text{for } Q_t = \frac{Q_s}{t} = \text{even number} \right) \\ q' &= \frac{Q_s}{mt} \left(\text{for } Q_t = \frac{Q_s}{t} = \text{odd number} \right) \end{aligned} \tag{3.23}$$

Analogous to q and q', an apparent value of the angle α can be defined as

$$\alpha' = \frac{180^0}{mq'} = \frac{180^0}{3 \cdot 3} = 20^0 \tag{3.24}$$

The angle α' is the angle between the phasors which are added to form the voltage of one apparent pole zone. In terms of distribution factor calculation, the fractional slot winding is equivalent to the integral slot winding with q' slots per pole and phase and with phase difference α' between the voltages induced in two consecutive slots. A familiar formula can be used to calculate the distribution factor for the fundamental component [73, 74]

$$k_d = \frac{\sin\left(q'\frac{\alpha'}{2}\right)}{q' \sin\left(\frac{\alpha'}{2}\right)} \tag{3.25}$$

An equivalent approach to the analysis of the fractional slot winding is to represent the number of slots per pole and phase in the form of a fraction

$$q = \frac{Q_s}{2pm} = \frac{a}{b} \tag{3.26}$$

where $\frac{a}{b}$ is obtained by dividing the numerator and denominator by their greatest common factor. The denominator b represents the number of poles after which the winding pattern repeats. The numerator a is equal to previously calculated q' because it represents the number of slots per phase in one repetitive winding pattern which occupies b poles. In that case the apparent phase shift between the voltage phasors in two consequtive slots is b times smaller and hence

$$\alpha' = \frac{\alpha}{b} = p\frac{360^0}{Q_s b} = \frac{180^0}{mqb} = \frac{180^0}{mq'} \tag{3.27}$$

A winding table can now be assembled which contains information for each coil about the actual pole where the upper or lower side of the coil is located, its orientation and the phase to which it belongs. The table has $2p$ rows and $m \cdot a$ columns, i.e. a columns per phase. Hence each phase occupies $q'\alpha' = 60^0$. The phase shift between two columns in the table is α' degrees. The slot numbers are thus entered until the winding table is filled out. The table contains information for only one coil side in the upper or lower layer of the slot. The other coil side is located according to the same table, but phase shifted by the coil pitch. The winding table for the fractional slot winding with $Q_s = 27$ and $2p = 6$ is given in Table 3.1.

Table 3.1 Winding table for the three phase fractional slot winding with $Q_s = 27$, $2p = 6$, $q = a/b = 3/2$. The slots 1, 4 and 7 are starting points for the phases A, B and C respectively.

b columns

	Phase A			**Phase C**			**Phase B**		
N	**1**		2		3		**4**		5
S		6		**7**		8		9	
N	10		11		12		13		14
S		15		16		17		18	
N	19		20		21		22		23
S		24		25		26		27	

$m \cdot a$ columns

The previously analyzed six pole surface PM motor with 36 slots has a double layer integral slot winding for which

$$q = \frac{Q_s}{2pm} = \frac{36}{2 \cdot 3 \cdot 3} = \frac{2}{1} = \frac{a}{b}$$

$$\alpha \;=\; p\frac{360^0}{Q_s} = 3 \cdot \frac{360^0}{36} = 30^0$$

Hence, the winding table can be assembled as shown in Table 3.2 using the same principle as previously described.

Table 3.2 Winding table for the three phase integral slot winding with $Q_s = 36$, $2p = 6$, $q = a/b = 2/1$. The phases A, B and C start at the slots 1, 5 and 9 respectively.

	Phase A		**Phase C**		**Phase B**	
N	**1**	2	3	4	**5**	6
S	7	8	**9**	10	11	12
N	13	14	15	16	17	18
S	19	20	21	22	23	24
N	25	26	27	28	29	30
S	31	32	33	34	35	36

In order to use the information from Table 3.2 for the armature winding field calculation, Table 3.3 can be formed which contains information about the phase shifts, the values of the currents and their signs for all the coils. Note that phase shifts in Table 3.3 are expressed in terms of mechanical degrees. This table is convenient for implementation in a computer program.

The field solution in Fig. 3.5 is given for the coil of phase A which starts in the slot number 1. Therefore, the air gap field solution at the radius $R_m < r < R_s$ for the entire armature winding can be written in the form

$$\begin{aligned}
B_{ar}(r,\theta,t) &= N_c \sum_{i=1}^{\frac{Q_s}{m}} \sum_{n=1}^{N_a} B_{arn}(r) \left\{ i_A(t)\mathrm{sgn}_{Ai} \cos[n(\theta-\alpha_{Ai})] + i_B(t)\mathrm{sgn}_{Bi} \cos[n(\theta-\alpha_{Bi})] + \right. \\
&\quad \left. i_C(t)\mathrm{sgn}_{Ci} \cos[n(\theta-\alpha_{Ci})] \right\} \\
B_{a\theta}(r,\theta,t) &= N_c \sum_{i=1}^{\frac{Q_s}{m}} \sum_{n=1}^{N_a} B_{a\theta n}(r) \left\{ i_A(t)\mathrm{sgn}_{Ai} \sin[n(\theta-\alpha_{Ai})] + i_B(t)\mathrm{sgn}_{Bi} \sin[n(\theta-\alpha_{Bi})] + \right. \\
&\quad \left. i_C(t)\mathrm{sgn}_{Ci} \sin[n(\theta-\alpha_{Ci})] \right\}
\end{aligned} \tag{3.28}$$

Table 3.3 Information about the phase shift, the value of the current and its sign for each coil and each phase of the integral slot winding with $Qs = 36$ and $2p = 6$.

$i = 1 \cdots \frac{Q_s}{m}$	**Phase A**											
Coil numbers: n_{Ai}	1	2	7	8	13	14	29	20	25	26	32	32
Phase shifts: $\alpha_{Ai} = (n_{Ai} - 1)\frac{360^0}{Q_s}$	0^0	10^0	60^0	70^0	120^0	130^0	180^0	190^0	240^0	250^0	300^0	310^0
Current: i(t)	$i_A(t)$											
Sign: sgn_{Ai}	+	+	-	-	+	+	-	-	+	+	-	-
	Phase B											
Coil numbers: n_{Bi}	5	6	11	12	17	18	23	24	29	30	35	36
Phase shifts: $\alpha_{Bi} = (n_{Bi} - 1)\frac{360^0}{Q_s}$	40^0	50^0	100^0	110^0	160^0	170^0	220^0	230^0	280^0	290^0	340^0	350^0
Current: i(t)	$i_B(t)$											
Sign: sgn_{Bi}	+	+	-	-	+	+	-	-	+	+	-	-
	Phase C											
Coil numbers: n_{Ci}	3	4	9	10	15	16	21	22	27	28	33	34
Phase shifts: $\alpha_{Ci} = (n_{Ci} - 1)\frac{360^0}{Q_s}$	20^0	30^0	80^0	90^0	140^0	150^0	200^0	210^0	260^0	270^0	320^0	330^0
Current: i(t)	$i_C(t)$											
Sign: sgn_{Ci}	-	-	+	+	-	-	+	+	-	-	+	+

where $i_A(t)$, $i_B(t)$, $i_c(t)$ are the instantaneous phase currents, sgn_{Ai}, sgn_{Bi}, sgn_{Ci}, α_{Ai}, α_{Bi}, α_{Ci} are the parameters defined according to Table 3.3 and B_{arn}, $B_{a\theta n}$ are the Fourier coefficients of the flux density waveforms in Fig. 3.5 calculated for a single coil with 1 A of current.

The total armature winding field has been calculated for the previously analyzed six pole surface PM motor. The rms value of the rated armature current is $I = 6.91A$. It is assumed that stator currents are sinusoidal. The rotor with permanent magnets is aligned with the phase A axis at the time instant when the phase A current is at its peak value. In that case the armature field is aligned with the phase A axis and the phase currents are $i_A = \sqrt{2} \cdot 6.91$ A, $i_B = i_C = -\frac{i_A}{2}$. The waveforms of the radial and tangential components of the analytically calculated armature field are shown in Fig. 3.7. They are compared in the same figure with the FE results calculated using FEMLAB 2.3 commercial software with third order triangular elements assuming infinite permeability of the core. There is some difference in the analytically and numerically calculated waveforms. This difference occurs because the field solution obtained by conformal mapping does not take into account the fact that magnets have a relative permeability μ_r slightly higher than one. This difference can be taken into account by multiplying the analytical field solution with the relative air gap permeance function. The presence of slots is not included in the permeance function because they have already been included by conformal mapping. In the area not occupied by magnets the slotless air gap permeance is defined as

$$\Lambda_{gsless} = \frac{\mu_0}{g + l_m} \tag{3.29}$$

where g is the air gap length and l_m is the magnet length. Since magnets have a permeability slightly higher than one, an equivalent air gap length needs to be determined to calculate the air gap permeance of the region occupied by magnets. For an infinitely thin slice of the magnet volume one can assume that the flux through the slice will be the same as the flux through an infinitely thin slice of the air gap volume. This implies that the flux densities in the PM and in the air must be the same.

$$\mathrm{d}\lambda = B_m \mathrm{d}A_m = B_g \mathrm{d}A_g \;\text{ and }\; \mathrm{d}A_m = \mathrm{d}A_g \;\;\Rightarrow\;\; B_m = B_g \tag{3.30}$$

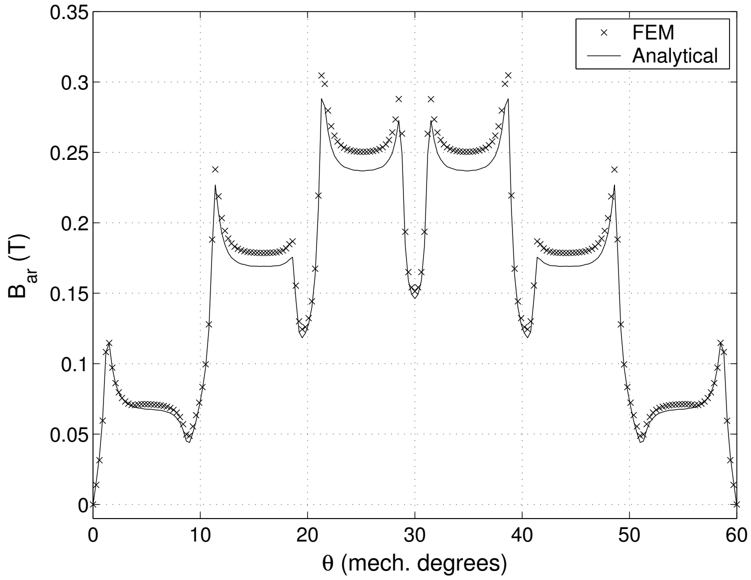

(a)

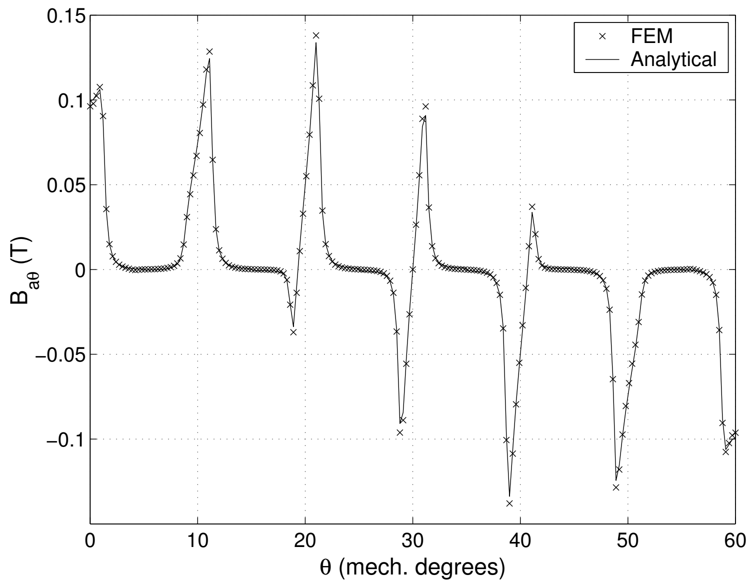

(b)

Fig. 3.7 Comparison of analytically and numerically calculated armature winding flux density in the middle of the air gap of a six pole surface PM motor: (a) radial component, (b) tangential component

At no load with an assumption of infinite iron permeability the Ampere's law for the magnetic circuit becomes

$$\int \vec{H}\mathrm{d}\vec{l} = H_m l_m + H_g l_g = 0 \quad \Rightarrow \quad H_m = -\frac{g}{l_m} H_g \tag{3.31}$$

Expressed in terms of the air gap flux density (3.31) becomes

$$H_m = -\frac{g}{l_m \mu_0} B_g \tag{3.32}$$

For a magnet with linear demagnetization characteristic the fundamental field equation is

$$B_m = \mu_m H_m + B_r \tag{3.33}$$

where $\mu_m = \mu_0 \mu_r$ is the magnet permeability and B_r is the remanent flux density. Substituting (3.32) into (3.33) yields

$$B_m = B_r - \frac{\mu_m}{\mu_0} \frac{g}{l_m} B_g \tag{3.34}$$

Since $B_g = B_m$, (3.34) transforms into

$$B_m = \frac{lm}{\mu_r} \frac{B_r}{g + \frac{l_m}{\mu_r}} \tag{3.35}$$

where μ_r is the magnet relative permeability. An effective air gap is then defined as

$$g\prime = g + \frac{l_m}{\mu_r} \tag{3.36}$$

and the air gap permeance as

$$\Lambda_{gmsless} = \frac{\mu_0}{g'} = \frac{\mu_0}{g + \frac{l_m}{\mu_r}} \tag{3.37}$$

The relative air gap permeance in the slotless air gap which takes into account the presence of magnets can be defined as

$$\lambda_{gsless} = \begin{cases} \frac{\Lambda_{gmsless}}{\Lambda_{gsless}} = \frac{g+l_m}{g+\frac{l_m}{\mu_r}} = \lambda_{gm} & \text{where magnets are present} \\ 1 & \text{where magnets are not present} \end{cases} \tag{3.38}$$

The waveform of the function defined by (3.38) for one pole pitch is shown in Fig. 3.8 This waveform can be expressed in the form of a Fourier series. Since it is symmetric about the ordinate, only cosine terms will exist in the series. The Fourier coefficients are given by

$$\lambda_{g0} = \frac{2p}{\pi}\int_0^{\frac{\pi}{2p}} \lambda_{gsless}(\theta)\mathrm{d}\theta = 1 + \alpha_p(\lambda_{gm} - 1) \tag{3.39}$$

$$\lambda_{gn} = \frac{4p}{\pi}\int_0^{\frac{\pi}{2p}} \lambda_{gsless}(\theta)\cos(2np\theta)\mathrm{d}\theta = \frac{2}{n\pi}\sin(n\alpha_p\pi)(\lambda_{gm} - 1) \tag{3.40}$$

The expression for the relative air gap permeance is then

$$\begin{aligned} \lambda_{gsless} &= \lambda_{g0} + \sum_{n=1}^{\infty} \lambda_{gn}\cos[2np(\theta - \alpha)] \\ &= 1 + \alpha_p(\lambda_{gm} - 1) + (\lambda_{gm} - 1)\sum_{n=1}^{\infty} \frac{2}{n\pi}\sin(n\alpha_p\pi)\cos[2np(\theta - \alpha)] \qquad (3.41) \end{aligned}$$

The permeance is also a function of the magnet angular position α because the waveform in Fig. 3.8 travels with the magnets as the rotor rotates.

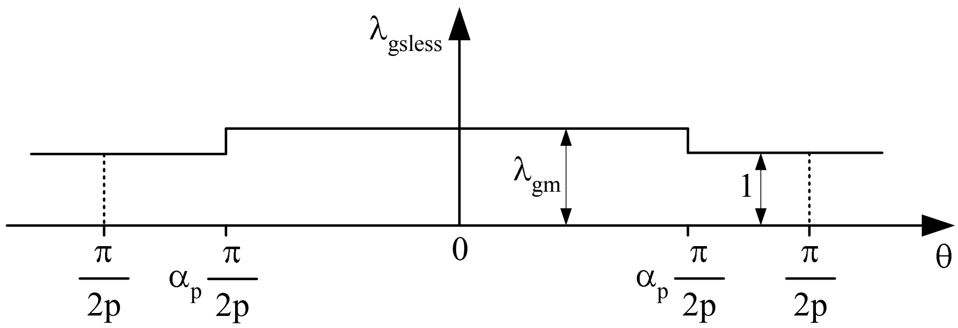

Fig. 3.8 Waveform of the relative air gap permeance of the slotless air gap used to take into account the presence of magnets in the analytical armature winding field calculation

A new armature winding field solution has been obtained in Fig. 3.9 after multiplying the previously calculated solution shown in Fig. 3.7 with the relative air gap permeance from (3.41). A much better agreement with finite element results can be noticed.

The radial and tangential components of the armature winding field after taking into account the magnet permeance can be written in the form of Fourier series as

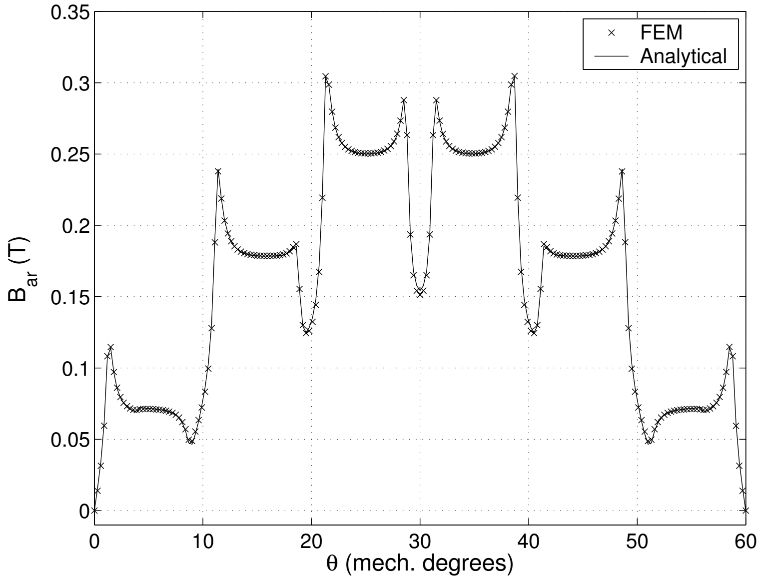

(a)

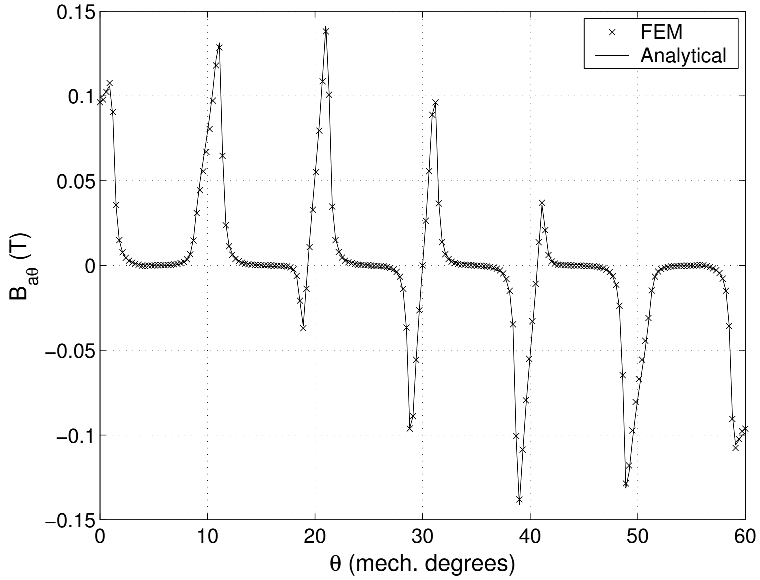

(b)

Fig. 3.9 Comparison of analytically and numerically calculated armature winding flux density in the middle of the air gap of a six pole surface PM motor. The analytical solution has been multiplied by the relative air gap permeance to take into account the fact that relative permeability of the magnets is greater than one; (a) radial component, (b) tangential component

$$\begin{aligned}
B_{ar}(r,\theta,t) &= N_c\lambda_{g0}\sum_{i=1}^{Q_{coil}}\sum_{n=1}^{N_a} B_{arn}(r)\left\{i_A(t)\mathrm{sgn}_{Ai}\cos[n(\theta-\alpha_{Ai})] + i_B(t)\mathrm{sgn}_{Bi}\cos[n(\theta-\alpha_{Bi})] + \right.\\
&\quad i_C(t)\mathrm{sgn}_{Ci}\cos[n(\theta-\alpha_{Ci})]\} + \\
&\quad N_c\sum_{i=1}^{Q_{coil}}\sum_{n=1}^{N_a}\sum_{h=1}^{\infty}\lambda_{gh}B_{arn}(r)\left\{i_A(t)\mathrm{sgn}_{Ai}\cos[n(\theta-\alpha_{Ai})] + \right.\\
&\quad i_B(t)\mathrm{sgn}_{Bi}\cos[n(\theta-\alpha_{Bi})] + i_C(t)\mathrm{sgn}_{Ci}\cos[n(\theta-\alpha_{Ci})]\}\cos[2hp(\theta-\alpha)] \qquad (3.42)
\end{aligned}$$

$$\begin{aligned}
B_{a\theta}(r,\theta,t) &= N_c\lambda_{g0}\sum_{i=1}^{Q_{coil}}\sum_{n=1}^{N_a} B_{a\theta n}(r)\left\{i_A(t)\mathrm{sgn}_{Ai}\sin[n(\theta-\alpha_{Ai})] + i_B(t)\mathrm{sgn}_{Bi}\sin[n(\theta-\alpha_{Bi})] + \right.\\
&\quad i_C(t)\mathrm{sgn}_{Ci}\sin[n(\theta-\alpha_{Ci})]\} + \\
&\quad N_c\sum_{i=1}^{Q_{coil}}\sum_{n=1}^{N_a}\sum_{h=1}^{\infty}\lambda_{gh}B_{a\theta n}(r)\left\{i_A(t)\mathrm{sgn}_{Ai}\sin[n(\theta-\alpha_{Ai})] + \right.\\
&\quad i_B(t)\mathrm{sgn}_{Bi}\sin[n(\theta-\alpha_{Bi})] + i_C(t)\mathrm{sgn}_{Ci}\sin[n(\theta-\alpha_{Ci})]\}\cos[2hp(\theta-\alpha)] \qquad (3.43)
\end{aligned}$$

where

$$Q_{coil} = \begin{cases} \frac{Q_s}{3} & \text{for two-layer winding} \\ \frac{Q_s}{6} & \text{for single-layer winding} \end{cases}$$

3.3 Calculation of Electromagnetic Torque Based on Maxwell's Stress Theory

In the previous chapters it has been shown how to calculate the field distribution in the air gap of a surface PM motor. Since both radial and tangential components of the armature winding and permanent magnet flux density are known, the integral of the Maxwell's stress tensor in the air gap can be used to calculate the total torque in the motor. The total air gap field is equal to the sum of the magnet field and the armature winding field which can be written in the form

$$\begin{aligned}
B_r(r,\theta,t) &= B_{sr}(r,\theta,t) + B_{ar}(r,\theta,t) \\
B_\theta(r,\theta,t) &= B_{s\theta}(r,\theta,t) + B_{a\theta}(r,\theta,t) \qquad (3.44)
\end{aligned}$$

where B_{sr} and $B_{s\theta}$ are the flux density components of the permanent magnet field calculated according to (2.128) and (2.129), while B_{ar} and $B_{a\theta}$ are the flux density components of the armature field calculated according to (3.42) and (3.43). The torque expression is then

$$\begin{aligned}T(t) &= \frac{1}{\mu_0} l_a R^2 \int_0^{2\pi} \left[B_{sr}(R,\theta,t) + B_{ar}(R,\theta,t)\right]\left[B_{s\theta}(R,\theta,t) + B_{a\theta}(R,\theta,t)\right] \mathrm{d}\theta \\ &= \frac{1}{\mu_0} l_a R^2 \int_0^{2\pi} \left[B_{sr}(R,\theta,t)B_{s\theta}(R,\theta,t) + B_{sr}(R,\theta,t)B_{a\theta}(R,\theta,t) + \right. \\ & \left. B_{s\theta}(R,\theta,t)B_{ar}(R,\theta,t) + B_{ar}(R,\theta,t)B_{a\theta}(R,\theta,t)\right] \mathrm{d}\theta \end{aligned} \tag{3.45}$$

where R is the radius in the air gap where the field is calculated. The terms $B_{sr}B_{s\theta}$ of the integrand in (3.45) involve flux density components of the magnets alone. Hence they contribute only to the cogging torque production. The integral of $B_{sr}B_{s\theta}$ has been solved in Chapter 2 for which a closed form solution has been given in (2.136). The last term $B_{ar}B_{a\theta}$ involves only flux density components of the armature winding. If the difference in the air gap permeance in d and q axes due to the fact that relative permeability of the magnet material is slightly higher than one is neglected, then the integral of this term will be equal to zero. The remaining terms $B_{sr}B_{a\theta}$ and $B_{ar}B_{s\theta}$ are responsible for the production of electromagnetic torque.

The basic principle behind the derivation of the closed form solution for the electromagnetic torque is very similar to the one presented in Chapter 2 for the cogging torque. Therefore, no detailed derivation will be presented here. The solution of the integral

$$T(t) = \frac{1}{\mu_0} l_a R^2 \int_0^{2\pi} \left[B_{sr}(R,\theta,t)B_{a\theta}(R,\theta,t) + B_{s\theta}(R,\theta,t)B_{ar}(R,\theta,t)\right] \mathrm{d}\theta \tag{3.46}$$

is then

$k - np = 0$

$$\begin{aligned}T_{em}(t) &= \frac{1}{\mu_0} l_a R^2 N_c \sum_{i=1}^{Q_{coil}} \sum_{n=1,3}^{\infty} \sum_{k=1}^{N_a} \lambda_0 \lambda_{g0} \pi (B_{rn}B_{a\theta k} - B_{\theta n}B_{ark})[i_A(t)\mathrm{sgn}_{Ai} \sin(np\alpha(t) - \\ & k\alpha_{Ai}) + i_B(t)\mathrm{sgn}_{Bi} \sin(np\alpha(t) - k\alpha_{Bi}) + i_C(t)\mathrm{sgn}_{Ci} \sin(np\alpha(t) - k\alpha_{Ci})]\end{aligned}$$

$k - np - mQ_s = 0$

$$\begin{aligned}T_{em}(t) &= \frac{1}{\mu_0} l_a R^2 N_c \sum_{i=1}^{Q_{coil}} \sum_{n=1,3}^{\infty} \sum_{m=1}^{N_\lambda} \sum_{k=1}^{N_a} \lambda_{g0} \frac{\pi}{2} (B_{rn}\lambda_{am}B_{a\theta k} - B_{\theta n}\lambda_{bm}B_{a\theta k} - \\ & B_{\theta n}\lambda_{am}B_{ark} + B_{rn}\lambda_{bm}B_{ark})[i_A(t)\mathrm{sgn}_{Ai} \sin(np\alpha(t) - k\alpha_{Ai}) + \\ & i_B(t)\mathrm{sgn}_{Bi} \sin(np\alpha(t) - k\alpha_{Bi}) + i_C(t)\mathrm{sgn}_{Ci} \sin(np\alpha(t) - k\alpha_{Ci})]\end{aligned}$$

$k - np + mQ_s = 0$

$$\begin{aligned} T_{em}(t) &= \frac{1}{\mu_0} l_a R^2 N_c \sum_{i=1}^{Q_{coil}} \sum_{n=1,3}^{\infty} \sum_{m=1}^{N_\lambda} \sum_{k=1}^{N_a} \lambda_{g0} \frac{\pi}{2} (B_{rn}\lambda_{am}B_{a\theta k} + B_{\theta n}\lambda_{bm}B_{a\theta k} - \\ &\quad B_{\theta n}\lambda_{am}B_{ark} - B_{rn}\lambda_{bm}B_{ark})[i_A(t)\mathrm{sgn}_{Ai}\sin(np\alpha(t) - k\alpha_{Ai}) + \\ &\quad i_B(t)\mathrm{sgn}_{Bi}\sin(np\alpha(t) - k\alpha_{Bi}) + i_C(t)\mathrm{sgn}_{Ci}\sin(np\alpha(t) - k\alpha_{Ci})] \end{aligned}$$

$k + np - mQ_s = 0$

$$\begin{aligned} T_{em}(t) &= \frac{1}{\mu_0} l_a R^2 N_c \sum_{i=1}^{Q_{coil}} \sum_{n=1,3}^{\infty} \sum_{m=1}^{N_\lambda} \sum_{k=1}^{N_a} \lambda_{g0} \frac{\pi}{2} (-B_{rn}\lambda_{am}B_{a\theta k} - B_{\theta n}\lambda_{bm}B_{a\theta k} - \\ &\quad B_{\theta n}\lambda_{am}B_{ark} - B_{rn}\lambda_{bm}B_{ark})[i_A(t)\mathrm{sgn}_{Ai}\sin(np\alpha(t) + k\alpha_{Ai}) + \\ &\quad i_B(t)\mathrm{sgn}_{Bi}\sin(np\alpha(t) + k\alpha_{Bi}) + i_C(t)\mathrm{sgn}_{Ci}\sin(np\alpha(t) + k\alpha_{Ci})] \end{aligned}$$

$k - np - 2hp = 0$

$$\begin{aligned} T_{em}(t) &= \frac{1}{\mu_0} l_a R^2 N_c \sum_{i=1}^{Q_{coil}} \sum_{n=1,3}^{\infty} \sum_{h=1}^{\infty} \sum_{k=1}^{N_a} \lambda_0 \frac{\pi}{2} (B_{rn}\lambda_{gh}B_{a\theta k} - B_{\theta n}\lambda_{gh}B_{ark}) \\ &\quad \{i_A(t)\mathrm{sgn}_{Ai}\sin[p(n+2h)\alpha(t) - k\alpha_{Ai}] + i_B(t)\mathrm{sgn}_{Bi}\sin[p(n+2h)\alpha(t) - k\alpha_{Bi}] + \\ &\quad i_C(t)\mathrm{sgn}_{Ci}\sin[p(n+2h)\alpha(t) - k\alpha_{Ci})\} \end{aligned}$$

$k - np + 2hp = 0$

$$\begin{aligned} T_{em}(t) &= \frac{1}{\mu_0} l_a R^2 N_c \sum_{i=1}^{Q_{coil}} \sum_{n=1,3}^{\infty} \sum_{h=1}^{\infty} \sum_{k=1}^{N_a} \lambda_0 \frac{\pi}{2} (B_{rn}\lambda_{gh}B_{a\theta k} - B_{\theta n}\lambda_{gh}B_{ark}) \\ &\quad \{i_A(t)\mathrm{sgn}_{Ai}\sin[p(n-2h)\alpha(t) - k\alpha_{Ai}] + i_B(t)\mathrm{sgn}_{Bi}\sin[p(n-2h)\alpha(t) - k\alpha_{Bi}] + \\ &\quad i_C(t)\mathrm{sgn}_{Ci}\sin[p(n-2h)\alpha(t) - k\alpha_{Ci})\} \end{aligned}$$

$k + np - 2hp = 0$

$$\begin{aligned} T_{em}(t) &= \frac{1}{\mu_0} l_a R^2 N_c \sum_{i=1}^{Q_{coil}} \sum_{n=1,3}^{\infty} \sum_{h=1}^{\infty} \sum_{k=1}^{N_a} \lambda_0 \frac{\pi}{2} (-B_{rn}\lambda_{gh}B_{a\theta k} - B_{\theta n}\lambda_{gh}B_{ark}) \\ &\quad \{i_A(t)\mathrm{sgn}_{Ai}\sin[p(n-2h)\alpha(t) + k\alpha_{Ai}] + i_B(t)\mathrm{sgn}_{Bi}\sin[p(n-2h)\alpha(t) + k\alpha_{Bi}] + \\ &\quad i_C(t)\mathrm{sgn}_{Ci}\sin[p(n-2h)\alpha(t) + k\alpha_{Ci})\} \end{aligned} \tag{3.47}$$

The terms that involve combinations of the type $k \pm np \pm mQ_s \pm 2hp = 0$ are also possible, but they are small compared to the terms in (3.47), so they can be neglected. The angle $\alpha(t)$ in (3.47) is defined as

$$\alpha(t) = \alpha_0 + \omega_{rm} t \tag{3.48}$$

where α_0 is the initial position of the rotor in which the magnet axis is aligned with the phase A axis.

The total torque in the motor is equal to the sum of the electromagnetic torque from (3.47) and the cogging torque from (2.136). The waveforms of the electromagnetic torque, cogging torque and total torque for the six pole surface PM motor have been calculated analytically and compared to the FE results in Figs. 3.10, 3.11 and 3.12 respectively. The difference between analytically and numerically calculated average torque for both cases of magnetization is around 2.5%. The difference is somewhat larger for the torque ripple component which is around 6.5% in both cases. It has been noticed earlier that the peak values of the cogging torque calculated analytically by integrating Maxwell's stress tensor in the air gap were larger than obtained from FE simulations. Similar differences from FE simulations can also be noticed for analytically calculated electromagnetic torque ripple components. Some reasons for such differences were explained earlier in the case of cogging torque. However, it would be quite difficult to repeat similar analysis and calculate electromagnetic torque by integrating lateral forces on the slot sides because the field in each slot is a function of its current and of the currents in all other slots as well. What remains certain is that the proposed analytical torque calculation based on integration of the Maxwell's stress tensor in the air gap takes into account all the effects that cause torque ripple in surface PM motors. Those effects are the cogging torque, the mismatch between the back emf shape and the current shape and the presence of stator slots.

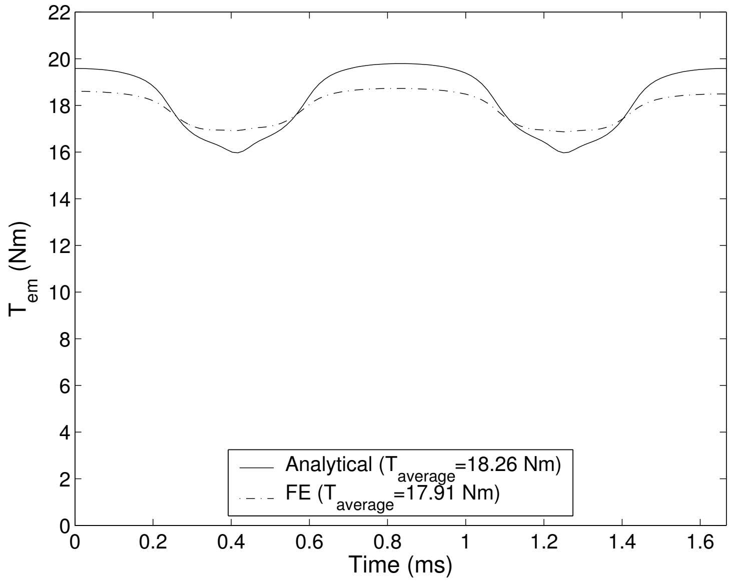

(a)

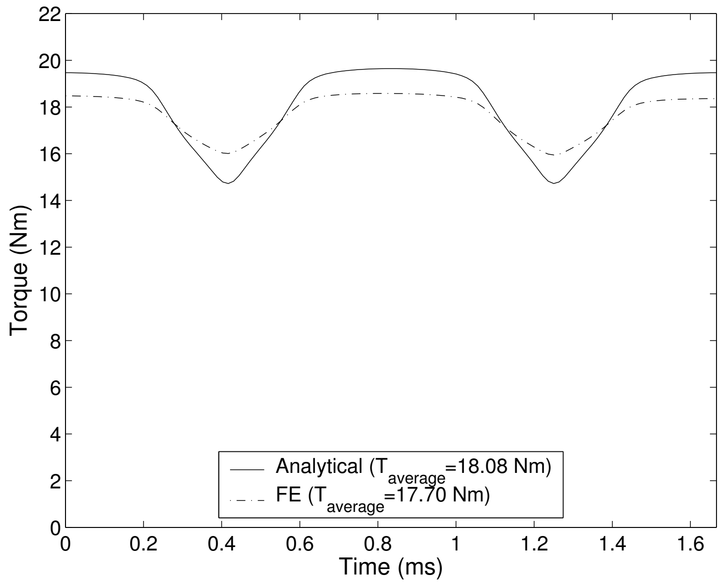

(b)

Fig. 3.10 Comparison of analytically and numerically calculated electromagnetic torque of the six pole surface PM motor: (a) radial magnetization, (b) parallel magnetization

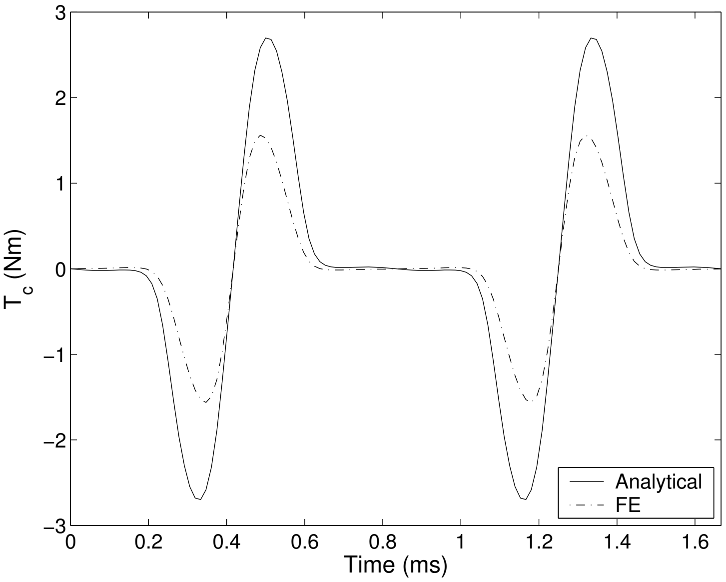

(a)

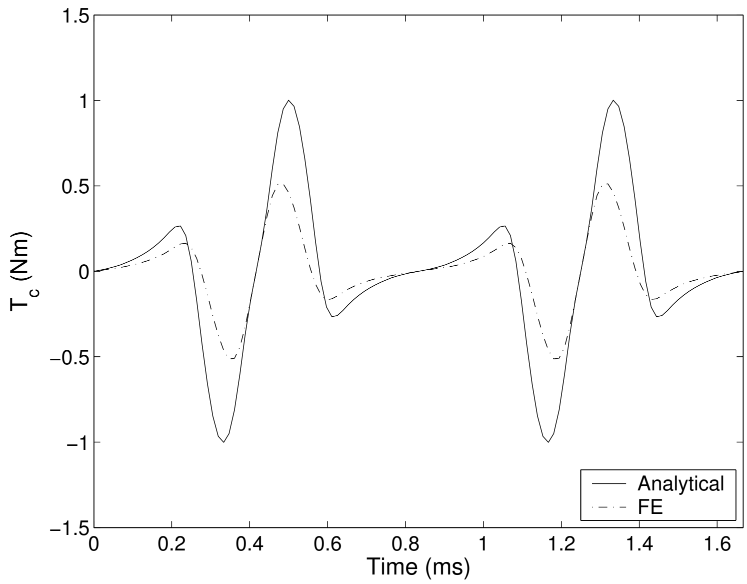

(b)

Fig. 3.11 Comparison of analytically and numerically calculated cogging torque of the six pole surface PM motor: (a) radial magnetization, (b) parallel magnetization

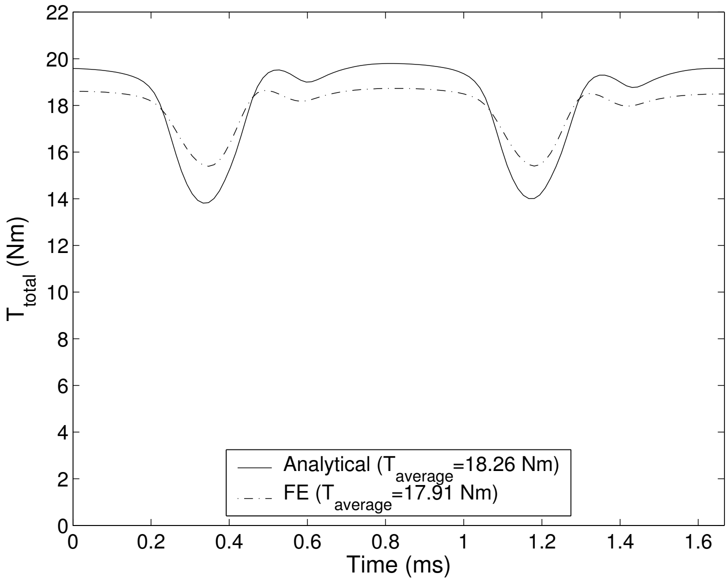

(a)

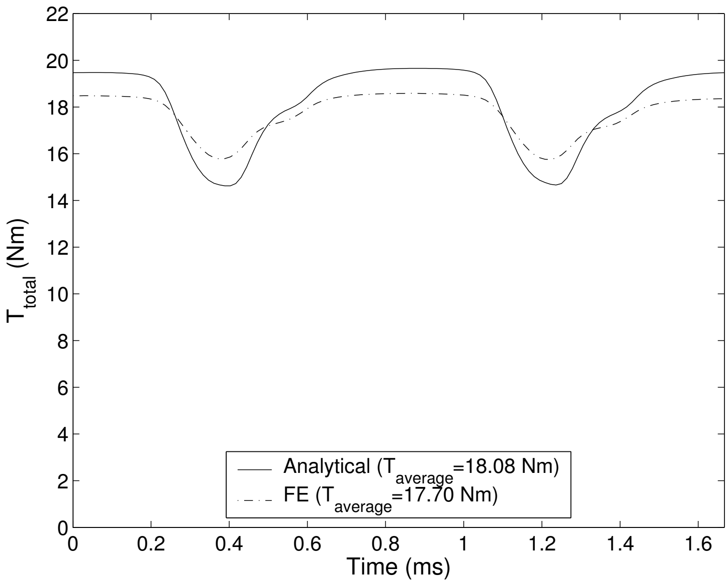

(b)

Fig. 3.12 Comparison of analytically and numerically calculated total torque of the six pole surface PM motor: (a) radial magnetization, (b) parallel magnetization

Chapter 4

Calculation of the Back Emf in Surface PM Motors

The back emf waveform of a surface PM motor can be calculated from the no-load flux density distribution with the knowledge of the armature winding distribution. According to Faraday's law the voltage induced in a single coil is equal to the negative derivative of the flux linked by the coil, i.e.

$$E_c(t) = -\frac{\mathrm{d}\psi_c}{\mathrm{dt}} = -N_c\frac{\mathrm{d}\phi_c}{\mathrm{dt}} \tag{4.1}$$

where N_c is the number of coil turns. The flux linkage ϕ_c is equal to the integral of the air gap flux density distribution across one coil pitch. It has been shown earlier that the flux density in the slotted air gap can be calculated according to

$$B_s(r,\theta) = [B_r(r,\theta) + jB_\theta(r,\theta)]\,[\lambda_a(r,\theta) - j\lambda_b(r,\theta)] \tag{4.2}$$

where B_r and B_θ are the radial and tangential components of the flux density in the slotless air gap and λ_a and λ_b are the real and imaginary components of the complex relative air gap permeance. For calculation of the flux linkage ϕ_c it is sufficient to know only the radial component of the flux density B_s which is given by

$$\begin{aligned} B_{sr}(r,\theta,t) &= B_r(r,\theta,t)\lambda_a(r,\theta) + B_\theta(r,\theta,t)\lambda_b(r,\theta) \\ &= \sum_n B_{rn}\cos\left[np(\theta-\omega_{rm}t)\right]\left\{\lambda_0 + \sum_m \lambda_{am}\cos[mQ_s(\theta-\theta_{s0})]\right\} + \\ &\quad \sum_n B_{\theta n}\sin[np(\theta-\omega_{rm}t)]\sum_m \lambda_{bm}\sin[mQ_s(\theta-\theta_{s0})] \end{aligned} \tag{4.3}$$

where B_{rn}, $B_{\theta n}$ are the Fourier coefficients of the slotless air gap flux density, λ_0, λ_{am}, λ_{bm} are the Fourier coefficients of the complex relative air gap permeance, p is the number of pole pairs, Q_s

is the number of slots, ω_{rm} is the rotor speed and θ_{s0} is the angle which sets the reference of the air gap permeance function to coincide with either the tooth axis or the slot axis. There are two distinctive cases which define the angle θ_{s0}. Since the initial reference for the air gap permeance calculated in Chapter 2 has been chosen to coincide with the tooth axis, the angle θ_s will be

$$\theta_{s0} = \begin{cases} 0, & \text{when the coil pitch is an } \textbf{odd} \text{ integer of the slot pitch} \\ \frac{\pi}{Q_s}, & \text{when the coil pitch is an } \textbf{even} \text{ integer of the slot pitch} \end{cases}$$

The flux linkage ϕ_c is then

$$\phi_c(t) = l_a R \int_{-\frac{\gamma_c}{2}}^{\frac{\gamma_c}{2}} B_{sr}(R,\theta,t)\mathrm{d}\theta \tag{4.4}$$

where R is the radius close to the stator surface where the field is calculated and γ_c is the coil pitch angle. The expression obtained after integration is

$$\begin{aligned} \phi_c(t) \;=\; & l_a R \sum_n \Bigg\{ \lambda_0 B_{rn} 2 \frac{1}{np} \sin\left(np\frac{\gamma_c}{2}\right) + \\ & \sum_m (B_{rn}\lambda_{am} - B_{\theta n}\lambda_{bm}) \frac{1}{np + mQ_s} \sin\left[(np + mQ_s)\frac{\gamma_c}{2}\right] + \\ & \sum_m (B_{rn}\lambda_{am} + B_{\theta n}\lambda_{bm}) \frac{1}{np - mQ_s} \sin\left[(np - mQ_s)\frac{\gamma_c}{2}\right] \Bigg\} \cos(np\omega_{rm}t) \end{aligned} \tag{4.5}$$

in the case when $\theta_{s0} = 0$ and

$$\begin{aligned} \phi_c(t) \;=\; & l_a R \sum_n \Bigg\{ \lambda_0 B_{rn} 2 \frac{1}{np} \sin\left(np\frac{\gamma_c}{2}\right) + \\ & \sum_m (B_{rn}\lambda_{am} - B_{\theta n}\lambda_{bm}) \frac{1}{np + mQ_s} \sin\left[(np + mQ_s)\frac{\gamma_c}{2}\right] \cos(m\pi) + \\ & \sum_m (B_{rn}\lambda_{am} + B_{\theta n}\lambda_{bm}) \frac{1}{np - mQ_s} \sin\left[(np - mQ_s)\frac{\gamma_c}{2}\right] \cos(m\pi) \Bigg\} \cos(np\omega_{rm}t) \end{aligned} \tag{4.6}$$

in the case when $\theta_{s0} = \frac{\pi}{Q_s}$.

In the case when $np = mQ_s$ the term

$$\frac{1}{np - mQ_s} \sin\left[(np - mQ_s)\frac{\gamma_c}{2}\right]$$

in (4.5) and (4.6) should be replaced with $\frac{\gamma_c}{2}$.

The voltage induced in a single coil can now be calculated according to (4.1). After finding the time derivatives of (4.5) and (4.6) and multiplying them by N_c the expression for the induced voltage per coil is

$$\begin{aligned} E_c(t) &= N_c\omega_{rm} l_a R \sum_n \left\{ \lambda_0 B_{rn} 2 \sin\left(np\frac{\gamma_c}{2}\right) + \right. \\ & \sum_m (B_{rn}\lambda_{am} - B_{\theta n}\lambda_{bm}) \frac{np}{np + mQ_s} \sin\left[(np + mQ_s)\frac{\gamma_c}{2}\right] + \\ & \left. \sum_m (B_{rn}\lambda_{am} + B_{\theta n}\lambda_{bm}) \frac{np}{np - mQ_s} \sin\left[(np - mQ_s)\frac{\gamma_c}{2}\right] \right\} \sin(np\omega_{rm} t) \end{aligned} \tag{4.7}$$

in the case when $\theta_{s0} = 0$ and

$$\begin{aligned} E_c(t) &= N_c\omega_{rm} l_a R \sum_n \left\{ \lambda_0 B_{rn} 2 \sin\left(np\frac{\gamma_c}{2}\right) + \right. \\ & \sum_m (B_{rn}\lambda_{am} - B_{\theta n}\lambda_{bm}) \frac{np}{np + mQ_s} \sin\left[(np + mQ_s)\frac{\gamma_c}{2}\right] \cos(m\pi) + \\ & \left. \sum_m (B_{rn}\lambda_{am} + B_{\theta n}\lambda_{bm}) \frac{np}{np - mQ_s} \sin\left[(np - mQ_s)\frac{\gamma_c}{2}\right] \cos(m\pi) \right\} \sin(np\omega_{rm} t) \end{aligned} \tag{4.8}$$

in the case when $\theta_{s0} = \frac{\pi}{Q_s}$.

The total back emf per phase is calculated by adding the voltages induced in all coils of the phase winding connected in series. The voltages induced in adjacent slots are phase shifted so they should be summed as vectors which is taken into account via distribution factor. The distribution factor for the n^{th} harmonic is given by

$$k_{dn} = \frac{\sin\left(nq\frac{\alpha}{2}\right)}{q \sin\left(n\frac{\alpha}{2}\right)} \tag{4.9}$$

where q is the number of slots per pole per phase and α is the phase shift between the voltages induced in two adjacent slots. In the case of a fractional slot winding, q' from (3.23) and α' from (3.24) should be used in (4.9). In a three phase winding the total number of turns per phase connected in series is given by

$$N_s = \begin{cases} N_c \frac{Q_s}{6a_p}, & \text{for a single-layer winding} \\ N_c \frac{Q_s}{3a_p}, & \text{for a two-layer winding} \end{cases}$$

where a_p is the number of parallel paths. The final expression for the back emf waveform per phase in a surface PM motor is then

$$\begin{aligned} E_{phase}(t) &= N_s\omega_{rm}l_aR\sum_n k_{dn}\left\{\lambda_0 B_{rn}2\sin\left(np\frac{\gamma_c}{2}\right)+\right. \\ &\sum_m (B_{rn}\lambda_{am}-B_{\theta n}\lambda_{bm})\frac{np}{np+mQ_s}\sin\left[(np+mQ_s)\frac{\gamma_c}{2}\right]+ \\ &\left.\sum_m (B_{rn}\lambda_{am}+B_{\theta n}\lambda_{bm})\frac{np}{np-mQ_s}\sin\left[(np-mQ_s)\frac{\gamma_c}{2}\right]\right\}\sin[n(p\omega_{rm}t-\beta_0)] \end{aligned} \tag{4.10}$$

in the case when $\theta_{s0} = 0$ and

$$\begin{aligned} E_{phase}(t) &= N_s\omega_{rm}l_aR\sum_n k_{dn}\left\{\lambda_0 B_{rn}2\sin\left(np\frac{\gamma_c}{2}\right)+\right. \\ &\sum_m (B_{rn}\lambda_{am}-B_{\theta n}\lambda_{bm})\frac{np}{np+mQ_s}\sin\left[(np+mQ_s)\frac{\gamma_c}{2}\right]\cos(m\pi)+ \\ &\left.\sum_m (B_{rn}\lambda_{am}+B_{\theta n}\lambda_{bm})\frac{np}{np-mQ_s}\sin\left[(np-mQ_s)\frac{\gamma_c}{2}\right]\cos(m\pi)\right\} \\ &\sin[n(p\omega_{rm}t-\beta_0)] \end{aligned} \tag{4.11}$$

in the case when $\theta_{s0} = \frac{\pi}{Q_s}$. The angle β_0 is equal to zero for phase A, $2\pi/3$ for phase B and $4\pi/3$ for phase C.

For the six pole surface PM motor analyzed in the previous chapters the line-to-line back emf waveform has been calculated analytically and numerically using the FE method for the cases of radial and parallel magnetization. The motor has 36 slots with coil pitch equal to five slot pitches. Since the coil pitch is an odd number, equation (4.10) has been used to calculate the back emf. The waveforms in Fig. 4.1 show very good agreement between the results obtained analytically and numerically.

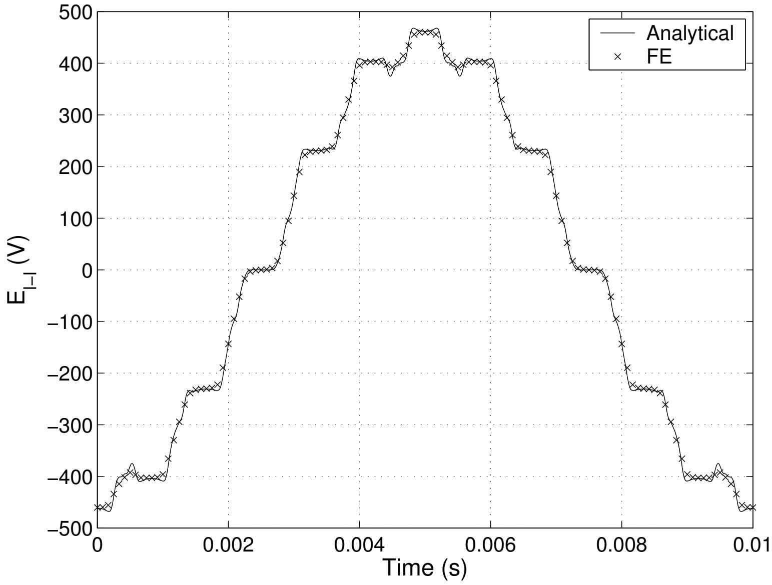

(a)

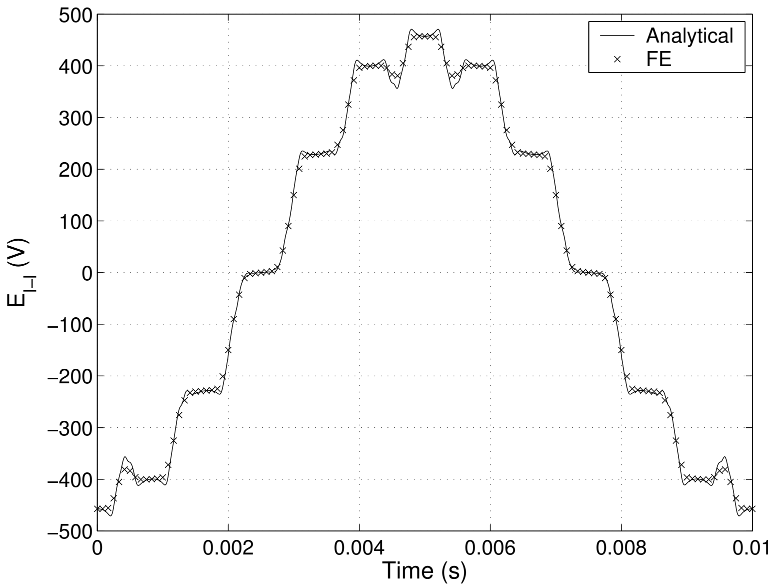

(b)

Fig. 4.1 Line-to-line back emf waveform calculated analytically and numerically: (a) radial magnetization, (b) parallel magnetization

Chapter 5

Calculation of the End Winding Leakage Inductance

The end winding leakage inductance is a part of the total leakage inductance of the phase winding. In the core region the coils are located in the slots which, with the assumption that iron is infinitely permeable, makes it easier to predict the distribution of the leakage flux and calculate the leakage inductance. The end winding region is more difficult to analyze because its magnetic circuit is entirely in the air and its winding structure is often characterized by complex three-dimensional geometry of the coils. An additional difficulty is the effect that adjacent coils and phases have on each other.

The most accurate approach to the end winding leakage inductance calculation would be to use the 3-D finite element method. The main problem with the 3-D FE method is the fact that the drawing of a complex 3-D geometric structure, mesh generation and solution of a very large system of equations are extremely time consuming. This is the main obstacle for practical utilization of the 3-D FE method for the end winding leakage inductance calculation in the design stage, especially if optimization is involved. The analytical approach is the remaining alternative.

There are different closed form analytical solutions that can be found in literature [74–76]. One of the major problems of these solutions is that they have been derived for an assumed geometric shape of the end coil which may not be applicable for all types of windings and all types of machines with different power ratings. Therefore a more flexible method has been used in this thesis which models the end coil as a set of serially connected straight filaments. This allows one to define the end coil geometry of an arbitrary shape and still calculate the inductance in a unique manner.

The mutual inductance between any two coils in the end region is calculated by adding the contributions of all possible pairs of filaments in both coils. The method has been described in detail in [77, 78] for the case of a turbogenerator with double-layer involute winding. It has been modified and adapted in this thesis to be used for a single-layer end winding structure typical for small permanent magnet motors. The method also takes into account the influence of the iron core by applying the method of images. Some assumptions on the magnetic properties of the core and the geometry of the end region are necessary to simplify the problem.

The following assumptions are made:

- The permeability of the iron core is constant,
- The iron core surface extends infinitely and fills the entire half-space,
- The influences of slots, air gap and rotor shaft are neglected,
- The coils are represented by infinitely thin conductors.

The principle model of the end coil is shown in Fig. 5.1(a). This model can be constructed out of the circuits shown in Fig. 5.1(b) and Fig. 5.1(c). The field due to the current in the circuit in Fig. 5.1(c) can be determined from that circuit and its mirror image (Fig. 5.1(d)). The mirror image of the circuit in Fig. 5.1(b) is identical to its original. The superposition of circuits shown in Fig. 5.1(b) and Fig. 5.1(d) yields the final circuit (Fig. 5.1(e)). The current that flows in the mirror image of the circuit in Fig. 5.1(c) is determined by the permeability of the iron and is calculated according to

$$I' = \frac{\mu_r - 1}{\mu_r + 1} I \tag{5.1}$$

where μ_r is the relative permeability of iron and I is the circuit current.

Two end coils are shown in Fig. 5.2 in a simplified manner. The influence of iron has been replaced by the image of the coil. Therefore, the mutual inductance of the two coils can be written in the form

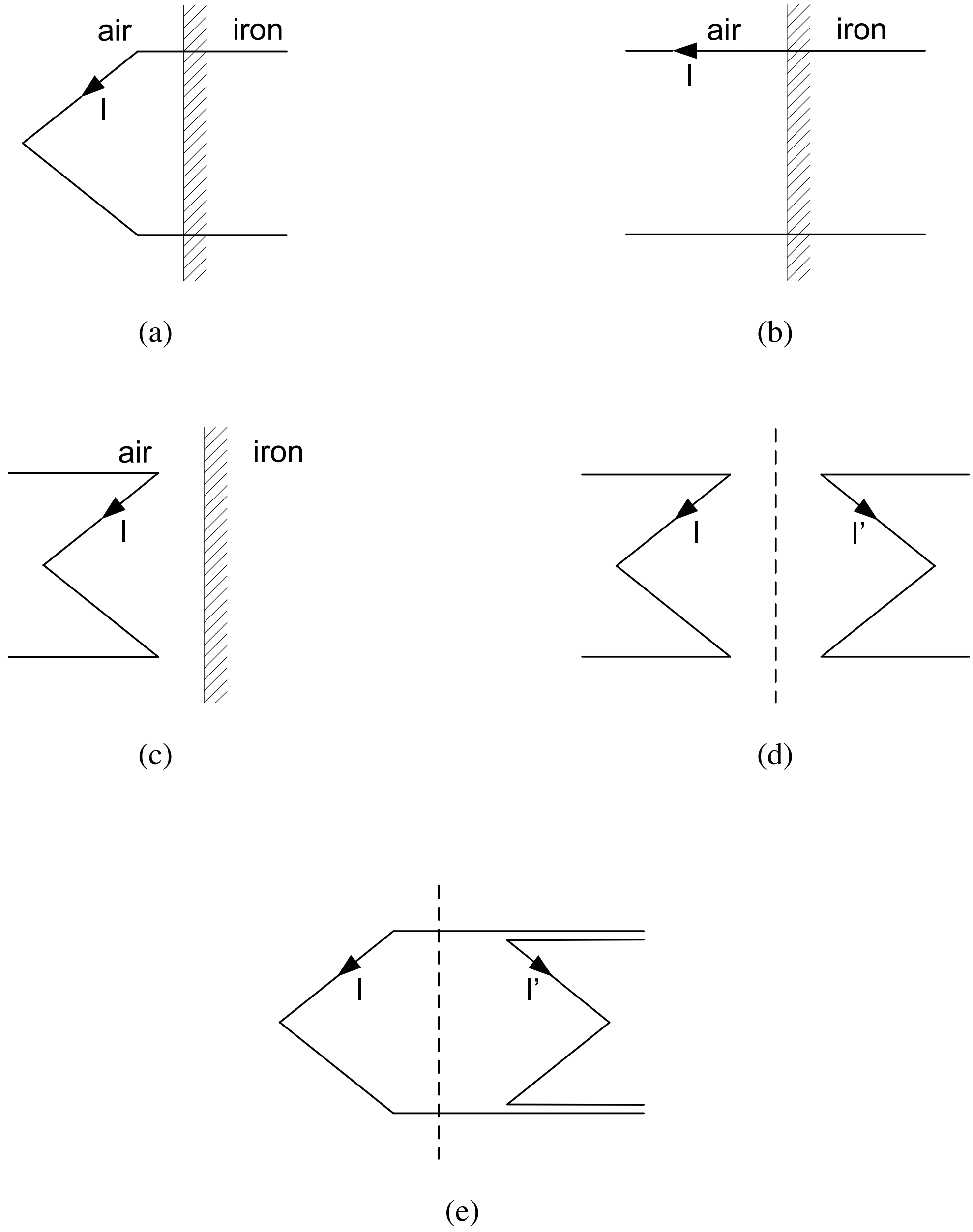

Fig. 5.1 Principle model for calculation of the mutual inductance of two coils

$$M = \frac{\mu_0}{4\pi I}\int_{ABCDE}\left[I\int_{GIJKM}\frac{\mathrm{d}\vec{l_1}\mathrm{d}\vec{l_2}}{r} + I'\int_{GPM}\frac{\mathrm{d}\vec{l_1}\mathrm{d}\vec{l_2}}{r} + (I+I')\left(\int_{\frac{FG}{F\to\infty}}\frac{\mathrm{d}\vec{l_1}\mathrm{d}\vec{l_2}}{r} + \int_{\frac{MN}{F\to\infty}}\frac{\mathrm{d}\vec{l_1}\mathrm{d}\vec{l_2}}{r}\right)\right] \quad (5.2)$$

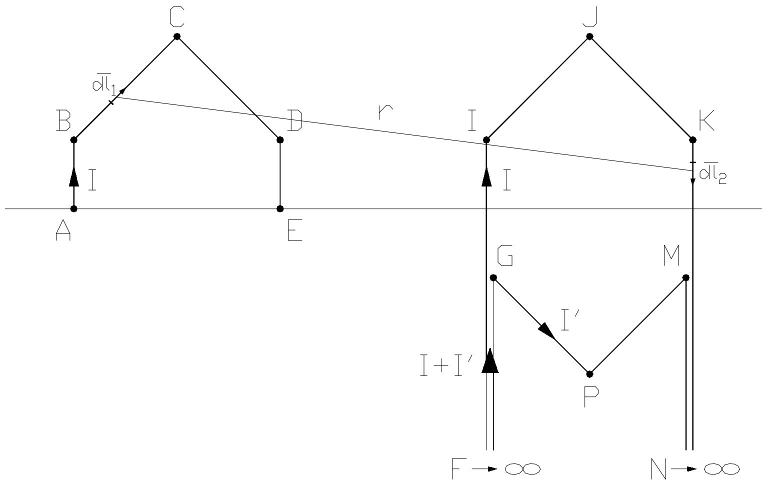

Fig. 5.2 Method of images applied to the end coil

The three-dimensional contour of the end coil is replaced by an arbitrary number of straight filaments depending on the desired accuracy of the geometric model of the coil. The integrals in (5.2) are Neumann integrals of the form

$$N = cos\varphi\int_A^B \mathrm{d}l_1\int_a^b\frac{\mathrm{d}l_2}{r} \quad (5.3)$$

which are solved for all possible combinations of straight filaments in both coils. This integral is based on the integration of the magnetic vector potential due to the current in one coil along the contour of the other coil and represents the flux linkage. The angle φ in (5.3) is the angle between the directional vectors of two straight lines in 3-D space. The general solution of the Neumann integral for two straight filaments in an arbitrary position relative to each other in space has been first published by Campbell [79]. This has been extended by the calculation of the Neumann integral for one finite and two semi-infinite antiparallel filaments in [77]. The results are given in the Appendix.

For the purpose of the mutual inductance calculation the coils are represented by infinitely thin wires with an assumption that all the coil turns are concentrated in one filament. With that assumption the mutual inductance can be evaluated using Neumann integrals. However, when the self inductance is evaluated, the finite dimensions of the coil are assumed. The portion of the coil self inductance due to the flux linkage inside the wire has been approximated using the expression for the internal inductance of an infinitely long circular wire

$$L_{csi} = \frac{\mu_0}{8\pi} l_c \tag{5.4}$$

where l_c is the length of the coil (central filament). The self inductance due to the flux linkage outside the wire requires the knowledge of the flux linkage from the surface of the conductor to infinity. Since the field at infinity is zero, the calculation of this portion of the self inductance basically reduces down to calculation of the Neumann integral between two parallel lines of length l_c, separated by the distance of r_c, where r_c is the radius of the circular conductor. Since the filaments in the end coil are not all parallel, the self inductance due to the flux linkage outside the coil wire is calculated by adding the Neumann integrals for all combinations of filaments along the contours $1-2-3-4-5$ and $1'-2'-3'-4'-5'$ as shown in Fig. 5.3. The simple coil shape shown in Fig. 5.3 is only used to explain the principle of the inductance calculation. The actual coil shape that has been modelled for the case of a surface PM motor is quite different and contains more than four segments.

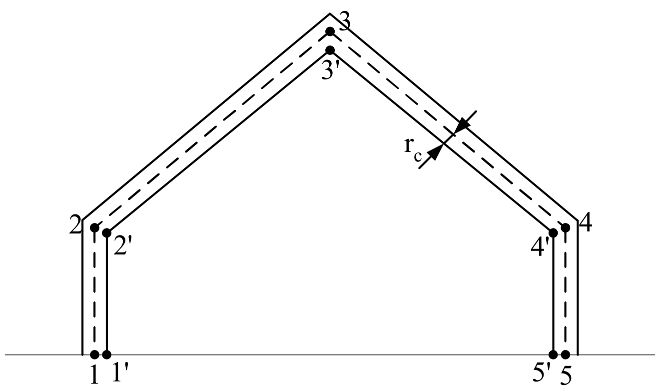

Fig. 5.3 Principle model of the end coil for calculation of the self inductance due to the flux linkage outside the wire

For each straight wire segment, the flux linkage is calculated due to the current flowing through it and due to the current flowing in all other segments. The total inductance of the coil is then equal to the sum of the self inductance and the mutual inductance with other coils.

The end winding leakage inductance has been calculated for the six pole surface PM motor analyzed in the previous chapters. The scheme of its two-layer short-pitched lap winding with six poles and 36 slots is shown in Fig. 5.4. The end coil has been modelled using 20 straight filaments as shown in Fig. 5.5. The coil pitch is equal to five slot pitches. The number of turns per coil is 14. The complete model of the end winding containing all the coils is shown in Fig. 5.6.

Very often the windings of small PM motors are built as single-layer overlapping or non-overlapping windings. For comparison, the full-pitched single-layer overlapping winding for the same motor has been modelled and shown in Figs. 5.7, 5.8 and 5.9. The number of turns per coil is 28.

The mutual inductances are calculated between the first coil and all other coils obtained by rotating every subsequent coil by an angle that corresponds to one slot pitch in the two-layer winding and two slot pitches in the single-layer overlapping winding. Thus, the mutual inductance between any two coils amounts to calculation of the mutual inductance of the first coil and another coil shifted by a certain number of slot pitches. The mutual inductance of the coils of one phase is calculated by adding the mutual inductance of the first coil and all the others that belong to the same phase. The obtained result is multiplied by two to take into consideration both sides of the machine. The mutual inductance of two phases contains the sum of mutual inductances of every coil from the first phase and every coil from the second phase. Due to symmetry, the mutual inductances of any two phases are equal. The total inductance per phase is equal to the sum of the self inductance and the mutual inductance with other two phases. With the existence of the parallel paths in the winding, the obtained result is divided by the squared number of paths (a_p^2) because the inductance per phase is proportional to the squared number of turns connected in series. The mutual inductances between the first coil and all other coils for different values of iron permeability are shown in Figs. 5.10 and 5.11 for the two-layer winding and the single-layer winding respectively. The curves obtained for $\mu_r = 0$ and $\mu_r = \infty$ represent the lower and upper bounds within which one would expect to find the actual value of the end winding inductance. Table 5.1 contains the values of the end winding

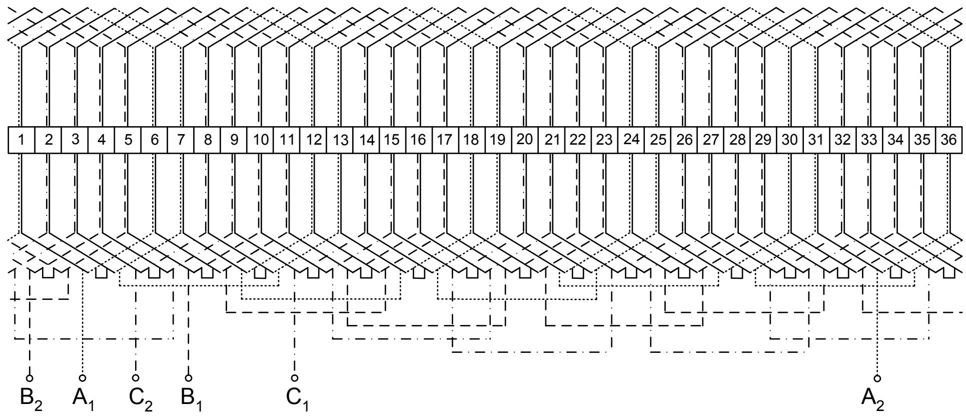

Fig. 5.4 Scheme of a two-layer, 36 slot, six pole lap winding

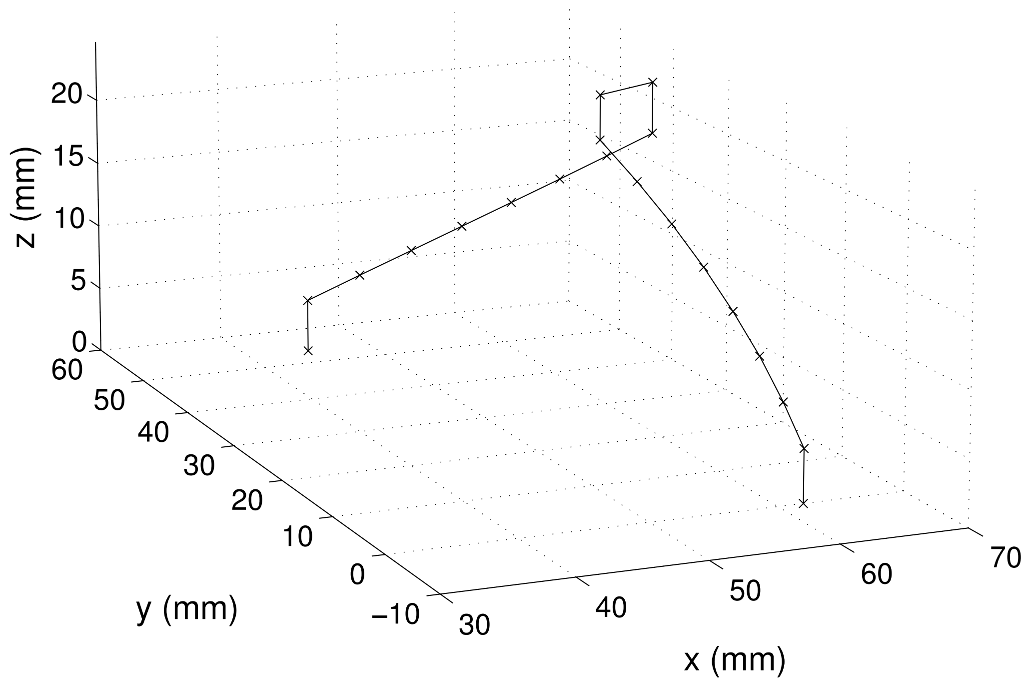

Fig. 5.5 3-D model of the end coil of a two-layer lap winding comprised of 20 straight filaments

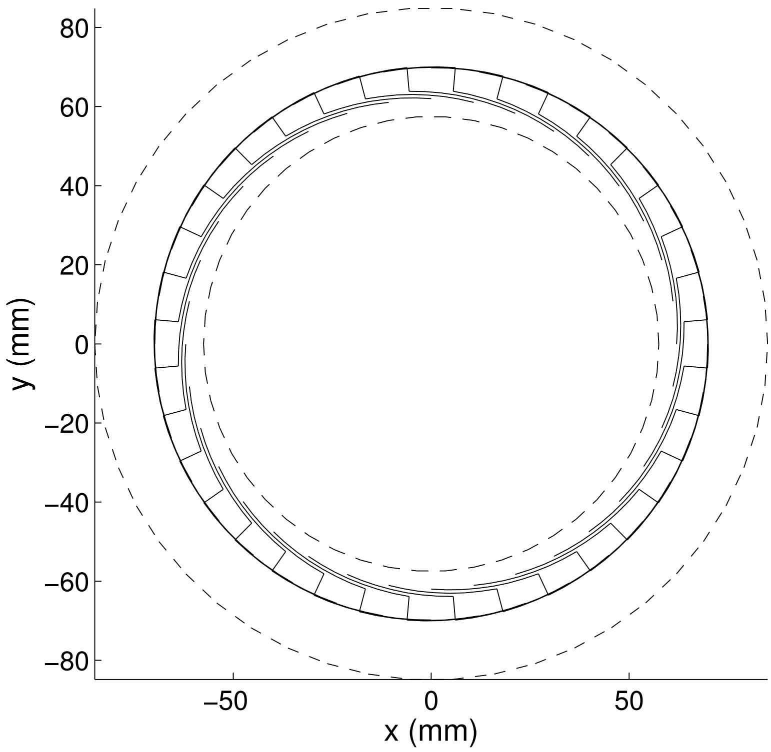

(a)

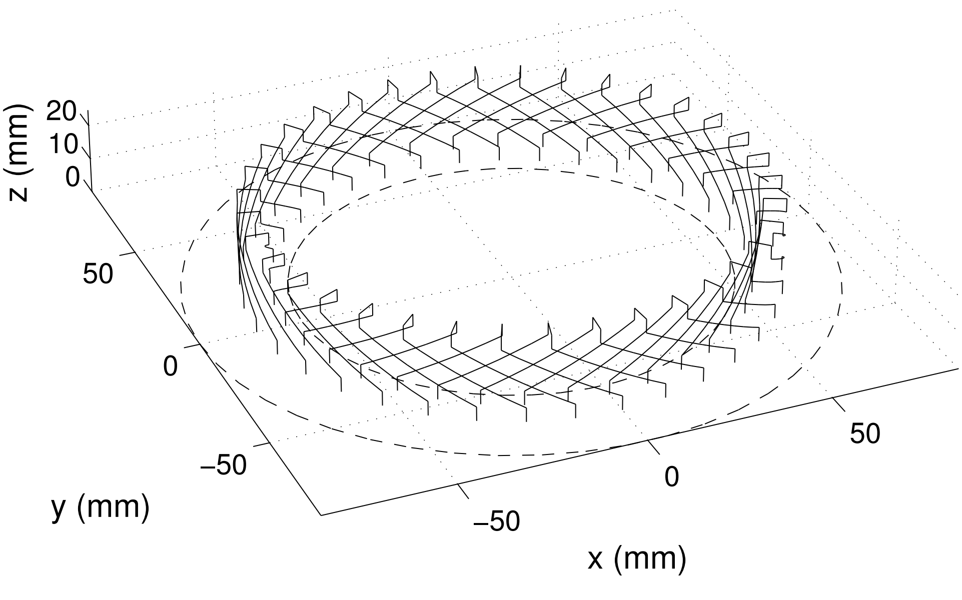

(b)

Fig. 5.6 Full 3-D model of the two-layer end winding of the six pole surface PM motor: (a) xy plane, (b) perspective view

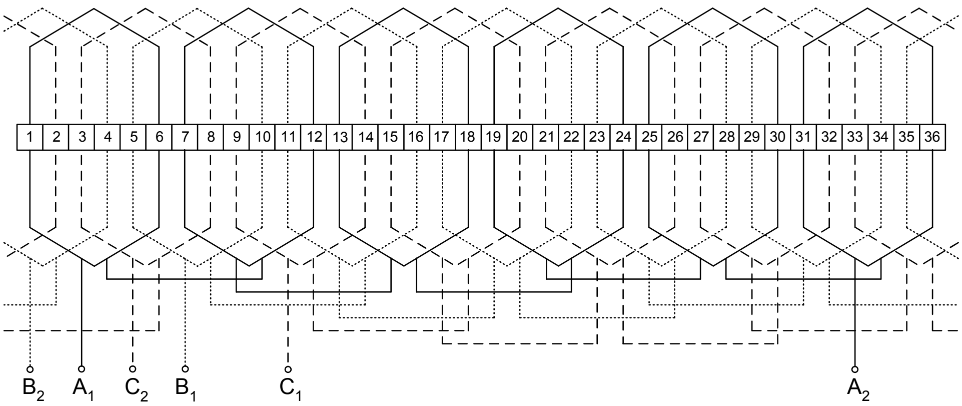

Fig. 5.7 Scheme of a single-layer, 36 slot, six pole overlapping winding

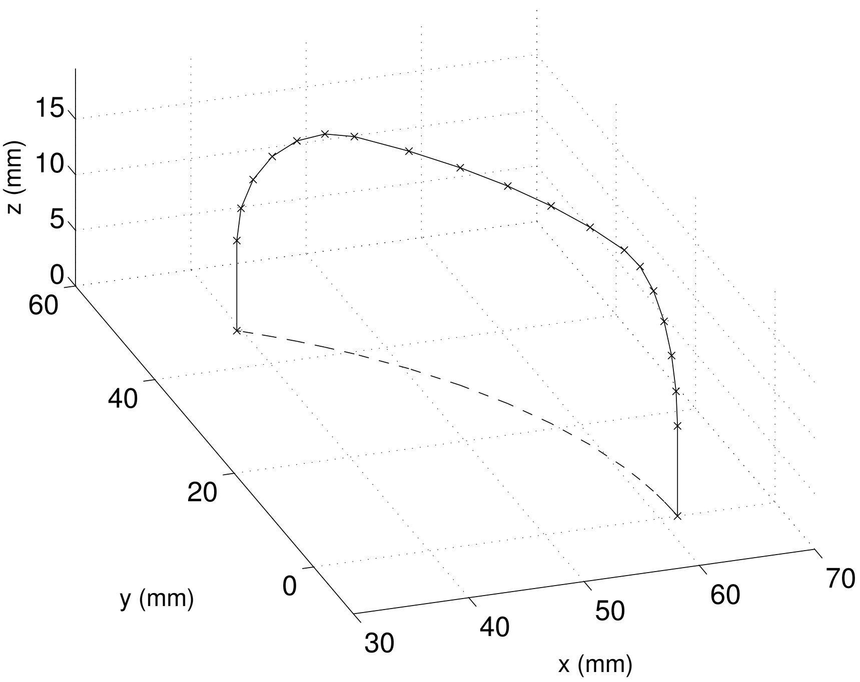

Fig. 5.8 3-D model of the end coil of a single-layer overlapping winding comprised of 20 straight filaments

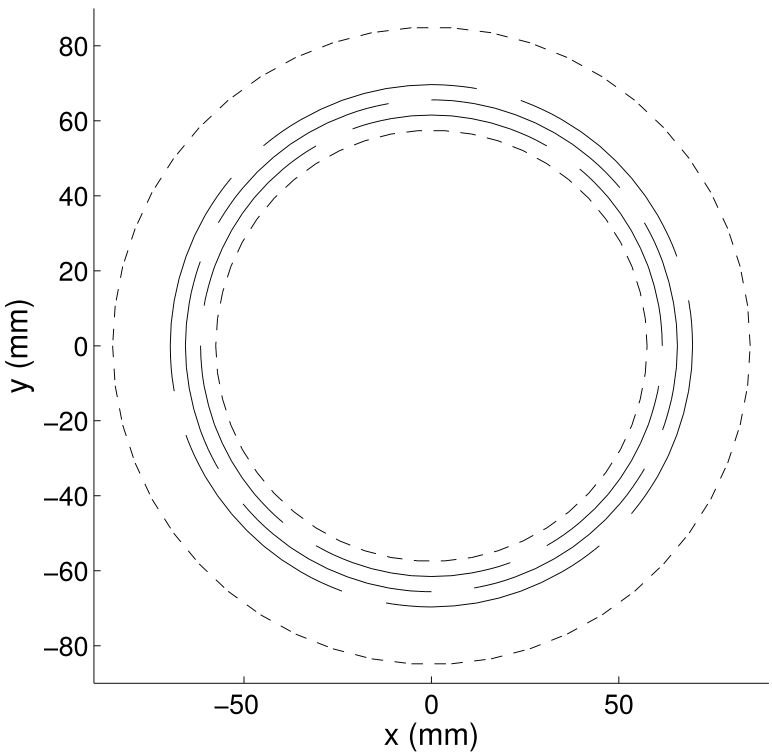

(a)

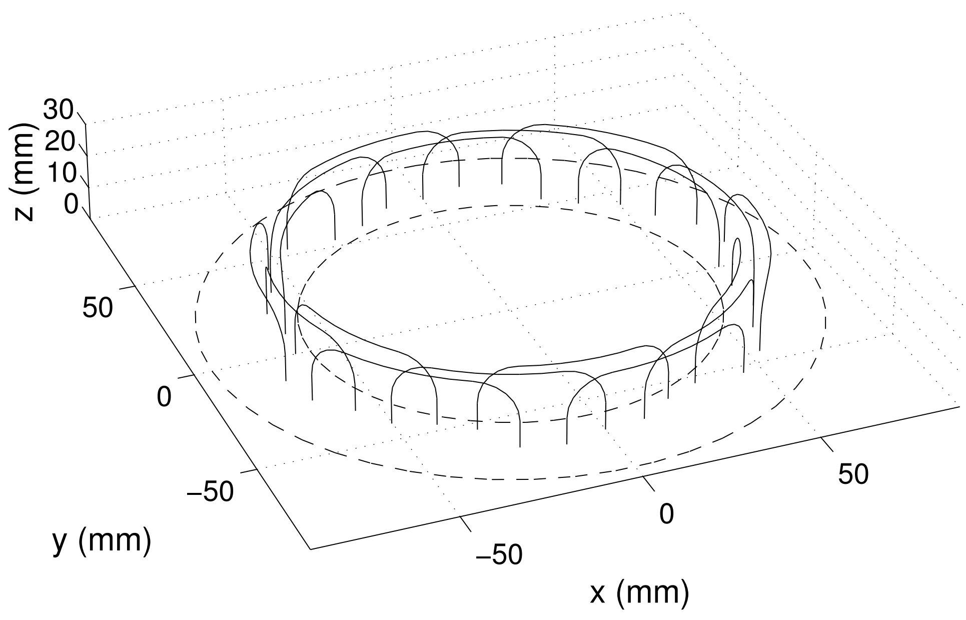

(b)

Fig. 5.9 Full 3-D model of the single-layer overlapping end winding of the six pole surface PM motor. (a) XY plane, (b) Perspective view leakage inductance for the two windings calculated for different values of relative permeability of iron. When $\mu_r = 0$, it is assumed that the iron is infinitely conductive and impermeable. When $\mu_r = 1$, the influence of iron is neglected. Finally, when $\mu_r = \infty$, it is assumed that the iron is infinitely permeable and infinitely resistive. For calculation purposes, infinity is replaced by the value of 10^9 for the relative permeability.

Table 5.1 End winding leakage inductance for different values of relative iron permeability

Relative permeability of iron core μ_r	Self inductance of one phase L_{sew} [mH]	Mutual inductance between two phases M_{ew} [mH]	Total leakage inductance $L_{ew} = L_{sew} - M_{ew}$ [mH]
Two-layer winding			
0	0.418	-0.077	0.495
1	0.475	-0.103	0.578
∞	0.532	-0.129	0.661
Single-layer winding			
0	0.755	-0.093	0.848
1	0.791	-0.113	0.904
∞	0.826	-0.133	0.959

It can be noticed in Table 5.1 that the mutual inductance between two phases relative to the self inductance of one phase is significantly smaller than in the core region where it is equal to the negative one half of the phase self inductance for the fundamental component of the flux if the core leakage and saturation are neglected.

The leakage inductance of the two-layer winding is somewhat lower which can be attributed to the fact this winding is more distributed around the perimeter than the single-layer winding. Each of the two-layer coils has half as many turns as the single-layer coil. Hence the self inductance per coil is lower, but there are twice as many coils. In the case of a perfect magnetic coupling and identical shapes of the coils, these two windings would have the same inductance. However, in

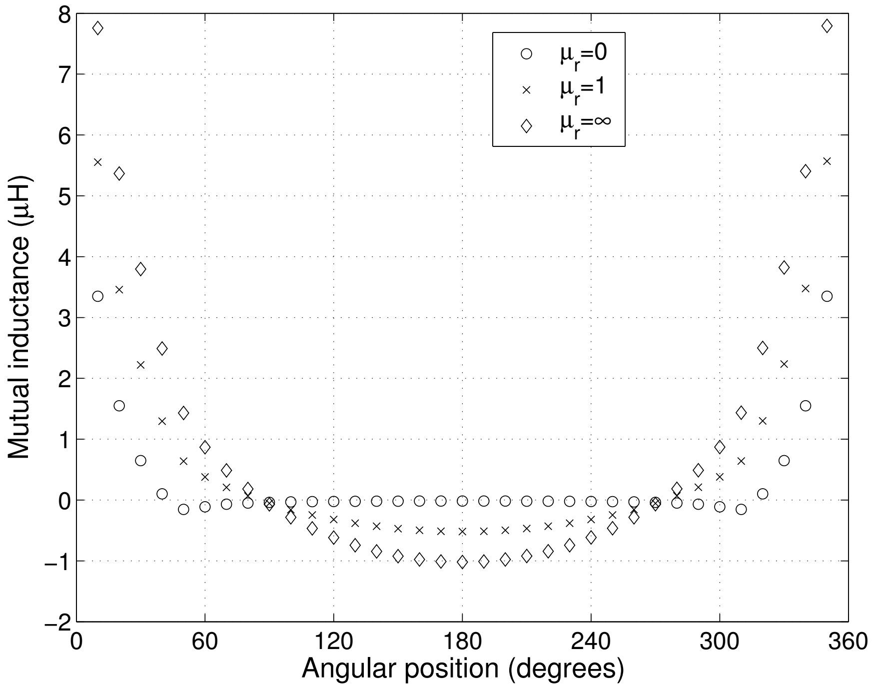

Fig. 5.10 Mutual inductance between two end coils as a function of relative coil positions for the two-layer winding

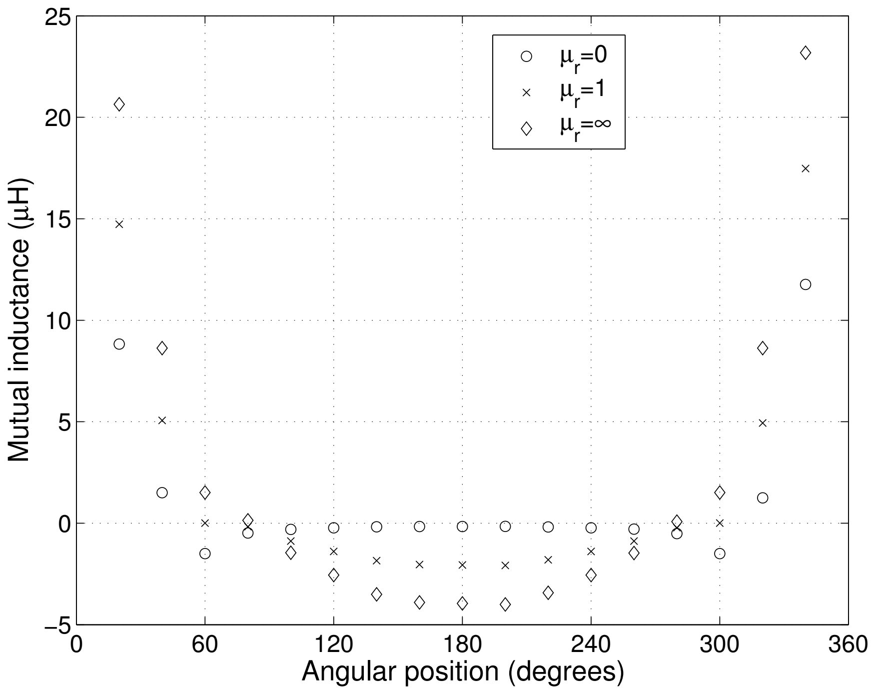

Fig. 5.11 Mutual inductance between two end coils as a function of relative coil positions for the single-layer winding

the two-layer winding the mutual inductances between the coils of one phase do not contribute to the self inductance of the phase winding as much as the additional turns of each single-layer coil contribute to the self inductance of the single-layer winding. Unlike the self inductance, the mutual inductance between different phase windings does not differ significantly.

The relative permeability of the iron core also affects the value of the end winding leakage inductance. For higher values of μ_r the core is more permeable which increases the leakage inductance. In an actual motor, the core, the shaft and the frame would act more as a conductive screen than as a permeable, highly resistive surface. Therefore, it is reasonable to take the value of the end winding leakage inductance calculated with $\mu_r = 0$ as an actual motor parameter.

It is useful to compare the end winding leakage inductance for the two-layer winding from Table 5.1 with the results calculated using formulas given by Liwschitz-Garik [75] and Lipo [74]. According to [75] the end winding leakage inductance is given by

$$L_{ew} = 2\mu_0 \frac{N_s^2}{p} k_{p1}^2 k_{w1}^2 2.4 \left(l_{e2} + \frac{l_{e1}}{2} \right) \tag{5.5}$$

where N_s is the number of turns per phase connected in series, p is the number of pole pairs, k_{p1} is the pitch factor, k_{d1} is the distribution factor and l_{e1} and l_{e2} are dimensions according to Fig. 5.12. In his formulas Lipo [74] also takes into account the effect of the iron core and replaces the core with an image of the coil. However, his model of the end coil has a simple geometry and it is assumed that the entire end coil lies in one plane.

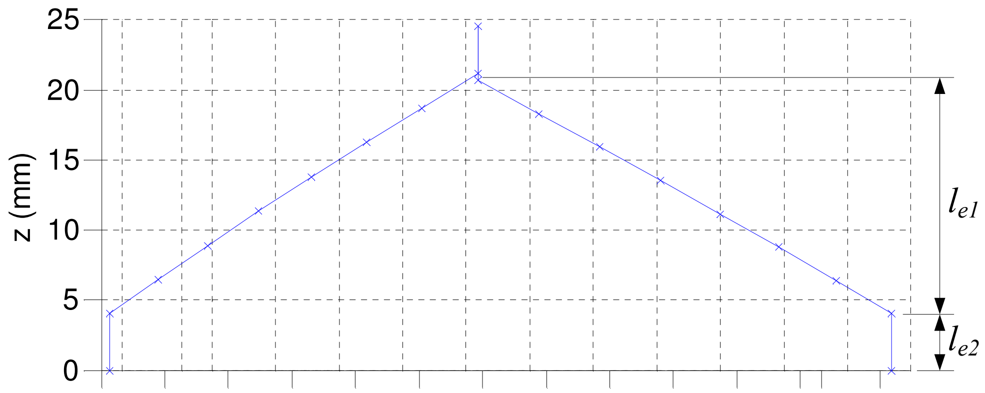

Fig. 5.12 Model of the end coil used in analytical formulas by Liwschitz-Garik and Lipo

The end winding leakage inductance calculated using these two alternative analytical approaches is given in Table 5.2. The values in Table 5.2 are somewhat higher than the ones given in Table 5.1. Nevertheless, they are in the same order of magnitude. A 3-D FE model of the end winding region should be used to ascertain which of the these results is the most accurate.

Table 5.2 End winding leakage inductance calculated using alternative analytical formulas

	Leakage inductance L_{ew} [mH]
Liwschitz-Garik	0.716
Lipo	0.944

Chapter 6

Calculation of Inductances in Surface PM Motors

The armature winding air gap field solution derived in Chapter 3 can be used to calculate the phase winding self and mutual inductances based on integration of flux linkages. The phase winding self inductance is equal to the ratio of total flux linkage of the winding and the winding current. Due to symmetry it is sufficient to calculate the self inductance for only one phase (e.g. phase A) since inductances for the other two phases are equal to the phase A inductance. The same is valid for different combinations of mutual inductance between the phases.

The total flux linkage of phase A is equal to the sum of the flux linkages of each phase A coil due to the current that flows through that coil and the currents that flow through all other coils of phase A. From (3.42) it follows that the total flux linkage of phase A due to current i_A is

$$\begin{aligned}\psi_a(t) = {} & l_a R N_c^2 \sum_{j=1}^{Q_{coil}} \mathrm{sgn}_{Aj} \int_{-\frac{\gamma_c}{2}+\alpha_{Aj}}^{\frac{\gamma_c}{2}+\alpha_{Aj}} \sum_{i=1}^{Q_{coil}} \sum_{n=1}^{N_a} B_{arn}(R)\lambda_{g0} i_A(t) \mathrm{sgn}_{Ai} \cos[n(\theta-\alpha_{Ai})]\mathrm{d}\theta + \\ & l_a R N_c^2 \sum_{i=1}^{Q_{coil}} \mathrm{sgn}_{Aj} \int_{-\frac{\gamma_c}{2}+\alpha_{Aj}}^{\frac{\gamma_c}{2}+\alpha_{Aj}} \sum_{i=1}^{Q_{coil}} \sum_{n=1}^{N_a} \sum_{h=1}^{\infty} B_{arn}(R)\lambda_{gh} i_A(t) \mathrm{sgn}_{Ai} \\ & \cos[n(\theta-\alpha_{Ai})]\cos[2hp(\theta-\alpha)]\mathrm{d}\theta \end{aligned} \tag{6.1}$$

Knowing that $L_a = \frac{\psi_a(t)}{i_a(t)}$ and after solving the integrals in (6.1), the expression for the phase A self inductance is

$$
\begin{aligned}
L_a \;=\;& l_a R N_c^2 \sum_{j=1}^{Q_{coil}} \sum_{i=1}^{Q_{coil}} \sum_{n=1}^{N_a} B_{arn}(R)\lambda_{g0}\frac{2}{n}\mathrm{sgn}_{Aj}\mathrm{sgn}_{Ai}\cos[n(\alpha_{Aj}-\alpha_{Ai})]\sin\left(n\frac{\gamma_c}{2}\right)+\\
& l_a R N_c^2 \sum_{j=1}^{Q_{coil}} \sum_{i=1}^{Q_{coil}} \sum_{n=1}^{N_a} \sum_{h=1}^{\infty} B_{arn}(R)\lambda_{gh}\mathrm{sgn}_{Aj}\mathrm{sgn}_{Ai}\left\{\frac{1}{n+2hp}\cos[n(\alpha_{Aj}-\alpha_{Ai})+\right.\\
& 2hp(\alpha_{Aj}-\alpha)]\sin\left[(n+2hp)\frac{\gamma_c}{2}\right]+\frac{1}{n-2hp}\cos[n(\alpha_{Aj}-\alpha_{Ai})-2hp(\alpha_{Aj}-\alpha)]\\
& \left.\sin\left[(n-2hp)\frac{\gamma_c}{2}\right]\right\} \qquad (6.2)
\end{aligned}
$$

In the case when $n = 2hp$, the term

$$\frac{1}{n-2hp}\sin\left[(n-2hp)\frac{\gamma_c}{2}\right]$$

in (6.2) should be replaced with $\frac{\gamma_c}{2}$. The first part of (6.2) represents the average phase A self inductance, while the second part is the saliency term dependent on the rotor position α. The second part is a consequence of taking into account the magnet relative permeance which is slightly higher than one. The saliency term is very small and can readily be neglected. Due to symmetry one has $L_a = L_b = L_c = L_{ss}$. Equation (6.2) does not take into account the slot leakage inductance. Therefore, it needs to be calculated separately and added to the results in (6.2) together with the end winding leakage inductance L_{ew} from Chapter 5 to obtain the total self inductance. A classical approach is used for slot leakage inductance calculation which is based on the assumption that the core is infinitely permeable and that the flux lines which cross the slot are horizontal. The slot shape commonly used in PM motors is shown Fig. 6.1. With a general assumption that one has a two-layer short pitched winding, the slot leakage inductance per one phase is given by [74]

$$L_{sl} = \mu_0 \frac{Q_s}{3a_p^2} N_c^2 l_a (p_T + p_B + k_{sl} p_{TB}) \qquad (6.3)$$

where p_T and p_B are the specific permeances of the top and bottom coil sides, p_{TB} is the specific permeance corresponding to mutual flux linkage between the top and bottom coil sides and k_{sl} is the coefficient which takes into account the phase shift between the phase belts due to short pitching of the coils. The coefficient k_{sl} is defined as [74]

$$k_{sl} = 3\frac{yc}{\frac{Q_s}{2p}} - 1 \qquad (6.4)$$

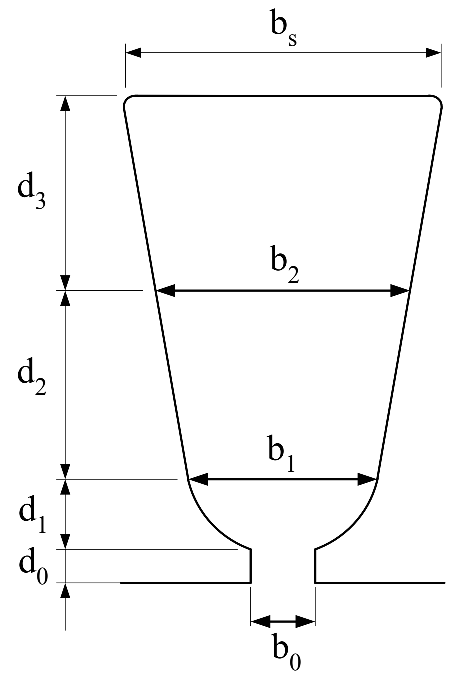

Fig. 6.1 Slot shape used for calculation of the slot leakage inductance

where y_c is the coil pitch expressed as the number of slot pitches. The specific permeances for the slot shape in Fig. 6.1 are given by [74, 80]

$$\begin{aligned} p_B &= \frac{d_3}{b_s}k_{t1} + \frac{d_2}{b_2-b_1}\ln\frac{b_2}{b_1} + 0.1424 + 0.5\arcsin\sqrt{1-\left(\frac{b_o}{b_1}\right)^2} + \frac{d_o}{b_o} \\ p_T &= \frac{d_2}{b_2}k_{t2} + 0.1424 + 0.5\arcsin\sqrt{1-\left(\frac{b_o}{b_1}\right)^2} + \frac{d_o}{b_o} \\ p_{TB} &= \frac{d_2}{b_2}k_{t12} + 0.1424 + 0.5\arcsin\sqrt{1-\left(\frac{b_o}{b_1}\right)^2} + \frac{d_o}{b_o} \end{aligned} \tag{6.5}$$

where

$$\begin{aligned} k_{t1} &= \frac{4t_1^2 - t_1^4 - 4\ln t_1 - 3}{4(1-t_1)(1-t_1^2)^2} \quad , \quad t_1 = \frac{b_2}{b_s} \\ k_{t2} &= \frac{4t_2^2 - t_2^4 - 4\ln t_2 - 3}{4(1-t_2)(1-t_2^2)^2} \quad , \quad t_1 = \frac{b_1}{b_2} \\ k_{t12} &= \frac{t_{12}^2 - 2\ln t_{12} - 1}{2(1-t_{12})(1-t_{12}^2)} \quad , \quad t_1 = \frac{b_1}{b_2} \end{aligned}$$

In the case of mutual inductance between phases A and B, the flux linkage of phase A is equal to the sum of the flux linkages of each phase A coil due to the current that flows in all the coils of phase B.

$$\begin{aligned}\psi_{ab}(t) &= l_a R N_c^2 \sum_{j=1}^{Q_{coil}} \mathrm{sgn}_{Aj} \int_{-\frac{\gamma_c}{2}+\alpha_{Aj}}^{\frac{\gamma_c}{2}+\alpha_{Aj}} \sum_{i=1}^{Q_{coil}} \sum_{n=1}^{N_a} B_{arn}(R)\lambda_{g0} i_B(t) \mathrm{sgn}_{Bi} \cos[n(\theta-\alpha_{Bi})]\mathrm{d}\theta + \\ & l_a R N_c^2 \sum_{i=1}^{Q_{coil}} \mathrm{sgn}_{Aj} \int_{-\frac{\gamma_c}{2}+\alpha_{Aj}}^{\frac{\gamma_c}{2}+\alpha_{Aj}} \sum_{i=1}^{Q_{coil}} \sum_{n=1}^{N_a} \sum_{h=1}^{\infty} B_{arn}(R)\lambda_{gh} i_B(t) \mathrm{sgn}_{Bi} \\ & \cos[n(\theta-\alpha_{Bi})]\cos[2hp(\theta-\alpha)]\mathrm{d}\theta \end{aligned} \tag{6.6}$$

After integrating (6.6) the mutual inductance is

$$\begin{aligned}L_{ab} &= l_a R N_c^2 \sum_{j=1}^{Q_{coil}} \sum_{i=1}^{Q_{coil}} \sum_{n=1}^{N_a} B_{arn}(R)\lambda_{g0} \frac{2}{n} \mathrm{sgn}_{Aj}\mathrm{sgn}_{Bi} \cos[n(\alpha_{Aj}-\alpha_{Bi})] \sin\left(n\frac{\gamma_c}{2}\right) + \\ & l_a R N_c^2 \sum_{j=1}^{Q_{coil}} \sum_{i=1}^{Q_{coil}} \sum_{n=1}^{N_a} \sum_{h=1}^{\infty} B_{arn}(R)\lambda_{gh} \mathrm{sgn}_{Aj}\mathrm{sgn}_{Bi} \left\{ \frac{1}{n+2hp} \cos[n(\alpha_{Aj}-\alpha_{Bi}) + \right. \\ & +2hp(\alpha_{Aj}-\alpha)] \sin\left[(n+2hp)\frac{\gamma_c}{2}\right] + \frac{1}{n-2hp} \cos[n(\alpha_{Aj}-\alpha_{Bi}) - 2hp(\alpha_{Aj}-\alpha)] \\ & \left. \sin\left[(n-2hp)\frac{\gamma_c}{2}\right] \right\} \end{aligned} \tag{6.7}$$

The expression for the mutual inductance also consists of the constant term which is the average mutual inductance and the saliency term dependent on the rotor position. The saliency term can readily be neglected. Due to symmetry one has $L_{ab} = L_{bc} = L_{ca} = L_{sm}$.

Since phases are mutually coupled, their total flux linkages are

$$\begin{aligned}\psi_a &= (L_{ew} + L_{sl} + L_{ss})i_A + L_{sm}i_B + L_{sm}i_C \\ \psi_b &= L_{sm}i_A + (L_{ew} + L_{sl} + L_{ss})i_B + L_{sm}i_C \\ \psi_c &= L_{sm}i_A + L_{sm}i_B + (L_{ew} + L_{sl} + L_{ss})i_C \end{aligned} \tag{6.8}$$

Since in a Y connected three phase machine without a neutral return

$$i_A + i_B + i_C = 0$$

the flux linkages in (6.8) become

$$\psi_a = (L_{ew} + L_{sl} + L_{ss} - L_{sm})i_A$$

$$\begin{aligned}\psi_b &= (L_{ew} + L_{sl} + L_{ss} - L_{sm})i_B \\ \psi_c &= (L_{ew} + L_{sl} + L_{ss} - L_{sm})i_C\end{aligned} \tag{6.9}$$

The total inductance per phase is then

$$L_s = L_{ew} + L_{sl} + L_{ss} - L_{sm} \tag{6.10}$$

Note that L_{ss} and L_{sm} already include harmonic leakage inductance because they have been derived by integrating the air gap flux density with all the harmonics included and not only the fundamental.

The analytically and numerically calculated inductances for the six pole surface PM motor previously used in the analysis have been compared in Table 6.1. Inductances L_{ss} and L_{sm} have been calculated using only the average terms from (6.2) and (6.7) since the saliency terms are negligible. When the self inductance is calculated using the FE method, the slot leakage inductance is already included. Therefore, the comparison has to be made between the FE result and the sum of analytically calculated L_{ss} and L_{sl} as indicated in Table 6.1.

Table 6.1 Inductances of the six pole surface PM motor calculated analytically and numerically

<table>
<tr><th></th><th>L_{ew} [mH]</th><th>L_{sl} [mH]</th><th>L_{ss} [mH]</th><th>L_{sm} [mH]</th><th>L_s [mH]</th></tr>
<tr><td>Analytical</td><td>0.495</td><td>1.207</td><td>9.608</td><td>-4.25</td><td>15.56</td></tr>
<tr><td>FE</td><td>–</td><td colspan="2">10.59</td><td>-4.33</td><td></td></tr>
</table>

Chapter 7

Calculation of Losses in Surface PM Motors

The prediction of losses in the design stage of any electrical machine is one the basic requirements, especially when optimization is involved. In the case of surface PM motors the emphasis is put on high efficiency, high torque density, and low torque ripple, which are all conflicting requirements. The requirement for high torque density naturally leads to designs of reduced size with high flux densities in the stator and rotor core. High flux densities in turn lead to higher core losses and lower efficiency. The task of the designer is to find a good balance between these conflicting requirements. Another important issue is the maximum temperature of the winding insulation and the temperature of the magnets which need to be limited in all regimes of operation.
The main types of losses in PM motors are winding losses, core losses, magnet losses and mechanical losses due to windage and friction.

7.1 Winding Losses

The copper losses in the armature winding can be calculated with the knowledge of the armature rms current and the winding resistance. The resistance is given by

$$R_a = \frac{1}{\sigma} \frac{N_s}{a_p} \frac{l_c}{A_c} \tag{7.1}$$

where σ is the conductivity of the coil material, N_s is the number of turns per phase connected in series , a_p is the number of parallel paths, l_c is the mean length of the coil and A_c is the cross-sectional area of one conductor in the coil. The conductivity of copper at 75° C, which is $47.6 \cdot 10^6$ S/m, is commonly used for calculation of the resistance.

The mean length of the coil is

$$l_c = 2l_a + 2l_{ec} \tag{7.2}$$

where l_a is the core stack length and l_{ec} is the length of the end coil on one side of the machine. The end coil length l_{ec} is calculated by adding the lengths of the straight filaments which have been used in Chapter 5 to model the three dimensional shape of the coil.

The total winding losses are calculated according to

$$P_a = 3I^2R_a \tag{7.3}$$

where I is the rms value of the armature current.

For the analyzed six pole surface PM motor with $Q_s = 36$, $N_c = 14$, $a_p = 1$, $A_c = 1.33\ \mathrm{mm}^2$, $l_a = 90$ mm, $l_{ec} = 88.7$ mm the resistance per phase at 75° C is

$$R_a = \frac{1}{\sigma_{75}}\frac{N_s Q_s}{3a_p^2}\frac{2(l_a + l_{ec})}{A_c} = \frac{1}{47.6 \cdot 10^6}\frac{14 \cdot 36}{3 \cdot 1^2}\frac{2 \cdot (90 + 88.7) \cdot 10^{-3}}{1.33 \cdot 10^{-6}} = 0.96\ \Omega \tag{7.4}$$

With $I = 6.91$ A the total winding losses are

$$P_a = 3 \cdot 6.91^2 \cdot 0.96 = 137.5\ W \tag{7.5}$$

7.2 Core Losses

The variation of flux density in the stator teeth and yoke of PM motors is generally not sinusoidal. Therefore, the approach to core loss calculations based on the assumption that only fundamental component of the flux density exists is not valid [81–83]. For good estimation of core losses the effects of harmonics have to be taken into account. The general expression for core losses which considers the nonsinusoidal shape of the flux density variation is given by

$$P_c = k_h f B_m^{\alpha(B_m)} + \frac{k_e}{2\pi^2}\left(\frac{\mathrm{d}B}{\mathrm{d}t}\right)^2_{rms} \tag{7.6}$$

where k_h is the hysteresis loss coefficient, k_e is the eddy current loss coefficient, B_m is the peak value of the flux density waveform, $\alpha(B_m)$ is an exponent dependent on B_m and f is the frequency. Coefficients k_h, k_e and $\alpha(B_m)$ can be determined by curve fitting the data provided by manufacturers of the steel laminations. The basic procedure for the extraction of the core loss coefficients given by Hendershot and Miller [84] will be explained on an example of U.S. Steel M36, 29 Gauge steel lamination. The manufacturer provides information about core losses measured with sinusoidal fields at different frequencies and flux densities. Fig. 7.1 shows the core losses for three values of the flux density, i.e. 0.3 T, 0.5 T and 0.7 T, with the frequency ranging from 60 Hz to 200 Hz.

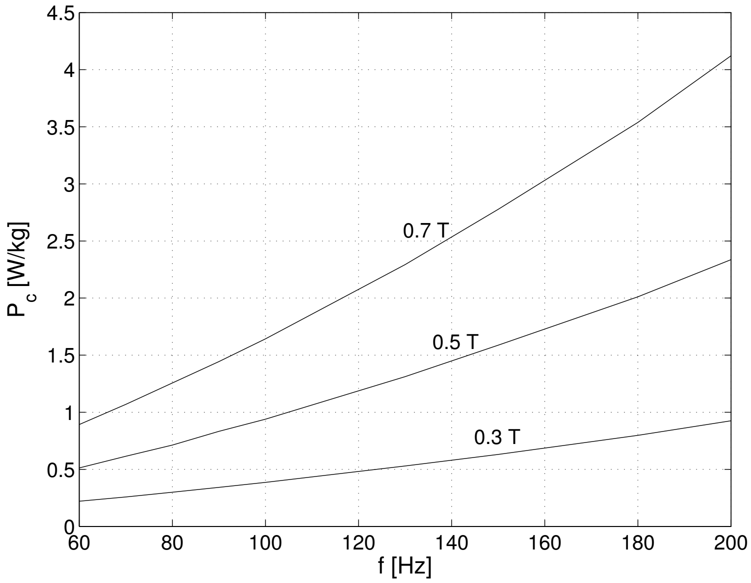

Fig. 7.1 Core losses for U.S. Steel M36, 29 Gauge steel laminations given as a function of frequency for three different values of flux density

In the case of sinusoidal fields the flux density is given by

$$B = B_m \sin(2\pi f t) \tag{7.7}$$

The derivative of its rms value is then

$$\left(\frac{\mathrm{d}B}{\mathrm{d}t}\right)_{rms} = \frac{2\pi f}{\sqrt{2}} B_m \tag{7.8}$$

Substituting (7.8) into (7.6) gives an expression for the core losses in the form

$$P_c = k_h f B_m^{\alpha(B_m)} + k_e f^2 B_m^2 \tag{7.9}$$

If $\alpha(B_m)$ is written in the form

$$\alpha(B_m) = a_h + b_h B_m \tag{7.10}$$

then (7.9) becomes

$$P_c = k_h f B_m^{a_h + b_h B_m} + k_e f^2 B_m^2 \tag{7.11}$$

The next step is to divide (7.11) by f which yields

$$\frac{P_c}{f} = k_h B_m^{a_h + b_h B_m} + k_e f B_m^2 \tag{7.12}$$

The data in Fig. 7.1 is then used to plot the graphs of $\frac{P_c}{f}$ for each of the three values of B_m. The resulting graphs are practically straight lines which can be expressed in the form

$$\frac{P_c}{f} = D + Ef \tag{7.13}$$

The coefficients D and E can be determined for each line using linear regression. The graphs of $\frac{P_c}{f}$, together with their approximations by straight lines, are shown in Fig. 7.2.

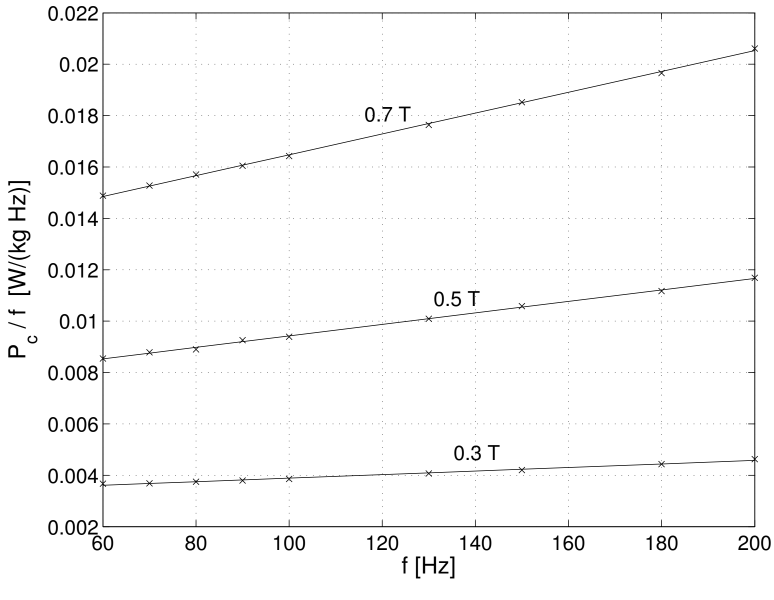

Fig. 7.2 Plots of $\frac{core\ \ losses}{freqency}$ for U.S. Steel M36, 29 Gauge steel laminations given as a function of frequency for three different values of flux density

Equations (7.12) and (7.13) can now be combined to determine the core loss coefficients. It is easy to recognize that

$$D \quad = \quad k_h B_m^{a_h + b_h B_m} \tag{7.14}$$

$$E = k_e B_m^2 \tag{7.15}$$

The three values of k_e can be determined directly from (7.15) for the three values of B_m. The final value can be taken as an average.

$$\begin{aligned} k_e &= \frac{1}{3}\left(\frac{E_1}{B_{m1}^2} + \frac{E_2}{B_{m2}^2} + \frac{E_3}{B_{m3}^2}\right) \\ &= \frac{1}{3}\left(\frac{7.669 \cdot 10^{-5}}{0.3^2} + \frac{8.944 \cdot 10^{-5}}{0.5^2} + \frac{8.280 \cdot 10^{-5}}{0.7^2}\right) \\ &= 8.298 \cdot 10^{-5}\,\frac{\mathrm{W}}{\mathrm{kgHz^2T^2}} \end{aligned} \tag{7.16}$$

The coefficients k_h, a_h and b_h can be determined by solving the system of linear equations which is formed by substituting D_1, D_2 and D_3 obtained for the three values of B_m into the logarithm of equation (7.14). The system of equations is then

$$\begin{bmatrix} 1 & \ln B_{m1} & B_{bm1} \ln B_{m1} \\ 1 & \ln B_{m2} & B_{bm3} \ln B_{m2} \\ 1 & \ln B_{m3} & B_{bm3} \ln B_{m3} \end{bmatrix} \begin{bmatrix} \ln k_h \\ a_h \\ b_h \end{bmatrix} = \begin{bmatrix} D_1 \\ D_2 \\ D_3 \end{bmatrix} \tag{7.17}$$

The system is solved for $\ln k_h$, a_h and b_h. The coefficient k_h is then simply

$$k_h = e^{\ln k_h} \tag{7.18}$$

The coefficients for $M36$ sheet steel calculated from (7.17) are

$$\begin{aligned} k_h &= 0.02264\,\frac{\mathrm{W}}{\mathrm{kgT^{\alpha(B_m)}Hz}} \\ a_h &= 1.582 \\ b_h &= 0.147\,\mathrm{T}^{-1} \end{aligned}$$

The flux density waveforms in the stator and rotor core need to be calculated next so that B_m and $\left(\frac{\mathrm{d}B}{\mathrm{d}t}\right)_{rms}$ can be determined and used in (7.6) to calculate the core losses.

The flux density in the stator tooth can be determined from the waveform of the flux passing through the tooth. This flux can be calculated by integrating the radial component of the magnet field given by (4.3) within one slot pitch. Hence

$$\phi_{ts}(t) = l_a R \int_{-\frac{\pi}{Q_s}}^{\frac{\pi}{Q_s}} B_{sr}(R, \theta, t)\mathrm{d}\theta \tag{7.19}$$

The expression obtained after integration of (7.19) is

$$\begin{aligned}\phi_{ts}(t) \quad = \quad & l_a R \sum_n \left\{ \lambda_0 B_{rn} 2 \frac{1}{np} \sin\left(np\frac{\pi}{Q_s}\right) + \right. \\ & \sum_m (B_{rn}\lambda_{am} - B_{\theta n}\lambda_{bm}) \frac{1}{np + mQ_s} \sin\left[(np + mQ_s)\frac{\pi}{Q_s}\right] + \\ & \left. \sum_m (B_{rn}\lambda_{am} + B_{\theta n}\lambda_{bm}) \frac{1}{np - mQ_s} \sin\left[(np - mQ_s)\frac{\pi}{Q_s}\right] \right\} \cos(n\omega t)\end{aligned} \tag{7.20}$$

If $np = mQ_s$, the term

$$\frac{1}{np - mQ_s} \sin\left[(np - mQ_s)\frac{\pi}{Q_s}\right]$$

is replaced with $\frac{\pi}{Q_s}$.

The stator yoke flux waveform can be determined from the tooth flux waveform. The basic scheme of tooth and yoke fluxes is shown in Fig. 7.3.

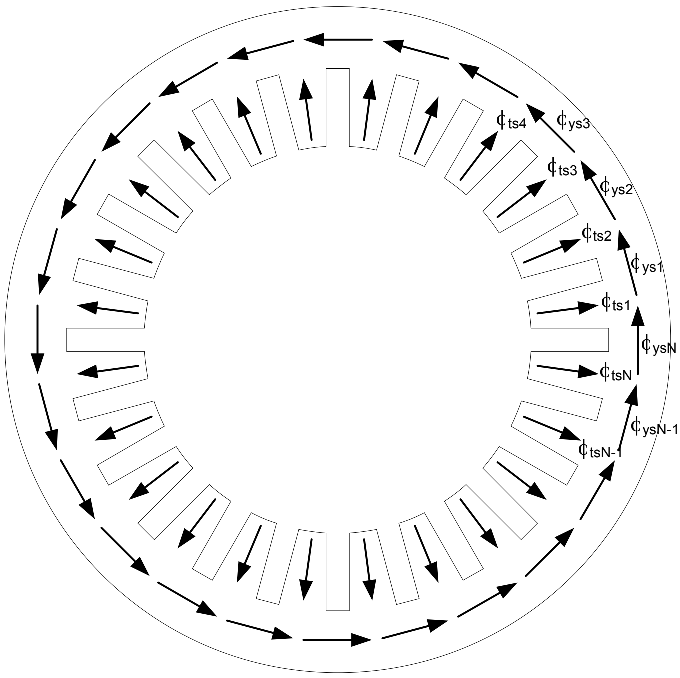

Fig. 7.3 The scheme of stator tooth and yoke fluxes

If only the fundamental component of the flux is considered, then the flux waveforms of two adjacent teeth will be phase shifted by an angle

$$\alpha = p\frac{2\pi}{Q_s} \tag{7.21}$$

The same is valid for the flux in two adjacent yoke segments. From Fig. 7.3 it follows that

$$\begin{aligned} \phi_{ts2} &= \phi_{ts1} e^{-j\alpha} \\ \phi_{ys2} &= \phi_{ys1} e^{-j\alpha} \end{aligned} \tag{7.22}$$

For the fluxes one has

$$\phi_{ts2} = \phi_{ys2} - \phi_{ys1} \tag{7.23}$$

Substituting (7.22) into (7.23) yields

$$\begin{aligned} \phi_{ts1} e^{-j\alpha} &= \phi_{ys1} \left(e^{-j\alpha} - 1 \right) \\ \phi_{ts1} &= \phi_{ys1} \left(1 - e^{j\alpha} \right) = \phi_{ys1} \left(1 - \cos\alpha - j \sin\alpha \right) \end{aligned} \tag{7.24}$$

The relationship between the flux magnitudes is

$$|\phi_{ts1}| = |\phi_{ys1}| 2 \sin\frac{\alpha}{2} = |\phi_{ys1}| 2 \sin\left(p \frac{\pi}{Q_s} \right) \tag{7.25}$$

It can be easily shown that the general relationship between the n^{th} harmonic components of the tooth and yoke flux densities is

$$|\phi_{tsn}| = |\phi_{ysn}| 2 \sin\left(np \frac{\pi}{Q_s} \right) \tag{7.26}$$

Since the components of ϕ_{tsn} are known from (7.20), the harmonic components of the yoke flux simply follow from (7.26).

The flux in the rotor yoke can be calculated in a similar manner. However, in this case one must recognize that the rotor yoke is travelling with the magnets. Hence for the rotor yoke it appears that the slots are travelling while the magnets are fixed. In that case the expression for the flux density in the slotted air gap is given by

$$\begin{aligned} B_{sr}(r,\theta,t) = & \sum_n B_{rn} \cos(np\theta) \left\{ \lambda_0 + \sum_m \lambda_{am} \cos[mQ_s(\theta - \omega_{rm} t)] \right\} + \\ & \sum_n B_{\theta n} \sin(np\theta) \sum_m \lambda_{bm} \sin[mQ_s(\theta - \omega_{rm} t)] \end{aligned} \tag{7.27}$$

The rotor yoke flux is equal to one half of the flux per pole calculated by integrating (7.27) which can be written as

$$\phi_p(t) = l_a R \int_{-\frac{\pi}{2p}}^{\frac{\pi}{2p}} B_{sr}(R,\theta,t) \mathrm{d}\theta \tag{7.28}$$

After substituting (7.27) into (7.28) and performing integration the flux per pole is

$$\begin{aligned}\phi_p(t) &= l_a R \sum_n \lambda_0 B_{rn} 2 \frac{1}{np} \sin\left(\frac{n\pi}{2}\right) + \\ & l_a R \left\{ \sum_m (B_{rn}\lambda_{am} - B_{\theta n}\lambda_{bm}) \frac{1}{np + mQ_s} \sin\left[(np + mQ_s)\frac{\pi}{2p}\right] + \right. \\ & \left. \sum_m (B_{rn}\lambda_{am} + B_{\theta n}\lambda_{bm}) \frac{1}{np - mQ_s} \sin\left[(np - mQ_s)\frac{\pi}{2p}\right] \right\} \cos(mQ_s\omega_{rm}t)\end{aligned} \tag{7.29}$$

If $np = mQ_s$, the term

$$\frac{1}{np - mQ_s} \sin\left[(np - mQ_s)\frac{\pi}{2p}\right]$$

is replaced with $\frac{\pi}{2p}$. The rotor yoke flux is then

$$\phi_{yr}(t) = \frac{1}{2}\phi_p(t) \tag{7.30}$$

The flux densities in the teeth and yoke can now be easily calculated by dividing the corresponding flux waveforms with the cross-sectional areas, i.e.

$$\begin{aligned} B_{ts} &= \frac{\phi_{ts}}{A_{ts}} \\ B_{ys} &= \frac{\phi_{ys}}{A_{ys}} \\ B_{yr} &= \frac{\phi_{yr}}{A_{yr}} \end{aligned} \tag{7.31}$$

Since different segments of the stator tooth from the tooth tip to the bottom of the slot have different widths, the flux density waveforms can be calculated for each segment separately as suggested in Fig 7.4. The segments II and IV can be further subdivided for more accurate flux density calculations.

The flux density waveforms in the stator and rotor teeth and yoke for the analyzed six pole surface PM motor have been calculated using (7.32) and are shown in Figs. 7.5 to 7.7. The stator tooth flux density has been calculated in the narrowest segment III. It is apparent from Figs. 7.5 and 7.6 that the stator tooth and yoke flux density waveforms are nonsinusoidal, especially in the case of stator teeth. The flux density in the rotor yoke, according to Fig. 7.7, is practically constant with a small ripple component. Hence, the losses in the rotor yoke will be negligible.

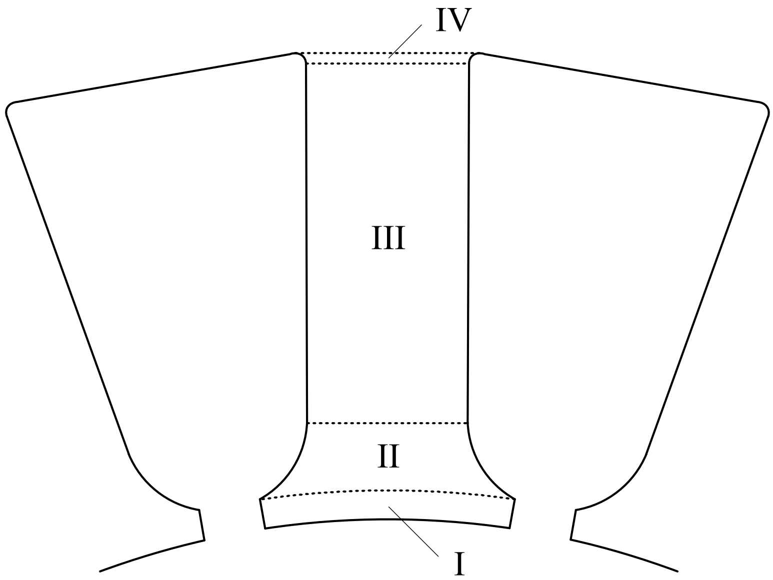

Fig. 7.4 Different segments of the stator tooth where the flux density is evaluated

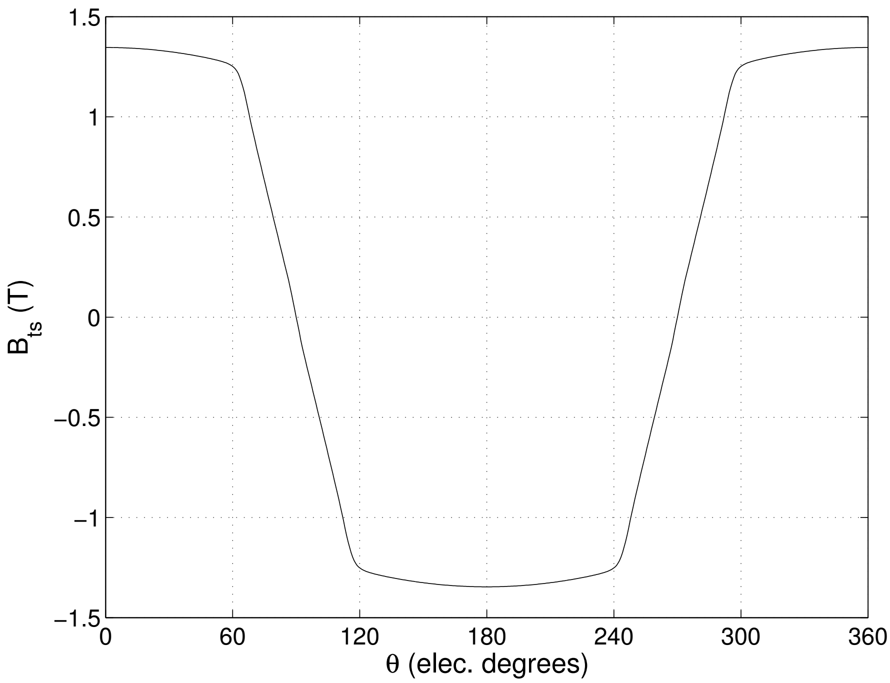

Fig. 7.5 Flux density waveform in the stator teeth

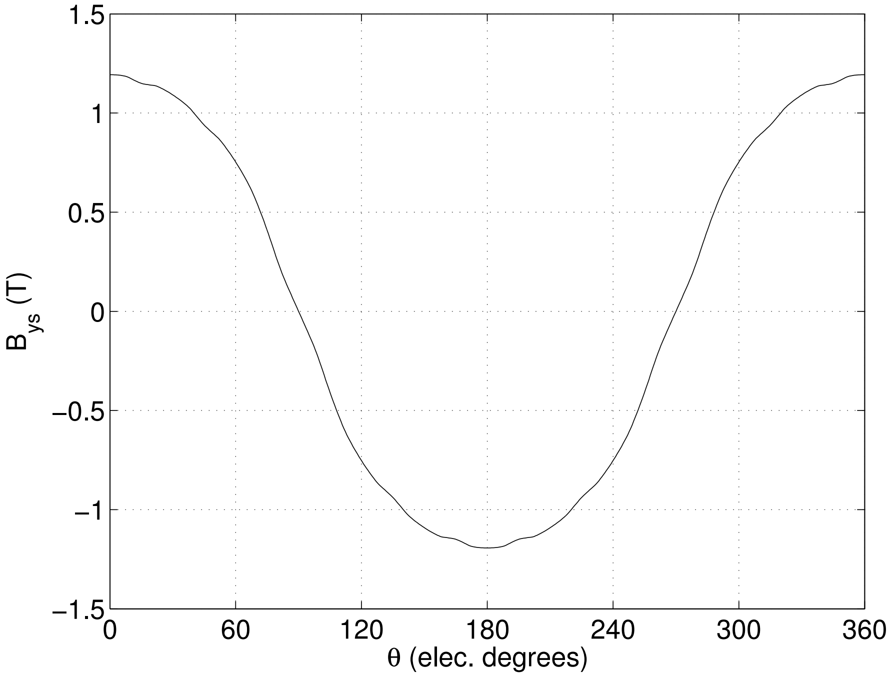

Fig. 7.6 Flux density waveform in the stator yoke

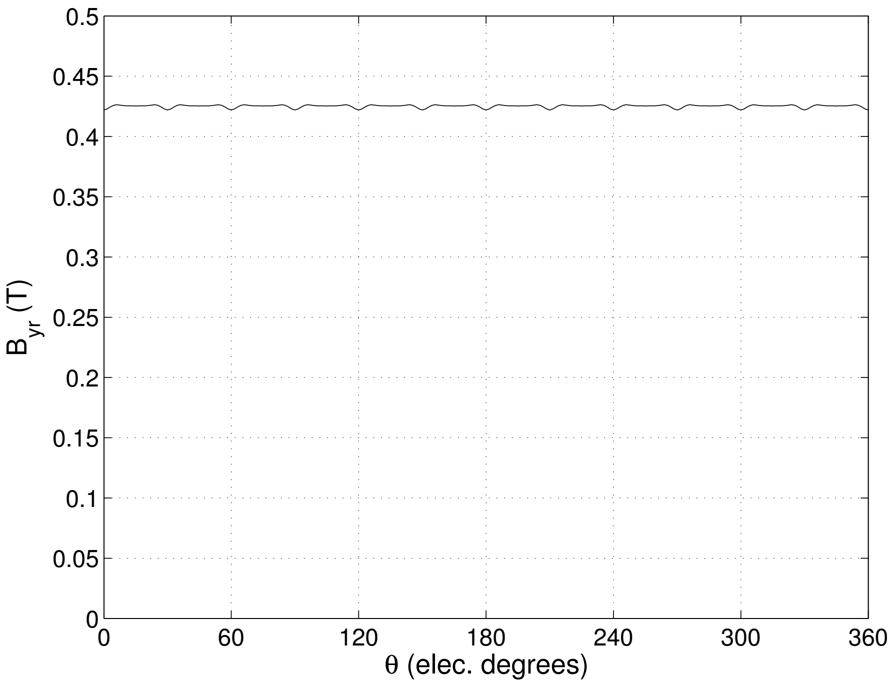

Fig. 7.7 Flux density waveform in the rotor yoke

Since the flux density waveforms for the stator teeth and yoke are given in the form of Fourier series, it is easy to show that the values of $\left(\frac{\mathrm{d}B}{\mathrm{d}t}\right)^2_{rms}$ needed for calculation of the core losses are equal to

$$\begin{aligned}\left(\frac{\mathrm{d}B_{ts}}{\mathrm{d}t}\right)^2_{rms} &= 2\pi^2 f^2 \sum_n n^2 B_{tsn}^2 \\ \left(\frac{\mathrm{d}B_{ys}}{\mathrm{d}t}\right)^2_{rms} &= 2\pi^2 f^2 \sum_n n^2 B_{ysn}^2 \end{aligned} \tag{7.32}$$

The final expression for the core losses can now be written in the form

$$P_c = \left[k_h f B_m^{a_h + b_h B_m} + k_e f^2 \sum_n n^2 B_n^2\right] \rho_c V_c \quad [\mathrm{W}] \tag{7.33}$$

where ρ_c is the density of the core material in $\mathrm{kg/m^3}$, V_c is the volume of the core segment in $\mathrm{m^3}$, B_n are the Fourier coefficients of the flux density waveform and B_m is the peak value of the flux density waveform defined as

$$B_m = \max_t \left[\sum_n B_n cos(n\omega t)\right]$$

7.3 Magnet Losses

The space harmonics in the armature winding MMF distribution and time harmonics in the current waveform, together with the harmonics in the air gap permeance function due to slotting, create field components which do not rotate in synchronism with the rotor. Consequently these field harmonics induce eddy currents in the rotor magnets and core which in some cases can generate significant losses.

In surface PM motors rare earth magnets are commonly used which have a moderate conductivity [85] ($\mathrm{Nd_2Fe_{14}B} : 0.63 - 0.83\,\mathrm{Sm/mm^2}, \mathrm{Sm_2Co_{17}} : 1.2 - 1.3\,\mathrm{Sm/mm^2}, \mathrm{SmCo_5} : 1.6 - 2\,\mathrm{Sm/mm^2}$). These magnets also have relatively high temperature coefficients of remanence and coercivity, which in cases of high local heat dissipation due to eddy currents can lead to irreversible demagnetization. This is why magnet losses are an important issue, especially in the case of high speed operation of surface PM motors.

The mathematical model which has been used to calculate the magnet losses in a surface PM motor is based on the following assumptions:

a) The model is developed in 2-D polar coordinates, thus end effects are ignored and induced eddy currents flow in the axial direction only.

b) The rotor core is laminated and infinitely permeable, thus no core losses are incurred.

c) The magnet material is homogenous, isotropic and characterized by constant permeability μ and conductivity σ.

d) The motor is excited with sinusoidal currents, i.e. only the fundamental component of the armature current is considered.

e) The total losses are calculated by adding the losses obtained separately for each harmonic component of the field.

f) The phasor form is used to analyze individual field harmonics since they vary sinusoidally with time.

The eddy current induced in the rotor magnet due to the n^{th} harmonic component of the armature field satisfies the Helmholtz equation [60]

$$\Delta J_{zn} - \mu\sigma \frac{\partial J_{zn}}{\partial t} = 0 \tag{7.34}$$

For sinusoidally varying fields, (7.34) can be written in 2-D polar coordinates in the phasor form

$$\frac{\partial^2 \widetilde{J}_{zn}}{\partial r^2} + \frac{1}{r}\frac{\partial \widetilde{J}_{zn}}{\partial r} + \frac{1}{r^2}\frac{\partial^2 \widetilde{J}_{zn}}{\partial \theta'^2} = k_n^2 \widetilde{J}_{zn} \tag{7.35}$$

where $k_n^2 = j\omega_n\mu\sigma$ and θ' is the angle with respect to the rotor. The relationship between angle with respect to the rotor (θ') and angle with respect to the stator (θ) is given by

$$\theta' = \theta - \omega_{rm} t \tag{7.36}$$

where ω_{rm} is the rotor mechanical speed.

The general solution of (7.35) can be expressed as [86]

$$\widetilde{J}_{zn}(r,\theta') = \sum_{m=0}^{\infty} \left[A_m I_m(k_n r) + B_m K_m(k_n r)\right] \left(C_m \cos m\theta' + D_m \sin m\theta'\right) \tag{7.37}$$

where I_m and K_m are the modified Bessel functions of the first and second kind respectively, both of order m. A_m, B_m, C_m and D_m are constants.

After taking into account that in the phasor form

$$\begin{aligned} \nabla \times \vec{E}_n &= -j\omega_n \mu \vec{H}_n \\ \vec{J}_n &= \sigma \vec{E}_n \end{aligned} \tag{7.38}$$

the following equation can be written

$$\nabla \times \vec{J}_n = -j\omega_n \mu\sigma \vec{H}_n = -k_n^2 \vec{H}_n \tag{7.39}$$

Since $\vec{J}_n = \vec{a}_z \widetilde{J}_{zn}$, i.e. eddy currents flow only in the axial direction, then

$$\nabla \times \vec{J}_n = \frac{1}{r}\frac{\partial \widetilde{J}_{zn}}{\partial \theta'}\vec{a}_r - \frac{\partial \widetilde{J}_{zn}}{\partial r}\vec{a}_{\theta'} = -k_n^2 (\widetilde{H}_{rn}\vec{a}_r + \widetilde{H}_{\theta' n}\vec{a}_{\theta'}) \tag{7.40}$$

Equation (7.40) defines relations between the radial and tangential components of the field intensity in the magnet and the induced eddy currents, i.e.

$$\begin{aligned} \widetilde{H}_{rn} &= -\frac{1}{k_n^2}\frac{1}{r}\frac{\partial \widetilde{J}_{zn}}{\partial \theta'} = -\frac{m}{k_n^2 r}\sum_{m=0}^{\infty}\left[A_m I_m(k_n r) + B_m K_m(k_n r)\right] \\ &\quad \left(-C_m \sin m\theta' + D_m \cos m\theta'\right) \qquad (7.41) \\ \widetilde{H}_{\theta' n} &= \frac{1}{k_n^2}\frac{\partial \widetilde{J}_{zn}}{\partial r} = \frac{1}{k_n}\sum_{m=0}^{\infty}\left[A_m I'_m(k_n r) + B_m K'_m(k_n r)\right] \\ &\quad \left(C_m \cos m\theta' + D_m \sin m\theta'\right) \qquad (7.42) \end{aligned}$$

Similar relations can also be written for the flux density, since $\widetilde{B}_n = \mu \widetilde{H}_n$.

The unknown constants in (7.37) can be determined by applying boundary conditions on the rotor and magnet surfaces. Since the rotor core is infinitely permeable, the tangential component of the field intensity on its surface is equal to zero. At the same time the radial components of the flux density in the magnet (region II) and in the air gap (region I) have to be equal on the boundary between them. The corresponding relations are

$$\begin{aligned} \widetilde{H}_{\theta' nII}(r,\theta')\Big|_{r=R_r} &= 0 \\ \widetilde{B}_{rnI}(r,\theta')\Big|_{r=R_m} &= \widetilde{B}_{rnII}(r,\theta')\Big|_{r=R_m} \end{aligned} \tag{7.43}$$

The armature winding field solution in the air gap is given by (3.28). These equations need to be written in the phasor form so that boundary conditions can be applied directly. Since only the fundamental component of the armature current is considered, the instantaneous currents are given by

$$\begin{aligned} i_A(t) &= I_m \cos(\omega t - \beta) \\ i_B(t) &= I_m \cos(\omega t - \beta - \frac{2\pi}{3}) \\ i_C(t) &= I_m \cos(\omega t - \beta + \frac{2\pi}{3}) \end{aligned} \tag{7.44}$$

where I_m is the peak value of the current and β is the initial phase shift. After substituting (7.44) and (7.36) into (3.28) and considering that a general relation between an instantaneous value $x(t)$ and its phasor representation $\widetilde{x} = |\widetilde{x}|e^{j\varphi}$ is given by $x(t) = Re\left(\widetilde{x}e^{j\omega t}\right)$, the radial component of the armature winding air gap flux density on the magnet surface is

$$\begin{aligned} B_{arn}(t) &= Re\left\{ N_c B_{arn}(R_m)\frac{1}{2}I_m \sum_{i=1}^{\frac{Q_s}{3}} \left[\mathrm{sgn}_{Ai} e^{jn\alpha_{Ai}} + \mathrm{sgn}_{Bi} e^{j\left(n\alpha_{Bi} - \frac{2\pi}{3}\right)} + \right.\right. \\ &\quad \left.\left. \mathrm{sgn}_{Ci} e^{j\left(n\alpha_{Ci} + \frac{2\pi}{3}\right)}\right] e^{-j\beta} e^{-jn\theta'} e^{j(\omega - n\omega_{rm})t} \right\} + \\ &\quad Re\left\{ N_c B_{arn}(R_m)\frac{1}{2}I_m \sum_{i=1}^{\frac{Q_s}{3}} \left[\mathrm{sgn}_{Ai} e^{-jn\alpha_{Ai}} + \mathrm{sgn}_{Bi} e^{j\left(-n\alpha_{Bi} - \frac{2\pi}{3}\right)} + \right.\right. \\ &\quad \left.\left. \mathrm{sgn}_{ci} e^{-j\left(n\alpha_{Ci} + \frac{2\pi}{3}\right)}\right] e^{-j\beta} e^{jn\theta'} e^{j(\omega + n\omega_{rm})t} \right\} + \\ &= Re\left\{\widetilde{C}_{r1n} e^{-jn\theta'} e^{j\omega_{1n}t}\right\} + Re\left\{\widetilde{C}_{r2n} e^{jn\theta'} e^{j\omega_{2n}t}\right\} \end{aligned} \tag{7.45}$$

where

$$\widetilde{C}_{r1n} = N_c B_{arn}(R_m)\frac{1}{2}I_m \sum_{i=1}^{\frac{Q_s}{3}} \left[\mathrm{sgn}_{Ai} e^{jn\alpha_{Ai}} + \mathrm{sgn}_{Bi} e^{j\left(n\alpha_{Bi} - \frac{2\pi}{3}\right)} + \right.$$

$$
\begin{aligned}
& \qquad \operatorname{sgn}_{Ci} e^{j\left(n\alpha_{Ci}+\frac{2\pi}{3}\right)}\Big] e^{-j\beta} = \left|\widetilde{C}_{r1n}\right| e^{j\varphi_{r1n}} \\
\widetilde{C}_{r2n} &= N_c B_{arn}(R_m)\frac{1}{2} I_m \sum_{i=1}^{\frac{Q_s}{3}} \Big[\operatorname{sgn}_{Ai} e^{-jn\alpha_{Ai}} + \operatorname{sgn}_{Bi} e^{j\left(-n\alpha_{Bi}-\frac{2\pi}{3}\right)} + \\
& \qquad \operatorname{sgn}_{Ci} e^{j\left(-n\alpha_{Ci}+\frac{2\pi}{3}\right)}\Big] e^{-j\beta} = \left|\widetilde{C}_{r2n}\right| e^{j\varphi_{r2n}} \\
\omega_{1n} &= \omega - n\omega_{rm} \\
\omega_{2n} &= \omega + n\omega_{rm}
\end{aligned}
$$

The wave function $Re\left\{\widetilde{C}_{r1n} e^{-jn\theta'} e^{j\omega_{1n}t}\right\}$ represents a direct field component which rotates in the same direction as the rotor, while $Re\left\{\widetilde{C}_{r2n} e^{jn\theta'} e^{j\omega_{2n}t}\right\}$ represents an inverse field component which rotates in the opposite direction from the rotor. Direct and inverse components of the field are considered separately. Superposition is then used to take into account their contributions to the magnet losses.

Comparing (7.41) and (7.45) one can write for the direct field component

$$
\begin{aligned}
m &= n \\
C_m &= j \\
D_m &= 1
\end{aligned} \tag{7.46}
$$

and for the inverse field

$$
\begin{aligned}
m &= n \\
C_m &= -j \\
D_m &= 1
\end{aligned} \tag{7.47}
$$

Furthermore, one can write for the direct field

$$
\begin{aligned}
& A_{n1} I_n'(k_{n1}R_r) + B_{n1} K_n'(k_{n1}R_r) = 0 \\
& -\frac{\mu n}{k_{n1}^2 R_m}\left[A_{n1} I_n(k_{n1}R_m) + B_{n1} K_n(k_{n1}R_m)\right] = \widetilde{C}_{r1n}
\end{aligned} \tag{7.48}
$$

and for the inverse field

$$
A_{n2} I_n'(k_{n2}R_r) + B_{n2} K_n'(k_{n2}R_r) = 0
$$

$$-\frac{\mu n}{k_{n2}^2 R_m}[A_{n2}I_n(k_{n2}R_m) + B_{n2}K_n(k_{n2}R_m)] = \widetilde{C}_{r2n} \tag{7.49}$$

where

$$k_{n1}^2 = j\omega_{n1}\mu\sigma$$
$$k_{n2}^2 = j\omega_{n2}\mu\sigma$$

The constants A_{n1}, B_{n1}, A_{n2} and B_{n2} can then be easily calculated from (7.48) and (7.49).

$$\begin{aligned}
A_{n1} &= -\frac{\widetilde{C}_{r1n}\frac{k_{n1}^2 R_m}{\mu n}K_n'(k_{n1}R_r)}{K_n'(k_{n1}R_r)I_n(k_{n1}R_m) - K_n(k_{n1}R_m)I_n'(k_{n1}R_r)} \\
B_{n1} &= \frac{\widetilde{C}_{r1n}\frac{k_{n1}^2 R_m}{\mu n}I_n'(k_{n1}R_r)}{K_n'(k_{n1}R_r)I_n(k_{n1}R_m) - K_n(k_{n1}R_m)I_n'(k_{n1}R_r)} \\
A_{n2} &= -\frac{\widetilde{C}_{r2n}\frac{k_{n2}^2 R_m}{\mu n}K_n'(k_{n2}R_r)}{K_n'(k_{n2}R_r)I_n(k_{n2}R_m) - K_n(k_{n2}R_m)I_n'(k_{n2}R_r)} \\
B_{n2} &= \frac{\widetilde{C}_{r2n}\frac{k_{n2}^2 R_m}{\mu n}I_n'(k_{n2}R_r)}{K_n'(k_{n2}R_r)I_n(k_{n2}R_m) - K_n(k_{n2}R_m)I_n'(k_{n2}R_r)}
\end{aligned} \tag{7.50}$$

Once the field solution in the magnet region is known, the power losses due to induced eddy currents can be calculated as an integral of the average Poynting vector across the magnet surface. The average Poynting vector for sinusoidally varying field components is equal to [60]

$$\vec{N}_{av} = Re\left\{\frac{1}{2}\left(\vec{\widetilde{E}} \times \vec{\widetilde{H}}^*\right)\right\} = Re\left\{\frac{1}{2}\left(\frac{\vec{\widetilde{J}}}{\sigma} \times \vec{\widetilde{H}}^*\right)\right\} \tag{7.51}$$

where $\widetilde{H}^*$ is the complex conjugate of the field intensity phasor $\widetilde{H}$. The integral of the average Poynting vector represents the average power that enters through the magnet surface which is equal to the power dissipated inside the magnet volume, i.e.

$$P_{pm} = \oint_S \vec{N}_{av}\vec{n}\mathrm{d}S = -\int_V \vec{\widetilde{E}}\vec{\widetilde{J}}^*\,\mathrm{d}V \tag{7.52}$$

The power losses in the magnets due to eddy currents at all frequencies are equal to

$$\begin{aligned}
P_{pm} \;=\; & 2p\sum_{n=1}^{N_a} Re\left\{\int_{\alpha_0-\alpha_p\frac{\pi}{2p}}^{\alpha_0+\alpha_p\frac{\pi}{2p}} \frac{1}{2}\frac{\widetilde{J}_{zn1}}{\sigma}\widetilde{H}_{\theta' n1}^* R_m l_a \mathrm{d}\theta'\right\} + \\
& 2p\sum_{n=1}^{N_a} Re\left\{\int_{\alpha_0-\alpha_p\frac{\pi}{2p}}^{\alpha_0+\alpha_p\frac{\pi}{2p}} \frac{1}{2}\frac{\widetilde{J}_{zn2}}{\sigma}\widetilde{H}_{\theta' n2}^* R_m l_a \mathrm{d}\theta'\right\}
\end{aligned} \tag{7.53}$$

where α_0 is the initial angular position of the rotor, α_p is the magnet pole arc to pole pitch ratio, R_m is the radius at the magnet surface and l_a is the effective stack length.
After substituting (7.37) and (7.42) into (7.53) and performing integration, the final expression for magnet losses is

$$\begin{aligned} P_{pm} \;=\; & 2p\sum_{n=1}^{N_a} Re\left\{\frac{1}{2\sigma}\left[A_{n1}I_n(k_{n1}R_m)+B_{n1}K_n(k_{n1}R_m)\right]\right. \\ & \left.\left[\frac{1}{k_{n1}}\left(A_{n1}I'_n(k_{n1}R_m)+B_{n1}K'_n(k_{n1}R_m)\right)\right]^* R_m l_a \alpha_p \frac{\pi}{p}\right\}+ \\ & 2p\sum_{n=1}^{N_a} Re\left\{\frac{1}{2\sigma}\left[A_{n2}I_n(k_{n2}R_m)+B_{n2}K_n(k_{n2}R_m)\right]\right. \\ & \left.\left[\frac{1}{k_{n2}}\left(A_{n2}I'_n(k_{n2}R_m)+B_{n2}K'_n(k_{n2}R_m)\right)\right]^* R_m l_a \alpha_p \frac{\pi}{p}\right\} \end{aligned} \quad (7.54)$$

The magnet losses of the six pole surface PM motor calculated analytically using (7.54) and calculated numerically using commercial FE software Magsoft, Flux 2-D are given in Table 7.1.

Table 7.1 Eddy current losses in the magnets of the analyzed six pole surface PM motor

	Magnet losses		
	Direct field	Inverse field	Total
Analytical	0.57 W	8.70 W	9.27 W
FE	—		7.55 W

7.4 Friction and Windage losses

No detailed analysis has been carried out to determine accurate expressions for friction and windage losses. Instead, simple equations given by Gieras [80] have been used to estimate these losses. According to [80] the friction losses are given by

$$P_{fr} = k_{fb} m_r n_r 10^{-3} \quad (7.55)$$

where k_{fb} is an empirical coefficient ranging from 1 to 3, m_r is the mass of the rotor and n_r is the rotor speed in rpm. The windage losses for the speeds below 6000 rpm can be approximated using

$$P_{wind} = 2D_{ro}^3 l_a n_r^3 10^{-6} \quad (7.56)$$

where D_{ro} is the outer diameter of the rotor l_a is the core length and n_r is the rotor speed in rpm.

7.5 Efficiency

The motor efficiency is defined as

$$\eta = \frac{P_{out}}{P_{in}} \tag{7.57}$$

where P_{out} is the mechanical output power and P_{in} is the electrical input power. The output power at the shaft is given by

$$P_{out} = P_{em} - P_c - P_{pm} - P_{fr} - P_{wind} \tag{7.58}$$

where P_{em} is the electromechanical power, P_c are the core losses, P_{pm} are the magnet losses, P_{fr} are the friction losses and P_{wind} are the windage losses. The electromechanical power is given by

$$P_{em} = T_{em}\omega_{rm} \tag{7.59}$$

where T_{em} is the electromagnetic torque determined in Chapter 3. The input power to the motor is

$$P_{in} = P_{em} + P_a \tag{7.60}$$

where P_a are the winding losses.

The power balance and efficiency for the six pole surface PM motor calculated using expressions for losses derived earlier in this chapter are shown in Table 7.2.

Table 7.2 Power balance and efficiency of the analyzed six pole surface PM motor

Parameter	*Symbol*	*Value*	*Unit*
Electromechanical power	P_{em}	3729	W
Winding losses	P_a	137.5	W
Core losses	P_c	29.6	W
Magnet losses	P_{pm}	9.27	W
Friction losses	P_{fr}	18.5	W
Windage losses	P_{wind}	2.1	W
Output power	P_{out}	3669.5	W
Input power	P_{in}	3866.5	W
Efficiency	η	0.949	–

Chapter 8

Optimization

The theory presented in the previous chapters has been developed to predict the motor performance and calculate its parameters. That knowledge can be used in the design stage to determine the motor dimensions and the parameters required to fulfill a specific design task. For surface PM motors the emphasis is usually put on high efficiency, high torque density, low cost and for some applications low pulsating torque. For interior PM motors the design goals are similar. However, since their tasks usually involve applications where wide speed range is required, there are some additional requirements that can be set for this type of motor which are discussed in more detail in Section 8.3.

Most of the requirements for both types of motors are in contradiction to each other. Therefore finding a design that will satisfy all of them can be an overwhelming task due to a large number of parameters whose effects on the motor performance and quality of the design are strongly coupled. There is an obvious need for a systematic approach to decision making based on an iterative scheme that would gradually lead to an optimal motor design which satisfies all the constraints imposed upon it and still fulfills its main task to produce torque. There is a wide variety of optimization techniques which can be used for motor design. Some of the techniques require providing a feasible starting point for the search process to begin. Finding a feasible starting point that would lead to a global minimum of the objective function is an almost impossible task. The optimization techniques which do not require a specific starting point represent a more flexible and attractive approach. Evolutionary algorithms are such techniques capable of solving global optimization problems subject to nonlinear constraints. One of the most promising novel evolutionary algorithms is the Differential Evolution (DE) first introduced by Price and Storn [54] in 1995. Since then several authors have tested the algorithm using some well known and difficult test problems [56, 59] and showed that it was capable of outperforming several other well known algorithms. These are the reasons why DE has been selected to be used in this thesis for the optimized design of surface and interior PM motors.

8.1 Differential Evolution Algorithm

The optimized motor design can be generally formulated as a single objective or multiobjective minimization problem. The single objective approach can be used if enough is known about all of the constraints imposed upon the design so that a fixed limit can be determined for each constraint while leaving one global objective function to be minimized. For instance, efficiency, torque density, power factor and flux densities in the stator and rotor core can have some fixed minimum requirements while cost minimization can be set as the main objective. However, sometimes it may be desirable to get more insight into compromises which have to be made between different design solutions. In that case more than one objective is observed and minimized simultaneously. The choice of the optimal design is then left to the decision maker who chooses the design which is the best compromise between the competing objectives. For instance, an optimization problem can be defined in which efficiency, power factor, minimum pulsating torque and flux densities in the core are set as constraints while minimum cost and maximum torque density are chosen as the objectives. The cost and torque density are competing objectives because the designs with high torque density naturally lead to a selection of magnets with high remanence which are more expensive. Consequently, the selection of these magnets deteriorates the other objective which is to minimize the cost. It is apparent that a compromise needs to be made here to achieve the satisfying level of both goals.

The multiobjective approach has been used in this thesis from which a single solution can be selected as the best compromise between the competing multiple objectives. The general multiobjective optimization problem can be defined as:

Find the vector of parameters

$$\vec{x} = [x_1, x_2, \ldots, x_D],\ \vec{x} \in R^D$$

subject to m inequality constraints

$$g_j(\vec{x}) \leq 0, \quad j = 1, \ldots, m$$

and subject to D boundary constraints

$$x_i^{(L)} \leq x_i \leq x_i^{(U)}, \quad i = 1, \ldots, D$$

which will minimize the vector function

$$f(\vec{x}) = [f_1(\vec{x}), f_2(\vec{x}), \ldots, f_k(\vec{x})]$$

The result of the optimization is a population of solutions which belong to a *Pareto optimal set*. The vector of decision variables $\vec{x}_0 \in \mathcal{F}$ is *Pareto optimal* if there exists no other $\vec{x} \in \mathcal{F}$ such that $f_i(\vec{x}) \leq f_i(\vec{x}_0)$ for all $i = 1, \ldots, k$ and there exists at least one $i = 1, \ldots, k$ for which $f_i(\vec{x}) < f_i(\vec{x}_0)$. Here, $\mathcal{F}$ denotes the region of the problem where the constrains are satisfied. In other words the vectors of the Pareto set are not dominated by any other vector in the set. Since none of the vectors dominate, they are all equally good solutions which provide invaluable insight to the decision maker on how to choose the best design to satisfy the performance criteria. The plot of the objective functions whose nondominant vectors are in the Pareto optimal set is called the *Pareto front*.

The Differential Evolution operates on a population of candidate solutions. The population is of constant size NP. In each iteration a new generation of solutions is created and compared to the population members of the previous generation. The process is repeated until the maximum number of generations G_{max} is reached. The population of the G^{th} generation can be written in the form

$$P_G = [\vec{x}_{1,G}, \vec{x}_{2,G}, \ldots, \vec{x}_{NP,G}], \quad G = 0, \ldots, G_{max} \tag{8.1}$$

Each vector in P_G contains D real parameters

$$\vec{x}_{i,G} = \left[x^i_{1,G}, x^i_{2,G}, \ldots, x^i_{D,G}\right], \quad i = 1, \ldots, NP, \quad G = 0, \ldots, G_{max} \tag{8.2}$$

The initial population $P_{G=0}$ is generated using random values within the given boundaries which can be written in the form

$$x_{j,0}^{i} = \mathrm{rand}_j[0,1]\left(x_j^{(U)} - x_j^{(L)}\right) + x_j^{(L)}, \quad i = 1,\ldots,NP \quad j = 1,\ldots,D \tag{8.3}$$

where $\mathrm{rand}_j[0,1]$ is the uniformly distributed random number on the interval [0,1] which is chosen anew for each j.

In every generation new candidate vectors are created by randomly sampling and combining the vectors from the previous generation in the following manner:

$$\begin{aligned} & i = 1,\ldots,NP, \quad j = 1,\ldots,D, \quad G = 1,\ldots,G_{max} \\ & u_{j,G}^{i} = \begin{cases} x_{j,G-1}^{r3} + F\left(x_{j,G-1}^{r1} - x_{j,G-1}^{r2}\right) & \text{if} \quad \mathrm{rand}_j[0,1] \le CR \quad \text{or} \quad j = k \\ x_{j,G-1}^{i} & \text{otherwise} \end{cases} \end{aligned} \tag{8.4}$$

where $F \in \langle 0,1]$ and $CR \in [0,1]$ are DE control parameters which are kept constant during optimization, $r_1, r_2, r_3 \in \{1,\ldots,NP\}$, $r_1 \neq r_2 \neq r_3 \neq i$ are randomly selected vectors from the previous generation, different from each other and different from the current vector with index i, and $k \in \{1,\ldots,D\}$ is a randomly chosen index which insures that at least one $u_{j,G}^{i}$ is different from $x_{j,G-1}^{i}$. The choice of different values for CR and F significantly affects the convergence speed and can for some values lead to divergence as well. It has been reported in literature [57, 59] that generally lower values of F and CR are recommended for multiobjective optimization. The values $F = 0.3$ and $C = 0.3$ have proven to be a good combination for most optimization problems covered in this thesis.

The population for the new generation P_G will be assembled from the vectors of the previous generation P_{G-1} and the candidate vectors $\vec{u}_G^{i}$ according to the following selection scheme:

$$\begin{aligned} & i = 1,\ldots,NP, \quad G = 1,\ldots,G_{max} \\ & \vec{x}_G^{i} = \begin{cases} \vec{u}_G^{i} & \text{if} \quad \forall\, l \in \{1,\ldots,k\},\ f_l(\vec{u}_G^{i}) \le f_l(\vec{x}_{G-1}^{i}) \\ \vec{x}_{G-1}^{i} & \text{otherwise} \end{cases} \end{aligned} \tag{8.5}$$

The result of the selection scheme is that a candidate vector will be chosen into the next generation only if it dominates its predecessor from the previous generation.

Parallel to the selection of vectors that will survive into the next generation another selection occurs which decides whether a candidate vector can be added to a set of nondominant solutions. This set is built separately and as the optimization progresses its members converge towards the Pareto optimal set. At the beginning of the optimization the set of nondominant solutions is empty. The first feasible solution which satisfies all the constraints is added into the set. Each newly generated candidate which satisfies the constraints is compared with the solutions within the set. If it is dominated by any of the solutions in the set, the comparison with the rest of the set is stopped and the new candidate is discarded. If, however, the new candidate dominates any of the solutions in the set, those solutions are removed from the set and the new vector is added to the set. This basic principle of selection was proposed by Chang [57].

Since the Pareto set is infinite, the total number of vectors that will be present in the set at any time during optimization has to be limited. If the maximum allowed number of vectors in the set is exceeded, then a criterion is used to identify the vector which should be discarded. The criterion proposed by Abbass [59] is used which is the nearest neighbor distance function defined as

$$D(\vec{x}_G^i) = \frac{\min||\vec{x}_G^i - \vec{x}_G^j|| + \min||\vec{x}_G^i - \vec{x}_G^k||}{2}, \quad i, j, k \in \{1, \dots, NP\} \tag{8.6}$$

where $\vec{x}_G^i \neq \vec{x}_G^j \neq \vec{x}_G^k$. Equation (8.6) defines the nearest neighbor distance as the average Euclidian distance between the closest two vectors in the Pareto set. The nondominant solution with the smallest neighbor distance is removed from the set to retain the maximum allowed size of the set. This criterion helps to achieve diversity in the Pareto set.

8.1.1 Constraint Handling

In problems with boundary conditions it is required to have all the parameters of the vector within the prescribed boundaries. After reproduction some parameters of the newly created candidate vectors may fall out of boundaries. These parameters can be fixed using random values generated within the feasible range using the scheme proposed by Lampinen [56]

$$i = 1, \dots, NP, \quad j = 1, \dots, D, \quad G = 1, \dots, G_{max}$$

$$u_{j,G}^{i} = \begin{cases} \text{rand}_j[0,1]\left(x_j^{(U)} - x_j^{(L)}\right) + x_j^{(L)} & \text{if} \quad u_{j,G}^{i} < x_j^{(L)} \quad \text{or} \quad u_{j,G}^{i} > x_j^{(L)} \\ u_{j,G}^{i} & \text{otherwise} \end{cases} \tag{8.7}$$

The inequality constraints are slightly more difficult to handle. A traditional approach uses penalty functions to penalize the solutions which violate constraints. This principle is implemented in the form of weighted sums, which modifies each objective function into the following form:

$$f_l'(\vec{x}) = f(\vec{x}) + \sum_{j=1}^{m} w_j \max[0, g_j(\vec{x})], \quad l = 1, \ldots, k \tag{8.8}$$

where w_j is the weight factor for each constraint. This method suffers from problems related to poor choice of the weight factors which can affect the convergence. Therefore, an alternative approach proposed by Lampinen [56] is used in which the following scheme is applied:

$$i = 1, \ldots, NP, \quad G = 1, \ldots, G_{max}$$
$$\vec{x}_G^i = \begin{cases} \vec{u}_G^i & \text{if} \begin{cases} \left(\forall\, j \in \{1, \ldots, m\} : g_j(\vec{u}_G^i) \le 0 \wedge g_j(\vec{x}_{G-1}^i) \le 0\right) \wedge \left(\forall\, l \in \{1, \ldots, k\} : f_l(\vec{u}_G^i) \le f_l(\vec{x}_{G-1}^i)\right) \\ \vee \\ \left(\forall\, j \in \{1, \ldots, m\} : g_j(\vec{u}_G^i) \le 0\right) \wedge \left(\exists\, j \in \{1, \ldots, m\} : g_j(\vec{x}_{G-1}^i) > 0\right) \\ \vee \\ \left(\exists\, j \in \{1, \ldots, m\} : g_j(\vec{u}_G^i) > 0\right) \wedge \left(\forall\, j \in \{1, \ldots, m\} : \max\left(g_j(\vec{u}_G^i), 0\right) \le \max\left(g_j(\vec{x}_{G-1}^i), 0\right)\right) \end{cases} \\ \vec{x}_{G-1}^i & \text{otherwise} \end{cases}$$

The main advantages of this approach are:

- it forces the selection towards feasible regions where constraints are satisfied thus resulting in faster convergence,
- it saves time since no evaluation of the objective function occurs if constraints are violated.

8.1.2 Handling of Integer and Discrete Variables

The Differential Evolution algorithm assumes that the parameters in the population are continuous real numbers. However, in the motor design some of the parameters, e.g. the number of pole pairs, can have only integer values. The example of discrete variables are the standard wire diameters which can be used for the armature winding. The main difference between integer and discrete variables is that although they both have a discrete nature, only discrete variables can assume floating point values. The discrete variables can also be unevenly spaced.

In the presence of integer and discrete variables our optimization problem can be redefined as follows:
Find the vector of parameters

$$\vec{x} = [x_1, x_2, \ldots, x_D] = [\vec{x}^{(i)}, \vec{x}^{(d)}, \vec{x}^{(c)}],\ \vec{x} \in R^D$$

subject to m inequality constraints

$$g_j(\vec{x}) \leq 0, \quad j = 1, \ldots, m$$

and subject to D boundary constraints

$$x_i^{(L)} \leq x_i \leq x_i^{(U)}, \quad i = 1, \ldots, D$$

which will minimize the vector function

$$f(\vec{x}) = [f_1(\vec{x}), f_2(\vec{x}), \ldots, f_k(\vec{x})]$$

where $\vec{x}^{(i)}$, $\vec{x}^{(d)}$, $\vec{x}^{(c)}$ are feasible subsets of integer, discrete and continuous variables respectively. The handling of these types of variables in the DE can be made quite simple when using the approach proposed by Lampinen and Zelinka [87]. The basic idea is to let the DE handle all the variables internally as continuous floating point values, but when the constraints g_j and the cost function f are evaluated, a new vector is formed which is defined as

$$\begin{aligned} &i = 1, \ldots, D, \\ &x'_i = \begin{cases} x_i & \text{for continuous variables} \\ \mathrm{INT}(x_i) & \text{for integer variables} \end{cases} \end{aligned} \tag{8.9}$$

where $\mathrm{INT}(x_i)$ is the function which converts a real value to an integer by truncation. This new vector is then used to calculate the constraints $g_j(\vec{x}')$ and to calculate the cost function $f(\vec{x}') = [f_1(\vec{x}'), f_2(\vec{x}'), \ldots, f_k(\vec{x}')]$. The discrete variables can also be handled as integer variables if instead of using the discrete value itself, its index is used as an integer variable which is being optimized. To clarify this approach suppose that a subset of discrete variables $\vec{x}^{(d)}$ is defined as

$$\vec{x}^{(d)} = [x_1^{(d)}, x_2^{(d)}, \ldots, x_{N_d}^{(d)}], \quad N_d \leq D$$

where

$$x_i^{(d)} < x_{i+1}^{(d)}, \quad i = 1, \ldots, N_d \tag{8.10}$$

Now the index i ranging from 1 to N_d is used as a variable in the optimization scheme. However, when the constraints and the cost function are evaluated, the actual discrete value is used for the index i which resulted from the DE algorithm.

The vector parameters of the initial population which are integer variables are generated using a modified equation (8.3)

$$x_{j,0}^i = \mathrm{rand}_j[0,1]\left(x_j^{(U)} - x_j^{(L)} + 1\right) + x_j^{(L)}, \quad i = 1, \ldots, NP \quad j = 1, \ldots, N_i \tag{8.11}$$

where $N_i \leq D$ is the number of integer variables in the vector $\vec{x}^i_{G=0}$.

In the case when an integer variable falls out of feasible range, the modified scheme (8.7) is used.

$$\begin{aligned} & i = 1, \ldots, NP, \quad j = 1, \ldots, N_i, \quad G = 1, \ldots, G_{max} \\ & u_{j,G}^i = \begin{cases} \mathrm{rand}_j[0,1]\left(x_j^{(U)} - x_j^{(L)} + 1\right) + x_j^{(L)} \text{ if } \mathrm{INT}(u_{j,G}^i) < x_j^{(L)} \text{ or } \mathrm{INT}(u_{j,G}^i) > x_j^{(L)} \\ u_{j,G}^i \quad \text{otherwise} \end{cases} \end{aligned} \tag{8.12}$$

8.2 Optimized Design of a Surface PM Motor

The general procedure for the multiobjective optimized design of a surface PM motor can be divided into several stages:

1. Define power level, voltage, speed and type of excitation (trapezoidal or sinusoidal) of the motor.

2. Define the variables, i.e. motor parameters, which are to be optimized and their limits.

3. Define the objectives of the optimization.

4. Identify other objectives of interest which are not to be optimized, transform them into inequality constraints and set their limits.

5. Select the optimization method and define its control parameters.

6. Select the best compromise solution from the Pareto set after completing the optimization.

Stage 1

The surface PM motor which is used as an example of the design optimization based on the DE algorithm has the following desired specifications:

Rated power: $P = 5$ kW

Rated voltage: $V = 400$ V

Rated speed: $n_r = 2000$ rpm

Excitation: sinusoidal

Stage 2

The design variables contain information about motor dimensions. The basic guideline for the selection of variables is to minimize their total number and avoid the selection of those which are redundant, i.e. which can be expressed in terms of other variables. This is important from the aspect of reduction of time needed to carry out the optimization, but is also important because it prevents a situation where variables contradict each other. For instance, if the stator outer diameter D_o and inner diameter D_s, together with the yoke thickness d_{ys}, are the design variables, then the total slot depth d_s should not be used as another variable because it has already been defined by the first three variables, i.e. $d_s = \frac{1}{2}(D_o - D_s) - d_{ys}$.

The design variables selected for this study, together with their limits, are listed in Table 8.1. All the variables which are geometric are expressed as non-dimensional rather than using their absolute values.

The information about permanent magnet remanence is given in Table 8.2, which is assembled using the data on selected permanent magnet materials from the manufacturer Vacuumschmelze [85]. This table also provides other important information about the magnet materials which are needed in the design. The remanent flux density is treated as a discrete variable because magnets are usually ordered from one particular manufacturer which can supply magnetic material only with several distinct values of the remanent flux density. From the standpoint of optimal utilization of the magnets it is desirable to have them magnetized to their full remanence when assembled on the motor. Therefore, the design choices during optimization should be limited only to available distinct values of the permanent magnet remanence.

Besides the design variables there are also a number of parameters with assigned constant values that do not change during optimization. Those parameters are:

1. Magnetization type: radial
2. Air gap length: $g = 0.5$ mm
3. Width of the slot opening: $b_o = 2.5$ mm (see Fig. 6.1)
4. Depth of the slot opening: $d_o = 0.6$ mm (see Fig. 6.1)
5. Armature current density: $J = 6\ \mathrm{A/mm^2}$
6. Slot fill factor: $f_{fill} = 0.4$

The armature current density and the slot fill factor are used to calculate the available number of ampere-turns per slot using equation

$$N_c I = J S f_{fill} \tag{8.13}$$

where N_c is the number of turns per coil and S is the surface area of the slot. The slot area is calculated from the slot dimensions which result from the stator outer and inner diameters and the the yoke and tooth thicknesses which are all design variables.

The coil turns and the current need to be separated. The separation can be done in a straightforward manner using a phasor diagram and considering the fact that the sum of the motor back emf and the voltage drops on the armature resistance and inductance have to be equal to the terminal voltage V. The phasor diagram for the surface PM motor is shown in Fig. 8.1. The current phasor is aligned with the q axis for maximum torque per amp operation.

The steady state equations after resolving voltages and currents into d and q components can be written in the general form

Table 8.1 Variables used in the optimized design of a surface PM motor

	Variable	Variable type	Limits
1.	Ratio of stator outer diameter to maximum outer diameter	continuous	$0.6 < D_o / D_{o0} < 1 \quad (D_{o0} = 230 \text{ mm})$
2.	Ratio of stator inner diameter to outer diameter	continuous	$0.55 < D_s / D_o < 0.75$
3.	Ratio of stack length to maximum stack length	continuous	$0.4 < l_a / l_{a0} < 1 \quad (l_{a0} = 150 \text{ mm})$
4.	Ratio of yoke thickness to difference between stator outer and inner radius	continuous	$0.3 < 2d_{ys} / (D_o - D_s) < 0.6$
5.	Permanent magnet data	discrete	Table input
6.	Number of slots	discrete	$Q_s = 6, 9, 12, \ldots, 72$
7.	Number of pole pairs	integer	$p = 2, 3, 4, 5, 6$
8.	Ratio of tooth width to slot pitch at D_S	continuous	$0.3 < b_{ts} / \tau_s < 0.7$
9.	Ratio of magnet length to air gap length	continuous	$4 < l_m / g < 10$
10.	Angular span of the magnets relative to the pole pitch	continuous	$2/3 < \alpha_p < 1$

Table 8.2 Parameters of the available permanent magnet materials

	Type	**Remanent flux density B_r [T]**	**Relative permeability μ_r**	**Demagnetization limit at 100^0 C B_D [T]**	**Density ρ_m [kg/m^3]**	**Conductivity σ [Sm/mm^2]**
1.	$SmCo_5$	0.90	1.085	-1	8400	1.82
2.	$SmCo_5$	0.95	1.05	-0.6	8400	1.82
3.	$SmCo_5$	1.01	1.0645	-0.3	8400	1.82
4.	Sm_2Co_{17}	1.04	1.089	-1	8400	1.25
5.	Sm_2Co_{17}	1.10	1.0675	-1	8400	1.25
6.	$Nd_2Fe_{14}B$	1.08	1.0355	-1	7800	0.71
7.	$Nd_2Fe_{14}B$	1.13	1.0456	-1	7700	0.71
8.	$Nd_2Fe_{14}B$	1.16	1.043	-0.5	7700	0.71
9.	$Nd_2Fe_{14}B$	1.19	1.052	0.1	7600	0.71
10.	$Nd_2Fe_{14}B$	1.23	1.0525	0.4	7600	0.71
11.	$Nd_2Fe_{14}B$	1.26	1.039	0.25	7700	0.71
12.	$Nd_2Fe_{14}B$	1.30	1.04	0.4	7600	0.71
13.	$Nd_2Fe_{14}B$	1.32	1.0885	0.65	7500	0.71
14.	$Nd_2Fe_{14}B$	1.34	1.04	0.65	7600	0.71

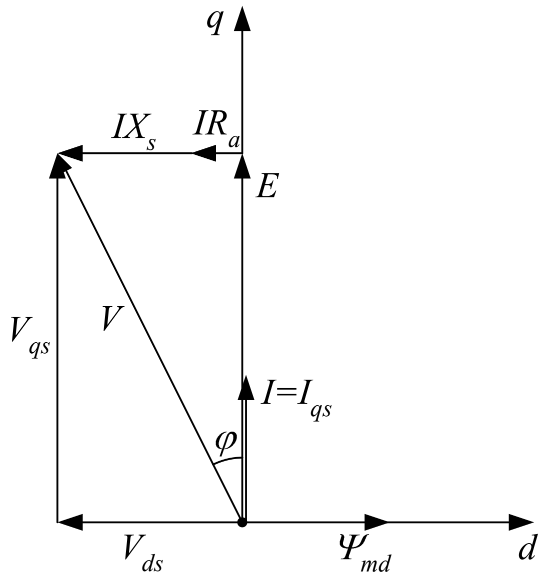

Fig. 8.1 Phasor diagram of a surface PM motor with current phasor aligned for maximum torque per amp operation

$$
\begin{aligned}
V_{qs} &= R_a I_{qs} + \omega \Psi_{ds} \\
V_{ds} &= R_a I_{ds} - \omega \Psi_{qs} \\
\Psi_{ds} &= \Psi_{md} + L_s I_{ds} \\
\Psi_{qs} &= L_s I_{qs}
\end{aligned} \tag{8.14}
$$

At maximum torque per amp operation the d component of the current is equal to zero. Equations (8.14) then become

$$
\begin{aligned}
V_{qs} &= RI + \omega \Psi_{md} \\
V_{ds} &= -\omega L_s I
\end{aligned} \tag{8.15}
$$

Combining (8.15) into a single expression yields

$$V^2 = V_{qs}^2 + Vds^2 = (R_a I + \omega \Psi_{md})^2 + (\omega L_s I)^2 \tag{8.16}$$

Each of the parameters R_a, L_s and Ψ_{md} can be written in the form

$$
\begin{aligned}
R_a &= N_c^2 R_{a0} \\
L_s &= N_c^2 L_{s0} \\
\Psi_{md} &= N_c \Psi_{md0}
\end{aligned}
\tag{8.17}
$$

where R_{a0}, L_{s0} and Ψ_{md0} are parameters calculated assuming that there is only one turn per coil with $N_c I$ as the total current in that single-turn coil. Substituting (8.17) into (8.16) yields

$$
V^2 = \left(N_c^2 R_{a0} \frac{N_c I}{N_c} + \omega N_c \Psi_{md0}\right)^2 + \left(\omega N_c^2 L_{s0} \frac{N_c I}{N_c}\right)^2 \tag{8.18}
$$

From (8.18) the number of turns per coil is equal to

$$
N_c = \frac{V}{\sqrt{\left(R_{a0} N_c I + \omega \Psi_{md0}\right)^2 + \left(\omega L_{s0} N_c I\right)^2}} \tag{8.19}
$$

Note that $N_c I$ is known from (8.13). Once the number of turns per coil is known, the armature current is simply

$$
I = \frac{N_c I}{N_c} \tag{8.20}
$$

Stage 3

The main objectives of the optimized design of a surface PM motor are selected as following:

a) Maximize efficiency,

b) Minimize active volume.

These two objectives are in conflict since the requirement for high efficiency naturally leads to designs of larger volume, which have lower flux densities in the core, smaller number of turns per coil, smaller linear current density and larger flux linkage per pole. The objective functions have been defined in the following manner:

a) Efficiency: $OF_1 = \eta$ (see Chapter 7)

b) Normalized active volume: $OF_2 = \frac{\frac{D_o^2}{4}\pi l_a}{\frac{D_{o0}^2}{4}\pi l_{a0}}$

where D_{o0} and l_{a0} are the maximum allowed outer diameter and stack length according to Table 8.1. The goal is to obtain a set of nondominant design solutions which show the trade-offs between these two objectives and provide substantial information, based on which the optimal solution can be selected as the best compromise between the conflicting requirements.

Stage 4

There are several other important motor parameters for which inequality constraints are set to assure that they meet minimum requirements. These constraints are:

a) Minimum torque requirement at rated speed: $T \geq 24\ \mathrm{Nm}$

b) Maximum torque ripple: less than 2.5% of the rated torque

c) Minimum power factor: $cos\varphi \geq 0.8$,

d) Maximum flux density in the stator core tooth: $B_{ts} \leq 1.7$ T

e) Maximum flux density in the stator and rotor yoke: $B_y \leq 1.4$ T

f) Maximum rms linear current density: $K_{1s} \leq 25000$ A/m

g) Maximum allowed fundamental component of the armature winding MMF for magnet protection: $\mathrm{MMF}_{1max} \leq k_{safe}\frac{1}{\mu_0}\left[B_r\frac{l_m}{\mu_r} - B_D\left(g + \frac{l_m}{\mu_r}\right)\right]$ [A], $k_{safe} = 0.7$ - safety factor

The desired torque is to be higher than 24 Nm so that a design goal to have a 5 kW motor at 2000 rpm is met. The maximum allowed value of the torque has not been limited. Its limit is set indirectly by limiting the design variables and by setting the design constraints.

The minimum allowed torque ripple is set since the emphasis of the thesis is on the design of PM motors with reduced torque pulsations. The design variables which are used to control the level of torque pulsations are the number of slots, number of poles and the magnet arc to pole pitch ratio.

The minimum power factor is set to limit the required kVA rating of the inverter relative to the power rating of the motor.

The flux densities in the core region are limited to prevent extreme saturation of the core and high core losses.
Since the thermal model of the motor is not included in the analysis, the linear current density has been used as a thermal constraint to prevent potential overheating of the armature winding insulation. The limit of 25000 A/m has been selected based on typical values found in literature for this power rating of the motor [74, 80]. For more precise calculations the thermal model should be included to estimate the maximum winding temperature and constrain it according to specifications for the wire insulation.
The magnet protection constraint imposed on the armature winding is used to protect the magnets from demagnetization. The safety factor k_{safe} has been used to shift the margin between the minimum operating flux density of the magnets which occurs when all the armature MMF opposes the magnet field and the demagnetization flux density B_D.

Stage 5

The selected optimization method is the Differential Evolution which has been explained in detail in Section 8.1. The decisions that need to be made prior to running the DE algorithm are the size of the population, the number of vectors in the Pareto set and the values of the DE control parameters F and CR. The size of the population is usually related to the number of design variables. In most cases a good initial guess is to set the population size at 3-5 times larger than the number of design variables. If the population size chosen is too small, there will not be enough variety among the members of the population. This can lead to a premature convergence to some local minimum. Alternatively, if the population size is too large, then it will take a lot more computational time to evaluate all the members of the population without significantly reducing the number of generations needed to reach the optimal solution. In the case of a surface PM motor design there are 10 variables so the selected population size is **NP=50**. The maximum number of nondominant vectors in the Pareto set is chosen to be 50. The values of the DE control parameters F and CR which would lead to the fastest convergence cannot be determined in a straightforward manner. Therefore, several runs of the DE algorithm have been carried out for different combinations of

F and CR to observe their influence on the final results and determine which combination is the best for this particular motor design problem. These parameters also affect the total number of nondominant solutions in the Pareto set that can be found in a given number of iterations which is another important issue in the case of multiobjective optimization. For each simulation the results were collected after 200 iterations.

Stage 6

The values of the objective functions for the solutions in the Pareto set calculated using different combinations of DE control parameters have been plotted in Fig. 8.2. It is apparent from this figure that combination F=0.3 and CR=0.3 is the best choice because it yields the highest efficiency for any volume of the motor. However, it does not yield the highest number of solutions in the Pareto set which is a minor trade-off. The Pareto front calculated with F=0.3 and CR=0.3 is shown separately in Fig. 8.3.

The slope of the Pareto front reduces as both the efficiency and active volume increase. This means that initially at lower values of efficiency an increase in volume yields a higher increase in efficiency. The choice of the best solution in the Pareto set is left to the designer as the primary decision maker. This decision can be based on priority where higher importance can be given to a smaller size motor while sacrificing the efficiency or vice versa. Another approach to selection can be based on compromise, where the best design could be selected in the section of the Pareto front where further increase in volume is no longer significantly beneficial in terms of increased efficiency. Regardless of the selection strategy, the mere fact that a choice exists among a whole set of solutions which provide insight into design trade-offs is the principle benefit of the multiobjective approach to optimized design.

The results obtained with F=0.3 and CR=0.3 after 200 generations are shown in Table 8.3. The last two columns of the table are values of the objective functions. The solutions in Table 8.3 are nondominant according to the definition of Pareto optimality given in Section 8.1.

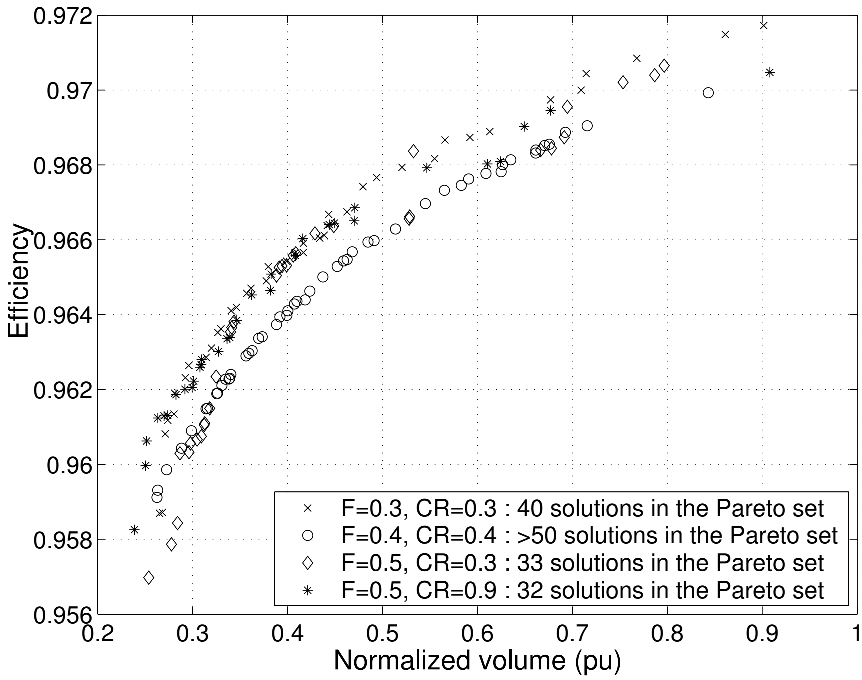

Fig. 8.2 Pareto fronts resulting from multiobjective design optimization of a 5 kW surface PM motor using different combinations of DE control parameters

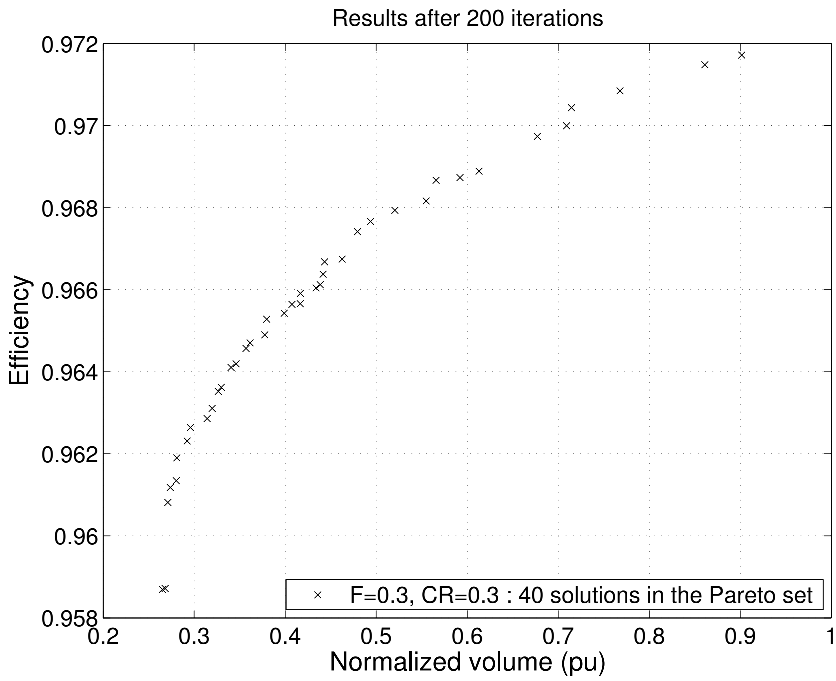

Fig. 8.3 Pareto front resulting from multiobjective design optimization of a 5 kW surface PM motor with DE control parameters set to F=0.3, CR=0.3

Table 8.3 Set of nondominant solutions as a result of multiobjective optimization of a 5 kW surface PM motor using Differential Evolution with control parameters F=0.3, CR=0.3

	D_o [mm]	D_s [mm]	l_a [mm]	d_{ys} [mm]	b_{ts} [mm]	l_m [mm]	α_p	B_r [T]	Q_s	$2p$	T_{em} [Nm]	η [%]	V/V_0 [%]
1	171.9	108.8	71.2	14.0	5.14	4.53	0.829	1.19	39	8	24.8	0.9587	0.265
2	168.4	107.4	75.1	13.5	5.07	4.27	0.829	1.19	39	8	24.3	0.9587	0.268
3	156.1	101.6	88.3	11.4	5.35	4.82	0.821	1.32	39	8	23.9	0.9608	0.271
4	161.4	99.6	83.4	13.3	5.26	4.42	0.836	1.32	39	8	25.0	0.9612	0.274
5	163.3	97.9	83.4	14.1	5.13	4.50	0.785	1.32	39	8	25.8	0.9613	0.281
6	166.7	106.6	80.3	12.6	5.61	4.82	0.827	1.32	39	8	27.1	0.9619	0.281
7	175.1	112.1	75.6	14.4	5.95	4.62	0.807	1.32	39	8	26.6	0.9623	0.292
8	167.8	104.5	83.4	12.8	5.43	4.94	0.821	1.32	39	8	30.5	0.9626	0.296
9	165.0	103.5	91.6	12.9	5.45	4.62	0.807	1.32	39	8	29.9	0.9629	0.314
10	167.8	104.5	90.2	13.7	5.47	4.50	0.830	1.32	39	8	30.6	0.9631	0.320
11	176.2	109.7	83.4	14.4	5.75	4.50	0.790	1.32	39	8	32.5	0.9635	0.327
12	182.5	115.8	78.6	16.9	6.08	4.78	0.836	1.32	39	8	28.7	0.9636	0.330
13	180.0	114.3	83.4	14.2	5.99	4.50	0.819	1.32	39	8	34.8	0.9641	0.341
14	178.9	113.3	85.8	13.7	5.97	4.46	0.822	1.32	39	8	36.1	0.9642	0.346
15	181.4	115.5	86.1	14.2	6.05	4.50	0.823	1.32	39	8	36.8	0.9646	0.357
16	185.4	115.4	83.4	15.1	6.05	4.50	0.842	1.32	39	8	39.0	0.9647	0.362
17	189.3	120.3	83.6	18.0	6.33	4.64	0.809	1.32	39	8	32.3	0.9649	0.378
18	194.8	121.7	79.4	15.8	6.63	4.84	0.817	1.32	39	8	40.8	0.9653	0.380
19	189.3	119.5	88.4	18.2	6.29	4.64	0.820	1.32	39	8	34.4	0.9654	0.399
20	192.5	119.7	87.3	20.0	6.31	4.96	0.822	1.32	39	8	33.4	0.9656	0.408
21	183.0	113.8	98.7	15.0	6.20	4.84	0.817	1.32	39	8	41.9	0.9659	0.417
22	188.5	117.1	93.1	19.2	6.17	4.64	0.820	1.32	39	8	34.2	0.9657	0.417
23	194.6	119.1	90.9	18.8	6.15	3.80	0.826	1.32	39	8	41.7	0.9660	0.434
24	191.1	122.5	95.3	15.7	6.59	4.23	0.828	1.32	39	8	43.1	0.9661	0.439
25	193.6	125.2	93.6	15.7	6.85	5.00	0.814	1.32	39	8	43.2	0.9664	0.442
26	207.5	132.7	81.7	16.7	7.27	5.00	0.833	1.32	39	8	49.0	0.9667	0.443
27	183.0	112.6	109.6	15.3	6.13	4.84	0.817	1.32	39	8	46.7	0.9667	0.463
28	200.4	122.6	94.7	19.6	6.57	4.93	0.811	1.32	39	8	45.8	0.9674	0.480
29	202.0	125.9	96.0	17.4	6.89	5.00	0.833	1.32	39	8	52.3	0.9677	0.494
30	207.5	134.2	96.0	16.8	7.35	5.00	0.825	1.32	39	8	55.3	0.9679	0.521
31	187.6	119.2	125.1	14.8	6.25	4.50	0.830	1.32	39	8	59.8	0.9682	0.555
32	204.5	124.4	107.4	20.8	6.55	4.64	0.822	1.32	39	8	54.1	0.9687	0.566
33	207.5	134.2	109.2	16.8	7.35	4.87	0.836	1.32	39	8	63.0	0.9687	0.592
34	199.4	123.5	122.3	17.6	6.38	3.80	0.826	1.32	39	8	65.9	0.9689	0.613
35	203.7	125.3	129.4	19.8	6.66	4.81	0.846	1.32	39	8	67.2	0.9697	0.677
36	207.5	129.4	130.8	17.9	6.96	4.23	0.836	1.32	39	8	78.0	0.9700	0.709
37	209.3	128.7	129.4	20.3	6.79	4.77	0.811	1.32	39	8	72.7	0.9704	0.715
38	209.3	128.7	139.1	20.3	6.79	4.75	0.811	1.32	39	8	78.1	0.9708	0.768
39	222.6	129.8	137.9	26.3	6.83	4.62	0.807	1.32	39	8	79.4	0.9715	0.861
40	227.9	140.7	137.7	22.0	7.57	4.33	0.794	1.32	39	8	96.2	0.9717	0.902

Note that all designs have a fractional slot winding with 8 poles and 39 slots. The least common multiple between the number of slots and poles is 312, which means that the fundamental component of the cogging torque is 1/8 of the slot pitch. Such a high common multiple is desirable from the aspect of cogging torque reduction because it pushes the cogging torque and also the electromagnetic torque ripple components to higher frequencies where their magnitudes are significantly smaller. Since small torque ripple has been one of the design constraints, it is reasonable that the DE found a slot/pole combination with intrinsically small torque pulsations as the best design solution.

Table 8.3 also shows that as the volume and efficiency of the motor increase, the produced torque also increases and for most designs significantly exceeds the torque requirement for the 5 kW power output at 2000 rpm. This means that with constant current density (6 $\mathrm{A/mm^2}$) it is not possible to find designs with higher efficiency without oversizing the motor in terms of its torque production. The only way to maintain the output torque close to the required 24 Nm and observe the trade-offs between the efficiency and the motor volume is to add current density as the design variable and vary its value. The current density, the slot area and the slot fill factor determine the total ampere-turns per slot which are proportional to the developed torque. In other words the design trade-off required to increase the efficiency of the motor for a given power output is to reduce its current density which in turn reduces the armature winding losses. Since the torque is proportional to the number of ampere-turns per slot, the reduction of current density requires larger slot area and consequently larger volume of the motor to produce the desired torque.

To demonstrate this principle another simulation has been carried out with current density added as a design variable with the constraint

$$1\ \mathrm{A/mm^2} \leq J \leq 6\ \mathrm{A/mm^2}$$

Moreover, the torque constraint has been modified as follows:

$$24\ \mathrm{Nm} \leq T \leq 25\ \mathrm{Nm}$$

This modified torque constraint insures that all designs in the Pareto set have a power output close to the desired 5 kW. The DE control parameters have been set to F=0.3, CR=0.3.

The Pareto front resulting from this modified design scheme with varying current density is shown in Fig. 8.4, while solutions in the Pareto set are given in Table 8.4.

Table 8.4 Set of nondominant solutions as a result of multiobjective optimization of a 5 kW surface PM motor using Differential Evolution with current density used as a design variable

	D_o [mm]	D_s [mm]	l_a [mm]	d_{ys} [mm]	b_{ts} [mm]	l_m [mm]	α_p	B_r [T]	Q_s	$2p$	J [A/mm^2]	T_{em} [Nm]	η [%]	V/V_0 [%]
1	169.6	111.4	77.1	10.50	5.83	4.44	0.824	1.04	33	8	5.19	24.68	0.9574	0.279
2	173.6	110.5	76.9	11.07	4.55	4.34	0.807	1.04	39	8	4.51	24.08	0.9603	0.292
3	170.5	100.8	81.5	11.04	7.89	4.21	0.852	1.32	27	10	4.28	24.52	0.9612	0.299
4	170.5	99.3	81.5	11.29	7.77	4.66	0.825	1.32	27	10	4.28	24.61	0.9615	0.299
5	177.7	103.4	81.5	11.76	8.10	4.21	0.787	1.32	27	10	3.89	24.76	0.9619	0.324
6	177.0	108.0	86.0	12.89	6.04	4.68	0.788	1.16	39	8	4.79	24.33	0.9621	0.339
7	178.0	108.6	86.0	12.96	5.45	4.33	0.804	1.16	39	8	4.10	24.17	0.9637	0.343
8	209.0	121.1	63.0	14.95	4.98	4.40	0.794	1.04	39	8	3.02	24.58	0.9639	0.347
9	167.6	94.3	102.8	13.21	4.55	4.53	0.789	1.19	39	8	3.81	24.85	0.9647	0.364
10	170.5	94.9	109.0	12.79	4.63	4.22	0.806	1.23	39	8	3.09	24.26	0.9653	0.399
11	200.7	111.3	87.6	15.43	5.65	4.53	0.815	1.10	39	8	2.73	24.56	0.9663	0.445
12	209.0	121.1	95.3	23.03	4.98	4.40	0.794	1.04	39	8	3.02	24.08	0.9670	0.525
13	210.0	115.5	104.2	24.98	5.17	3.92	0.793	1.04	39	8	3.09	24.87	0.9674	0.579

Note that the number of solutions in the Pareto set found after 200 iterations is only 13 which is significantly smaller than found in the cases shown in Fig. 8.2. The reason for such a result is due to the fact that the output torque the motor is required to produce has been constrained more severely (24 Nm≤T≤25 Nm) than before ($T \geq 24$ Nm). This constraint significantly reduces the number of feasible solutions in the design space and makes it more difficult for the DE to find those solutions. Since all designs in the Pareto set have a similar torque output, the design trade-off between the motor size (i.e. volume) and the efficiency is now more apparent. In order to increase the motor efficiency by 1% it is required to increase its volume by approximately 100%. Such a significant increase in motor volume is a serious penalty which must be paid if one desires to improve the motor efficiency.

8.3 Optimized Design of an Interior PM motor

Interior PM motors are attractive for applications where operation in a wide speed range is required (e.g. traction). Unlike surface PM motors which have the same value of inductance in d and q axes

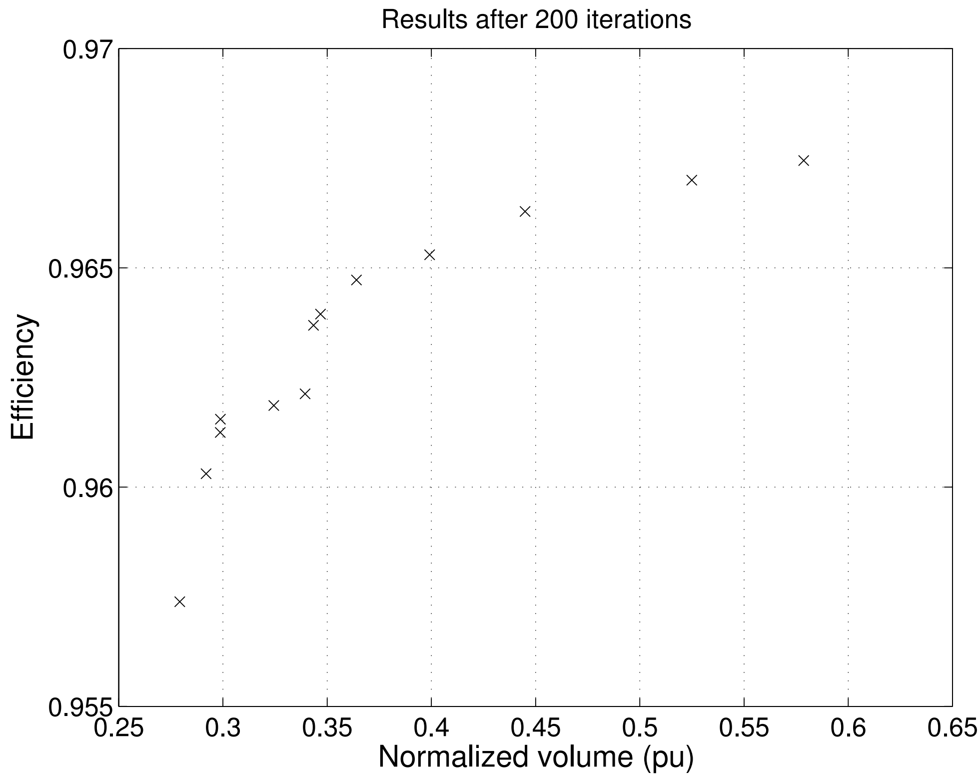

Fig. 8.4 Pareto front resulting from multiobjective design optimization of a 5 kW surface PM motor with current density used as a design variable

and where all the torque is produced by the magnet flux, interior PM motors have different d and q inductances which results in an additional torque component called reluctance torque. The fundamental torque equation for an IPM motor is given by

$$T_{em} = \frac{3}{2}p[\underbrace{\Psi_{md}I_{qs}}_{\text{Magnet torque}} - \underbrace{(L_q - L_d)I_{qs}I_{ds}}_{\text{Reluctance torque}}],\ L_q > L_d \tag{8.21}$$

where p is the number of pole pairs, Ψ_{md} is the magnet flux, L_d, L_q, I_{ds} and I_{qs} are the d and q axis inductances and currents respectively. This torque equation can be derived from the phasor diagram shown in Fig. 8.5. The maximum torque per amp operation in this case will occur when the current phasor is shifted by an angle γ relative to the q axis. In surface PM motors the maximum torque per amp operation occurs at $\gamma = 0$.

There are two distinct regimes of operation of an IPM motor: constant torque below corner speed and constant power above corner speed, as indicated in Fig 8.6. The corner speed is defined as the maximum speed at which rated torque can be developed with rated current flowing without exceeding the maximum terminal voltage available from the inverter. Above that speed it is possible to maintain constant power, but it is not possible to develop rated torque without exceeding the voltage constraint imposed by the power supply. Moreover, the ability to maintain constant power is not universally attainable for all interior PM motor designs. Only designs which satisfy the optimal flux weakening condition first derived by Schiferl and Lipo [52] will give the maximum constant power output in the field weakening regime above corner speed. This condition is given by

$$\Psi_{md} = L_d I_R \tag{8.22}$$

where Ψ_{md} is the flux of the magnets alone linked by the armature winding, L_d is the d axis inductance and I_R is the rated armature current. The normalized characteristic current is the quantity used to show the properties of the IPM motor in the flux weakening regime with respect to the optimal flux weakening condition. It is defined as

$$I_c = \frac{\Psi_{md}}{L_d I_R} \tag{8.23}$$

The IPM motor design which satisfies (8.22) apparently has $I_c = 1$.

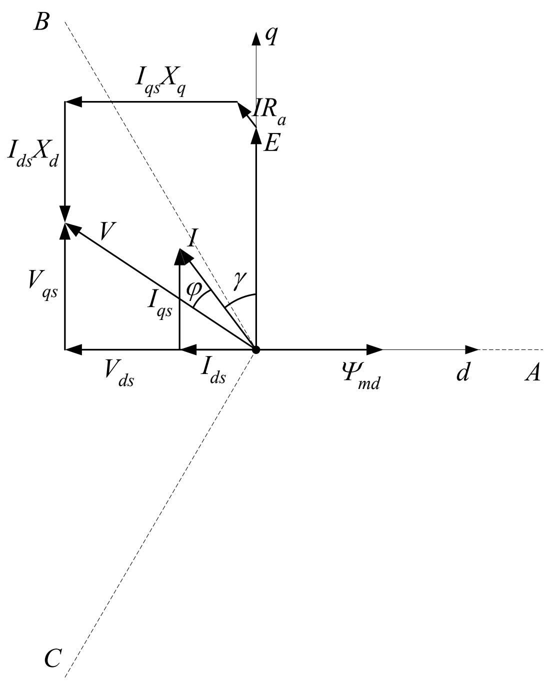

Fig. 8.5 Phasor diagram of an interior PM motor

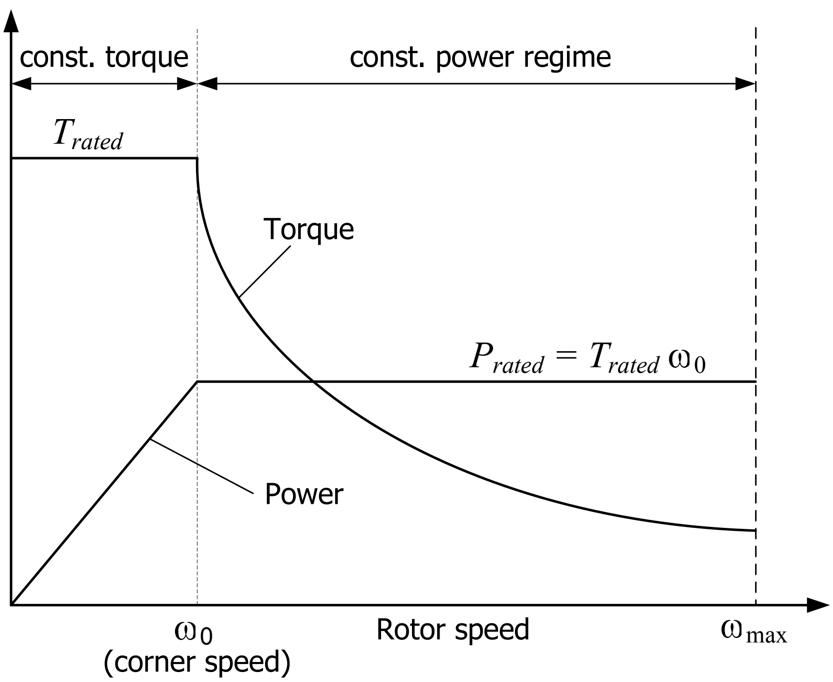

Fig. 8.6 Capability curves of an interior PM motor

Since optimal flux weakening condition has such a profound effect on the IPM motor performance at high speed, it has been considered as one of the main objectives in the optimization scheme. The other objective is to minimize cogging torque by shaping the magnets and adjusting their angular span.

There are many possible configurations of the cavities in the rotor, where the magnets are placed, with a common purpose to increase the saliency ratio

$$\xi = \frac{L_q}{L_d} \tag{8.24}$$

thereby increasing the reluctance torque. Soong and Miller [88] showed that there is an apparent trade off between the saliency ratio ξ and the required magnet flux Ψ_{md} to satisfy the optimal flux weakening condition. The higher the saliency ratio the lower the magnet flux. This means that for higher ξ the magnets with lower remanence B_r, and thereby lower cost, can be used for the same constant power output. Another benefit of low Ψ_{md} is lower back emf at high speeds. This relates to the problem of uncontrolled generation which occurs if the inverter switches lose their gating signals and the motor back emf induces currents which flow back to the DC bus through anti parallel diodes.

The IPM motor topology proposed in this thesis follows the work by Lovelace et al. [51]. The IPM motor in [51] was designed as an integrated starter-alternator and optimized to minimize the cost of the motor. The motor had two layers of cavities in the rotor. The design proposed here is a modified version of the one in [51]. The modification of the rotor design has been done so that magnets of a simple rectangular shape can be used which are cheaper to manufacture. The design by Lovelace is shown in Fig. 8.7, while the proposed modified design is shown in Fig. 8.8. The main purpose of this design is to confirm that the proposed multiobjective optimization scheme based on Differential Evolution can be successfully used for the optimized design of IPM motors.

The IPM motor in [51] was designed using the lumped parameter model. That model can be solved very quickly on a digital computer which is a great advantage in the optimized design. However, it does not provide information about cogging torque which is one of the design goals in this thesis. Therefore, the finite element method remains as an alternative. The FE method has been used here to calculate the motor parameters, including cogging torque, and find the optimal design of

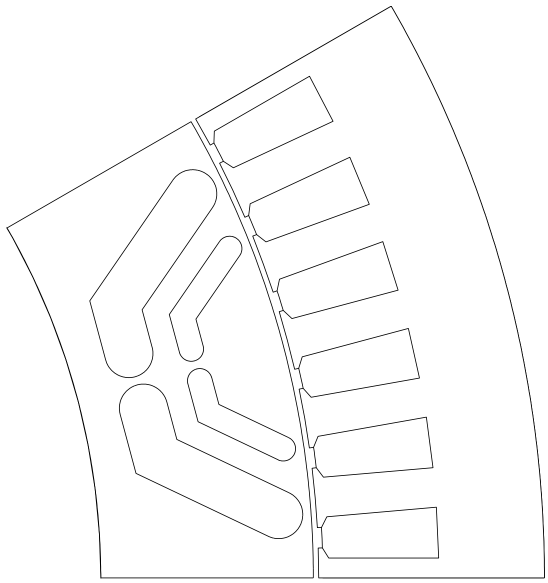

Fig. 8.7 One pole pitch of a 10 pole interior PM motor designed by Lovelace

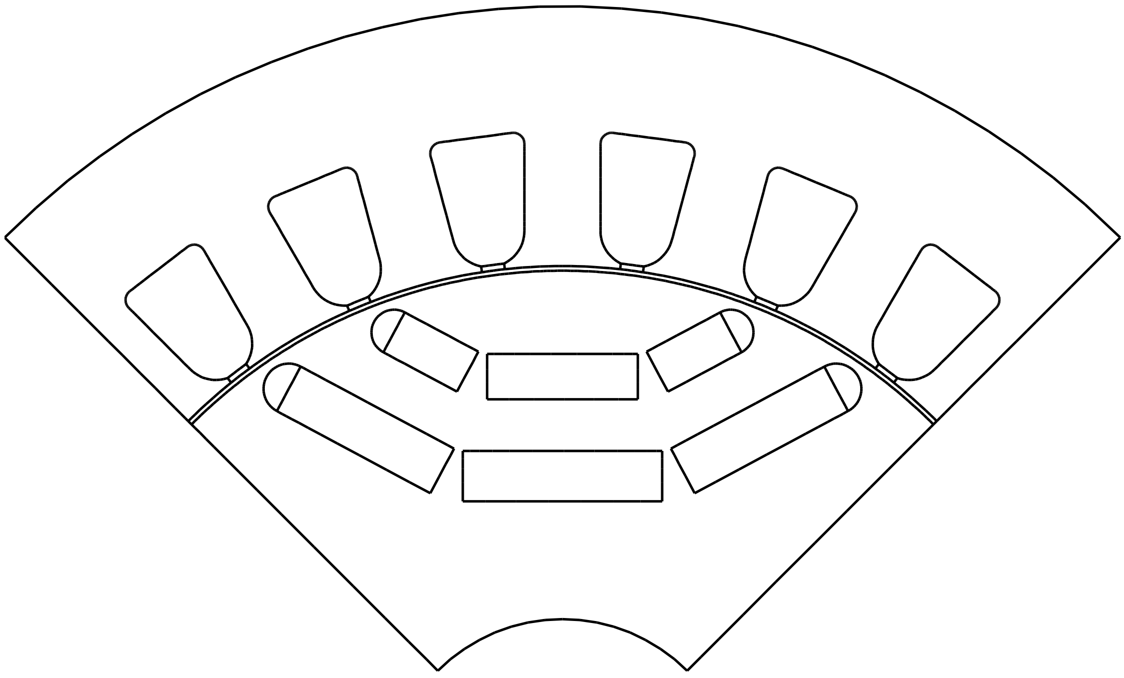

Fig. 8.8 Interior PM motor topology proposed in this thesis

the motor in Fig. 8.8 which comes as close as possible to satisfying the optimal flux weakening condition and has a minimum cogging torque. The downside of the FE approach is that it is computationally more demanding than the lumped parameter model which significantly extends the computational time needed to find the optimal design solution. To reduce the computational time, especially for cogging torque calculation, the FE method has been combined with the model of the complex relative air gap permeance derived in Chapter 2 to estimate the cogging torque waveform using the results of only two magnetostatic FE simulations. This approach is explained in more detail in Section 8.3.2.

8.3.1 FE Approach to Calculation of Parameters of an IPM Motor

The motor parameters that have to be calculated for each set of design variables which are being optimized are the winding resistance and inductances, the magnet flux and the number of turns per coil. In addition, power factor, efficiency and cogging torque must be calculated as well. The motor is designed for a rated operating point at corner speed. Each vector of design variables generated by the DE algorithm which satisfies the inequality constraints must also satisfy the terminal voltage constraint at corner speed. This constraint is used to separate the number of turns per coil N_c from the armature current I as done earlier in the case of a SPM motor design. As before, the parameters are calculated with an assumption that there is only one turn per coil with N_cI as the total current in the coil. The available number of ampere turns per coil N_cI is obtained from (8.13). The additional problem with the IPM motor is the lack of knowledge about the current control angle γ_{Tmax} (see Fig. 8.5) at which maximum torque per amp is achieved. To determine γ_{Tmax}, five nonlinear magnetostatic simulations with γ ranging from -20^0 to -60^0 are run first. The electromagnetic torque is calculated for each value of γ using the well known equation

$$T_{em} = \frac{3}{2}p(\Psi_{ds}i_{qs} - \Psi_{qs}i_{ds}) \tag{8.25}$$

where p is the number of pole pairs, Ψ_{ds}, Ψ_{qs}, i_{ds} and i_{qs} are the d and q components of the flux linkage and current respectively. The flux linkages Ψ_{ds} and Ψ_{qs} are determined from the flux linkages of phases A, B and C. For instance, the phase A flux linkage is calculated as a sum of the flux linkages of all phase A coils. The flux linkage of each individual coil is equal to the line integral of the magnetic vector potential A_z along the contour of the coil. In a 2-D FE model this integral is proportional to the difference between the average potential in the meshed geometric regions occupied by the coil sides located in different pole regions. The phase A flux linkage is then

$$\Psi_a = p \sum_{k=1}^{Q_{coilp}} \Psi_{coilk} = p \sum_{k=1}^{Q_{coilp}} \frac{1}{S} \left(\int_{S_1} A_z \mathrm{d}S - \int_{S_2} A_z \mathrm{d}S \right) N_c l_a \tag{8.26}$$

where Q_{coilp} is the number of coil sides per phase in one pole region, p is the number of pole pairs, N_c is the number of turns of each coil, l_a is the length of the stator core and S is the cross-section of the coil region. Subscripts 1 and 2 denote coil sides located in different pole regions. Since the number of turns per coil is not known at this stage, the flux linkages Ψ_{a0}, Ψ_{b0} and Ψ_{c0} are calculated assuming $N_c = 1$. The flux vector can now be formed

$$\underline{\Psi}_0 = \Psi_{ds0} + j\Psi_{qs0} = \frac{2}{3} \left(\Psi_{a0} + a\Psi_{b0} + a^2\Psi_{c0} \right),\ a = e^{j\frac{2\pi}{3}} \tag{8.27}$$

with

$$\begin{aligned} \Psi_{ds0} &= \frac{2}{3} \left(\Psi_{a0} - \frac{1}{2}\Psi_{b0} - \frac{1}{2}\Psi_{c0} \right) \\ \Psi_{qs0} &= \frac{1}{\sqrt{3}} \left(\Psi_{b0} - \Psi_{c0} \right) \end{aligned} \tag{8.28}$$

The subscript 0 is used to emphasize the fact that flux linkages are calculated with $N_c = 1$.

The currents i_{qs} and i_{ds} are also not known, but the total ampere turns per slot $N_c I$ are known from (8.13). Using γ and $N_c I$ one can calculate

$$\begin{aligned} N_c i_{qs} &= N_c I \cos\gamma \\ N_c i_{ds} &= N_c I \sin\gamma \end{aligned} \tag{8.29}$$

Considering the fact that $\Psi_{ds} = N_c \Psi_{ds0}$ and $\Psi_{qs} = N_c \Psi_{qs0}$, the torque equation (8.25) can be written in the form

$$T_{em} = \frac{3}{2} p (\Psi_{ds0} N_c i_{qs} - \Psi_{qs0} N_c i_{ds}) \tag{8.30}$$

where $N_c i_{qs}$ and $N_c i_{ds}$ are calculated from (8.29).

With the torque calculated for five values of γ, cubic spline is used to generate a smooth T_{em} vs. γ curve as shown in Fig. 8.9 and find the value of γ_{Tmax} where the maximum torque occurs.

Another nonlinear simulation with γ_{Tmax} as the control angle is run to get the field solution for this operating point. The most effective approach to calculate saturated L_d, L_q and Ψ_{md} and still preserve all the information about the saturation in the motor is to "freeze" the permeabilities in the nodes of the finite element mesh. Once the permeabilities are frozen the problem becomes linear and the parameters can be determined one at the time. This is the only approach that can be used to accurately calculate saturated parameters at an operating point. Three linear magnetostatic simulations are needed to determine L_d, L_q and Ψ_{md}. In addition, cross-saturation parameters L_{qd}, L_{dq} and Ψ_{mqd} can be determined from the same simulations. Although small in this particular case, the effect of cross-saturation has been generally recognized as the phenomenon caused by saturation which manifests itself as the flux linkage in the axis perpendicular to the axis where the excitation is applied. At this stage the inductances will be calculated for $N_c = 1$ since the actual N_c is still unknown.

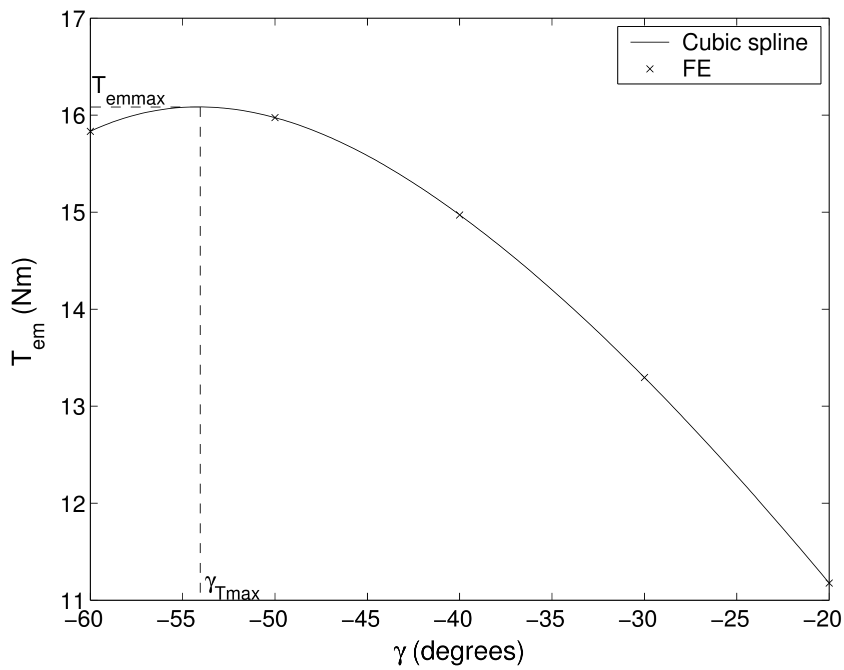

Fig. 8.9 Torque versus control angle curve used to find the control angle for maximum torque. Cubic spline is used to generate the curve from five points obtained by FE method.

Simulation 1

The first linear simulation is used to calculate L_{d0} and L_{qd0}. The magnet flux is turned off by setting the remanence B_r to zero. The current vector must be aligned with the d axis. Since the problem has become linear after freezing the permeabilites, the magnitude of the current vector can be chosen arbitrarily. If the magnitude is chosen to be 1 A, then to align the current vector with the d axis the instantaneous phase currents have to be defined as

$$i_a = 1 \text{ A}, \; i_b = i_c = -\frac{i_a}{2} \tag{8.31}$$

The d and q components of the current vector are then

$$i_{ds} = 1 \text{ A}, \; i_{qs} = 0 \tag{8.32}$$

The flux linkages of phases A, B and C are calculated according to (8.26). The flux vector is formed and its d and q components are calculated using (8.27) and (8.28). The inductances for one turn per coil are then

$$\begin{aligned} L_{d0} &= \frac{\Psi_{ds0}}{i_{ds}} \\ L_{qd0} &= \frac{\Psi_{qs0}}{i_{ds}} \end{aligned} \tag{8.33}$$

Simulation 2

The inductances L_{q0} and L_{dq0} are calculated in a similar manner, only in this case the current vector needs to be aligned with the q axis. The phase currents are then

$$i_a = 0, \; i_b = -i_c = \frac{\sqrt{3}}{2} \text{ A} \tag{8.34}$$

which in turns gives

$$i_{ds} = 0 \text{ A}, \; i_{qs} = 1 \text{ A} \tag{8.35}$$

After calculating the flux components, the inductances for one turn per coil are given by

$$\begin{aligned} L_{q0} &= \frac{\Psi_{qs0}}{i_{qs}} \\ L_{dq0} &= \frac{\Psi_{ds0}}{i_{qs}} \end{aligned} \tag{8.36}$$

Simulation 3

This simulation is used to calculate magnet flux linked by the armature winding. In this case the magnets are turned on by setting the magnet remanence B_r to the actual value while phase currents are equal to zero. The flux linkages of the phase windings are calculated again using the previously described procedure. Equation (8.28) is then used to calculate the flux linkages Ψ_{md0} and Ψ_{mqd0}. Note that although the magnets act only in the direction of the d axis, there will also be a small cross saturation flux linkage in the q axis.

The relationship between the actual parameters and the ones calculated for one turn per coil is given by

$$\begin{aligned} R_a &= N_c^2 R_{a0} \\ L_d &= N_c^2 L_{d0} \\ L_{qd} &= N_c^2 L_{qd0} \\ L_q &= N_c^2 L_{q0} \\ L_{dq} &= N_c^2 L_{dq0} \\ \Psi_{md} &= N_c \Psi_{md0} \\ \Psi_{mqd} &= N_c \Psi_{mqd0} \end{aligned} \tag{8.37}$$

The number of turns per coil can now be calculated from the equations for d and q components of the voltage. Those equations, including the cross saturation terms, are

$$\begin{aligned} v_{qs} &= R_a i_{qs} + \omega \Psi_{ds} \\ v_{ds} &= R_a i_{ds} - \omega \Psi_{qs} \\ V &= \sqrt{v_{qs}^2 + v_{ds}^2} \end{aligned} \tag{8.38}$$

where

$$\begin{aligned} \Psi_{ds} &= \Psi_{md} + L_d i_{ds} + L_{dq} i_{qs} \\ \Psi_{qs} &= \Psi_{mqd} + L_q i_{qs} + L_{qd} i_{ds} \end{aligned} \tag{8.39}$$

Combining (8.38) and (8.39) yields

$$N_c = \frac{V}{\sqrt{\left[R_{a0}N_c i_{ds} - \omega L_{q0}N_c i_{qs} - \omega L_{qd0}N_c i_{ds} - \omega\Psi_{mqd0}\right]^2 + \left[R_{a0}N_c i_{qs} + \omega L_{d0}N_c i_{ds} + \omega L_{dq0}N_c i_{qs} + \omega\Psi_{md0}\right]^2}} \quad (8.40)$$

8.3.2 Approximate Calculation of the Cogging Torque Waveform Using Magnetostatic FE Simulations

The accurate calculation of the cogging torque using the FE method requires field solutions at multiple rotor positions to get at least a dozen points per half-period of the cogging torque. This would require an additional computational effort and would increase the total time needed to find the optimal design by several times. Therefore, in order to save time a combined numerical and analytical approach has been developed to approximate the cogging torque waveform. It has been shown earlier in Chapter 2 that cogging torque can be calculated using (2.136) which requires the knowledge of the flux density distribution in the slotless air gap and the knowledge of the complex air gap permeance. The problem is that in the case of an IPM motor saturation plays a crucial role in the basic concept of the motor and hence should not be excluded from the cogging torque calculations.

The information about open-circuit flux density in the slotless air gap of an IPM motor can be obtained if the flux density waveform in the slotted air gap obtained by the FE method is divided by the complex relative air gap permeance derived in Chapter 2. Once the flux density in the slotless air gap and the complex air gap permeance are known, the cogging torque of an IPM motor can be calculated approximately using (2.136). This approach requires the results of only two magnetostatic FE simulations, one when the rotor axis is aligned with the centerline of the stator tooth and the other when it is aligned with the centerline of the slot opening. The examples of field solutions for these two cases of rotor alignment are shown in Fig. 8.10. In the case of an open-circuit field it is sufficient to generate the FE model only for one half of the pole pitch since the other half, due to symmetry, can be replaced by a Dirichlet boundary condition which sets zero magnetic vector potential along the centerline of the pole.

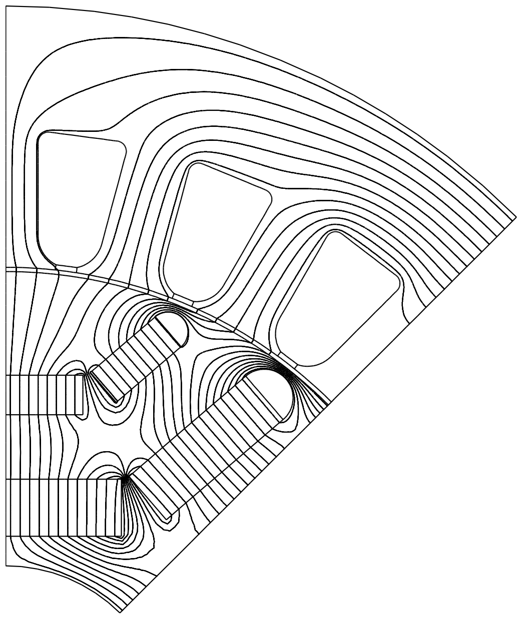

(a)

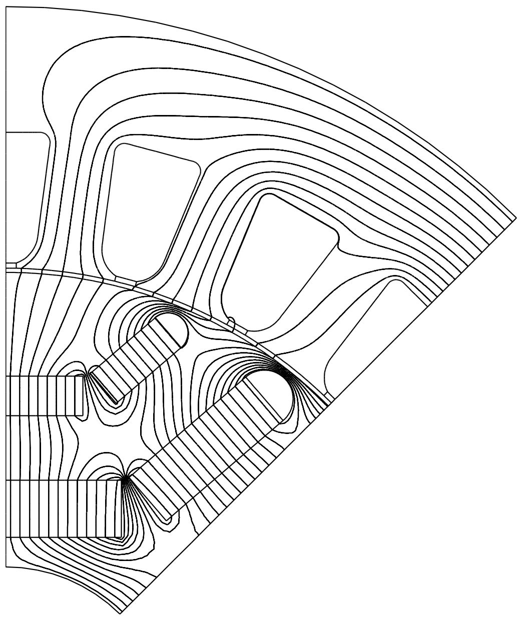

(b)

Fig. 8.10 Flux lines of the open-circuit field solution for two cases of rotor alignment with respect to the slot: (a) rotor aligned with the centerline of the stator tooth, (b) rotor aligned with the centerline of the slot opening

The radial and tangential components of the air gap flux density are calculated from these solutions, divided by the complex air gap permeance to approximate their shapes in the slotless air gap and used to calculate the cogging torque. The waveforms of the radial and tangential components of the open-circuit air gap flux density for both rotor positions are shown in Figs. 8.11 and 8.12. The real and imaginary parts of the complex relative air gap permeance are shown in Figs. 8.13 and 8.14. To approximate the air gap flux density distribution in a slotless motor the waveforms in Figs. 8.11 and 8.12 have been divided by the waveforms in Figs. 8.13 and 8.14 respectively. The radial and tangential components of the flux density in the slotted air gap have been treated as the real and imaginary part of complex vectors $B_{rtc}+jB_{\theta tc}$ and $B_{rsc}+jB_{\theta sc}$. Hence, the flux densities in the slotless air gap for both rotor positions shown in Figs. 8.15 and 8.16 have been calculated as

$$\begin{aligned} B_{rtc(sless)} + jB_{\theta tc(sless)} &= \frac{B_{rtc} + jB_{\theta tc}}{(\lambda_{atc} + j\lambda_{btc})^*} \\ B_{rsc(sless)} + jB_{\theta sc(sless)} &= \frac{B_{rsc} + jB_{\theta sc}}{(\lambda_{asc} + j\lambda_{bsc})^*} \end{aligned} \tag{8.41}$$

For all intermediate rotor positions between the centerline of the tooth and the centerline of the slot opening the waveforms of the flux density in the slotless air gap are obtained by combining the waveforms in Figs. 8.11 and 8.12. Since the motor has 24 slots and four poles, the period of the cogging torque corresponds to one slot pitch. Within one slot pitch the rotor travels from the centerline of the tooth across the centerline of the slot opening (half-period of the cogging torque waveform) and aligns again with the centerline of the next tooth. Hence, the transition from the waveforms in Fig. 8.11 to the waveforms in Fig. 8.12 can be described using

$$\begin{aligned} B_{r(sless)}(\theta) &= \sqrt{\left[B_{rtc}(\theta)\cos\left(\frac{Q_s}{2}\theta\right)\right]^2 + \left[B_{rsc}(\theta)\sin\left(\frac{Q_s}{2}\theta\right)\right]^2}\,\mathrm{sgn}[\cos(p\theta)] \\ B_{\theta(sless)}(\theta) &= \sqrt{\left[B_{\theta tc}(\theta)\cos\left(\frac{Q_s}{2}\theta\right)\right]^2 + \left[B_{\theta sc}(\theta)\sin\left(\frac{Q_s}{2}\theta\right)\right]^2}\,\mathrm{sgn}[\cos(p\theta)] \end{aligned} \tag{8.42}$$

where p is the number of slots, θ is the mechanical angle and sgn is the sign function defined as

$$\mathrm{sgn}(x) = \begin{cases} 1 & \text{, for } x > 0 \\ -1 & \text{, for } x < 0 \end{cases}$$

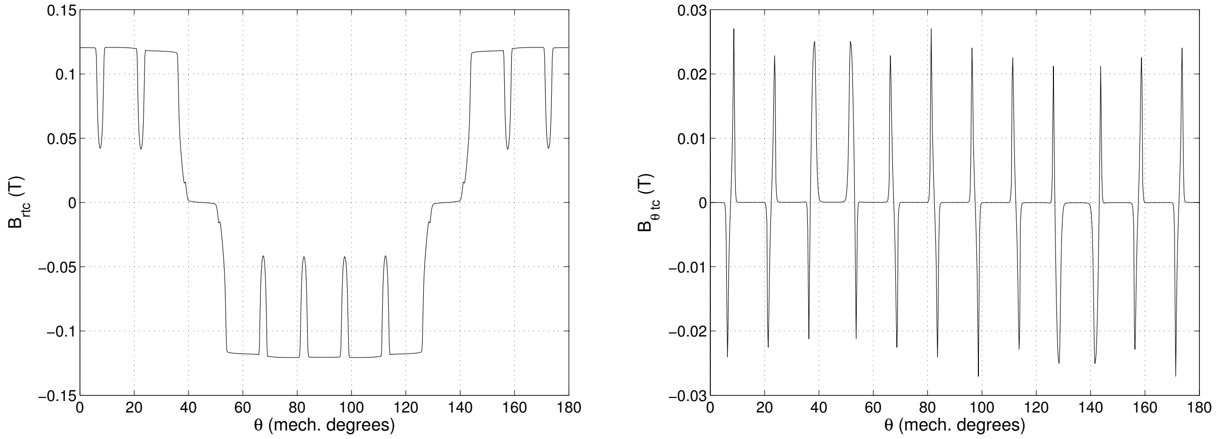

(a) (b)

Fig. 8.11 Waveforms of the open-circuit air gap flux density of an IPM motor with rotor aligned with the centerline of the tooth: (a) radial component, (b) tangential component

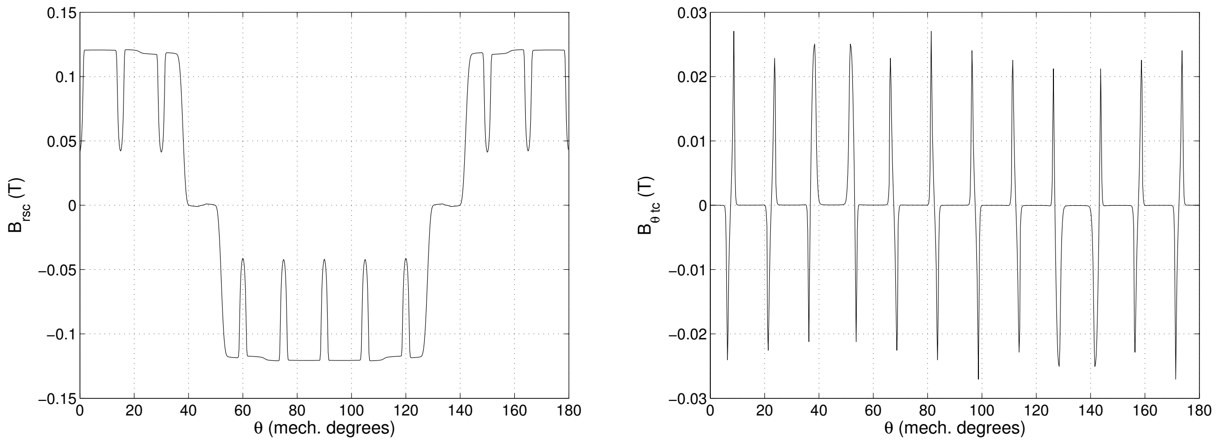

(a) (b)

Fig. 8.12 Waveforms of the open-circuit air gap flux density of an IPM motor with rotor aligned with the centerline of the slot: (a) radial component, (b) tangential component

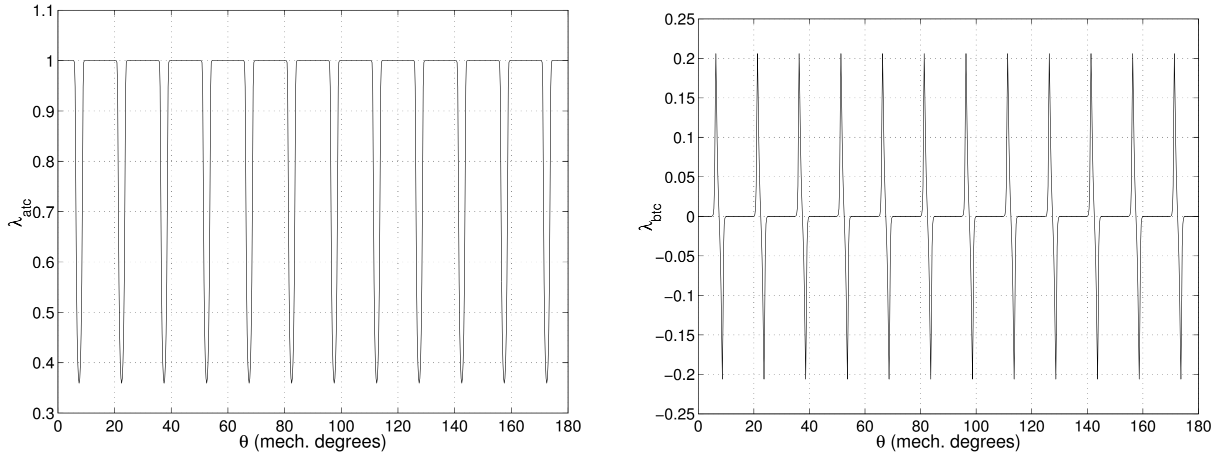

(a) (b)

Fig. 8.13 Waveforms of the complex relative air gap permeance of an IPM motor with rotor aligned with the centerline of the tooth: (a) real component, (b) imaginary component

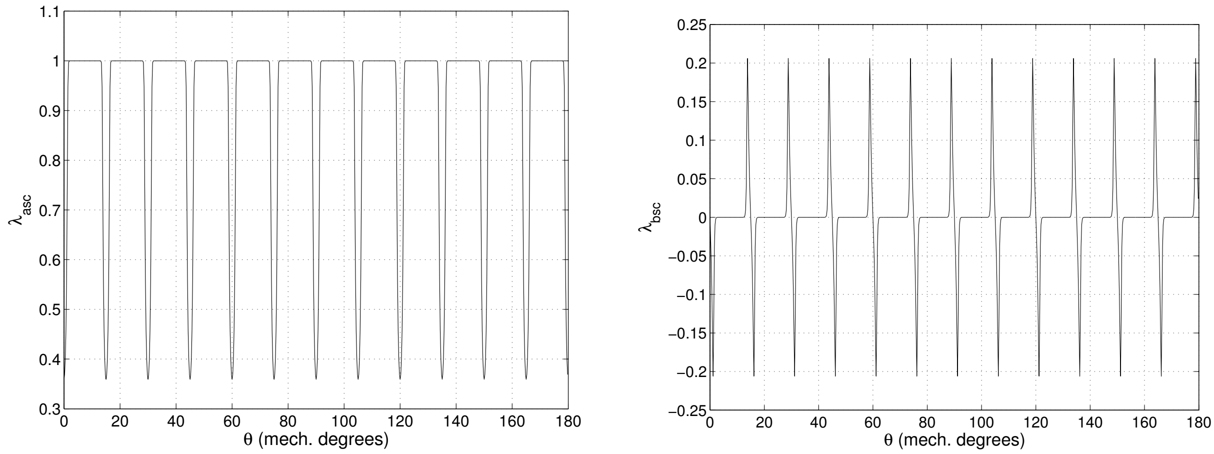

(a) (b)

Fig. 8.14 Waveforms of the complex relative air gap permeance of an IPM motor with rotor aligned with the centerline of the slot: (a) real component, (b) imaginary component

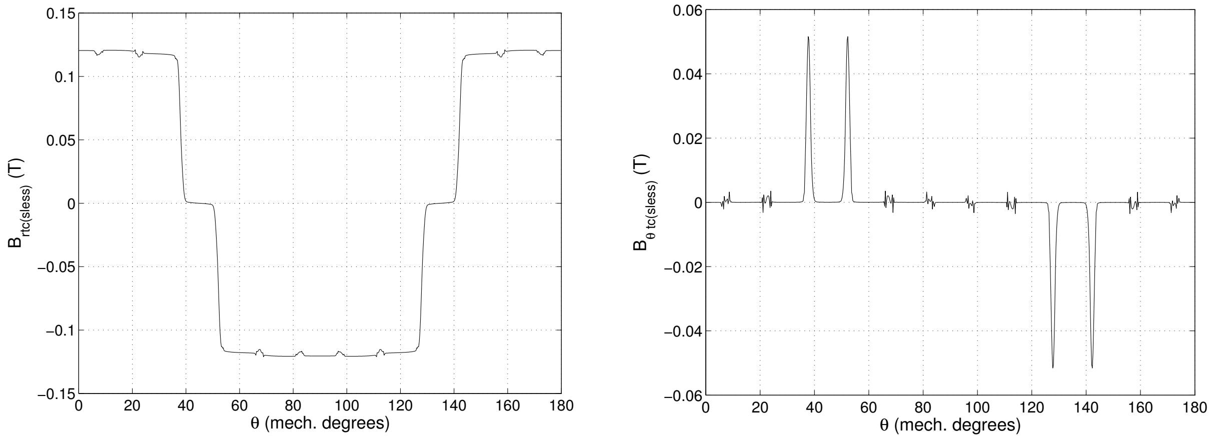

(a) (b)

Fig. 8.15 Waveforms of the open-circuit *slotless* air gap flux density of an IPM motor with rotor aligned with the centerline of the tooth: (a) radial component, (b) tangential component

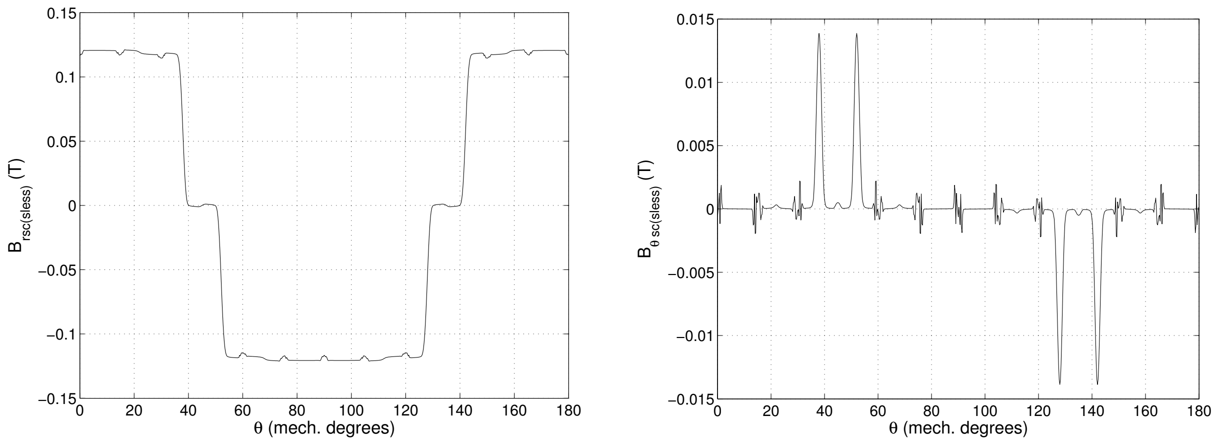

(a) (b)

Fig. 8.16 Waveforms of the open-circuit *slotless* air gap flux density of an IPM motor with rotor aligned with the centerline of the slot: (a) radial component, (b) tangential component

The Fourier coefficients are calculated for each waveform using discrete Fourier transform. The cogging torque is then calculated using (2.136), as done in the case of a surface PM motor.

8.3.3 Calculation of Losses in an IPM Motor

The basic approach to calculation of losses in an IPM motor is quite similar to the one used for the SPM motor described in Chapter 7. The armature winding losses and friction and windage losses are calculated in an identical manner for both motors. However, since calculation of core losses requires the knowledge of time domain waveforms of flux density in the stator teeth and yoke, the procedure for extracting these waveforms in the case of an IPM motor is slightly different. For that motor only single magnetostatic FE simulation for rated load at corner speed is being used. The information which can be extracted from that simulation relates only to a single time instant when the rotor is aligned with the phase A axis. Nevertheless, the information about flux densities in the teeth and yoke in more than one time instant can still be extracted from a single magnetostatic FE simulation. If one considers that a flux passing through each tooth or through each yoke segment above each slot is identical to the flux passing through only one tooth or yoke segment, but at different rotor positions, then from a single magnetostatic FE simulation one can obtain information about tooth and yoke flux waveforms within one half-period at as many time instances as the number of slots per pole. That information can be then used to assemble the approximate flux density waveforms in the teeth and yoke.

The information about the total flux passing through the stator tooth or yoke can be simply extracted from the FE results as the difference between the values of the magnetic vector potential evaluated at the points as indicated in Figs. 8.17 and 8.18 multiplied by the stack length. With two slots per pole per phase this approach yields six sample points per half-period of the flux waveform or 12 points per one full period. The cubic spline is used to interpolate the tooth and yoke flux waveforms anywhere between the sample points. The typical tooth and yoke flux waveforms, together with the original sample points calculated from FE simulation, are shown in Figs. 8.19 and

8.20. The flux density waveforms are then equal to the flux waveforms divided by the corresponding surface areas as done in Chapter 7. The Fourier coefficients needed for calculation of the core losses are obtained using discrete Fourier transforms of the interpolated flux density waveforms.
The magnet losses in the case of an IPM motor are not an issue. However, there are some additional losses on the rotor core surface associated with space harmonics of the armature winding MMF which have not been taken into account in this thesis.

8.3.4 Calculation of the Back Emf in an IPM Motor

The back emf waveform can be estimated from a single magnetostatic finite element simulation by evaluating the distribution of the magnetic vector potential inside the air gap. An example of a no-load field solution from which the back emf waveform is extracted is shown in Fig. 8.21. The distribution of the magnetic vector potential along the circular arc inside the air gap is calculated from this FE solution. Since the FE model represents only one half of the pole pitch, the waveform of magnetic vector potential for one full period, i.e. two pole pitches, can be easily extrapolated using the portion of the waveform calculated for one half of the pole pitch. This is shown in Fig. 8.22.
The instantaneous flux linkage of an armature winding coil is proportional to the difference between the values of the magnetic vector potential in the air gap at locations along the centerlines of the slots occupied by both coil sides. The spatial distribution of the magnetic vector potential in Fig. 8.22 can be also interpreted as the time waveform of the vector potential at one location inside the air gap, but at different rotor positions. In that case its waveform is proportional to the flux linkage of a full pitch coil. The derivative of this flux linkage is equal to the voltage induced in the coil.
The waveform in Fig. 8.22 can be written in the form of Fourier series

$$A_z(t) = \sum_{n=1}^{N_{Az}} A_{zn} \cos(n\omega t) \tag{8.43}$$

where A_{zn} are the Fourier coefficients calculated using discrete Fourier transform, N_{Az} is the maximum order of the Fourier coefficients and ω is the frequency in rad/s. The flux linkage of a

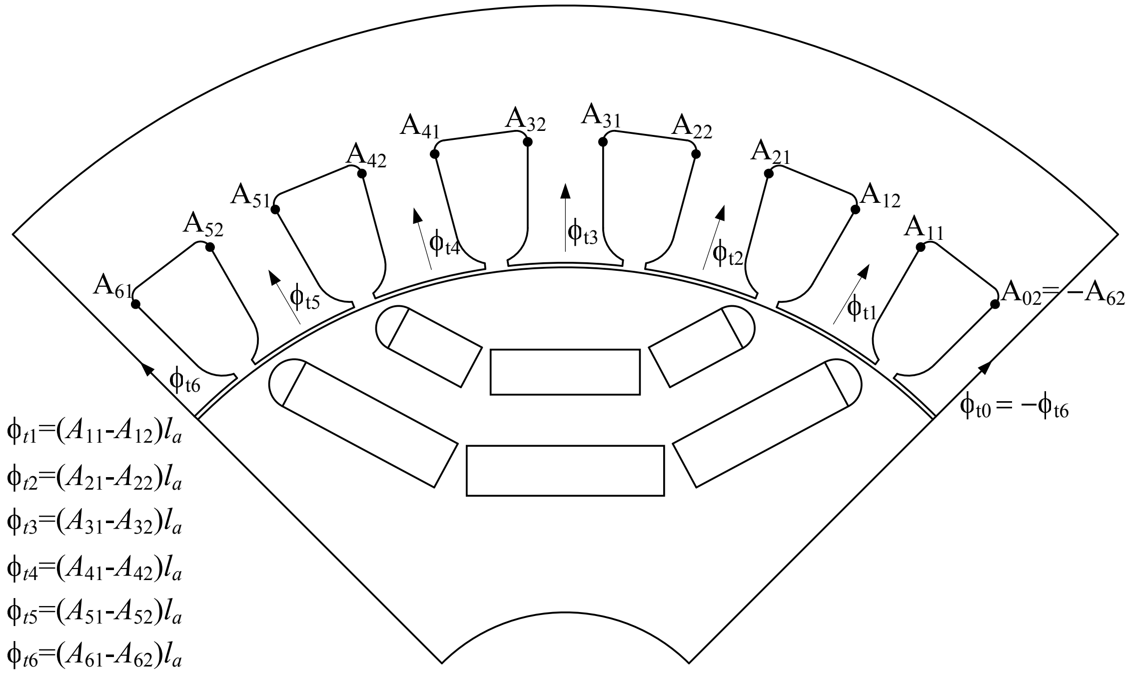

Fig. 8.17 Principle of calculating the tooth fluxes from FE magnetostatic simulation utilized to approximate the tooth flux waveform

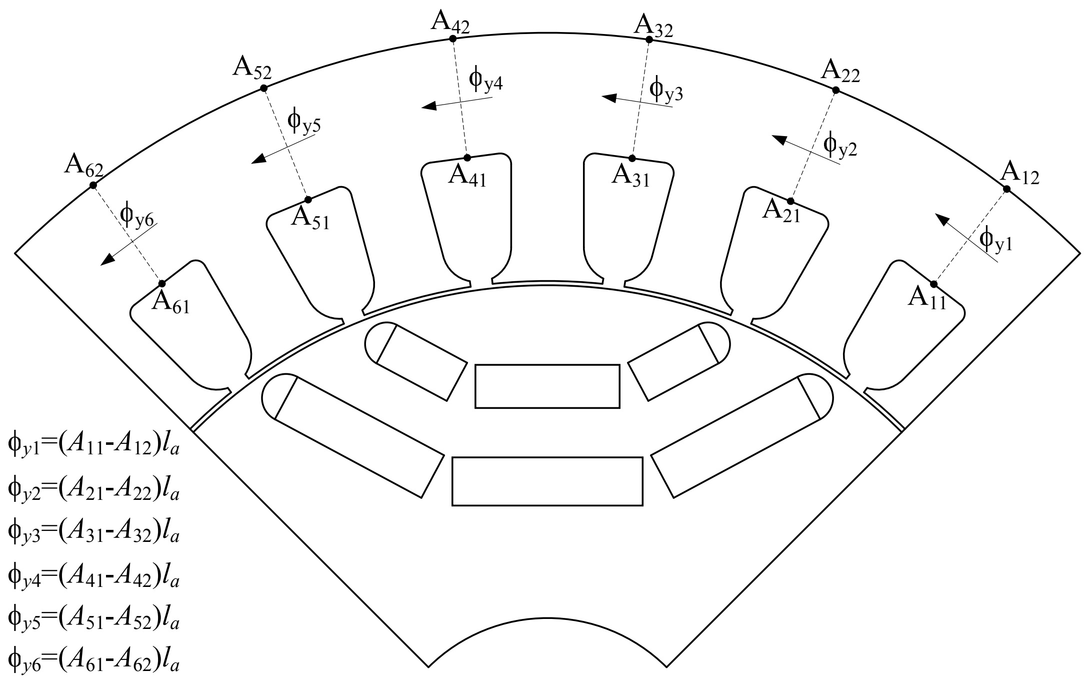

Fig. 8.18 Principle of calculating the yoke fluxes from FE magnetostatic simulation utilized to approximate the yoke flux waveform

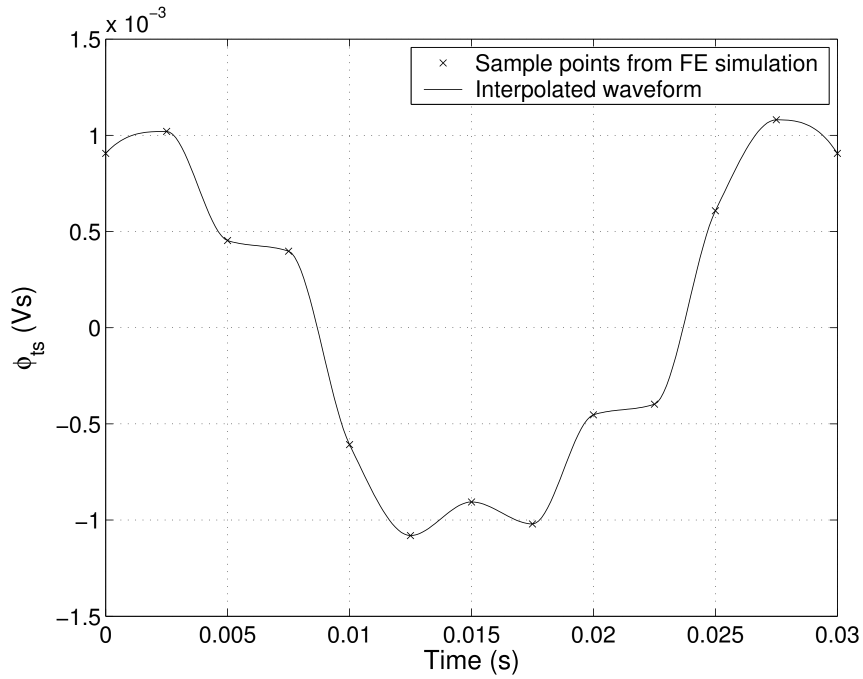

Fig. 8.19 Approximate waveform of the stator tooth flux for the case of rated load at corner speed obtained by interpolating the sample points calculated from magnetostatic FE simulation

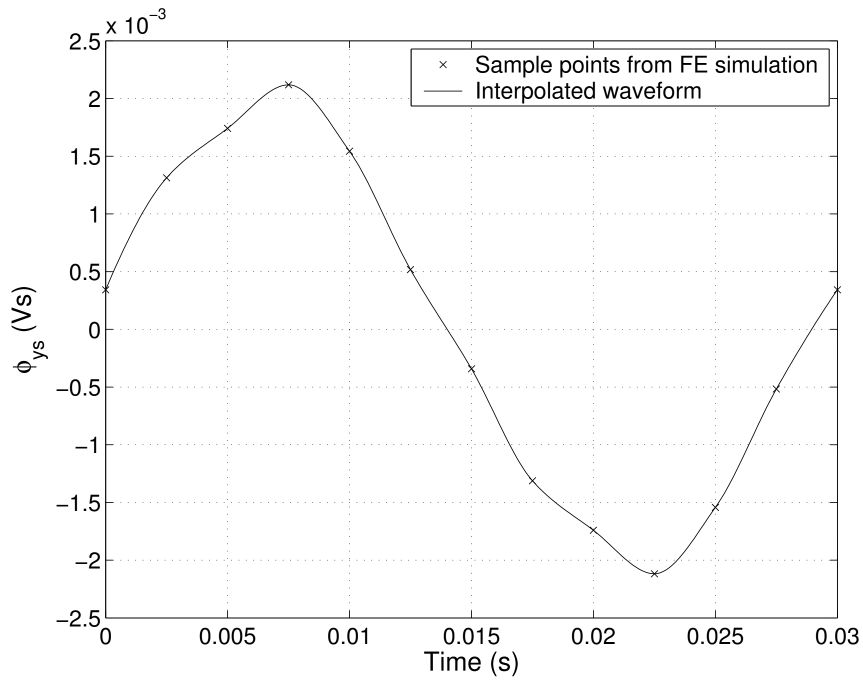

Fig. 8.20 Approximate waveform of the stator yoke flux for the case of rated load at corner speed obtained by interpolating the sample points calculated from magnetostatic FE simulation

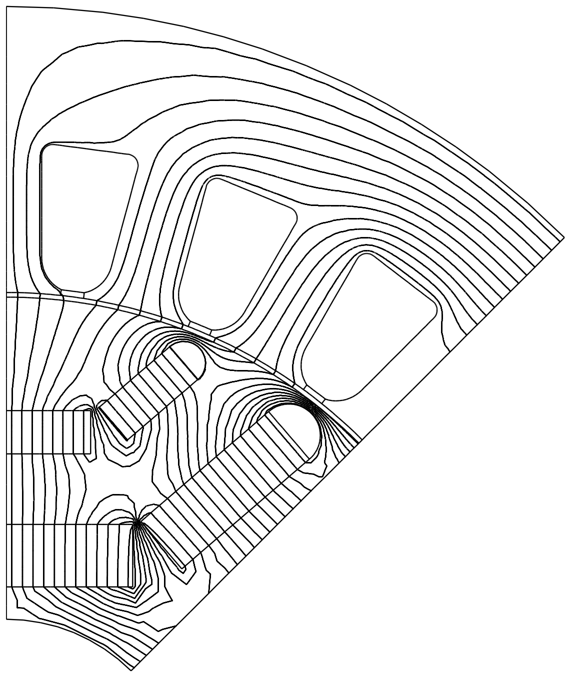

Fig. 8.21 Example of a no-load field solution used for calculation of the back emf waveform

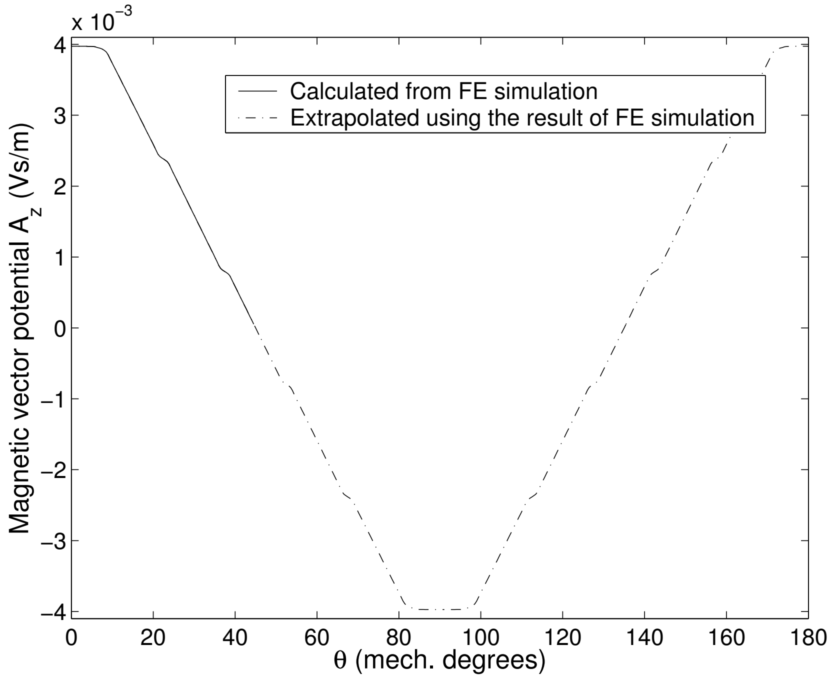

Fig. 8.22 Distribution of the magnetic vector potential inside the air gap of an IPM motor at no-load

full pitch coil is then

$$\Psi_c(t) = 2N_c l_a A_z(t) \tag{8.44}$$

The voltage induced in a coil is

$$E_c(t) = -\frac{\mathrm{d}\Psi_c(t)}{\mathrm{d}t} = 2N_c l_a \omega \sum_{n=1}^{N_{Az}} nA_{zn} \sin(n\omega t) \tag{8.45}$$

The voltages induced in all the coils of a single phase can be added via distribution and pitch factors to take into account the phase shifts between them. The distribution factor for the n^{th} harmonic is defined as

$$k_{dn} = \frac{\sin\left(nq\frac{\alpha}{2}\right)}{q\sin\left(n\frac{\alpha}{2}\right)} \tag{8.46}$$

where q is the number of slots per pole per phase and α is the phase shift between the voltages induced in two adjacent slots. The pitch factor is equal to

$$k_{pn} = \sin\left(p\frac{y_c}{Q_s}\pi\right) \tag{8.47}$$

where y_c is the coil pitch expressed as the number of slot pitches, Q_s is the number of slots and p is the number of pole pairs. The back emf induced in a single phase winding is then

$$E_{phase}(t) = 2N_s l_a \omega \sum_{n=1}^{N_{Az}} k_{dn} k_{pn} nA_{zn} \sin(n\omega t) \tag{8.48}$$

where N_s is the number of turns per phase connected in series. This number of turns is calculated as

$$N_s = \begin{cases} N_c\frac{Q_s}{6a_p}, & \text{for a single-layer winding} \\ N_c\frac{Q_s}{3a_p}, & \text{for a two-layer winding} \end{cases}$$

where a_p is the number of parallel paths. The phase and line-to-line back emf waveforms at 1000 rpm calculated using (8.48) for the motor in Fig. 8.21 are shown in Figs. 8.23 and 8.24.

8.3.5 Definition of Objectives and Constraints

The interior PM motor for which an optimized design is sought has the following specifications:

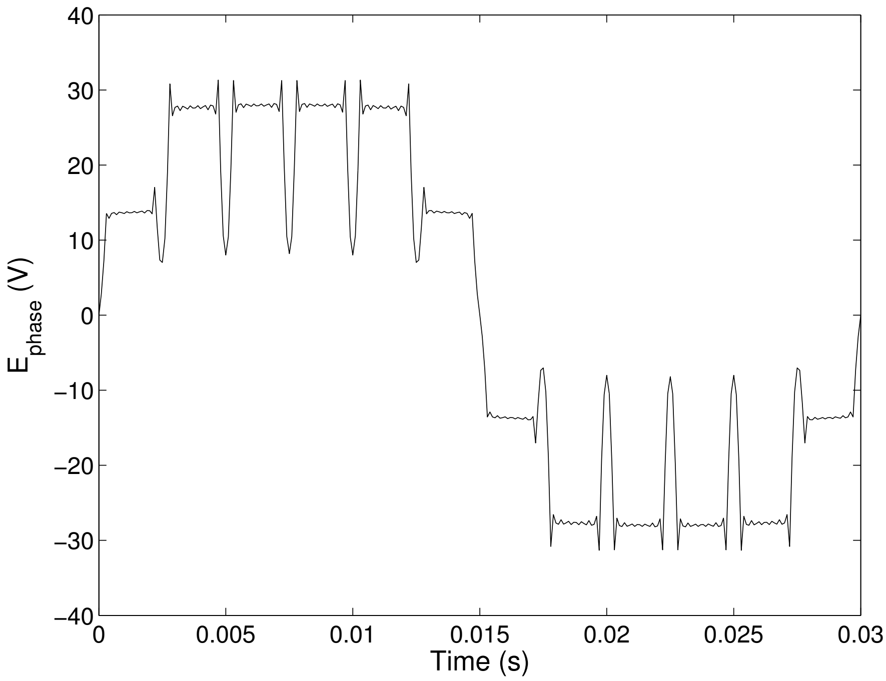

Fig. 8.23 Waveform of the phase back emf of an IPM motor calculated from a single magnetostatic FE simulation

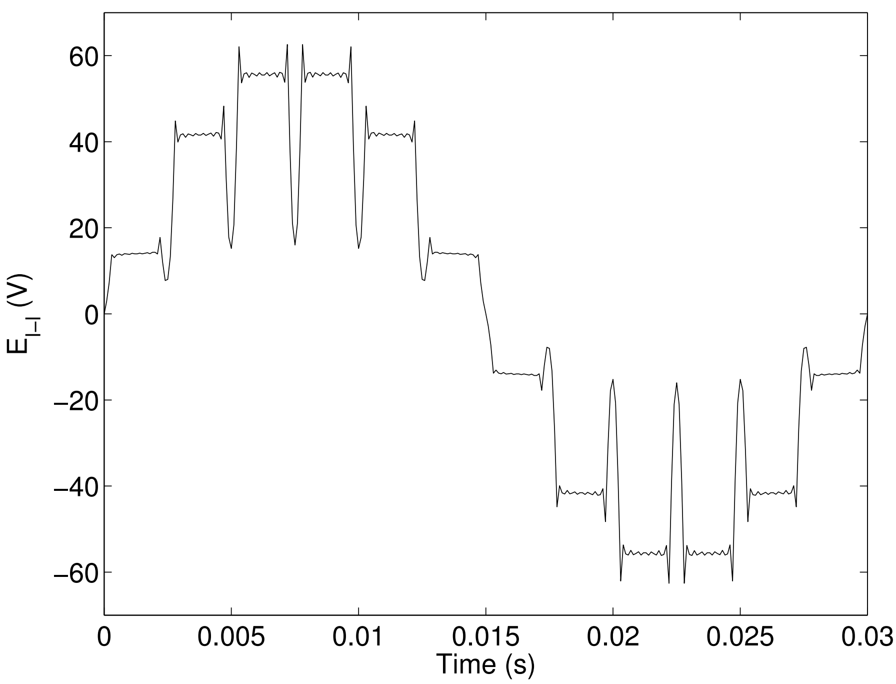

Fig. 8.24 Waveform of the line-to-line back emf an IPM motor calculated from a single magnetostatic FE simulation

Rated power: $P = 1.6$ kW

Rated line voltage: $V = 230$ V

Corner speed: $n_r = 1000$ rpm

Maximum speed: $n_{max} = 6000$ rpm

The main objectives of the design are:

a) Minimize cogging torque,

b) Maximize characteristic current of the motor.

The corresponding objective functions are defined as:

a) Cogging torque: $OF_1 = 1 - \frac{1}{max(T_c)+1}$

b) Normalized characteristic current: $OF_2 = \left|\frac{\Psi_{md}}{L_d I_R} - 1\right|$

There are a number of constraints imposed on the design. Those constraints are:

a) Minimum efficiency: $\eta \geq 0.8$,

b) Minimum torque requirement: $T \geq 15\ \mathrm{Nm}$

c) Maximum flux density in the stator core tooth: $B_{ts} \leq 1.8$ T

d) Maximum flux density in the stator yoke: $B_y \leq 1.5$ T

e) Maximum rms linear current density: $K_{1s} \leq 22000$ A/m

f) Maximum allowed rms value of the fundamental component line-to-line back emf at maximum speed: $E_{1max} \leq 230$ V

The back emf constraint at maximum speed has been set equal to the rated terminal voltage of the motor. This is a fairly conservative back emf constraint since the rating of the inverter switches is usually chosen to be 80%-100% higher than required for their rated output voltage. Therefore, the back emf constraint could be set somewhat higher than rated voltage of the motor without endangering the inverter switches in the case of uncontrolled generation at maximum speed. However, since the emphasis of this thesis is on motor design, the inverter which would power the motor and the rating of its switches for a particular practical purpose have not been analyzed. Hence this particular choice of the back emf constraint is more universal since the inverter switches have to be rated at least for the rated voltage of the motor.

The negative consequence of the back emf constraint is the inability to design a motor which would satisfy the optimum flux weakening condition. To have the back emf lower than rated voltage of the motor at the maximum speed of 6000 rpm requires weak magnets with low remanence and consequently low magnet flux Ψ_{md}. In such a case only designs with extremely high saliency ratios can satisfy both the optimum flux weakening condition and the back emf constraint. Therefore, most practical IPM motor designs will have a characteristic current I_c less than 1 pu which results in a lower power output in the field weakening regime than attainable at the corner speed. In order to maximize the power output of the motor at high speed, one of the objectives of the optimized design is to maximize the characteristic current of the motor and make it as close to 1 pu as possible.

Some of the parameters have constant values which do not change during optimization. Those parameters are:

1. Stator outer diameter: $D_o = 170$ mm
2. Rotor inner diameter: $D_{in} = 38$ mm
3. Air gap length: $g = 0.5$ mm
4. Width of the slot opening: $b_o = 2.5$ mm (see Fig. 6.1)
5. Depth of the slot opening: $d_o = 0.6$ mm (see Fig. 6.1)
6. Rotor bridge thickness: $d_{r0} = 1$ mm
7. Radius at the slot bottom: $r_{s2} = 1.2$ mm (see Fig. 8.25)
8. Armature current density: $J = 5.5\ \mathrm{A/mm^2}$

9. Slot fill factor: $f_{fill} = 0.4$

10. Number of slots per pole per phase: $q = 2$

The diameters D_o and D_{in} have been set as constant parameters so that the motor can be fitted into the standard frame size with standard shaft dimensions used by the manufacturer of the prototype. The cross-section of the IPM motor with all dimensions needed to fully define the design is shown in Fig. 8.25. A minimum of 12 design variables can be extracted to be used in the optimization. The variables are listed in Table 8.5 together with their limits. All geometric design variables have been normalized. The information about the relevant motor parameters shown in Fig. 8.25 can be extracted from the design variables in the following manner:

$$
\begin{aligned}
R_{in} &= \frac{D_{in}}{2},\ R_s = \frac{D_s}{2},\ R_r = R_s - g,\ R_o = \frac{D_o}{2} \\
\lambda_{h1} &= 1 - \lambda_{h2} \\
\lambda_{md3} &= 1 - \lambda_{md1} - \lambda_{md2} \\
d_{yr} &= R_r - R_{in} \\
d_{m1} &= \lambda_{h1}\lambda_m d_{yr} \\
d_{m2} &= \lambda_{h2}\lambda_m d_{yr} \\
d_{r1} &= \lambda_{md1}(1 - \lambda_m)d_{yr} \\
d_{r2} &= \lambda_{md2}(1 - \lambda_m)d_{yr} \\
d_{r3} &= \lambda_{md3}(1 - \lambda_m)d_{yr} \\
\alpha_p &= \lambda_p \frac{\pi}{p} \\
r_{m1} &= \frac{d_{m1}}{2},\ r_{m2} = \frac{d_{m2}}{2},\ R_{r1} = Rr - dr0
\end{aligned}
$$

The magnets used in the design are hard ceramic ferrites. The ferrite magnets available from the German manufacturer *Tridelta* are listed in Table 8.6. In general, ferrites have a lower remanence than rare earth magnets which in turn results in lower magnet flux Ψ_{md}. This is a desirable property from the standpoint of designing the motor which satisfies the back emf constraint.

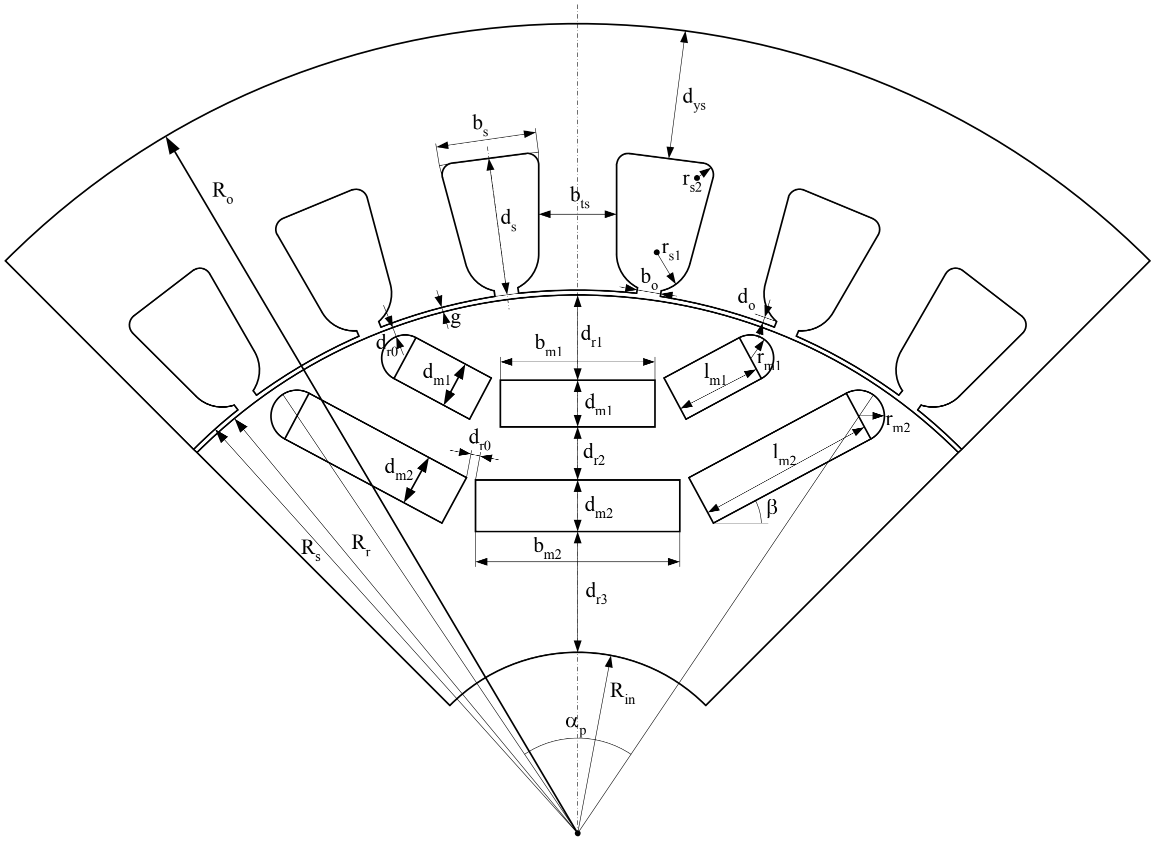

Fig. 8.25 Proposed IPM motor topology with geometric design parameters

Table 8.5 Variables used in the optimized design of an IPM motor

	Variable	Variable type	Limits
1.	Ratio of stator inner diameter to outer diameter	continuous	$0.45 < D_s / D_o < 0.75 \quad (D_o = 170 \text{ mm})$
2.	Ratio of stack length to maximum stack length	continuous	$0.6 < l_a / l_{a0} < 1 \quad (l_{a0} = 150 \text{ mm})$
3.	Ratio of yoke thickness to difference between stator outer and inner radius	continuous	$0.2 < 2d_{ys} / (D_o - D_s) < 0.6$
4.	Permanent magnet data	discrete	Table input
5.	Number of pole pairs	integer	$p = 2, 3, 4, 5, 6$
6.	Ratio of tooth width to slot pitch at D_s	continuous	$0.3 < b_{ts} / \tau_s < 0.7$
7.	Ratio of total cavity to total rotor depth	continuous	$0.1 < \lambda_m < 0.5$
8.	Percentage of total cavity depth for inner cavity	continuous	$0.25 < \lambda_{h2} < 0.7$
9.	Percentage of total rotor depth for the outermost rotor core section	continuous	$0.2 < \lambda_{md1} < 0.6$
10.	Percentage of total rotor depth for middle rotor core section	continuous	$0.1 < \lambda_{md2} < 0.4$
11.	Angular span of the inner cavity relative to the pole pitch	continuous	$0.6 < \lambda_p < 0.95$
12.	The angle of the slanted magnet	continuous	$0.5 < \beta / \beta_0 < 1, \quad \beta_0 = (1 - 1/p)\pi / 2$

Table 8.6 Parameters of the available ferrite magnets

	Remanent flux density B_r [T]	**Relative permeability μ_r**	**Density ρ_m [kg/m^3]**
1.	0.225	1.15	4800
2.	0.27	1.05	4700
3.	0.39	1.05	4700
4.	0.395	1.05	4800
5.	0.405	1.05	4800
6.	0.41	1.05	4800
7.	0.415	1.05	4800
8.	0.44	1.05	4900

The DE algorithm for multiobjective optimization described earlier has been used for the design. The population size is set to $NP = 35$ and the DE control parameters are $F = 0.3$, $CR = 0.3$.

8.3.6 Results

After 250 iterations the DE algorithm found nine solutions in the Pareto set. This is a significantly smaller number of solutions than found earlier in the case of a surface PM motor. One of the reasons could be that the DE control parameters which yielded good results for the analytical model of the SPM motor may not be the best choice for the FE based model of the IPM motor. However, one must also bear in mind that the back emf constraint is a rigorous limiting factor which significantly reduces the number of solutions generated during the optimization process which can be evaluated as the potential candidates to enter the Pareto set. In addition, there will also be a significant number of solutions generated which will not yield a feasible geometry due to overlapping of the rotor cavities in adjacent poles. These solutions are immediately discarded. This means that overall a significantly higher number of iterations may be required to obtain the total number of solutions in the Pareto set comparable to the size of the set yielded in the case of an SPM motor. The main obstacle for not running the DE algorithm with higher number of iterations is the long duration of the optimization process which is measured in days and the limited computer resources which were available for this purpose.

The values of the objective functions for the nine nondominant solutions are plotted against each other in Fig. 8.26 while the parameters of the IPM motor designs are listed in Table 8.7.

Note that all the solutions in Table 8.7 have converged to a very similar angular span λ_p of the cavities relative to the pole pitch. Moreover, all the solutions have four poles and 24 slots. This result can be explained by the fact that motors with a smaller number of poles have higher saliency ratios and thus can achieve higher values of the characteristic current while satisfying the back emf constraint.

Recently Zhu et al. [10] showed that a criterion used to determine the optimal angular span of the magnets in surface PM motors to achieve minimum cogging torque can be used for IPM motors as

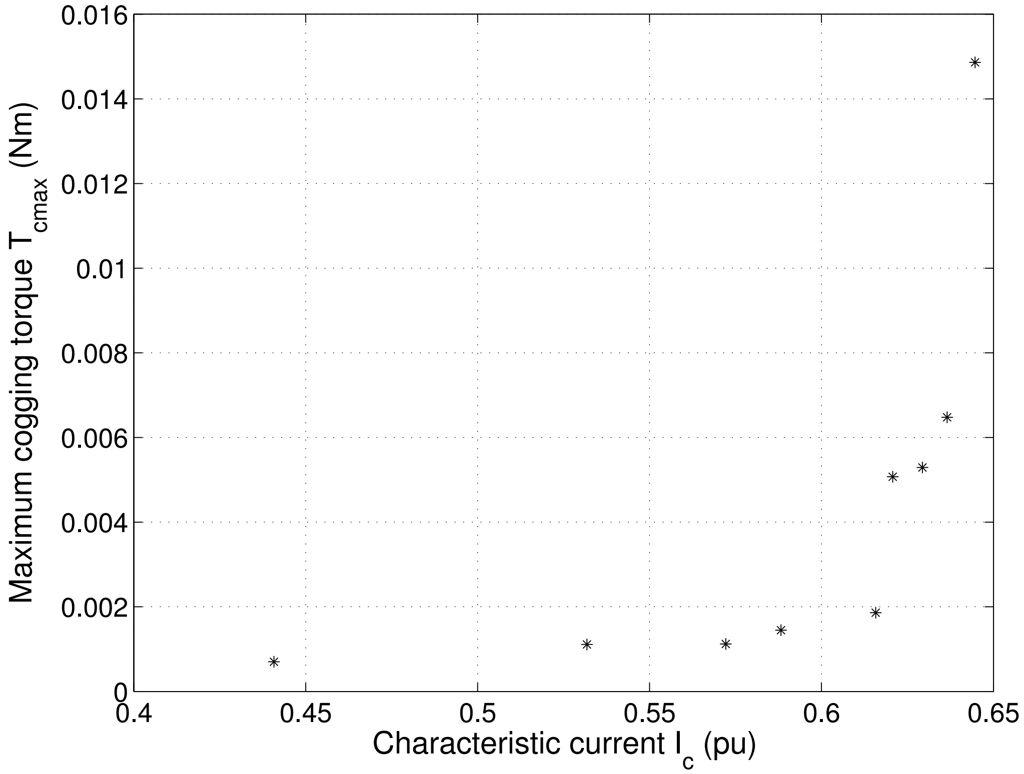

Fig. 8.26 Pareto front resulting from multiobjective optimization of an IPM motor using Differential Evolution with minimum cogging torque and maximum characteristic current as the main objectives

Table 8.7 Parameters of the IPM motor designs resulting from multiobjective optimization using Differential Evolution with minimum cogging torque and maximum characteristic current as the main objectives

	D_s [mm]	l_a [mm]	d_{ys} [mm]	b_{ts} [mm]	d_{m1} [mm]	d_{m2} [mm]	d_{r1} [mm]	d_{r2} [mm]	d_{r3} [mm]	β [deg.]	λ_p	B_r [T]	Q_s	2p	I_c [pu]	T_{cmax} [Nm]
1	102.0	113.3	16.0	8.51	3.87	6.06	12.58	6.49	2.51	32.14	0.8462	0.225	24	4	0.4408	0.0007
2	102.8	113.3	15.8	8.57	4.26	6.85	9.23	6.05	5.53	37.23	0.8482	0.270	24	4	0.5318	0.0011
3	108.3	112.9	15.8	9.03	3.38	7.72	8.10	7.44	8.00	32.39	0.8481	0.270	24	4	0.5721	0.0011
4	108.4	97.6	14.8	9.04	4.65	6.74	12.22	7.60	3.47	40.67	0.8471	0.270	24	4	0.5882	0.0014
5	108.4	108.1	14.7	9.04	3.20	5.55	14.24	8.45	3.27	37.80	0.8452	0.270	24	4	0.6158	0.0019
6	108.3	112.9	16.5	9.03	3.62	5.26	15.01	7.75	3.00	32.39	0.8462	0.270	24	4	0.6207	0.0051
7	111.9	118.3	15.3	9.33	4.39	7.14	8.80	6.82	9.31	27.99	0.8468	0.270	24	4	0.6294	0.0053
8	111.9	116.7	14.6	9.33	4.88	6.65	14.20	6.82	3.91	27.99	0.8468	0.270	24	4	0.6365	0.0065
9	109.8	113.1	16.2	9.16	4.78	6.22	14.18	7.58	2.64	34.23	0.8450	0.270	24	4	0.6446	0.0149

well. This criterion is defined as

$$\lambda_p = \frac{\frac{\mathrm{lcm}(Qs,2p)}{2p} - k_1}{\frac{\mathrm{lcm}(Q_s,2p)}{2p}} + k_2 \tag{8.49}$$

where $\mathrm{lcm}(Q_s, 2p)$ is the least common multiple between the number of slots and the number of poles, p is the number of pole pairs, $k_1 = 1, 2, \ldots, \frac{Q_s}{2p}$ and k_2 is the factor usually ranging from 0.01 to 0.03 [4] which is used to take into account the fringing flux of the magnets. For the 24 slot, 4 pole combination the optimal angular span of the magnets calculated from (8.49) ranges between 0.8433 and 0.8633. The angular span of the inner cavities of the optimized IPM motor designs from Table 8.7 calculated by the DE using the cogging torque estimation described in Section 8.3.2 is between 0.8450 and 0.8482 which agrees with the criterion (8.49) and with similar results shown in [10].

8.4 Design and Evaluation of the Prototype IPM Motor

The prototype of the IPM motor has been designed and built to confirm that physical properties of the motor predicted in the design stage can be actually achieved in practice. The motor has been designed using the multiobjective optimization algorithm previously described. Since the emphasis has been to reduce the cost of the prototype, some of its dimensions have been adjusted to standard sizes used by the manufacturer of the prototype. The manufacturer is KONČAR-MES, Zagreb, Croatia.

The outer diameter of the stator core has been fixed in order to fit inside the standard aluminum cast frame. The same has been done with the inner diameter of the rotor core to fit the standard shaft size. The stack length has been fixed to 120 mm.

There was only one type of hard ferrite permanent magnet material available on the market to be purchased in a fairly short time with specifications according to Table 8.8. The magnet properties in Table 8.8 are taken from the magnet vendor specification sheet.

Table 8.8 Properties of hard ferrite permanent magnets from magnet vendor specification sheet

	Remanent flux density B_r [T]	Coercivity H_c [kA/m]
Minimum	0.2	130
Typical	0.22	145

The magnet properties were also measured on three samples of purchased magnets which had already been cut according to design specifications for the prototype. The results of these measurements are shown in Table 8.9. It is apparent that the actual magnet specifications were closer to the minimum, rather than typical values specified by the vendor.

Table 8.9 Measured properties of three samples of purchased hard ferrite permanent magnets

	Dimensions W×L×H [mm]	Remanent flux density B_r [T]	Coercivity H_c [kA/m]
Sample 1	21.9×20.4×3.67	0.205	128.0
Sample 2	19.3×30.4×3.67	0.207	133.6
Sample 3	14.5×30.4×3.67	0.2098	135.2

The magnets were available in two standard sizes: 30.4×20.4×3.67 mm and 30.4×20.4×6.67 mm. This means that sizes of the cavities (d_{m1} and d_{m2} in Fig. 8.25) were allowed to be either 3.67 mm or 6.67 mm to accommodate the magnets. The actual sizes of the cavities which were to be laser cut in each rotor lamination had to be made larger by 0.15 mm to take into account the tolerance of the laser cut and the tolerance of the core assembly because of the accidental shifting of individual laminations.

During the design process a decision had to be made if during the assembly the magnets were to be magnetized first and then inserted into the cavities or if they were to be installed first and then magnetized using the standard manufacturer's fixture. The fixture is designed for the six pole motors with stator bore size of 115 mm. It was decided to leave both options open which consequently led to a decision to utilize the standard six pole stator lamination punching used by the manufacturer for their product line of surface PM servo motors.

Since the motor has six poles and 36 slots, the angular span of the cavities relative to the pole pitch which yields minimum cogging torque could have the same value as calculated in Section 8.3.6 because the ratio lcm$(Qs, 2p)/2p$ in the cases of four poles and 24 slots and six poles and 36 slots is the same. Hence, the relative angular span of the cavities has been set to 0.846.

With the stator design already determined and with only one permanent magnet material available with two standard thicknesses, the total number of design variables utilized to design the rotor has been reduced to five. These variables with their limits are listed in Table 8.10.

Table 8.10 Variables used in the optimized design of a protoype IPM motor

	Variable	Variable type	Limits
1.	Thickness of the magnet in the upper layer	discrete	$d_{m1} = 3.67,\ 6.67$ mm
2.	Thickness of the magnet in the lower layer	discrete	$d_{m2} = 3.67,\ 6.67$ mm
3.	Percentage of total rotor depth for the outermost rotor core section	continuous	$0.2 < \lambda_{md1} < 0.7$
4.	Percentage of total rotor depth for middle rotor core section	continuous	$0.1 < \lambda_{md2} < 0.5$
5.	The angle of the slanted magnet	continuous	$0.5 < \beta/\beta_0 < 1$, $\beta_0 = (1-1/p)\pi/2$

The primary design specifications for the motor are:

Rated line voltage: $V = 230$ V

Corner speed: $n_r = 1000$ rpm

Maximum speed: $n_{max} = 6000$ rpm

The parameters of the motor which have fixed values during optimization are:

1. Number of slots: $Q_s = 36$
2. Number of poles: $2p = 6$
3. Stator outer diameter: $D_o = 170$ mm
4. Stator inner diameter: $D_s = 115$ mm
5. Rotor inner diameter: $D_{in} = 38$ mm

6. Stack length: $l_a = 120$ mm
7. Stator tooth width: $b_{ts} = 5.4$ mm
8. Stator yoke thickness: $d_{ys} = 11.3$ mm
9. Air gap length: $g = 0.5$ mm
10. Width of the slot opening: $b_o = 2.5$ mm (see Fig. 6.1)
11. Depth of the slot opening: $d_o = 0.62$ mm (see Fig. 6.1)
12. Rotor bridge thickness: $d_{r0} = 1$ mm
13. Radius at the slot bottom: $r_{s2} = 1.2$ mm (see Fig. 8.25)
14. Angular span of the cavities relative to the pole pitch: $\lambda_p = 0.846$
15. Armature current density: $J = 5.5\ \mathrm{A/mm^2}$
16. Slot fill factor: $f_{fill} = 0.4$
17. Number of parallel paths: $a_p = 1$

Since active volume of the motor is fixed, one of the objectives of optimization has been to maximize the electromagnetic torque attainable from the constant volume at corner speed. The other objective is to maximize the characteristic current. The corresponding objective functions are defined as:

a) Electromagnetic torque at corner speed: $OF_1 = -T_{em}$

b) Normalized characteristic current: $OF_2 = \left|\frac{\Psi_{md}}{L_d I_R} - 1\right|$

The first objective function has been defined as a negative value of torque since the DE optimization algorithm always attempts to minimize the objective function. The minimization problem can be simply converted into a maximization problem by adding a negative sign to the value of the objective function.

The constraints imposed on the design are:

a) Minimum efficiency: $\eta \geq 0.8$,

b) Maximum flux density in the stator core tooth: $B_{ts} \leq 1.8$ T

c) Maximum flux density in the stator yoke: $B_y \leq 1.5$ T

d) Maximum rms linear current density: $K_{1s} \leq 22000$ A/m

e) Maximum allowed rms value of the fundamental component line-to-line back emf at maximum speed: $E_{1max} \leq 230$ V

The DE control parameters have been set to F=0.3, CR=0.3.

The optimal solution for the prototype IPM motor design has been selected from the set of nondominant solutions obtained after 50 iterations of the DE algorithm. It was decided not to wait longer and extract results after 150 or more iterations due to time constraints and desire to accelerate the construction of the motor. However, the code was allowed to continue to run and was terminated after reaching 150 iterations. The results after 50 and 150 iterations are shown in Fig. 8.27. It is apparent that after 150 iterations a better result was achieved than after 50 iterations. However, the total number of solutions in the Pareto set is still small which is consistent with the results from Section 8.3.6. It is expected that with a higher number of iterations more solutions would have eventually been found.

According to Fig. 8.27 the design which has been selected as optimal after 50 iterations is the one with the highest torque. This choice has been made in spite of the fact that this design has the lowest characteristic current. This is a minor trade-off since the selected design has a characteristic current 0.41 pu while the highest characteristic current attained is 0.422 pu which is a small difference.

The cross section of the motor is shown in Fig. 8.28. All the dimensions in the figure are given in milimeters.

The main design specifications for the armature winding are given in Table 8.11. The winding scheme is identical to the one shown in Fig. 5.7.

The parameters of the motor are given in Table 8.12. The inductances and flux linkages in this table have been calculated for the rated operating point at corner speed using the FE analysis with

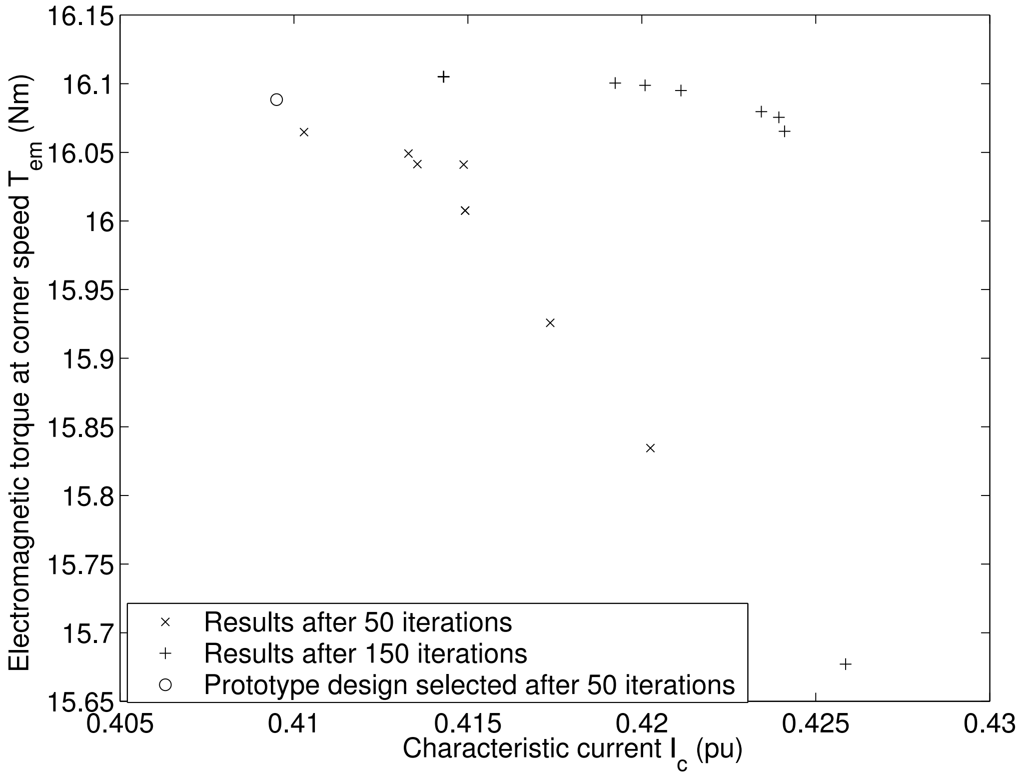

Fig. 8.27 Pareto front resulting from multiobjective optimization of a prototype IPM motor design using Differential Evolution with maximum torque at corner speed and maximum characteristic current as the main objectives

Table 8.11 Design specifications for a single layer full pitch lap winding of the prototype IPM motor

Winding parameter	*Value*
Connection	Y
Number of slots	36
Number of poles	6
Coil pitch	1-6
Slot fill factor	0.4
Number of turns per coil	27
Number of coils per phase	6
Number of turns per phase connected in series	162
Cross-sectional area of the conductor	1.388 mm^2

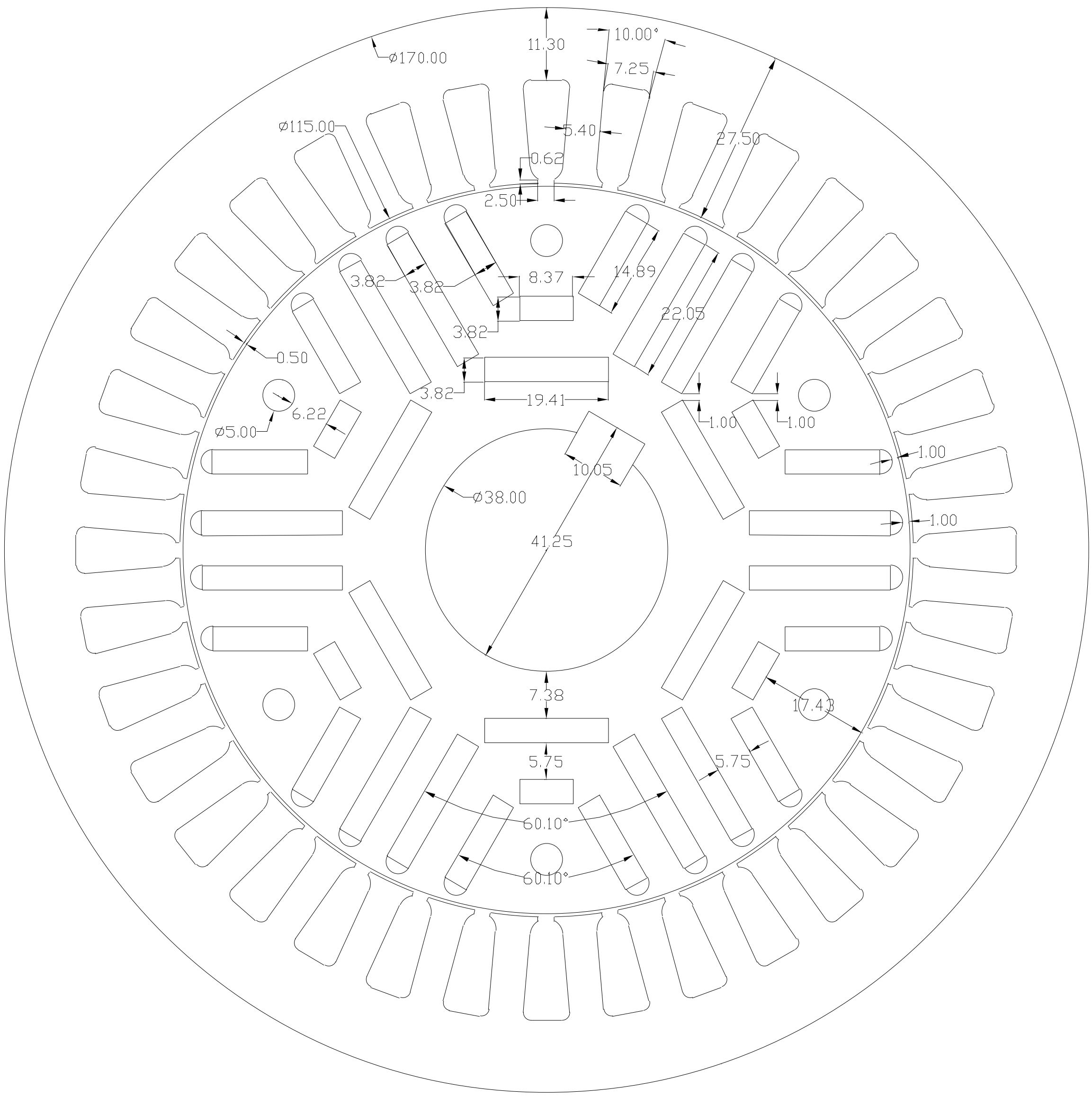

Fig. 8.28 Cross-section of the prototype IPM motor

permeance freezing. The permeance freezing allows one to separate the permanent magnet flux from the armature winding d and q axis fluxes while retaining information about localized saturation in all parts of the motor which occurs due to the presence of all three flux components simultaneously. In other words the superposition principle can now be applied to extract information about motor parameters, namely open-circuit d axis flux linkage Ψ_{md} and inductances L_d and L_q. One must not forget the additional cross-saturation parameters Ψ_{mqd}, L_{dq} and L_{qd} which also emerge after permeance freezing. The correctness of the IPM motor model based on parameters thus calculated can be verified by comparing the electromagnetic torque calculated directly from the FE simulation and calculated from the expression

$$T_{em} = 3p(\Psi_{ds} I_{qs} - \Psi_{qs} I_{ds}) \tag{8.50}$$

with d and q flux and current components given as rms values. After taking into account that

$$\begin{aligned} \Psi_{ds} &= \Psi_{md} + L_d I_{ds} + L_{dq} I_{qs} \\ \Psi_{qs} &= L_q I_{qs} + L_{qd} I_{ds} + \Psi_{mqd} \\ L_{dq} &= L_{qd} \\ I_{qs} &= I \cos\gamma \\ I_{ds} &= I \sin\gamma \end{aligned} \tag{8.51}$$

and substituting into (8.50), the torque equation takes the form

$$\begin{aligned} T_{em} &= 3p\left[\Psi_{md} I_{qs} - \Psi_{mqd} I_{ds} + (L_d - L_q) I_{ds} I_{qs} + L_{dq} I_{qs}^2 - L_{qd} I_{ds}^2\right] \\ &= 3p\left[\Psi_{md} I \cos\gamma - \Psi_{mqd} I \sin\gamma + \frac{1}{2}(L_d - L_q) I^2 \sin(2\gamma) + L_{dq} I^2 \cos(2\gamma)\right] \end{aligned} \tag{8.52}$$

The torque calculated using (8.52) with parameters from Table 8.12 is

$$\begin{aligned} T_{em} &= 3 \cdot 3 \cdot \Big[0.1012 \cdot 7.63 \cdot \cos(-46.83^0) - (-0.0017) \cdot 7.63 \cdot \sin(-46.83^0) + \\ &\quad \frac{1}{2} \cdot (0.0761 - 0.0324) \cdot 7.63^2 \cdot \sin(-2 \cdot 46.83^0) + 0.001039 \cdot 7.63^2 \cdot \cos(-2 \cdot 46.83^0)\Big] \\ &= 16.13 \text{ Nm} \end{aligned}$$

which is very close to 16.09 Nm in Table 8.12 calculated directly from the FE solution.

Table 8.12 Parameters of the prototype IPM motor

Parameter	*Symbol*	*Value*	*Unit*
Rated power	P	1651	W
Rated line voltage	V	230	V
Rated current	I	7.63	A
Rated corner speed	n_r	1000	rpm
Rated electromagnetic torque	T_{em}	16.09	Nm
Rated shaft torque	T	15.70	Nm
Power factor	$\cos \varphi$	0.628	–
Efficiency	η	0.887	–
RMS linear current density	K_{1s}	20538	A/m
Stator outer diameter	D_o	170	mm
Stator inner diameter	D_s	115	mm
Air gap length	g	0.5	mm
Rotor inner diameter	D_{in}	38	mm
Core length	l_a	120	mm
Magnet remanence	B_r	0.20	T
Magnet relative permeability	μ_r	1.15	–
Armature resistance at 75^{o}C	R_a	1.01	Ω
Saturated q axis inductance at corner speed	L_q	76.1	mH
Saturated d axis inductance at corner speed	L_d	32.4	mH
Saturated saliency ratio	ξ	2.35	–
Current control angle	γ	-46.83	degrees
Cross saturation inductance	L_{dq}	1.039	mH
Cross saturation inductance	L_{qd}	1.039	mH
Magnet flux (rms value)	ψ_{md}	0.1012	Vs
Magnet cross saturation flux (rms value)	ψ_{mqd}	-0.0017	Vs
RMS line-to-line back emf at 6000 rpm	E_{max}	160	V

The cogging torque has been calculated using Magsoft, Flux 2D FE software. The waveform is shown in Fig. 8.29. The peak value of the cogging torque is 0.0016 Nm which is only 0.01% of the rated torque. Small cogging torque was expected since the angular span of the cavities has been adjusted to minimize it.

Manufactured parts of the motor are shown in Fig. 8.30.

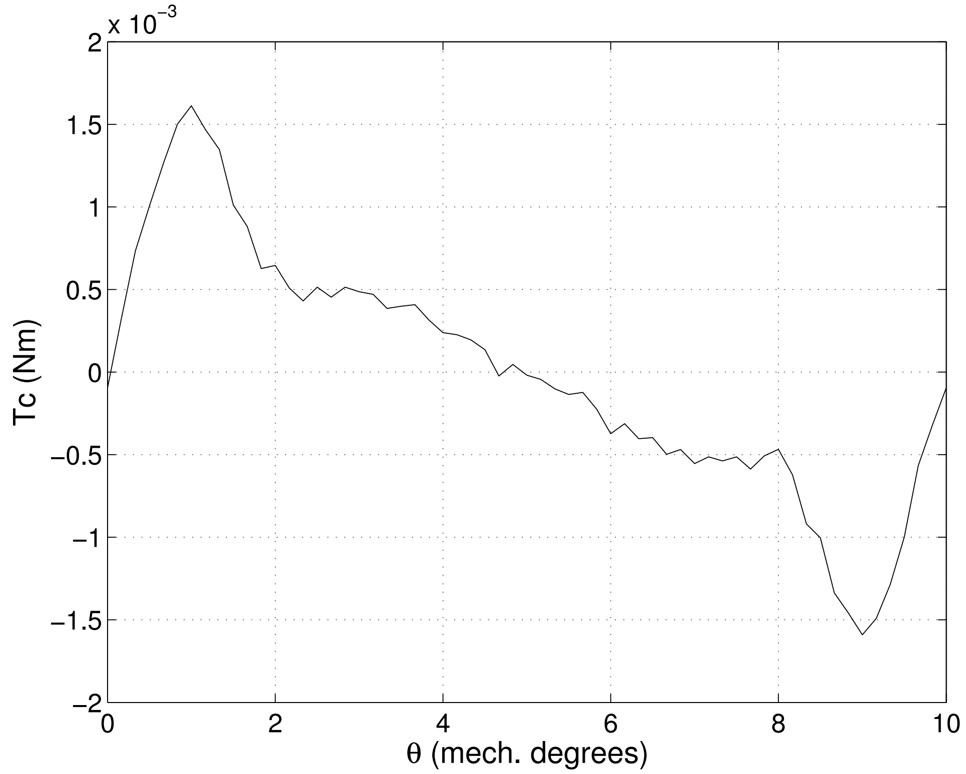

Fig. 8.29 Cogging torque waveform of the prototype IPM motor

8.4.1 Comparison of Calculated and Measured Results

The hardware setup which has been used for testing of the prototype IPM motor consists of a dynamometer coupled to the IPM motor via torque transducer, two 37 kW standard converters by Danfoss Drives, and a dSpace 1103 controller with interface board. Fig. 8.31 shows the simplified hardware configuration.

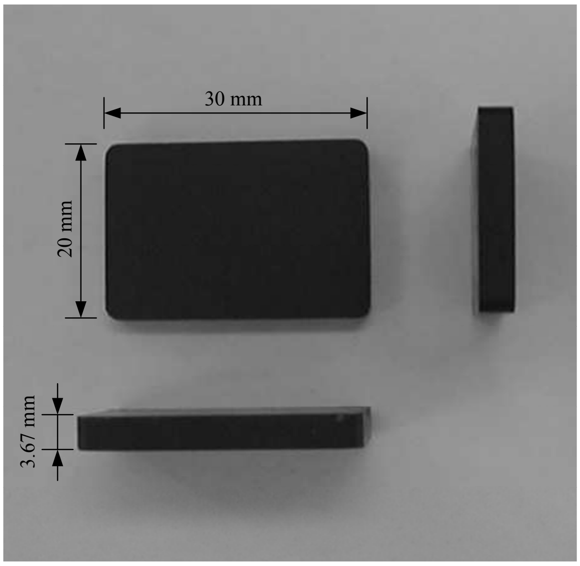

a) Permanent magnets

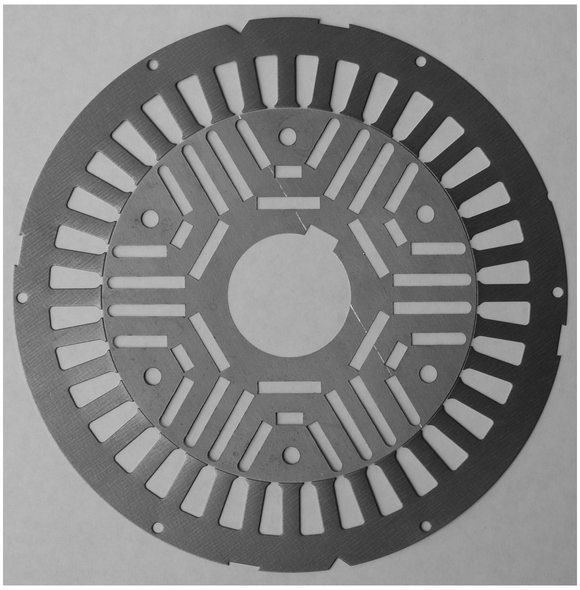

b) Stator and rotor laminations

c) Rotor

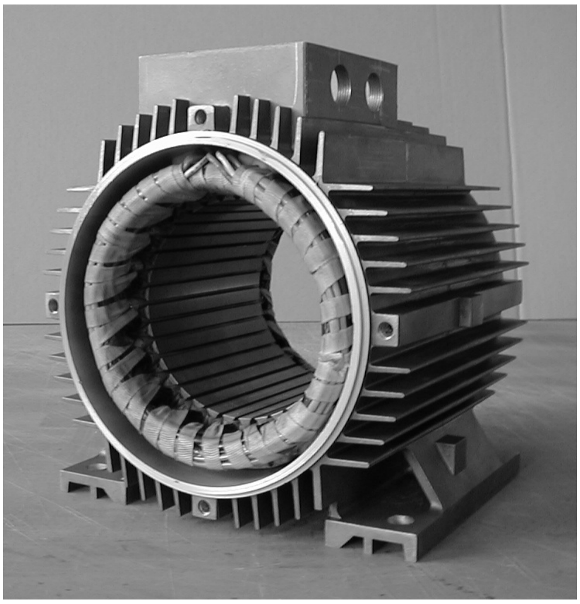

d) Stator

Fig. 8.30 Manufactured parts of the prototype IPM motor

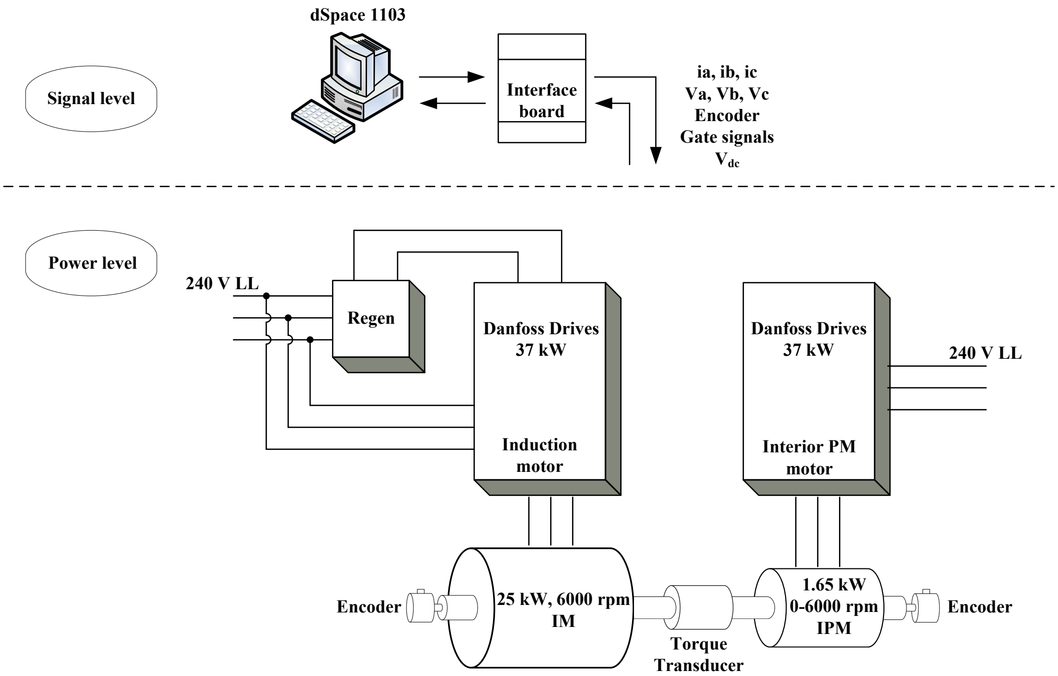

Fig. 8.31 Simplified hardware configuration used for testing of the prototype IPM motor

The dynamometer is a 25 kW induction machine which is used as a load for the tested IPM motor. This induction machine can operate at a maximum speed of 6000 rpm which is suitable for the operating range of the prototype motor (0-6000 rpm). This setup was originally utilized for testing of the integrated starter-alternator rated at 9.5 kW with 150 Nm of starting torque up to 600 rpm and rated current of 350 A rms [89]. Although the setup is oversized for the requirements of the prototype IPM motor, which is rated at 1.65 kW, its advantage is that it was available and ready to use. The IPM motor coupled to the induction machine is shown in Fig. 8.32.

One of the commercial Danfoss converters is used to power the IPM motor while the other is used for the induction machine. In addition, a separate regeneration unit by Danfoss Electronic Drives (REVCON) is included to allow bi-directional power flow for the dynamometer. The ratings for the converters and regeneration unit are given in Table 8.13. Fig. 8.33 shows both converters and regeneration unit.

Another important part of the experimental setup is the interface board, whose functions are outlined in Fig. 8.34. These functions include voltage and current filtering, transmission of gate drive

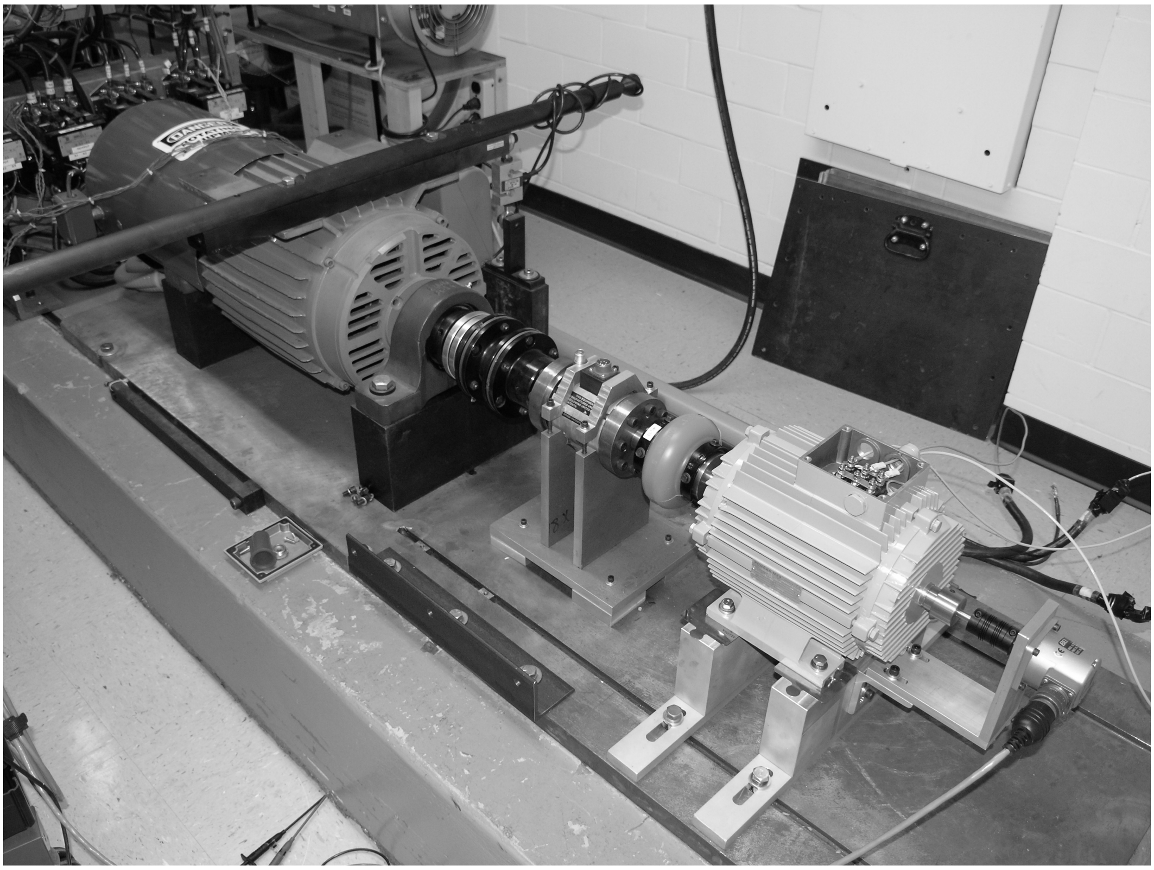

Fig. 8.32 Prototype IPM motor coupled to the induction machine via torque transducer

Table 8.13 Ratings of Danfoss converters and REVCON regen unit

Danfoss Converters
Model : VLT 5052 **In :** 3× 200 – 240 V rms, 50/60 Hz, 165 A rms **Out :** 3× 0 – V_{in}, 0 – 1000Hz, 37kW 170 A rms / 208 V rms, 154 A rms / 230 V rms
REVCON Regen Unit
Model : SVCD 40 – 230 – 1 – 230 V AC **Serial No. :** 07/01 SVCD 40-400 **Rating :** 3×230 V rms, 101A rms

signals and interface between the IPM motor encoder and dSpace 1103 controller. A more detailed description of the interface board can be found in [89].

Back emf measurement

The initial test performed on the prototype motor using the described hardware setup was the back emf measurement. Fig. 8.35 compares the line-to-line back emf waveform measured at 1000 rpm with the waveform calculated using a transient finite element simulation. The moving air gap feature of Magsoft, Flux 2D FE software has been used to simulate rotation in the FE model. There is excellent agreement between measured and simulated waveforms. However, a slight asymmetry can be noticed in the measured back emf. It is probably a consequence of uneven magnetization of the magnets.

During optimization the waveform of the back emf is estimated from a single magnetostatic FE simulation as previously described in Section 8.3.4. This estimated waveform is compared with the one calculated using transient FE simulation with motion in Fig. 8.36. The result in Fig. 8.36 shows that a fairly good estimate of the back-emf waveform is possible from only a single magnetostatic FE simulation. This saves significant computational time during optimization, compared to the transient simulation with motion.

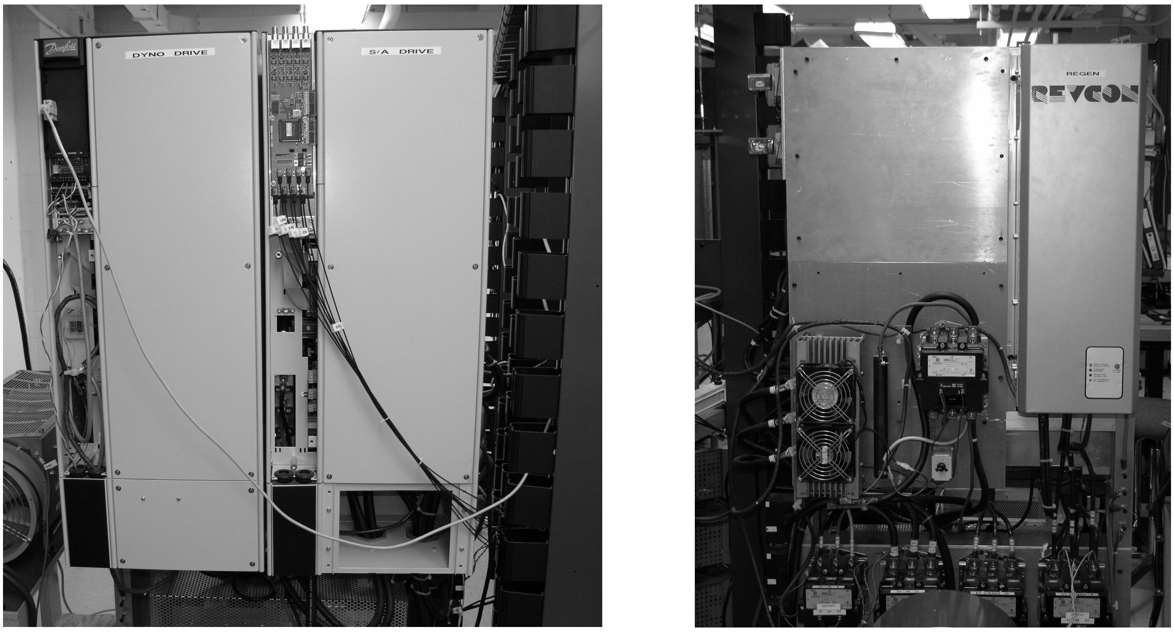

(a) (b)

Fig. 8.33 Experimental setup: (a) Danfoss converters, (b) REVCON regen unit

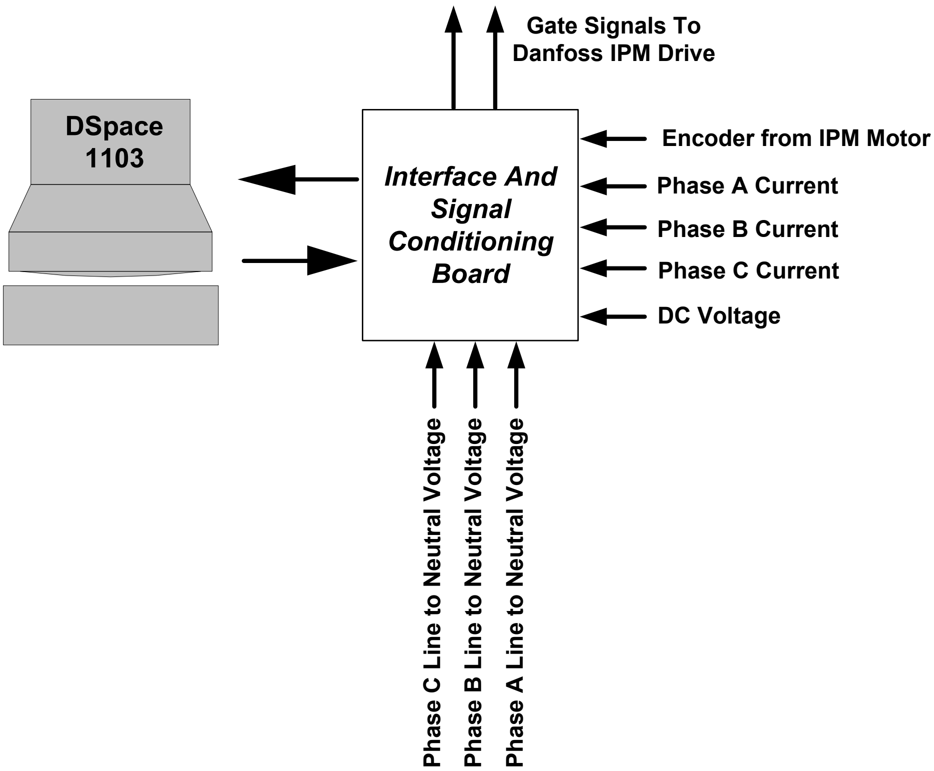

Fig. 8.34 Illustration of basic functions of the interface board

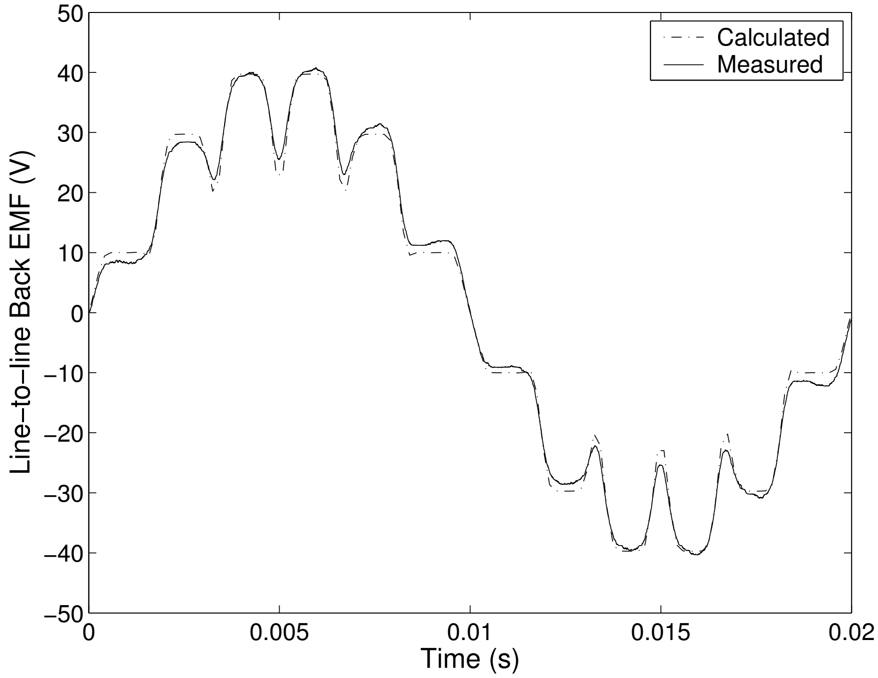

Fig. 8.35 Calculated and measured waveforms of line-to-line back emf of the prototype IPM motor at 1000 rpm

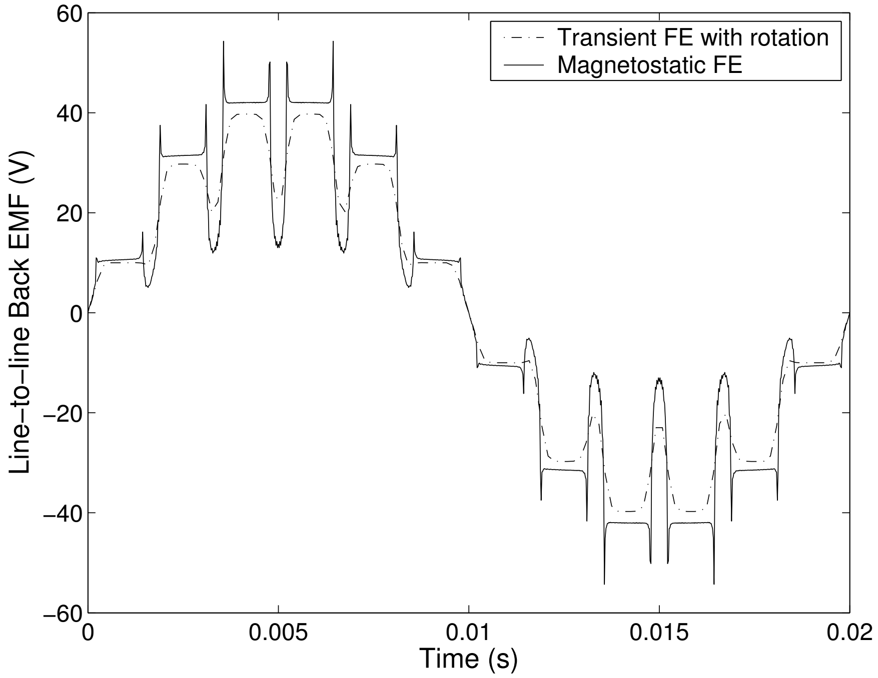

Fig. 8.36 Comparison of waveforms of the line-to-line back emf calculated using transient FE simulation with rotation and using single magnetostatic FE simulation for the prototype IPM motor at 1000 rpm

Inductance measurement

Armature winding inductances L_d and L_q have been measured using static tests with the locked rotor. Figs. 8.37 and 8.38 show the basic principle of measurement for both inductances. The rotor is aligned and locked in a position in which the magnet axis is aligned with the phase A axis. In the case of L_d the basic circuit consists of an AC voltage source applied across the phase A terminal and the short-circuited terminals of phases B and C. The resulting current which flows through the windings thus produces a pulsating armature field in the d axis. In the case of L_q the AC voltage is applied across the terminals of phases B and C, while the phase A terminal is open and the phase A current is zero. The resulting current produces a pulsating armature field in the q axis.

According to Figs. 8.37 and 8.38, the following equations can be written for the voltages and currents of phases A and B:

$$v_a = i_a R_a + (L_l + L_{md})\frac{\mathrm{d}i_a}{\mathrm{d}t} - \frac{1}{2}L_{md}\frac{\mathrm{d}i_b}{\mathrm{d}t} - \frac{1}{2}L_{md}\frac{\mathrm{d}i_c}{\mathrm{d}t} \tag{8.53}$$

$$v_b = i_b R_a + (L_l + L_{mq})\frac{\mathrm{d}i_b}{\mathrm{d}t} - \frac{1}{2}L_{mq}\frac{\mathrm{d}i_c}{\mathrm{d}t} \tag{8.54}$$

where R_a is the armature resistance, L_l is the total leakage inductance per phase, and L_{md} and L_{mq} are the main inductances per phase when the resulting armature field is aligned with the d and q axis respectively. The calculated armature resistance R_a, from Table 8.12, is equal to 1.01 Ω, while the measured resistance is 1.09 Ω. From Fig. 8.37 it follows that

$$i_b = i_c = -\frac{i_a}{2} \tag{8.55}$$

while from Fig. 8.38 it is apparent that

$$i_c = -i_b \tag{8.56}$$

Hence, (8.53) and (8.54) now become

$$v_a = i_a R_a + (L_l + \frac{3}{2}L_{mq})\frac{\mathrm{d}i_a}{\mathrm{d}t} \tag{8.57}$$

$$v_b = i_b R_a + (L_l + \frac{3}{2}L_{mq})\frac{\mathrm{d}i_b}{\mathrm{d}t} \tag{8.58}$$

The resulting inductances $L_l + \frac{3}{2}L_{md}$ and $L_l + \frac{3}{2}L_{mq}$ are equivalent to L_d and L_q inductances respectively. In addition, one can also write

$$v_a = v_d \quad , \quad i_a = i_d \tag{8.59}$$

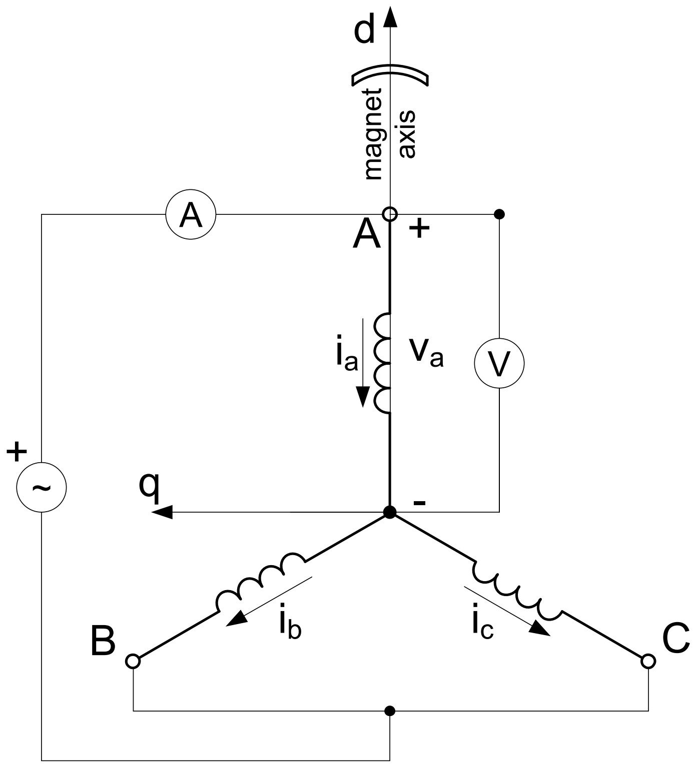

Fig. 8.37 Circuit used for measurement of inductance L_d

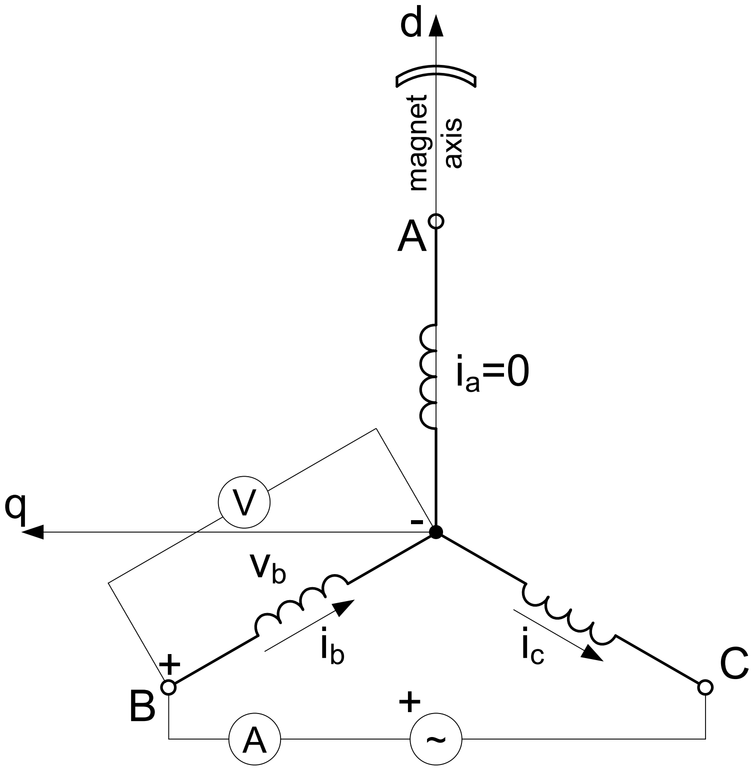

Fig. 8.38 Circuit used for measurement of inductance L_q

$$v_b = v_q \quad , \quad i_b = i_q \tag{8.60}$$

thus giving

$$v_d = i_d R_a + L_d \frac{\mathrm{d}i_d}{\mathrm{d}t} \tag{8.61}$$

$$v_q = i_q R_a + L_q \frac{\mathrm{d}i_q}{\mathrm{d}t} \tag{8.62}$$

The time dependent flux linkages in the d and q axes, $\psi_d(t)$ and $\psi_q(t)$, can now be determined from voltage equations (8.61) and (8.62) by integration

$$\psi_d(t) = \int_0^t (v_d(\tau) - i_d(\tau)R_a)\mathrm{d}\tau \tag{8.63}$$

$$\psi_q(t) = \int_0^t (v_q(\tau) - i_q(\tau)R_a)\mathrm{d}\tau \tag{8.64}$$

These flux linkages can be also written as

$$\psi_d(t) = \psi_{md} + L_d i_d(t) \tag{8.65}$$

$$\psi_q(t) = L_q i_q(t) \tag{8.66}$$

where ψ_{md} is the d axis flux linkage due to the permanent magnets, and L_d and L_q are the d and q axis inductances. The inductances are now defined as

$$L_d = \frac{\psi_d(t) - \psi_{md}}{i_d(t)} \tag{8.67}$$

$$L_q = \frac{\psi_q(t)}{i_q(t)} \tag{8.68}$$

For comparison, the described experiments have been simulated using transient FE simulation with the FE model coupled to an electric circuit. The measured and calculated v_a and i_a in the case of L_d,and v_b and i_b in the case of L_q, are compared in Figs. 8.39 and 8.40.

After performing integration of the measured voltages $v_a(t)$ and $v_b(t)$, and currents $i_a(t)$ and $i_b(t)$, the resulting instantaneous flux linkages $\Psi_d(t)$ and $\Psi_q(t)$ have been plotted as functions of the corresponding currents $i_d(t)$ and $i_q(t)$, which is shown in Figs. 8.41a and 8.41b. The same figures also show calculated flux vs current characteristics. The finite element approach does not require

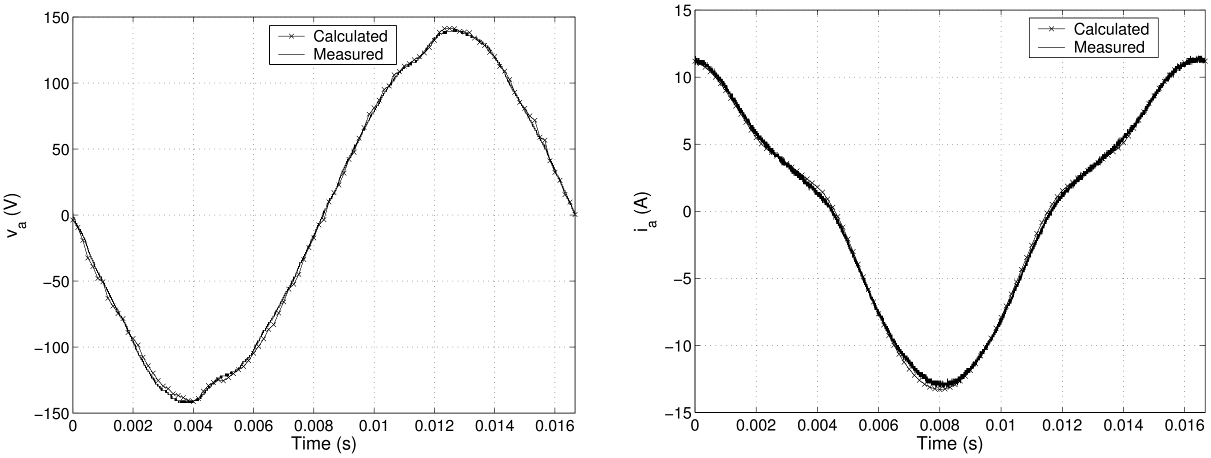

(a) (b)

Fig. 8.39 Waveforms of the phase A voltage and current measured with the locked rotor while the resulting armature field is aligned with the d axis: (a) voltage, (b) current

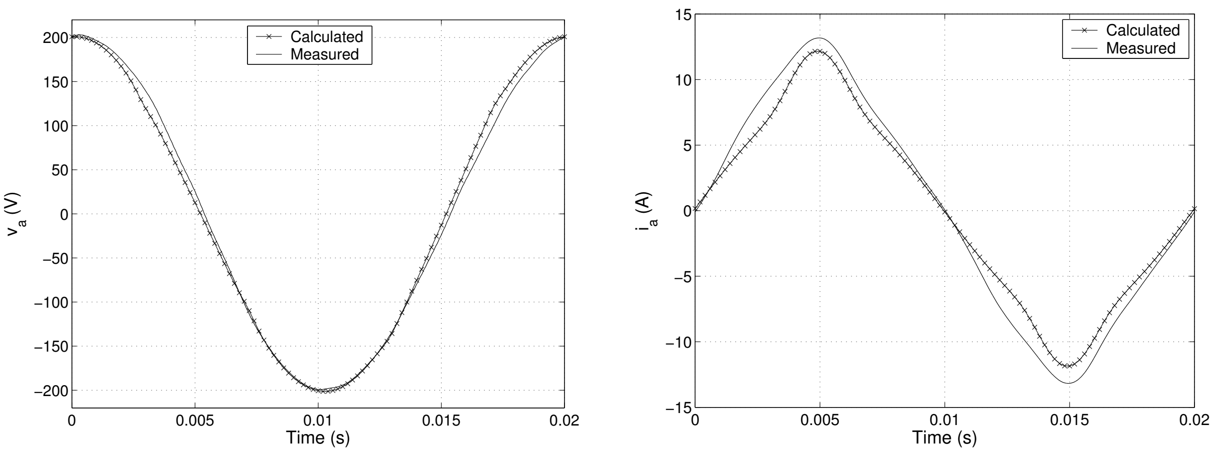

(a) (b)

Fig. 8.40 Waveforms of the phase B voltage and current measured with the locked rotor while the resulting armature field is aligned with the q axis: (a) voltage, (b) current integration of simulated voltage and current waveforms to determine Ψ_d and Ψ_q since those flux linkages can be calculated directly from the average magnetic vector potentials inside the slot areas. Since flux characteristics exhibit hysteresis effect, thus giving two values of flux for the same current, the actual flux has been taken as an average of the two values. This is shown in Figs. 8.42a and 8.42b. The hysteresis is also present in the simulated results, but it is very narrow. In addition, one must also take into account that integration of the measured current and voltage waveforms, which is used to calculate Ψ_d and Ψ_q, provides only correct information about the change in flux, and not about its exact instantaneous value. Consequently, the resulting flux characteristics have a correct shape, but they are shifted vertically. Moreover, the presence of the permanent magnet flux in the d axis also causes an offset in position of the flux characteristic with respect to the origin when determining L_d. Therefore, prior to calculating inductances L_d and L_q, the offsets of the flux characteristics have to be subtracted.

Figs 8.43a and 8.43b show inductances L_d and L_q determined from the averaged flux characteristics given in Fig 8.42. In the motoring mode of operation of an IPM machine the current i_d is negative and the current i_q is positive, so the plots L_d vs i_d for $i_d < 0$ and L_q vs i_q for $i_q > 0$ are usually of interest. These plots are shown in Figs. 8.44a and 8.44b. The measured d axis inductance is approximately 10% higher than calculated, while measured q axis inductance is 10-20% lower than calculated. This difference indicates that the motor will develop significantly lower reluctance torque than predicted in the design stage.

Three additional approaches have been used to calculate L_d to make comparison with the experimental results. These approaches are not equivalent to the one used in the experiment, but they give a useful insight into differences between the values of L_d, which are results of either using a different IPM machine model, or using a different approach to the separation of the magnet and armature flux linkages.

In the first magnetostatic simulation the field solution is found with the armature current applied to produce the field in the negative d axis with the magnet field present at the same time. Next, the permeabilities are frozen after which the magnets are ”turned off” and the field solution is found using the same armature current. The inductance L_d is then found as a ratio of the flux linkage Ψ_d

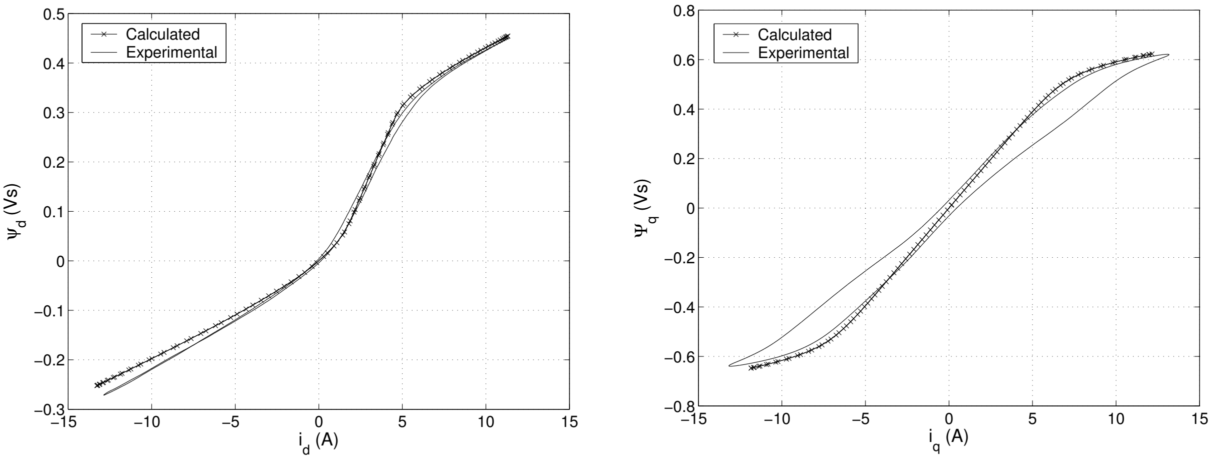

(a) (b)

Fig. 8.41 Comparison of calculated and experimentally determined flux characteristics: (a) Ψ_d vs i_d, (b) Ψ_q vs i_q

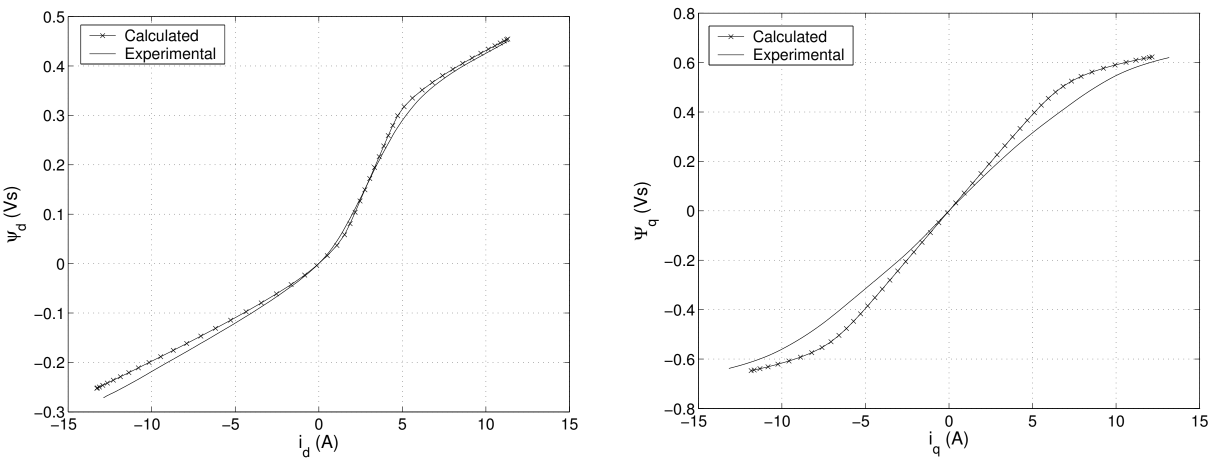

(a) (b)

Fig. 8.42 Comparison of calculated and experimentally determined flux characteristics averaged for each value of current: (a) Ψ_d vs i_d, (b) Ψ_q vs i_q

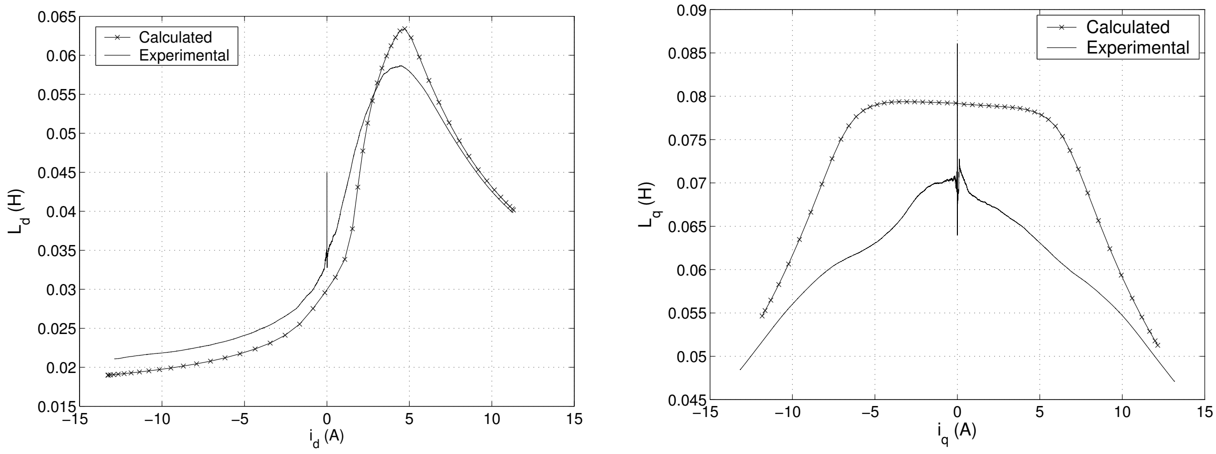

(a) (b)

Fig. 8.43 Comparison of calculated and experimentally determined inductances: (a) L_d, (b) L_q

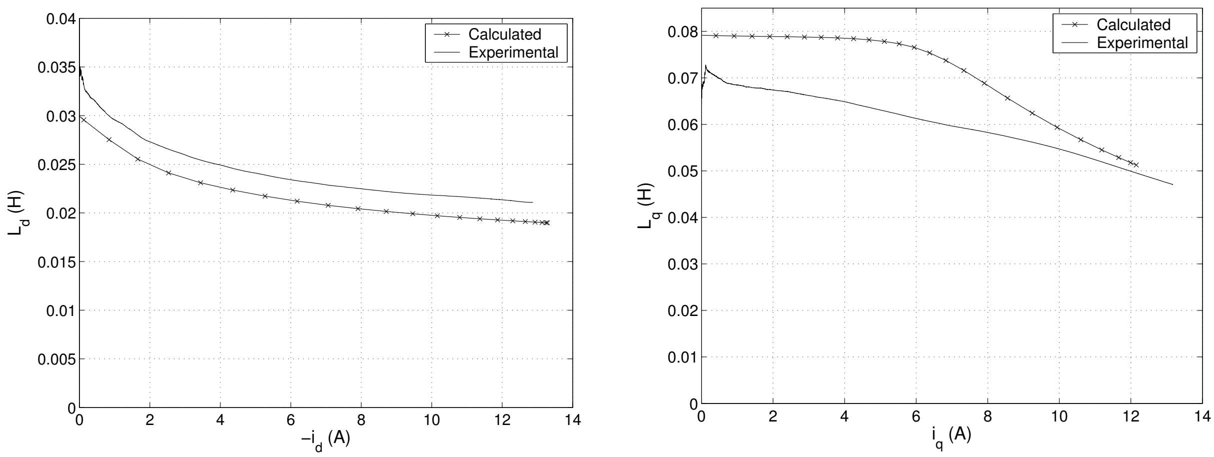

(a) (b)

Fig. 8.44 Comparison of calculated and experimentally determined inductances for $i_d < 0$ and $i_q > 0$: (a) L_d, (b) L_q

and the current i_d which are extracted from the FE solution using the same principle as described earlier in Section 8.3.1.

In the second approach the total flux in the d axis, ψ_{dtotal}, is calculated first, which takes into account both the magnet flux and the armature current flux. In order to separate these two flux components, the open-circuit magnet flux linkage ψ_{md} is subtracted from the total flux ψ_{dtotal}, thus giving the net armature winding flux ψ_d. The inductance L_d then follows as a ratio of ψ_d and i_d.

In the final approach the magnets are completely removed from the simulation and the rotor cavities are filled with air. The armature current is applied to produce field in the negative d axis and ψ_d and i_d are extracted to calculate L_d.

Fig. 8.45 compares inductances L_d calculated using the described approaches. It is apparent that L_d, calculated by subtracting the open-circuit flux, is closest to the one calculated and determined experimentally as ψ_d/i_d. The inductance based on permeance freezing corresponds to the model used during optimization. This model was shown on the example of the prototype IPM motor to be correct for the steady state torque calculation and for calculation of the terminal voltage constraints. For small values of i_d the inductance L_d, calculated with magnets replaced by air, is identical to the calculated inductance L_q in Fig. 8.44. This result is expected since initially the rotor bridges are not saturated, so the reluctance of the magnetic circuit in both axes for small current mainly consists of the air gap. As soon as the bridges start saturating as i_d increases, the inductance L_d drops faster and at a high current approaches the value calculated using permeance freezing.

Torque measurement

The measurement of torque as a function of speed has been conducted using SHC torque meter with ratings given in Table 8.14. The d and q components of the armature current which yield maximum torque per amp at every speed have been calculated using the FE method. These calculated current components are then used as the current command for the torque control algorithm. The current command trajectory thus calculated is shown in Fig. 8.46. Three modes of operation have been identified in Fig. 8.46. In mode I the current follows maximum torque per amp trajectory until reaching the rated value for the prototype motor. The mode I covers the speed range from zero to

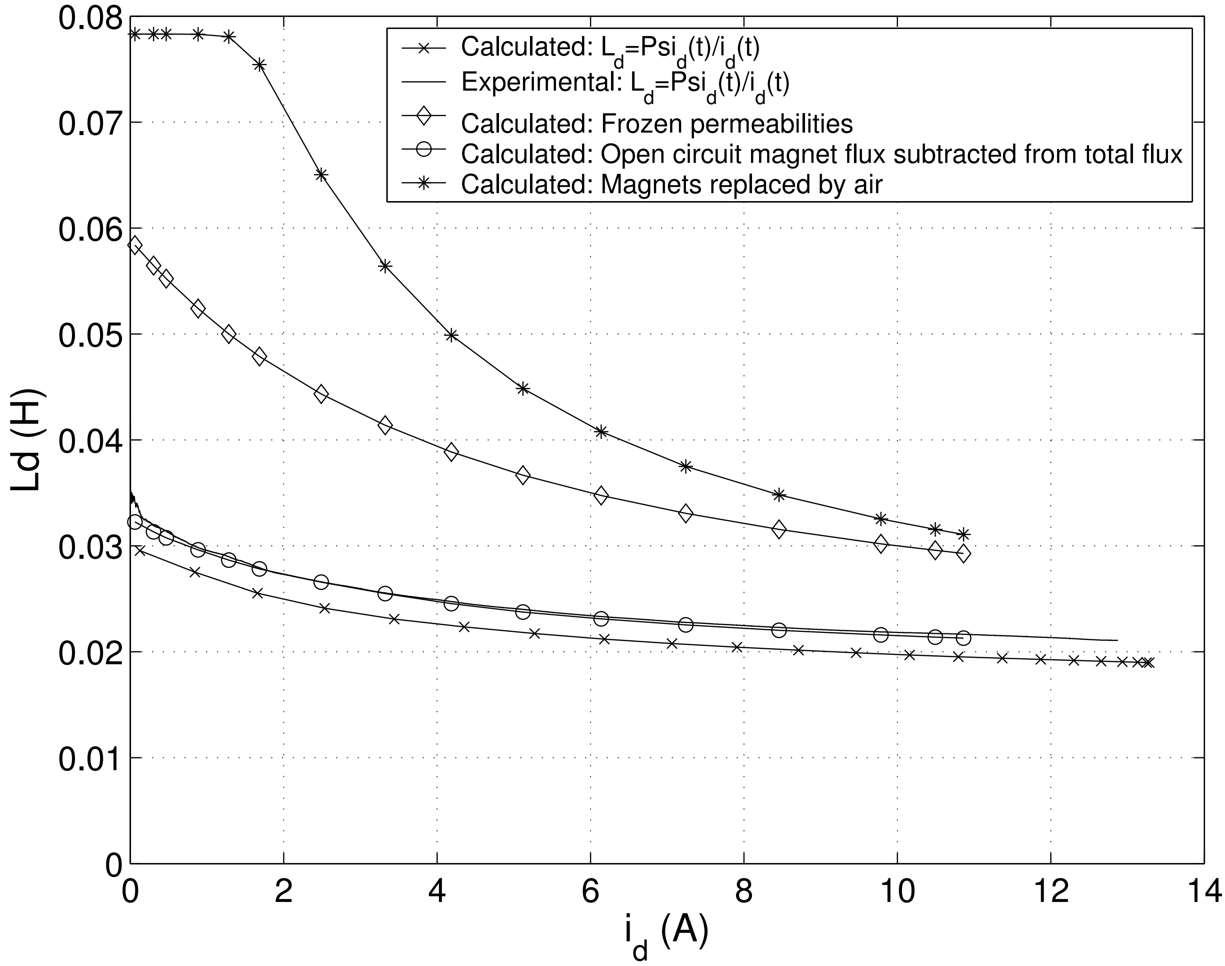

Fig. 8.45 Comparison of inductance L_d calculated using four different finite element based approaches

corner speed (1000 rpm). The motor can operate with any value of the current along the trajectory in mode I at any speed from zero to 1000 rpm without exceeding the voltage limit. The mode II is a part of the current trajectory where the current and voltage limits have been reached, but as the motor speed increases the current can still be kept at its rated value without exceeding the terminal voltage constraint. This is possible up to a certain speed (2000 rpm) after which it is no longer possible to sustain rated current without exceeding the voltage limit. The mode III is a part of the current trajectory from 2000 rpm up to a maximum speed of 6000 rpm. In mode III the current magnitude has to be modified for every speed so that the voltage constraint is not violated.

Table 8.14 Ratings of SHC torque meter

Torque meter
Make: SHC (S. Himmelstein & CO)
Model : MCRT 2660T (2-3)
Max. Speed : 8000 rpm
Range : 2000 lb. in. (226 Nm)

The torque vs. speed curve has been calculated for the entire speed range from zero to 6000 rpm. In the constant torque regime (0-1000 rpm) the current vector has been kept at its rated value at a constant control angle. In the flux weakening regime above corner speed (1000 rpm) the magnitude and the position of the current vector have been adjusted according to Fig. 8.46, so that the rated terminal voltage of 230 V is not exceeded.

During the torque measurement the maximum available voltage from the inverter was limited by the maximum DC bus voltage and by the modulation index used in PWM algorithm. The converter was connected to 230 V, 60 Hz power grid. Since the converter did not provide voltage boosting with modulation index set to 0.9, the maximum available fundamental voltage for the motor was $0.9 \cdot 230 = 207$ V. Fig 8.47 shows torque vs. speed curve calculated for the rated motor voltage (230 V) and for the maximum available voltage (207 V) so that differences between these two cases can be observed. The output power for these two cases is shown in Fig 8.48.

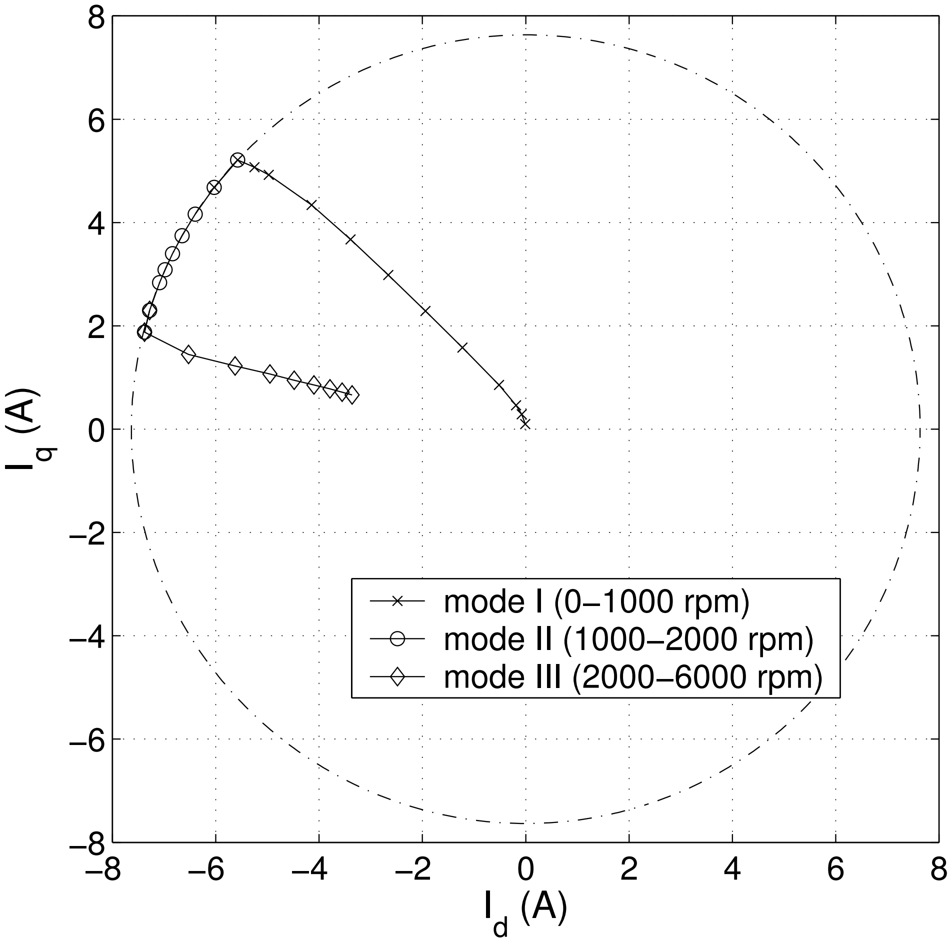

Fig. 8.46 Calculated current trajectory of the prototype IPM motor

The average torque has been calculated using magnetostatic FE simulations with first order elements, as described earlier in Section8.3.1. A more accurate approach has also been used to verify the results of magnetostatic simulations which is based on the transient FE solution with motion using second order elements. Fig. 8.49 compares both calculated results with the measured torque vs speed curve for the maximum voltage of 207 V. There is an apparent discrepancy between the measured torque and the one predicted in the design stage. During the experiment it was not possible to control the motor at a speed higher than 4000 rpm. Since the calculated and measured back emf waveforms in Fig. 8.35 matched quite closely, it is reasonable to assume that the motor was capable of producing the required electromagnetic component of the torque. However, the

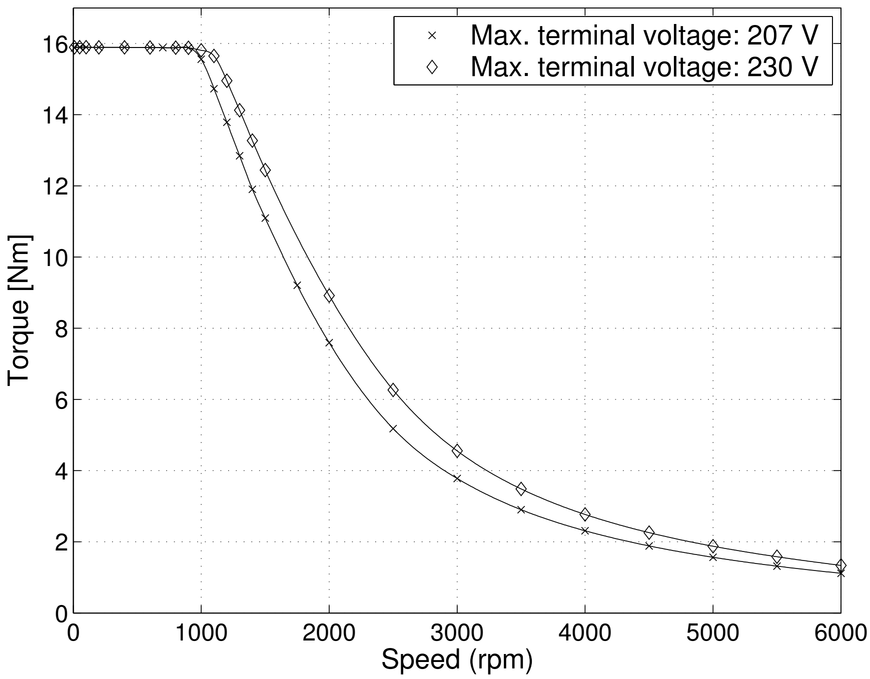

Fig. 8.47 Calculated torque vs. speed curve of the prototype IPM motor

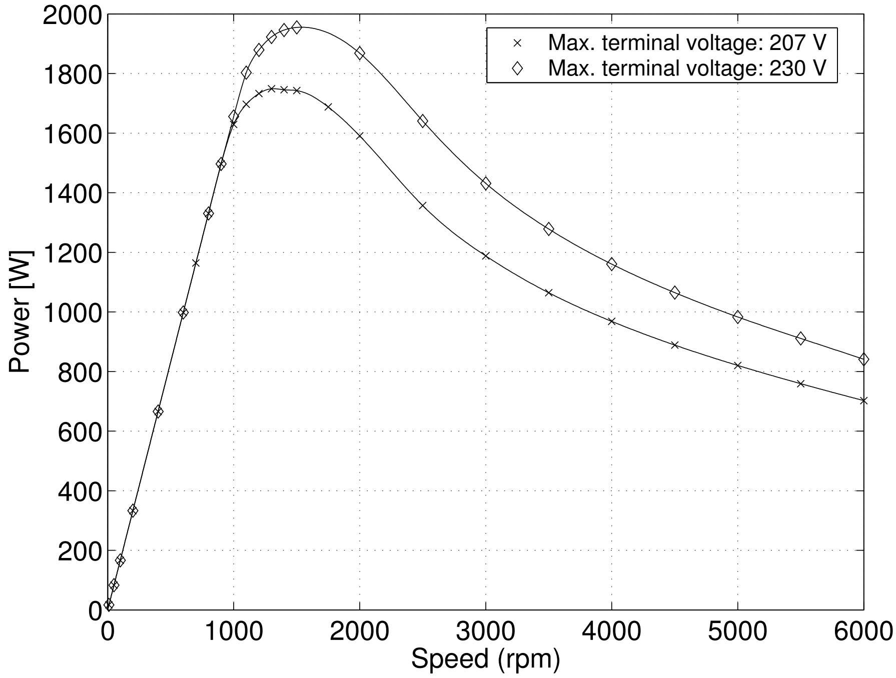

Fig. 8.48 Calculated output power vs. speed curve of the prototype IPM motor

experiments also showed that the measured q axis inductance was approximately 10-20% lower than the calculated one, while the measured d axis inductance was about 10% higher than calculated. Since the reluctance torque is proportional to the difference $L_q - L_d$, it is obvious that a significant reluctance torque will be lost in the actual motor due to discrepancies between the measured and calculated values of these two parameters. The lower value of the inductance L_q could be attributed to a larger effective air gap than assumed by the design. The larger air gap can occur due to manufacturing tolerances, but also can be created by changed properties of the core material due to punching and laser cutting of the rotor laminations. It is difficult to accurately confirm and assess these influences without more practical experience. This could be gained by building more than one prototype IPM motor.

8.5 Comparison of the Optimized IPM Motor Designs With Different Power Ratings and Two or Three Layers of Cavities

The number of variables used in the optimized design of the prototype motor was significantly reduced due to limitations imposed by the standard sizes of the shaft and the motor frame and due to limited availability of the permanent magnets, both in terms of their properties and sizes. These limitations were accepted as a necessary trade-off in order to accelerate the construction of the motor and reduce its cost. The small number of design variables and limited selection of permanent magnet materials have not allowed enough freedom to manipulate the motor parameters sufficiently to yield the best possible motor design. Therefore, a more comprehensive scheme for the optimized design has been developed in which a higher number of design variables have been used. As a consequence a wider variety of design choices has become available which gives more insight into design limitations for a particular power rating of the motor. The design variables with their limits are listed in Table 8.15.

Besides increasing the number of design variables, an additional comparison has been made between IPM motors with two and three layers of cavities in the rotor. The addition of one more cavity increases the saliency ratio of the motor which in turn increases the reluctance torque. Another benefit of the increased saliency ratio is a higher value of the characteristic current due to

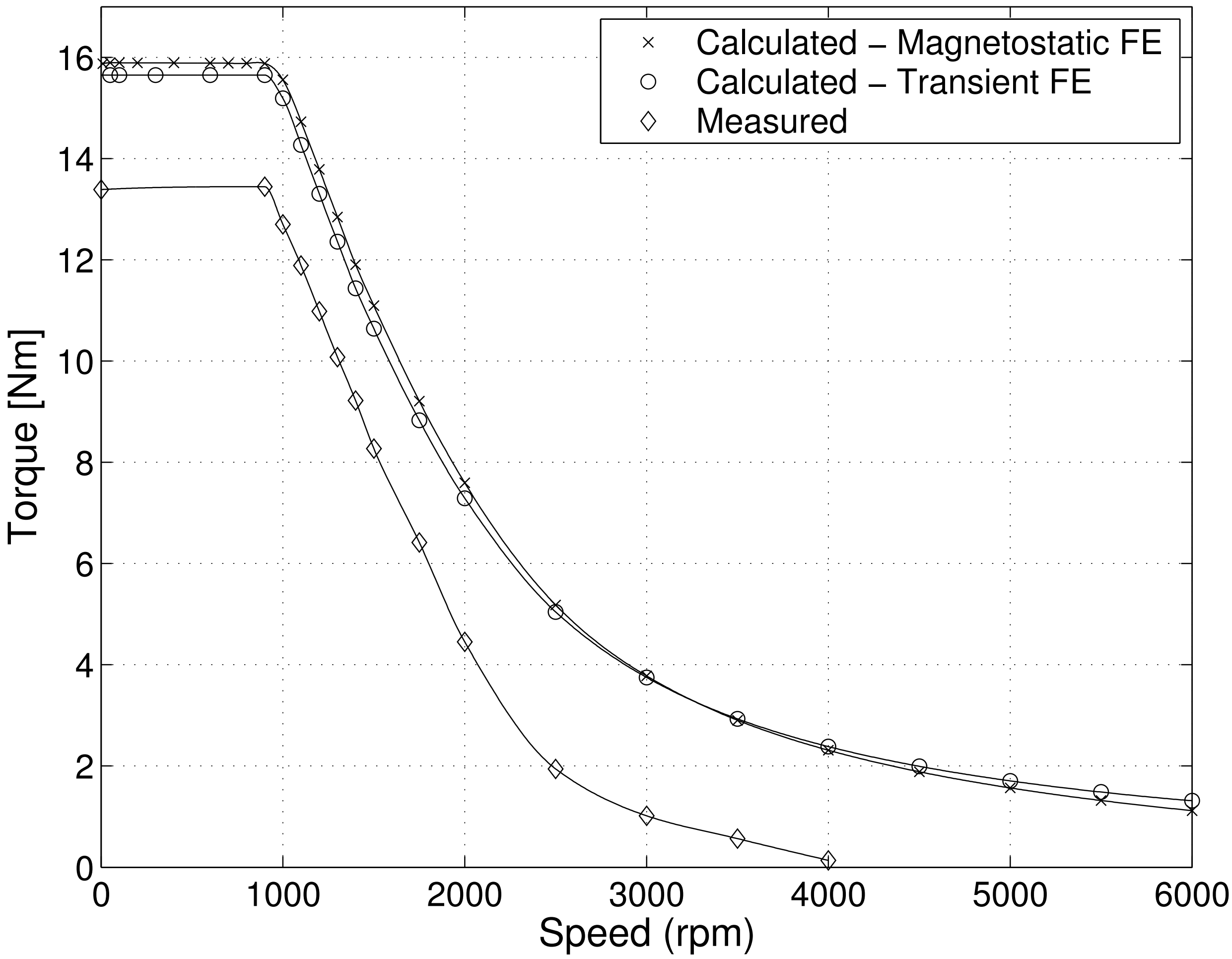

Fig. 8.49 Comparison of measured and calculated torque vs speed curve of the prototype IPM motor

reduced value of the d axis inductance. This results in higher power output in the flux weakening regime. However, the addition of one more cavity increases the complexity of the rotor construction and consequently its manufacturing cost. This analysis has been carried out to show whether or not the third layer of cavities is sufficiently beneficial for improving the motor performance to justify its higher manufacturing cost. The principle geometry of the IPM motor with three layers of cavities is shown in Fig 8.50. The design variables are listed in Table 8.16.

The maximum allowed outer diameter (350 mm) and stack length (150 mm) listed in Tables 8.15 and 8.16 are given for the 5 kW motor. For the 50 kW and 200 kW motors the limits for the outer diameter are set to 500 mm and 700 mm respectively, while the maximum allowed stack lengths are 350 mm and 500 mm.

The information about the relevant motor parameters shown in Fig. 8.50 can be extracted from the design variables in the following manner:

$$
\begin{aligned}
R_{in} &= \frac{D_{in}}{2},\ R_s = \frac{D_s}{2},\ R_r = R_s - g,\ R_o = \frac{D_o}{2} \\
\lambda_{h1} &= 1 - \lambda_{h2} - \lambda_{h3} \\
\lambda_{md4} &= 1 - \lambda_{md1} - \lambda_{md2} - \lambda_{md3} \\
d_{yr} &= R_r - R_{in} \\
d_{m1} &= \lambda_{h1}\lambda_m d_{yr} \\
d_{m2} &= \lambda_{h2}\lambda_m d_{yr} \\
d_{m3} &= \lambda_{h3}\lambda_m d_{yr} \\
d_{r1} &= \lambda_{md1}(1 - \lambda_m)d_{yr} \\
d_{r2} &= \lambda_{md2}(1 - \lambda_m)d_{yr} \\
d_{r3} &= \lambda_{md3}(1 - \lambda_m)d_{yr} \\
d_{r4} &= \lambda_{md4}(1 - \lambda_m)d_{yr} \\
\alpha_p &= \lambda_p \frac{\pi}{p} \\
r_{m1} &= \frac{d_{m1}}{2},\ r_{m2} = \frac{d_{m2}}{2},\ r_{m3} = \frac{d_{m3}}{2} \\
R_{r1} &= Rr - dr0
\end{aligned}
$$

The motor parameters which have fixed values during optimization are:

1. Air gap length: $g = 0.5$ mm
2. Width of the slot opening: $b_o = 2.5$ mm (see Fig. 6.1)
3. Depth of the slot opening: $d_o = 0.62$ mm (see Fig. 6.1)
4. Rotor bridge thickness: $d_{r0} = 1$ mm
5. Radius at the slot bottom: $r_{s2} = 1.2$ mm (see Fig. 8.25)
6. Angular span of the cavities relative to the pole pitch: $\lambda_p = 0.846$
7. Armature current density: $J = 5\ \mathrm{A/mm^2}$
8. Slot fill factor: $f_{fill} = 0.4$
9. Number of slots per pole per phase: $q = 2$
10. Number of parallel paths: $a_p = 1$ (5 kW and 50 kW), $a_p = 2$ (200 kW)

The main objectives of the optimized design are selected as following:

a) Minimize active volume,

b) Maximize characteristic current.

Since the volume of the motor is no longer fixed, the objective to maximize the output torque used in the design of the prototype has been replaced with minimization of the active volume. At the same time the motor has to produce the minimum required torque to provide a desired power output at a desired corner speed.

The IPM motors of 5 kW, 50 kW and 200 kW power ratings with two or three layers of cavities have been designed and compared. The primary design specifications for all power levels are:

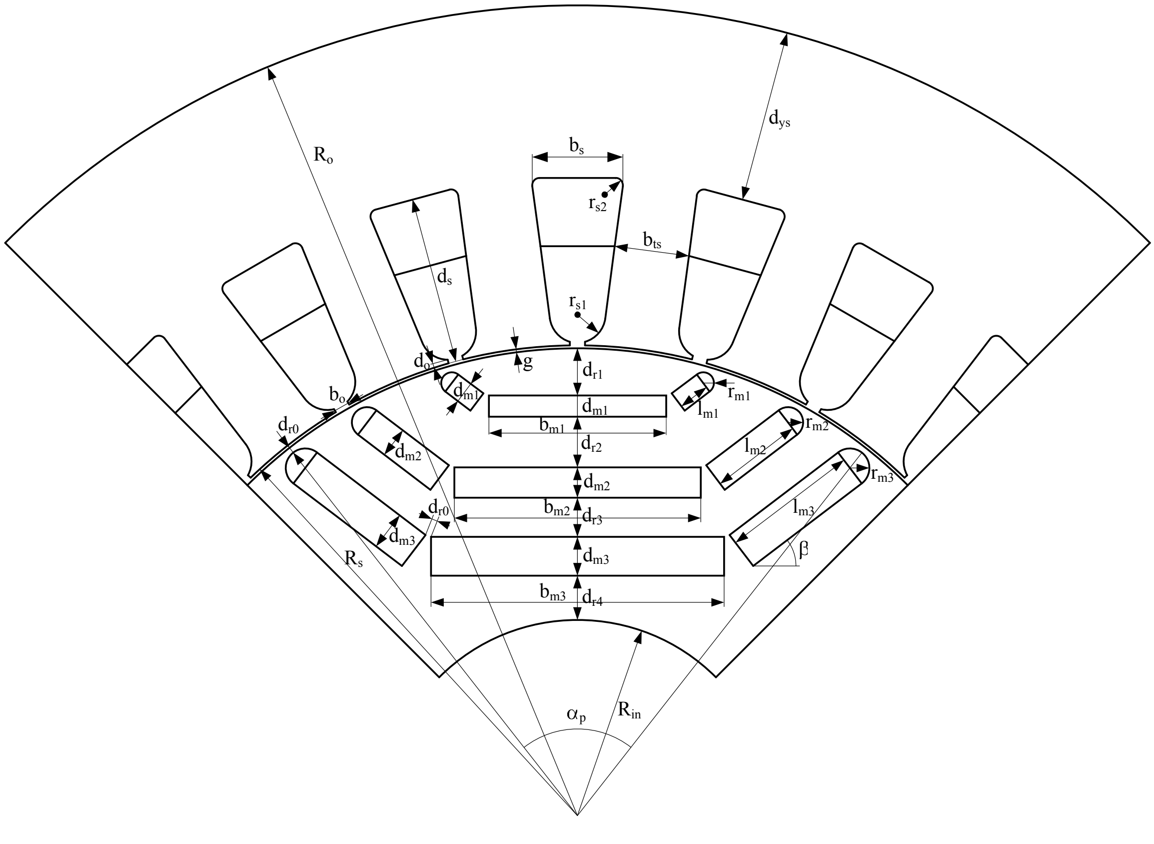

Fig. 8.50 Geometric design parameters of the IPM motor topology with three layers of cavities

Table 8.15 Design variables for an IPM motor with two layers of cavities in the rotor

	Variable	Variable type	Limits
1	Ratio of stator outer diameter to maximum outer diameter	continuous	$0.6 < D_o / D_{o0} < 1 \quad (D_{o0} = 350 \text{ mm})$
2.	Ratio of stator inner diameter to outer diameter	continuous	$0.45 < D_s / D_o < 0.75$
3	Ratio of rotor inner diameter to stator inner diameter	continuous	$0.2 < D_{in} / D_s < 0.6$
4.	Ratio of stack length to maximum stack length	continuous	$0.5 < l_a / l_{a0} < 1 \quad (l_{a0} = 150 \text{ mm})$
5.	Ratio of yoke thickness to difference between stator outer and inner radius	continuous	$0.2 < 2d_{ys} / (D_o - D_s) < 0.6$
6.	Ratio of tooth width to slot pitch at D_S	continuous	$0.3 < b_{ts} / \tau_s < 0.7$
7.	Permanent magnet remanence	continuous	$0.2 < B_r < 0.4$
8.	Number of pole pairs	integer	$p = 2, 3, 4, 5, 6$
9.	Ratio of total cavity to total rotor depth	continuous	$0.1 < \lambda_m < 0.5$
10.	Percentage of total cavity depth for inner cavity	continuous	$0.25 < \lambda_{h2} < 0.7$
11.	Percentage of total rotor depth for the outermost rotor core section	continuous	$0.2 < \lambda_{md1} < 0.6$
12.	Percentage of total rotor depth for middle rotor core section	continuous	$0.1 < \lambda_{md2} < 0.4$
13.	The angle of the slanted magnet	continuous	$0.5 < \beta / \beta_0 < 1 , \quad \beta_0 = (1 - 1/p)\pi / 2$

Table 8.16 Design variables for an IPM motor with three layers of cavities in the rotor

	Variable	Variable type	Limits
1	Ratio of stator outer diameter to maximum outer diameter	continuous	$0.6 < D_o / D_{o0} < 1 \quad (D_{o0} = 350 \text{ mm})$
2.	Ratio of stator inner diameter to outer diameter	continuous	$0.55 < D_s / D_o < 0.8$
3	Ratio of rotor inner diameter to stator inner diameter	continuous	$0.2 < D_{in} / D_s < 0.6$
4.	Ratio of stack length to maximum stack length	continuous	$0.5 < l_a / l_{a0} < 1 \quad (l_{a0} = 150 \text{ mm})$
5.	Ratio of yoke thickness to difference between stator outer and inner radius	continuous	$0.2 < 2d_{ys} / (D_o - D_s) < 0.6$
6.	Ratio of tooth width to slot pitch at D_S	continuous	$0.3 < b_{ts} / \tau_s < 0.7$
7.	Permanent magnet remanence	continuous	$0.2 < B_r < 0.4$
8.	Number of pole pairs	integer	$p = 2, 3, 4, 5, 6$
9.	Ratio of total cavity to total rotor depth	continuous	$0.1 < \lambda_m < 0.5$
10.	Percentage of total cavity depth for the second cavity	continuous	$0.15 < \lambda_{h2} < 0.7$
11.	Percentage of total cavity depth for the innermost cavity	continuous	$0.2 < \lambda_{h3} < 0.6$
12.	Percentage of total rotor depth for the outermost rotor core section	continuous	$0.1 < \lambda_{md1} < 0.6$
13.	Percentage of total rotor depth for the second rotor core section	continuous	$0.1 < \lambda_{md2} < 0.4$
14.	Percentage of total rotor depth for the third rotor core section	continuous	$0.1 < \lambda_{md3} < 0.4$
15.	The angle of the slanted magnet	continuous	$0.5 < \beta / \beta_0 < 1 , \quad \beta_0 = (1 - 1/p)\pi / 2$

Rated line voltage: $V = 400$ V

Corner speed: $n_r = 1000$ rpm

Maximum speed: $n_{max} = 6000$ rpm

The motor designs also need to satisfy the following constraints:

a) Minimum efficiency: $\eta \geq 0.8$,

b) Maximum flux density in the stator core tooth: $B_{ts} \leq 1.8$ T

c) Maximum flux density in the stator yoke: $B_y \leq 1.5$ T

d) Minimum torque requirement: $\begin{cases} T \geq 47.75 \text{ Nm}, & \text{5 kW motor} \\ T \geq 477.5 \text{ Nm}, & \text{50 kW motor} \\ T \geq 1910 \text{ Nm}, & \text{200 kW motor} \end{cases}$

e) Maximum rms linear current density: $\begin{cases} K_{1s} \leq 25000 \text{ A/m}, & \text{5 kW motor} \\ K_{1s} \leq 35000 \text{ A/m}, & \text{50 kW motor} \\ K_{1s} \leq 40000 \text{ A/m}, & \text{200 kW motor} \end{cases}$

f) Maximum allowed rms value of the fundamental component line-to-line back emf at maximum speed: $E_{1max} \leq 400$ V

The DE parameters for all simulations have been set to F=0.3, CR=0.3. For each motor design the results have been collected after 200 iterations of the DE algorithm. The population size for the motor with two layers of cavities has been set to 40 while in the case of three layers of cavities the population size has been set to 50.

The trade-offs between the two objective functions for the motor designs which emerged in the Pareto sets after 200 iterations for all three power levels and for both two and three layers of cavities are compared in Figs. 8.51 and 8.52. The active volumes of the motors for all power levels have been normalized with respect to the maximum allowed volume for the 5 kW motor. The characteristic current for each individual design has been normalized with respect to its rated current. The basic design parameters for all solutions are listed in Tables 8.17 and 8.18.

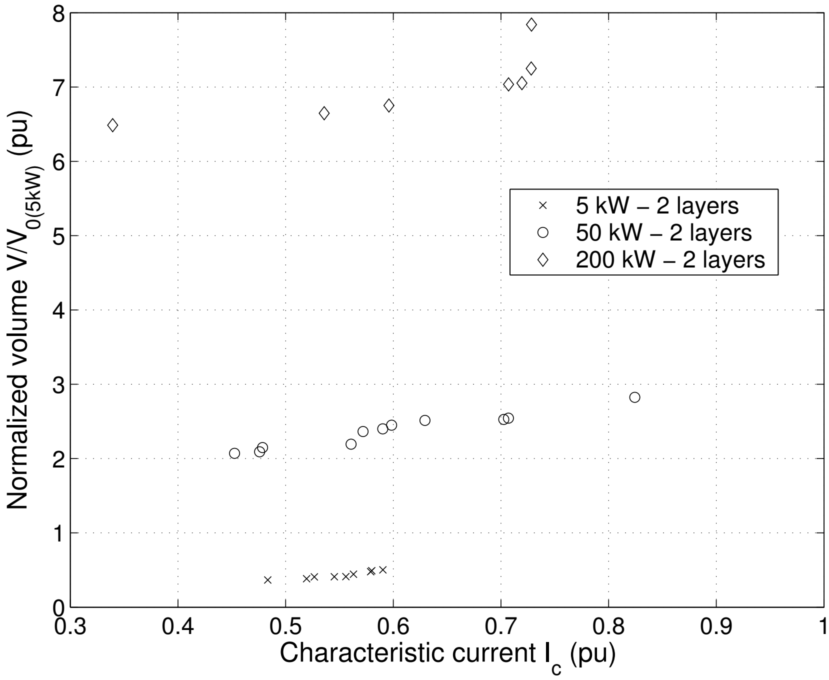

Fig. 8.51 Pareto fronts for 5 kW, 50 kW and 200 kW motors with two layers of cavities

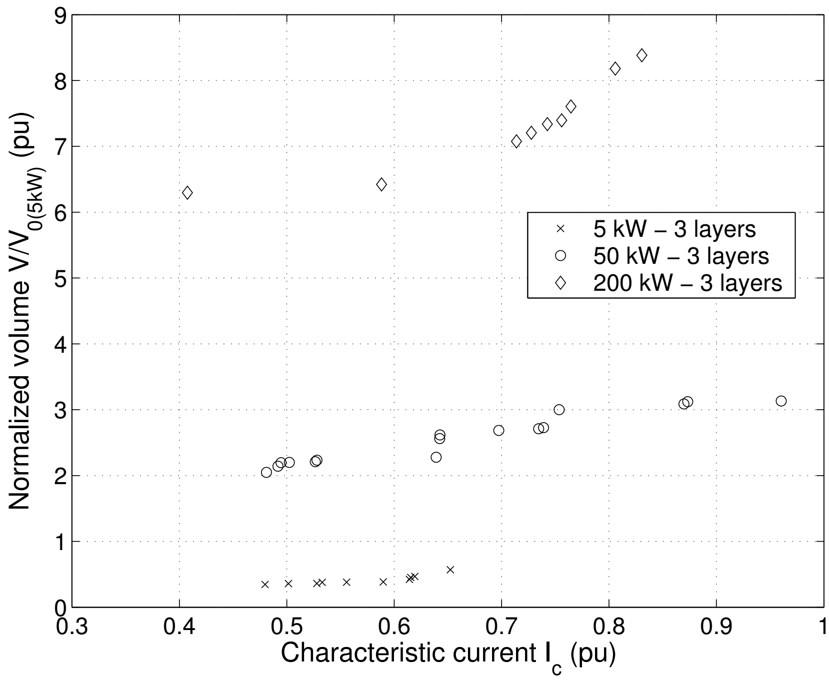

Fig. 8.52 Pareto fronts for 5 kW, 50 kW and 200 kW motors with three layers of cavities

Table 8.17 Design parameters of nondominant solutions resulting from multiobjective optimization of 5 kW, 50 kW and 200 kW IPM motors with two layers of cavities

	D_o [mm]	D_s [mm]	D_{in} [mm]	l_a [mm]	d_{ys} [mm]	b_{ts} [mm]	d_{m1} [mm]	d_{m2} [mm]	d_{r1} [mm]	d_{r2} [mm]	d_{r3} [mm]	β [deg.]	B_r [T]	Q_s	2p	I_c [pu]	$V/V_{0(5kW)}$ [pu]
5 kW design – Two layers of cavities																	
1	259.6	175.9	83.5	99.8	20.64	7.78	3.98	5.63	21.41	5.98	9.19	42.1	0.243	36	6	0.484	0.366
2	285.5	181.9	86.3	86.4	29.29	9.26	4.22	5.64	21.91	4.68	11.36	52.2	0.244	36	6	0.520	0.383
3	286.4	196.8	99.0	91.6	23.01	11.24	5.27	5.88	21.20	5.01	11.57	50.3	0.226	36	6	0.527	0.409
4	287.0	199.6	100.4	91.6	22.46	11.39	4.38	6.29	22.08	4.82	12.04	50.0	0.226	36	6	0.545	0.411
5	254.8	172.5	93.2	116.3	19.66	9.70	3.75	5.27	16.28	4.96	9.42	45.7	0.262	36	6	0.556	0.411
6	298.2	211.8	106.5	91.6	22.18	12.09	5.67	6.33	23.05	5.71	11.89	47.8	0.226	36	6	0.563	0.443
7	268.6	187.3	97.3	122.0	20.04	11.08	4.26	6.17	18.50	5.95	10.17	42.0	0.247	36	6	0.579	0.479
8	279.4	193.1	106.1	115.9	23.95	10.93	3.86	6.03	16.95	4.98	11.66	56.2	0.237	36	6	0.580	0.492
9	313.6	205.8	101.2	93.9	32.08	12.51	3.69	7.06	19.20	5.38	16.99	42.1	0.253	36	6	0.590	0.502
50 kW design – Two layers of cavities																	
1	413.5	275.0	124.8	222.5	30.93	12.26	7.48	8.35	16.57	6.28	36.40	56.48	0.288	48	8	0.453	2.071
2	437.6	284.7	148.5	200.7	39.55	12.12	4.53	6.77	27.19	6.41	23.19	57.56	0.270	48	8	0.476	2.092
3	423.1	279.7	123.7	220.5	40.49	9.94	4.42	6.40	23.42	8.79	34.97	59.58	0.272	48	8	0.479	2.148
4	425.6	297.4	139.7	222.5	35.60	10.86	6.01	8.07	21.84	6.81	36.08	52.88	0.288	48	8	0.561	2.193
5	371.3	237.4	116.7	315.2	35.49	13.63	3.90	5.55	25.79	6.26	18.83	48.29	0.316	36	6	0.572	2.365
6	371.3	237.4	116.7	319.9	35.21	14.08	3.90	5.55	25.79	6.26	18.83	48.29	0.321	36	6	0.590	2.400
7	436.2	301.9	166.1	236.5	38.42	7.68	4.21	3.61	16.11	7.74	36.23	64.00	0.326	72	12	0.598	2.449
8	436.2	301.9	166.1	242.7	38.85	7.86	4.21	3.61	16.11	7.74	36.23	64.00	0.333	72	12	0.629	2.514
9	449.5	318.0	167.0	229.8	37.24	10.21	3.13	4.74	34.79	8.22	24.65	61.28	0.315	60	10	0.703	2.527
10	450.9	320.9	168.5	229.8	36.83	10.31	3.16	4.78	35.11	8.30	24.87	59.51	0.315	60	10	0.707	2.543
11	457.8	340.2	200.4	247.6	33.69	12.04	3.77	5.93	19.29	7.09	33.83	66.85	0.327	60	10	0.824	2.824
200 kW design – Two layers of cavities																	
1	549.7	388.7	183.7	394.4	43.55	13.98	13.48	12.45	19.63	10.96	46.01	58.57	0.223	48	8	0.339	6.486
2	557.4	392.8	211.4	393.1	45.86	12.36	9.12	7.86	29.70	11.92	32.11	65.05	0.288	60	10	0.536	6.648
3	632.5	463.7	232.4	310.1	49.76	13.12	8.77	10.48	35.89	11.28	49.21	60.42	0.311	60	10	0.596	6.751
4	549.7	391.9	201.1	427.8	46.86	16.17	7.70	7.18	47.00	9.31	24.24	59.68	0.312	48	8	0.707	7.035
5	560.3	388.1	186.7	412.8	49.64	17.56	7.88	8.64	48.59	8.71	26.93	62.54	0.317	48	8	0.720	7.052
6	594.7	429.0	240.1	407.2	49.41	18.73	8.45	8.42	46.52	9.01	22.04	56.27	0.322	48	8	0.728	7.839
7	571.1	418.4	223.2	408.3	45.22	17.27	7.88	7.35	48.09	9.52	24.80	59.68	0.312	48	8	0.728	7.248

Table 8.18 Design parameters of nondominant solutions resulting from multiobjective optimization of 5 kW, 50 kW and 200 kW IPM motors with three layers of cavities

	D_o [mm]	D_s [mm]	D_{in} [mm]	l_a [mm]	d_{ys} [mm]	b_{ts} [mm]	d_{m1} [mm]	d_{m2} [mm]	d_{m3} [mm]	d_{r1} [mm]	d_{r2} [mm]	d_{r3} [mm]	d_{r4} [mm]	β [deg.]	B_r [T]	Q_s	2p	I_c [pu]	$V/V_{0(5kW)}$ [pu]
5 kW design – Three layers of cavities																			
1	254.1	165.6	97.3	98.5	21.11	10.49	0.78	1.93	3.57	12.80	5.49	4.29	5.27	42.3	0.249	36	6	0.480	0.346
2	270.1	169.7	88.2	90.6	24.27	10.75	1.86	3.42	4.50	6.28	5.35	4.25	15.09	42.3	0.256	36	6	0.502	0.360
3	251.9	165.1	86.7	104.6	21.63	10.46	1.98	3.31	3.68	10.42	9.92	5.67	4.24	42.3	0.237	36	6	0.528	0.361
4	267.1	155.1	80.8	97.2	31.21	14.74	2.05	2.93	3.74	6.83	10.50	6.11	4.97	31.7	0.275	24	4	0.533	0.377
5	280.9	182.1	99.6	88.5	24.91	11.54	2.60	2.63	4.64	7.81	8.72	6.19	8.69	42.3	0.258	36	6	0.556	0.380
6	259.1	151.0	49.6	105.1	29.37	14.35	2.87	3.03	5.52	10.97	9.79	6.11	12.42	31.7	0.277	24	4	0.590	0.384
7	267.1	155.1	64.5	108.6	32.78	14.74	2.50	3.58	4.56	8.32	12.81	7.46	6.06	31.7	0.275	24	4	0.614	0.422
8	270.7	192.5	110.6	113.5	21.23	12.19	3.04	3.96	5.19	10.58	9.47	4.78	3.88	42.3	0.216	36	6	0.615	0.453
9	259.1	182.6	103.3	128.0	19.07	11.57	2.71	2.76	5.30	10.64	6.63	4.68	6.94	42.3	0.237	36	6	0.619	0.468
10	298.6	207.1	124.1	117.4	26.42	13.12	2.03	3.62	3.87	11.43	4.83	5.08	10.61	42.3	0.240	36	6	0.652	0.570
50 kW design – Three layers of cavities																			
1	360.3	235.2	126.0	290.1	31.76	16.31	2.37	4.42	6.68	12.90	11.22	4.63	12.40	47.7	0.245	36	6	0.481	2.049
2	394.1	256.2	135.4	253.5	36.79	17.77	5.03	6.37	5.88	16.58	10.45	6.57	9.53	47.7	0.222	36	6	0.492	2.142
3	361.9	242.8	132.5	308.1	30.21	12.63	4.90	5.48	5.10	13.38	6.12	5.78	14.36	53.6	0.234	48	8	0.495	2.196
4	345.9	234.8	133.3	337.9	28.14	16.28	5.39	6.90	7.40	12.36	8.19	3.87	6.64	47.7	0.240	36	6	0.502	2.200
5	378.6	262.9	140.3	283.2	29.71	13.67	6.15	3.02	8.14	12.57	5.59	7.06	18.79	53.6	0.256	48	8	0.527	2.209
6	410.1	278.4	157.3	244.0	37.07	19.31	5.17	3.35	7.49	10.49	10.64	8.02	15.37	47.7	0.250	36	6	0.528	2.233
7	432.1	311.5	183.4	224.2	33.34	16.20	6.09	3.46	8.44	15.69	10.44	6.71	13.21	53.6	0.234	48	8	0.639	2.278
8	385.6	254.5	135.0	316.6	37.46	17.65	2.98	6.08	6.31	15.66	10.22	7.67	10.85	47.7	0.271	36	6	0.642	2.561
9	398.7	252.6	138.0	302.5	41.68	17.52	3.87	5.67	5.95	15.61	10.31	5.50	10.38	47.7	0.286	36	6	0.643	2.617
10	403.3	273.8	158.0	303.3	38.61	18.99	4.96	3.21	7.20	10.02	9.64	6.78	16.09	47.7	0.294	36	6	0.697	2.685
11	397.3	270.5	139.5	315.5	37.16	18.76	4.78	4.21	9.22	9.93	12.00	6.85	18.54	47.7	0.282	36	6	0.734	2.711
12	397.3	270.5	140.3	317.3	37.25	18.76	4.75	4.18	9.17	9.87	11.93	6.81	18.42	47.7	0.282	36	6	0.739	2.727
13	430.2	311.5	167.7	297.8	31.49	16.20	8.94	4.42	4.29	18.49	9.72	7.94	18.11	53.6	0.289	48	8	0.754	3.000
14	430.2	311.5	173.9	306.5	34.96	16.20	6.37	3.00	7.51	19.37	11.81	7.26	13.47	53.6	0.276	48	8	0.870	3.087
15	431.8	321.6	168.6	307.6	30.86	16.73	9.36	3.18	4.32	19.27	11.10	8.74	20.56	53.6	0.290	48	8	0.873	3.122
16	422.0	324.6	186.2	323.2	27.91	16.89	5.13	5.14	7.07	23.09	12.48	5.96	10.33	53.6	0.264	48	8	0.960	3.133
200 kW design – Three layers of cavities																			
1	542.5	414.3	316.4	393.1	37.54	11.78	1.37	4.57	3.42	17.05	5.69	4.30	12.55	50.9	0.237	36	6	0.408	6.297
2	540.1	412.4	315.0	404.6	36.60	11.68	1.86	4.79	3.30	5.20	10.91	4.83	17.85	60.7	0.316	36	6	0.588	6.422
3	534.6	408.2	311.7	455.0	33.97	9.26	1.71	2.79	3.52	7.18	7.65	4.84	20.54	54.4	0.362	48	8	0.714	7.075
4	534.6	408.2	311.7	463.4	37.55	9.26	1.71	2.79	3.52	7.18	7.65	4.84	20.54	54.4	0.362	48	8	0.728	7.206
5	534.6	408.2	311.7	471.8	33.97	9.26	1.71	2.79	3.52	7.18	7.65	4.84	20.54	54.4	0.362	48	8	0.743	7.338
6	546.1	417.0	318.5	455.6	37.57	9.31	4.16	4.38	2.73	16.22	5.27	3.92	12.60	76.4	0.307	48	8	0.756	7.395
7	542.5	414.3	316.3	474.9	37.14	8.72	1.73	3.13	4.24	13.85	7.04	4.36	14.61	68.1	0.323	48	8	0.765	7.605
8	551.7	421.3	321.8	493.8	36.90	8.85	1.71	3.40	5.97	6.24	4.90	4.05	23.52	78.2	0.325	48	8	0.806	8.181
9	573.5	438.0	334.5	468.3	38.68	9.81	1.74	3.48	6.30	6.77	7.90	4.04	21.54	66.7	0.321	48	8	0.831	8.384

The results of optimization indicate that the addition of the third layer of cavities is beneficial for increasing the characteristic current of the motor without sacrificing its size. This has been observed for all three power levels. Another observation is that in most cases a moderate increase in motor volume can yield quite a significant increase in characteristic current, thus improving significantly the motor performance in the flux weakening regime.

The highest characteristic currents have been obtained for the 50 kW motor design. In order to explain this result one must consider the parameters which affect the value of the characteristic current I_c. Its per unit value is defined as

$$I_{c(pu)} = \frac{\Psi_{md}}{L_d I_R} \tag{8.69}$$

where Ψ_{md} is the flux of the magnets alone linked by the armature winding, L_d is the d axis inductance and I_R is the rated armature current. The machine parameters can be expressed in terms of device dimensions and material properties in the following manner:

$$\begin{aligned}
&\text{Backemf}: \quad E = \sqrt{2}\pi N_s B A_c f \\
&\text{Current}: \quad I = \frac{J A_w}{N_s} \\
&\text{Flux}: \quad \Psi = N_s B A_c \\
&\text{Inductance}: \quad L = N_s^2 \frac{\mu A_c}{l_c}
\end{aligned}$$

where N_s is the number of turns connected in series, B is the flux density, A_c is the core area, J is the current density, A_w is the total area occupied by the winding, μ is the permeability and l_c is the length of the flux paths in the core and the air gap.

Motor designs for all three power levels have the same rated voltage and the same constant current density. If linear dimensions of the motor are marked with x, then the back emf varies as $N_s B f x^2$, the current as $\frac{x^2}{N_s}$, the flux as $N_s B x^2$ and the inductance as $N_s^2 x$. The characteristic current can now be expressed as

$$I_{c(pu)} = K \frac{N_s B x^2}{N_s^2 x \frac{x^2}{N_s}} = K \frac{B}{x} \tag{8.70}$$

where K is a constant term which takes into account the parameters that do not change. If the back emf is expressed as

$$E = k_e N_s B f x^2 \tag{8.71}$$

then the relationship between the back emf and the linear dimension x is

$$x = \sqrt{\frac{E}{k_e N_s B f}} \tag{8.72}$$

After substituting (8.72) into (8.70), the final expression for I_c is

$$I_{c(pu)} = K \sqrt{\frac{k_e N_s B^3 f}{E}} \tag{8.73}$$

Equation (8.73) indicates that the characteristic current can be increased if the number of turns, flux density, or frequency are increased while the back emf is decreased. In this particular case the back emf is constrained so the characteristic current can be increased only if the term $N_s B^3 f$ is increased without violating the back emf constraint. However, one must also not forget that the back emf is a function of all these parameters and that it is not possible to change either the number of turns, the flux density, or the frequency without changing the back emf. Hence, the maximization of the characteristic current is a complex process of finding the optimal balance between all these parameters with the back emf constraint as the main limiting factor in the design. It may also be possible to further increase the characteristic current if the voltage rating of the motor is used as a design variable. In that case a voltage level can be found for every required power output which could yield maximum characteristic current higher than obtained in Figs. 8.51 and 8.52. This analysis remains as a suggestion for future work on the optimized design of IPM motors.

Chapter 9

Conclusion and Suggestions for Future Work

This thesis has introduced new concepts related to analytical field calculations in surface PM motors. It has been recognized that the complex nature of conformal transformation can be utilized to extract useful information about the field distribution in the slotted air gap of a surface PM motor. The concept of complex relative air gap permeance has been developed from conformal transformation of the slot opening and used to accurately calculate the air gap field for both radial and tangential components of the flux density.

The knowledge of radial and tangential components of the air gap flux density led to development of the closed form solutions for cogging torque and electromagnetic torque based on the integral of Maxwell's stress tensor in the air gap.

The complex air gap permeance has also been utilized to determine the back emf waveform, the winding inductances, and the waveforms of the flux density in the core, which in turn are used for calculation of the core losses. It has also been shown how the armature winding air gap field solution can be used to calculate the magnet losses caused by the space harmonics in the armature winding MMF distribution and the time harmonics in the current waveform.

The main advantage of the proposed air gap permeance model over the existing models is its ability to provide reliable information about the radial and the tangential flux density components in the air gap of a surface PM motor. All the relevant motor parameters can be determined from this field solution. The correctness of the model has been verified by comparing it with the finite element model on an example of a 3.7 kW surface PM motor.

A systematic approach to the optimized design of surface and interior PM motors with the emphasis on reduced cogging torque and reduced electromagnetic torque ripple has also been developed. The

Differential Evolution (DE) has been introduced as a reliable method for design optimization which can solve single and multiobjective optimization problems with continuous, integer or discrete design variables. The effectiveness of the method has been demonstrated on examples of optimized design of surface and interior PM motors. The multiobjective approach to design optimization using the DE has been proposed as an alternative to a single objective optimization because it gives more insight into the correlation between the conflicting design objectives and provides more information about the compromises which need to be made between different design solutions.

The DE algorithm along with the analytical model of a 5 kW surface PM motor has been utilized to find a set of nondominant design solutions with minimized volume and maximized efficiency as the main design objectives. The correlation between these two objectives has been observed in the form of a Pareto front. It has been shown that it is not possible to maximize the motor efficiency for a desired torque output without oversizing the motor, both in terms of its physical dimensions and torque production, when the current density is kept constant. With current density introduced as a design variable it has been shown for the 5 kW motor that in order to increase the motor efficiency by 1%, it is required to increase its volume by 100%.

The same DE algorithm has been successfully used to find the optimal design of an interior PM motor which has a minimum cogging torque and a minimum difference between the characteristic current and the rated current. The second objective is important, because as the characteristic current approaches the rated current, the motor becomes capable of producing constant power in theoretically infinite speed range. However, this goal is usually compromised by the back emf constraint which does not allow the back emf at maximum speed to exceed a certain value to avoid uncontrolled generation in the case of inverter failure. The optimal angular span of the rotor cavities, which yields minimum cogging torque, has been found as a result of this simulation. This optimal angular span corresponds to the similar result for an IPM motor reported in literature. The IPM motor has been modelled using magnetostatic FE simulation. An approximative method for cogging torque calculation has been developed which utilizes the complex relative air gap permeance to estimate the cogging torque waveform based on only two magnetostatic FE simulations.

The described multiobjective approach to optimization has been used to design and build a prototype IPM motor with the goals of maximizing the torque output from the constant volume of the motor and maximizing the characteristic current of the motor. The experiments conducted on the motor showed that the motor was not capable of producing the torque predicted by the FE method in the design stage. This result was caused by a lower measured value of the q axis inductance ($\sim$10-20%) and higher value of the d axis inductance ($\sim$10%) compared to the calculated ones. This resulted in a significant loss of the reluctance torque. This difference between measured and calculated L_d and L_q has been attributed primarily to the altered properties of the core material in the vicinity of the air gap, where laminations had been punched and laser cut. This explanation remains to be verified in the future by comparing other IPM prototype motors which might be designed and constructed.

The optimized design and analysis of the IPM motor has been further expanded by comparing designs of different power levels with two or three layers of cavities in the rotor. It has been shown that the addition of the third layer of cavities increases the characteristic current of the motor for all power levels and thus increases the power output at high speed. An additional analysis needs to be done which would show if the addition of the third layer of cavities enhances the motor performance sufficiently to justify its higher manufacturing cost.

As a part of the future work, several issues should be further addressed to augment the scope of this thesis:

1. Make further improvements to the Differential Evolution optimization algorithm to accelerate its convergence and make it a more robust tool for single objective and multiobjective optimization of different types of electrical machines,

2. Expand the optimized design of IPM motors with two and three layers of cavities to include the rated terminal voltage as a design variable and assess the possibility to further increase the characteristic current of the motor,

3. Investigate more thoroughly how the manufacturing processes, like punching and laser cutting, influence the properties of the core laminations and how they affect the actual motor performance compared to the performance predicted in the design stage.

Bibliography

[1] T. M. Jahns and W. Soong, "Pulsating Torque Minimization Techniques for Permanent Magnet AC Motor Drives - A Review," *IEEE Transactions on Industrial Electronics*, vol. 43, no. 2, pp. 321–330, 1996.

[2] S. M. Hwang, J. B. Eom, G.-B. Hwang, W.-B. Jeong, and Y.-H. Yung, "Cogging Torque and Acoustic Noise Reduction in Permanent Magnet Motors by Teeth Pairing," *IEEE Transactions on Magnetics*, vol. 36, pp. 3144–3146, September 2000.

[3] S. M. Hwang, J. B. Eom, Y. H. Jung, D. W. Lee, and B. S. Kang, "Various Design Techniques to Reduce Cogging Torque by Controlling Energy Variation in Permanent Magnet Motors," *IEEE Transactions on Magnetics*, vol. 37, pp. 2806–2809, July 2001.

[4] Z. Q. Zhu and D. Howe, "Influence of Design Parameters on Cogging Torque in Permanent Magnet Machines," *IEEE Transactions on Energy Conversion*, vol. 15, no. 4, pp. 407–412, 2000.

[5] N. Bianchi and S. Bolognani, "Design Techniques for Reducing the Cogging Torque in Surface-Mounted PM Motors," *IEEE Transactions on Industry Applications*, vol. 38, no. 5, pp. 1259–1265, 2002.

[6] N. Bianchi and S. Bolognani, "Interior PM Synchronous Motor for High Performance Applications," *Proceedings of the Power Conversion Conference PCC Osaka 2002*, vol. 1, pp. 148–153, 2002.

[7] L. Parsa, L. Hao, and H. A. Toliyat, "Optimization of Average and Cogging Torque in 3-phase IPM Motor Drives," *Conference Record of the 37th IAS Annual Meeting*, vol. 1, pp. 417–424, 2002.

[8] T. Ohnishi and N. Takahashi, "Reduction of Cogging Torque in Interior-Magnet Brushless Machines," *IEEE Transactions on Magnetics*, vol. 36, pp. 3537–3539, September 2003.

[9] E. R. B. Filho, A. M. N. Lima, and T. Araujo, "Reducing Cogging Torque in Interior Permanent Magnet Machines Without Skewing," *IEEE Transactions on Magnetics*, vol. 34, pp. 3652–3655, September 1998.

[10] Z. Q. Zhu, S. Ruangsinchaiwanich, N. Schofield, and D. Howe, "Reduction of Cogging Torque in Interior-Magnet Brushless Machines," *IEEE Transactions on Magnetics*, vol. 38, pp. 3238–3240, September 2003.

[11] D. C. Hanselman, "Effect of Skew, Pole Count and Slot Count on Brushless Motor Radial Force, Cogging Torque and Back EMF," *IEE Proc.-Electric Power Applications*, vol. 144, no. 5, pp. 325–330, 1997.

[12] M. S. Islam, S. Mir, and T. Sebastian, "Issues in Reducing the Cogging Torque of Mass-Produced Permanent Magnet Brushless DC Motor," *Conference Record of the 38th IAS Annual Meeting*, vol. 1, pp. 393–400, 2003.

[13] R. P. Deodhar, D. A. Staton, and T. J. E. Miller, "Modelling of Skew Using the Flux-MMF Diagram," *Proceedings of the 1996 International Conference on Power Electronics, Drives and Energy Systems for Industrial Growth*, vol. 1, pp. 546–551, 1996.

[14] K.-H. Kim, D.-J. Sim, and J.-S. Won, "Analysis of Skew Effects on Cogging Torque and BEMF for BLDCM," *Conference Record of the 1991 IEEE Industry Applications Society Annual Meeting*, vol. 1, pp. 191–197, 1991.

[15] T. Sebastian and V. Gangla, “Analysis of Induced EMF and Torque Waveforms in a Brushless Permanent Magnet Machine,” *Conference Record of the 1994 IEEE Industry Applications Society Annual Meeting*, vol. 1, pp. 240–246, 1991.

[16] S. Hwang and D. K. Lieu, “Design Techniques for Reduction of Reluctance Torque in Brushless Permanent Magnet Motors,” *IEEE Transactions on Magnetics*, vol. 30, no. 6, pp. 4287–4289, 1994.

[17] M. Jug, B. Hribernik, A. Hamler, M. Trlep, and B. Kreca, “Investigation of Reluctance Torque of Brushless DC Motor,” *Proceedings of ICEM ’90*, pp. 132–137, 1990.

[18] J. D. L. Ree and N. Boules, “Torque Production in Permanent-Magnet Synchronous Motors,” *IEEE Transactions on Industry Applications*, vol. 25, pp. 107–112, January/February 1989.

[19] C. Studer, A. Keyhani, T. Sebastian, and S. K. Murthy, “Study of Cogging Torque in Permanent Magnet Machines,” *Conference Record of the Thirty-Second IAS Annual Meeting*, vol. 1, pp. 42–49, 1997.

[20] C. Breton, J. Bartolome, J. A. Benito, G. Tassinario, I. Flotats, C. W. Lu, and B. J. Chalmers, “Influence of Machine Symmetry on Reduction of Cogging Torque in Permanent-Magnet Brushless Motors,” *IEEE Transactions on Magnetics*, vol. 36, no. 5, pp. 3819–3823, 2000.

[21] C. A. Borghi, D. Casadei, A. Cristofolini, M. Fabbri, and G. Serra, “Application of a Multiobjective Minimization Technique for Reducing the Torque Ripple in Permanent-Magnet Motors,” *IEEE Transactions on Magnetics*, vol. 35, no. 5, pp. 4238–4246, 1999.

[22] E. Favre, L. Cardoletti, and M. Jufer, “Permanent-Magnet Synchronous Motors: A Comprehensive Approach to Cogging Torque Suppression,” *IEEE Transactions on Industry Applications*, vol. 29, no. 6, pp. 1141–1149, 1993.

[23] J. Y. Hung and Z. Ding, “Design of Currents to Reduce Torque Ripple in Brushless Permanent Magnet Motors,” *IEE Proceedings-Electric Power Applications*, pp. 260–266, 1993.

[24] D. C. Hanselman, “Minimum Torque Ripple, Maximum Efficiency Excitation of Brushless Permanent Magnet Motors,” *IEEE Transactions on Industrial Electronics*, vol. 41, no. 3, pp. 292–300, 1994.

[25] C. Marchand and A. Razek, “Optimal Torque Operation of Digitally Controlled Permanent Magnet Snchronous Motor Drives,” *IEE Proceedings-Electric Power Applications*, pp. 232–240, 1993.

[26] F. Colamartino, C. Marchand, and A. Razek, “Torque Ripple Minimization in Permanent Magnet Synchronous Servodrive,” *IEEE Transactions on Energy Conversion*, vol. 14, pp. 616–621, September 1999.

[27] T. S. Low, K. J. Tseng, T. H. Lee, K. W. Lim, and K. S. Lock, “Strategy for the Instantaneous Torque Control of Permanent-Magnet Brushless DC Drives,” *IEE Proceedings-Electric Power Applications*, vol. 137, no. 6, pp. 355–363, 1990.

[28] K. Y. Cho, J. D. Bae, S. K. Chung, and M. J. Youn, “Torque Harmonics Minimization in PM Synchronous Motor With Back EMF Estimation,” *IEEE Region 10 Conference on Computer, Communication, Control and Power Engineering*, vol. 5, no. 0, pp. 589–593, 1993.

[29] N. Matsui, T. Makino, and H. Satoh, “Autocompensation of Torque Ripple of Direct Drive Motor by Torque Observer,” *IEEE Transactions on Industry Applications*, vol. 29, pp. 187–194, Jan.-Feb. 1993.

[30] S.-J. Kang and S.-K. Sul, “Direct Torque Control of Brushless DC Motor With Nonideal Trapezoidal Back emf,” *IEEE Transactions on Industry Applications*, vol. 10, pp. 796–802, Jan.-Feb. 1995.

[31] B. Grcar, P. Cafuta, G. Stumberger, and A. M. Stankovic, “Control-Based Reduction of Pulsating Torque for PMAC Machines,” *IEEE Transactions on Energy Conversion*, vol. 17, no. 2, pp. 169–175, 2002.

[32] C. D. Angelo, G. Bossio, G. Garcia, J. Solsona, and M. I. Valla, "Sensorless Speed Control of Permanent Magnet Motors With Torque Ripple Minimization," *28th Annual Conference of the Industrial Electronics Society, IECON 02*, vol. 1, pp. 680–685, November 2002.

[33] H. J. Gutt, F. D. Scholl, and J. Blattner, "High Precision Servo Drives With DSP-Based Torque Ripple Reduction," *4th IEEE AFRICON*, vol. 2, pp. 632–637, September 1996.

[34] R. I. Davis and R. D.Lorenz, "Engine Torque Ripple Cancellation With an Integrated Starter Alternator in a Hybrid Electric Vehicle: Implementation and Control," *IEEE Transactions on Industry Applications*, vol. 39, pp. 1765–1774, Nov.-Dec. 2003.

[35] Y. Murai, Y. Kawase, K. Ohashi, K. Nagatake, and K. Okuyama, "Torque Ripple Improvement for Brushless DC Miniature Motors," *IEEE Transactions on Industry Applications*, vol. 25, pp. 441–450, February 1989.

[36] P. J. McCleer, J. S. Lawler, and B. Banerjee, "Torque Notch Minimization for Five Phase Quasi Square Wave Back EMF PM Synchronous Motors With Voltage Source Drives," *Conference Proceedings of ISIE'93 - Budapest*, pp. 25–32, 1993.

[37] T.-S. Kim, S.-C. Ahn, and D.-S. Hyun, "A New Current Control Algorithm for Torque Ripple Reduction of BLDC Motors," *The 27th Annual Conference of the IEEE Industrial Electronics Society*, vol. 2, pp. 1521–1526, 29 Nov.-2 Dec. 2001.

[38] Y. Sozer and D. A. Torrey, "Adaptive Torque Ripple Control of Permanent Magnet Brushless DC Motors," *Conference Proceedings of APEC '98*, vol. 1, pp. 86–92, February 2001.

[39] J. H. Song and I. Choy, "Commutation Torque Ripple Reduction in Brushless DC Motor Drives Using a Single DC Current Sensor," *IEEE Transactions on Power Electronics*, vol. 19, pp. 312–319, March 2004.

[40] J. Holtz and L. Springob, "Identification and Compensation of Torque Ripple in High-Precision Permanent Magnet Motor Drives," *IEEE Transactions on Industrial Electronics*, vol. 43, pp. 309–320, April 1996.

[41] V. Petrovic, R. Ortega, A. M. Stankovic, and G. Tadmor, “Design and Implementation of an Adaptive Controller for Torque Ripple Mminimization in PM Synchronous Motors,” *IEEE Transactions on Power Electronics*, vol. 15, pp. 871–880, September 2000.

[42] Z. Q. Zhu, D. Howe, and C. C. Chan, “Improved Analytical Model for Predicting the Magnetic Field Distribution in Brushless Permanent-Magnet Machines,” *IEEE Transactions on Magnetics*, vol. 38, no. 1, pp. 229–238, 2001.

[43] Z. Q. Zhu, D. Howe, E. Bolte, and B. Ackermann, “Instantaneous Magnetic Field Distribution in Brushless Permanent Magnet DC Motors, Part I: Open-Circuit Field,” *IEEE Transactions on Magnetics*, vol. 29, no. 1, pp. 124–135, 1993.

[44] Z. Q. Zhu and D. Howe, “Instantaneous Magnetic Field Distribution in Brushless Permanent Magnet DC Motors, Part III: Effect of Stator Slotting,” *IEEE Transactions on Magnetics*, vol. 29, no. 1, pp. 143–151, 1993.

[45] X. wang, Q. Li, S. Wang, and Q. Li, “Analytical Calculation of Air-Gap Magnetic Field Distribution and Instantaneous Characteristics of Brushless DC Motors,” *IEEE Transactions on Energy Conversion*, vol. 18, no. 3, pp. 424–432, 2003.

[46] A. B. Proca, A. Keyhani, A. El-Antably, W. Lu, and M. Dai, “Analytical Model for Permanent Magnet Motors With Surface Mounted Magnets,” *IEEE Transactions on Energy Conversion*, vol. 18, no. 3, pp. 386–391, 2003.

[47] J. F. Gieras, “Analytical Approach to Cogging Torque Calculation in PM Brushless Motors,” *International Electric Machines and Drives Conference, IEMDC ’03*, vol. 2, pp. 815–819, June 2003.

[48] B. Ackermann, J. H. H. Janssen, R. Sottek, and R. I. V. Steen, “New Technique for Reducing Cogging Torque in a Class of Brushless DC Motors,” *IEE Proc.-Electric Power Applications*, vol. 139, no. 4, pp. 315–320, 1992.

[49] W. J. Gibbs, *Conformal Transformations in Electrical Engineering*. 37 Essex Street W.C.2: Chapman & Hall LTD, 1958.

[50] Z. Q. Zhu and D. Howe, "Analytical Prediction of the Cogging Torque in Radial-Field Permanent Magnet Brushless Motors," *IEEE Transactions on Magnetics*, vol. 28, pp. 1371–1374, March 1992.

[51] J. H. L. E. C. Lovelace, T. M. Jahns, "Impact of Saturation and Inverter Cost on Interior PM Synchronous Machine Drive Optimization," *IEEE Transactions on Industry Applications*, vol. 36, pp. 723–729, May/June 2000.

[52] R. F. Schiferl and T. A. Lipo, "Power Capability of Salient Pole Permanent Magnet Synchronous Motors in Variable Speed Drive Applications," *IEEE Transactions on Industry Applications*, vol. 26, pp. 115–123, Jan./Feb. 1990.

[53] C. A. C. Coello and R. L. Becerra, "Evolutionary Multiobjective Optimization Using a Cultural Algorithm," *Proceedings of the 2003 IEEE Swarm Intelligence Symposium*, pp. 6–13, April 2003.

[54] R. Storn and K. Price, "Differential Evolution - a Simple and Efficient Adaptive Scheme for Global Optimization over Continuous Spaces," *Technical Report TR-95-012, ICSI*, March 1995.

[55] U. Pahner, R. Mertens, H. de Gersem, R. Belmans, and K. Hameyer, "A Parametric Finite Element Environment Tuned for Numerical Optimization," *IEEE Transactions on Magnetics*, vol. 34, pp. 2936–2939, September 1998.

[56] J. Lampinen, "Multi-Constrained Nonlinear Optimization by the Differential Evolution Algorithm," *6th On-line World Conference on Soft Computing in Industrial Applications (WSC6)*, September 2001.

[57] C. S. Chang, D. Y. Xu, and H. B. Quek, "Pareto-Optimal Set Based Multiobjective Tuning of Fuzzy Automatic Train Operation for Mass Transit System," *IEE Proceedings–Electric Power Applications*, vol. 146, pp. 577–583, September 1999.

[58] N. K. Madavan, "Multiobjective Optimization Using a Pareto Differential Evolution Approach," *Proceedings of the 2002 Congress on Evolutionary Computation, CEC '02*, vol. 2, pp. 1145–1150, May 2002.

[59] H. A. Abbass, R. Sarker, and C. Newton, "PDE: A Pareto-Frontier Differential Evolution Approach for Mmulti-Objective Optimization Problems," *Proceedings of the 2001 Congress on Evolutionary Computation*, vol. 2, pp. 971–978, May 2001.

[60] Z. Haznadar and Z. Stih, *Elektromagnetizam*, vol. I. Zagreb: Skolska knjiga, 1997.

[61] M. N. Sadiku, *Numerical Techniques in Electromagnetics - 2nd Edition*. CRC Press LLC, 2001.

[62] W. E. Boyce and R. C. Diprima, *Elementary Differential Equations and Boundary Value Problems*. John Wiley & Sons, 1986.

[63] R. Rabinovici, "Magnetic Field Analysis of Permanent Magnet Motors," *IEEE Transactions on Magnetics*, vol. 32, pp. 265–269, January 1996.

[64] J. Faiz and H. Jafari, "Two-Dimensional Magnetic Field Analysis of Internal-Rotor Permanent Magnet Motors," *IEEE Transactions on Magnetics*, vol. 35, pp. 4232–4237, September 1999.

[65] W. H. Beyer, *CRC Standard Mathematical Tables*. Boca Raton, Florida: CRC Press, Inc., 1981.

[66] P. J. Lawrenson and K. Gupta, "Conformal Transformation Employing Direct-Search Techniques of Minimisation," *Proc. IEE*, vol. 115, pp. 427–431, March 1968.

[67] J. S. Hsu, B. P. Scoggings, M. B. Scudierre, L. D. Marlino, D. J. Adams, and P. Pillay, "Nature and Assesment of Torque Ripples of Permanent-Magnet Adjustable-Speed Motors," *Thirtieth IAS Annual Meeting*, vol. 3, pp. 2696–2702, 1995.

[68] S. Huang, M. Aydin, and T. A. Lipo, "Torque Quality Assesment and Sizing Optimization for Surface Mounted Permanent Magnet Machines," *Thirty-Sixth IAS Annual Meeting*, vol. 3, pp. 1603–1610, 2001.

[69] R. Carlson, M. Lajoie-Mazenc, and J. C. dos S. Fagundes, "Analysis of Torque Ripple Due to Phase Commutation in Brushless DC Machines," *IEEE Transactions on Inductry Applications*, vol. 28, no. 3, pp. 632–638, 1992.

[70] Z. Q. Zhu and D. Howe, "Instantaneous Magnetic Field Distribution in Brushless Permanent Magnet DC Motors, Part II: Armature-Reaction Field," *IEEE Transactions on Magnetics*, vol. 29, no. 1, pp. 136–142, 1993.

[71] V. Gangla and J. D. L. Ree, "Electromechanical Forces and Torque in Brushless Permanent Magnet Machines," *IEEE Transactions on Energy Conversion*, vol. 6, no. 3, pp. 546–552, 1991.

[72] K. J. Binns and P. J. Lawrenson, *Analysis and Computation of Electrical and Magnetic Field Problems*. Pergamon Press, 1973.

[73] Z. Sirotic and Z. Maljkovic, *Sinkroni strojevi*. University of Zagreb, Faculty of Electrical and Engineering and Computing, 1996.

[74] T. A. Lipo, *Introduction to AC Machine Design*. Wisconsin Power Electronics Research Center, University of Wisconsin, 2004.

[75] M. Liwschitz-Garik and C. C. Whiple, *Electric Machinery, Vol. 2 AC Machines*. Van Nostrand Publishers, 1961.

[76] P. L. Alger, *Induction Machines - Their Behavior and Uses*. Gordon and Breach Science Publishers, 1965.

[77] I. Mandic, *Computation of Magnetic Fields in Saturated Iron Structures with Special Reference to the Computation of Short Circuit Performance of Induction Motors with Wound Rotors*. PhD thesis, University of Southampton, Faculty of Engineering and Applied science, Department of Electrical Engineering, Southampton, United Kingdom, 1974.

[78] D. Ban, D. Zarko, and I. Mandic, "Turbogenerator End Winding Leakage Inductance Calculation Using a 3-D Analytical Approach Based on the Solution of Neumann Integrals," *Accepted for publication in IEEE Transactions on Energy Conversion*, 2003.

[79] G. A. Campbell, "Mutual Inductance of Circuits Composed of Straight Wires," *Physical Review*, vol. 5, pp. 452–458, 1915.

[80] J. F. Gieras and M. Wing, *Permanent Magnet Motor Technology*. New York, Basel: Marcel Dekker, 2002.

[81] K. Attalah, Z. Q. Zhu, and D. Howe, "The Prediction of Iron Losses in Brushless Permanent Magnet DC Motors," *International Conference on Electrical Machines, ICEM '92*, pp. 814–818, September 1992.

[82] F. Deng, "An Improved Iron Loss Estimation for Permanent Magnet Brushless Machines," *IEEE Transactions on Energy Conversion*, vol. 14, pp. 1391–1395, December 1999.

[83] M. Chunting, G. R. Slemon, and R. Bonert, "Modeling of Iron Losses of Permanent-Magnet Synchronous Motors," *IEEE Transactions on Industry Applications*, vol. 39, pp. 734–742, May/June 2000.

[84] J. Hendershot and T. J. E. Miller, *Design of Brushless Permanent-Magnet Motors*. Oxford: Magna Physics Publishing and Clarendon Press, 1994.

[85] Vacuumschmelze, *Rare Earth Permanent Magnets VACODYM, VACOMAX*. Hanau: VACUUMSCHMELZE GmbH & Co. KG, 2003.

[86] F. Deng, "Commutation-Caused Eddy-Current Losses in Permanent-Magnet Brushless DC Motors," *IEEE Transactions on Magnetics*, vol. 33, no. 5, pp. 4310–4318, 1997.

[87] J. Lampinen and I. Zelinka, “Mixed Integer-Discrete-Continuous Optimization by Differential Evolution, Part 1: The Optimization Method,” *5th International Mendel Conference on Soft Computing*, pp. 71–76, June 1999.

[88] W. L. Soong and T. J. E. Miller, “Field-Weakening Performance of Brushless Synchronous AC Motor Drives,” *IEE Proc.-Electric Power Applications*, vol. 141, pp. 331–340, November 1994.

[89] J. Wai, “High Performance Testbed for an Automotive Direct-Drive Starter/Alternator Synchronous Machine,” Master’s thesis, University of Wisconsin-Madison, Department of Electrical and Computer Engineering, 2002.

APPENDIX
Solution of the Neumann Integral for Two Filaments in an Arbitrary Position in Space

The Neumann integral for two straight finite filaments in an arbitrary position to each other, or for one finite and two semi-infinite antiparallel filaments can be obtained in analytical form [77, 79]. The solution is presented here for all practical cases which may occur.

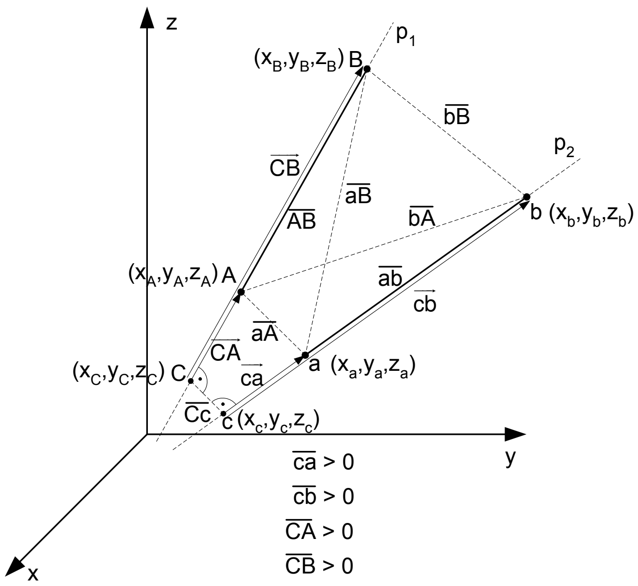

Fig. A.1 Two nonintersecting filaments $\overline{AB}$ and $\overline{ab}$ in space with common perpendicular $\overline{Cc}$

The solution of the Neumann integral for the filaments in Fig. A.1 is given by

$$\begin{aligned} N \;=\; & \cos\varphi \left[\overline{CB} \ln \frac{\left|\overline{aB}\right| + \left|\overline{bB}\right| + \left|\overline{ab}\right|}{\left|\overline{aB}\right| + \left|\overline{bB}\right| - \left|\overline{ab}\right|} - \overline{CA} \ln \frac{\left|\overline{aA}\right| + \left|\overline{bA}\right| + \left|\overline{ab}\right|}{\left|\overline{aA}\right| + \left|\overline{bA}\right| - \left|\overline{ab}\right|} + \right. \\ & \left. \overline{cb} \ln \frac{\left|\overline{bA}\right| + \left|\overline{bB}\right| + \left|\overline{AB}\right|}{\left|\overline{bA}\right| + \left|\overline{bB}\right| - \left|\overline{AB}\right|} - \overline{ca} \ln \frac{\left|\overline{aA}\right| + \left|\overline{aB}\right| + \left|\overline{AB}\right|}{\left|\overline{aA}\right| + \left|\overline{aB}\right| - \left|\overline{AB}\right|} \right] - \end{aligned}$$

$$
\left|\overline{Cc}\right| \cot\varphi \left[\arctan\left(\frac{\left|\overline{Cc}\right|}{\left|\overline{bB}\right|} \cot\varphi + \frac{\overline{cb}\overline{CB}}{\left|\overline{Cc}\right| \left|\overline{bB}\right|} \sin\varphi \right) - \right.
$$
$$
\arctan\left(\frac{\left|\overline{Cc}\right|}{\left|\overline{bA}\right|} \cot\varphi + \frac{\overline{cb}\overline{CA}}{\left|\overline{Cc}\right| \left|\overline{bA}\right|} \sin\varphi \right) - \arctan\left(\frac{\left|\overline{Cc}\right|}{\left|\overline{aB}\right|} \cot\varphi + \frac{\overline{ca}\overline{CB}}{\left|\overline{Cc}\right| \left|\overline{aB}\right|} \sin\varphi \right) +
$$
$$
\left. \arctan\left(\frac{\left|\overline{Cc}\right|}{\left|\overline{aA}\right|} \cot\varphi + \frac{\overline{ca}\overline{CA}}{\left|\overline{Cc}\right| \left|\overline{aA}\right|} \sin\varphi \right) \right] \tag{A.1}
$$

The distance $\overline{ca}$, $\overline{cb}$, $\overline{CA}$ or $\overline{CB}$ in (A.1) will be positive if the angle between its vector $\overrightarrow{ca}$, $\overrightarrow{cb}$, $\overrightarrow{CA}$ or $\overrightarrow{CB}$ and the directional vector of the infinite line p1 or p2 on which it lies is equal to zero. The distance will be negative if that angle is 180^0. All other distances in (A.1) are positive. The directional vectors of the infinite lines $p1$ and $p2$ are $\overrightarrow{AB}$ and $\overrightarrow{ab}$. The angle φ in (A.1) is the angle between the vectors $\overrightarrow{AB}$ and $\overrightarrow{ab}$. As an example, the case when $\overline{ca}$ and $\overline{CA}$ are negative is shown in Fig. A.2. The other cases when $\overline{ca}$, $\overline{cb}$, $\overline{CA}$ or $\overline{CB}$ are negative are also possible depending on the position of the common perpendicular.

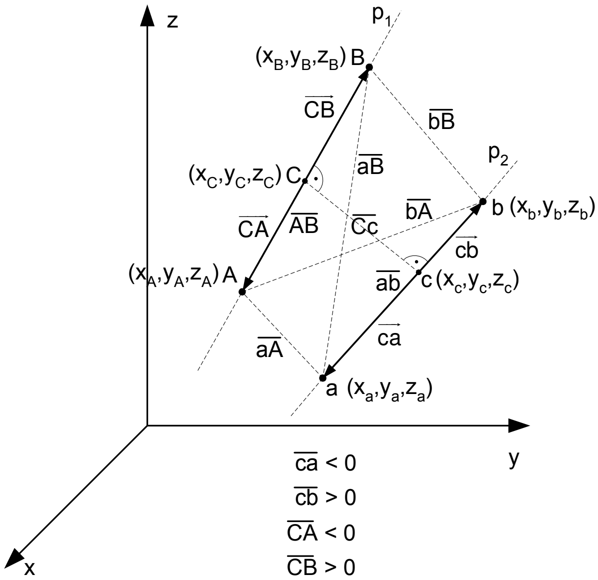

Fig. A.2 Two nonintersecting filaments $\overline{AB}$ and $\overline{ab}$ in space with common perpendicular $\overline{Cc}$ and negative $\overline{ca}$ and $\overline{CA}$

SPECIAL CASES

a) Filaments are perpendicular ($\varphi = 90^0$)

$$N = 0 \tag{A.2}$$

b) Filaments are parallel ($\varphi = 0^0$ or $\varphi = 180^0$)

$$\begin{aligned} N \;=\; & \left|\overline{AB}\right| \ln \frac{\left|\overline{aB}\right| + \overline{a'B}}{\left|\overline{bB}\right| + \overline{b'B}} - \overline{b'A} \ln \frac{\left|\overline{bB}\right| + \overline{b'B}}{\left|\overline{bA}\right| + \overline{b'A}} + \overline{a'A} \ln \frac{\left|\overline{aB}\right| + \overline{a'B}}{\left|\overline{aA}\right| + \overline{a'A}} - \\ & \left(-\left|\overline{aA}\right| + \left|\overline{bA}\right| + \left|\overline{aB}\right| - \left|\overline{bB}\right|\right) \end{aligned} \tag{A.3}$$

If either $\overline{AB}$ or $\overline{ab}$ is infinitely long, (A.1) will not give a finite result. However, a finite solution can be found in the case of two infinitely long parallel filaments which carry current in the opposite direction. This is shown in Fig. A.3.

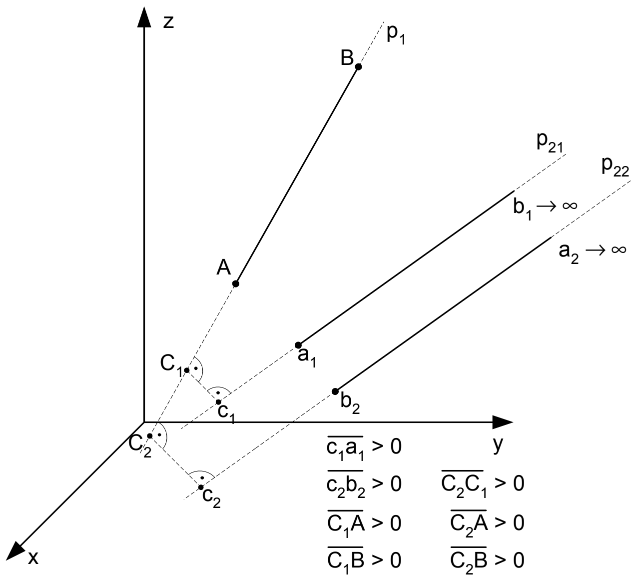

Fig. A.3 One finite length $\overline{AB}$ and two infinitely long nonintersecting filaments $\overline{a_1b_1}$ and $\overline{a_2b_2}$ with common perpendiculars $\overline{C_1c_1}$ and $\overline{C_2c_2}$

The Neumann integral for this case is

$$\begin{aligned}
N \;=\; & \cos\varphi\left[-\overline{c_2b_2}\ln\frac{\left|\overline{b_2A}\right|+\left|\overline{b_2B}\right|+\left|\overline{AB}\right|}{\left|\overline{b_2A}\right|+\left|\overline{b_2B}\right|-\left|\overline{AB}\right|}-\overline{c_1a_1}\ln\frac{\left|\overline{a_1A}\right|+\left|\overline{a_1B}\right|+\left|\overline{AB}\right|}{\left|\overline{a_1A}\right|+\left|\overline{a_1B}\right|-\left|\overline{AB}\right|}+\right.\\
& \overline{C_1B}\ln\frac{\left|\overline{b_2B}\right|-\overline{C_2B}\cos\varphi-\overline{c_2b_2}}{\left|\overline{a_1B}\right|-\overline{C_1B}\cos\varphi+\overline{c_1a_1}}+\overline{C_1A}\ln\frac{\left|\overline{a_1A}\right|-\overline{C_1A}\cos\varphi+\overline{c_1a_1}}{\left|\overline{b_2A}\right|-\overline{C_2A}\cos\varphi-\overline{c_2b_2}}+\\
& \left.\overline{C_2C_1}\ln\frac{\left|\overline{b_2B}\right|-\overline{C_2B}\cos\varphi-\overline{c_2b_2}}{\left|\overline{b_2A}\right|-\overline{C_2A}\cos\varphi-\overline{c_2b_2}}\right]-\left|\overline{C_1c_1}\right|\cot\varphi\left[\arctan\left(\frac{\overline{C_1B}}{\left|\overline{C_1c_1}\right|}\sin\varphi\right)-\right.\\
& \arctan\left(\frac{\overline{C_1A}}{\left|\overline{C_1c_1}\right|}\sin\varphi\right)-\arctan\left(\frac{\left|\overline{C_1c_1}\right|}{\left|\overline{a_1B}\right|}\cot\varphi+\frac{\overline{c_1a_1}\,\overline{C_1B}}{\left|\overline{C_1c_1}\right|\left|\overline{a_1B}\right|}\sin\varphi\right)+\\
& \left.\arctan\left(\frac{\left|\overline{C_1c_1}\right|}{\left|\overline{a_1A}\right|}\cot\varphi+\frac{\overline{c_1a_1}\,\overline{C_1A}}{\left|\overline{C_1c_1}\right|\left|\overline{a_1A}\right|}\sin\varphi\right)\right]+\left|\overline{C_2c_2}\right|\,cot\varphi\left[\arctan\left(\frac{\overline{C_2B}}{\left|\overline{C_2c_2}\right|}\sin\varphi\right)-\right.\\
& \arctan\left(\frac{\overline{C_2A}}{\left|\overline{C_2c_2}\right|}\sin\varphi\right)-\arctan\left(\frac{\left|\overline{C_2c_2}\right|}{\left|\overline{b_2B}\right|}\cot\varphi-\frac{\overline{c_2b_2}\,\overline{C_2B}}{\left|\overline{C_2c_2}\right|\left|\overline{b_2B}\right|}\sin\varphi\right)+\\
& \left.\arctan\left(\frac{\left|\overline{C_2c_2}\right|}{\left|\overline{b_2A}\right|}\cot\varphi-\frac{\overline{c_2b_2}\,\overline{C_2A}}{\left|\overline{C_2c_2}\right|\left|\overline{b_2A}\right|}\sin\varphi\right)\right]
\end{aligned}\tag{A.4}$$

All of the distances in (A.4) which are not placed inside the absolute value signs can be positive or negative, according to the rules given for (A.1).

SPECIAL CASES

a) Filaments are perpendicular ($\varphi = 90^0$)

$$N = 0 \tag{A.5}$$

b) Filaments are parallel ($\varphi = 0^0$ or $\varphi = 180^0$)

$$\begin{aligned}
N \;=\; & \left|\overline{AB}\right|\ln\frac{\left|\overline{a_1B}\right|+\overline{a_1'B}}{\left|\overline{b_2B}\right|+\overline{b_2'B}}-\overline{b_2'A}\ln\frac{\left|\overline{b_2B}\right|+\overline{b_2'B}}{\left|\overline{b_2A}\right|+\overline{b_2'A}}+\overline{a_1'A}\ln\frac{\left|\overline{a_1B}\right|+\overline{a_1'B}}{\left|\overline{a_1A}\right|+\overline{a_1'A}}-\\
& \left(-\left|\overline{a_1A}\right|+\left|\overline{b_2A}\right|+\left|\overline{a_1B}\right|-\left|\overline{b_2B}\right|\right)
\end{aligned}\tag{A.6}$$